

# Investigation in Crystal Growth/Morphology and Interface Engineering of Perovskite Solar Cells by Different Deposition Methods

Présentée le 18 mars 2022

Faculté des sciences de base  
Groupe SCI SB MN  
Programme doctoral en chimie et génie chimique

pour l'obtention du grade de Docteur ès Sciences

par

**Nadja Isabelle Désirée KLIPFEL**

Acceptée sur proposition du jury

Prof. A. Züttel, président du jury  
Prof. M. K. Nazeeruddin, directeur de thèse  
Prof. M. Lira-Cantú, rapporteuse  
Prof. P. Boix, rapporteur  
Prof. W. L. Queen, rapporteuse



# Acknowledgments

I would not have started on this learning path in solar technology without Prof. Mohammad Khaja Nazeeruddin. From the first day, he welcomed me into the Group for Molecular Engineering of Functional Materials in Switzerland. Special thanks go to him, as he has allowed me to develop my research projects and my research with freedom. His guidance helped me learn how to organize myself, collaborate with great scientists in the field, and learn from my mistakes with continuous improvement. His trust in my decision-making strengthened my self-confidence and helped me establish a safe work environment for myself and my colleagues. His advice and support helped me to develop myself professionally and personally.

I would like to express my gratitude, especially to Prof. Andreas Züttel, Prof. Wendy Queen, Prof. Pablo P. Boix, and Prof. Mónica Lira-Cantú, for dedicating their precious time to reading and evaluating my thesis and for being part of the jury during my oral exam.

Doing a Ph.D. is not only about learning the theory but also about experiences. A special thanks is therefore also going to Prof. Alison Walker, the project officer of MAESTRO, and her team, who continuously made sure that the project was running smoothly and that all the ESRs received an excellent education during the training events and secondments all over Europe. In this framework, special thanks are going to Prof. Francisco Fábregat-Santiago and Agustín, who made my research stay in Spain a fantastic one. I am grateful that I could learn the basics of Impedance Spectroscopy and enjoy the Spanish culture.

Without the past and present group members, my Ph.D. time would not have been so stimulating as it was. I, therefore, thank all of them for the exciting discussions, fruitful collaboration, and participation in group events outside the laboratory. An exceptional acknowledgment goes to Cristina Roldan-Carmona and Maria-Cristina Momblona, who have guided me since the early development of my Ph.D. study. Their collaboration, knowledge, and support were helping me through the good and the more

difficult times on a professional and personal level. Especially the collaborations and deep scientific discussions enabled me to develop many skills as a scientist. Thanks also for the hikes, travels, lunches, dinners, and many other activities. Muchas gracias!

I am also very grateful to Albertus, Cansu, Hiroyuki for their hard work and fruitful collaboration. Special thanks go in this context also to Prof. Dr. Naoyuki Shibayma. Without his effort and hard work for our collaborations, the perovskite and HTM orientation studies could not have been possible. I want to thank Mousa, Alex, Pavel, Alwani, and Keith for creating a pleasant atmosphere in the group and making my stay enjoyable. Without the hard work of Géraldine Gfeller and Isabel Wild, in assisting with traveling organization, administrative things, organizing of group activities, my visit would have been much more difficult. Thank you for your always-available support!

Another person to whom I am especially grateful is Mounir, who continuously supported me at any day or night hour with the XPS/UPS measurements. Without his help, I would not have been able to learn and master these techniques, which are now an essential contribution in all my research works. I am also indebted to Pascal S, who always ensured that the XRD was up and running.

A huge thanks also go to Stéphane and Robin, who were always ready to build and construct different parts for me, especially in urgent times. Other big thanks go to Cédric and Jean, who supported me with their expertise in all IT-related questions. In case of urgent security events, Fabio and Jérémie were ready to help at any time, which I am also very thankful for. Annabelle and Laurent, who managed the supplies in the magazine excellent and helped me ordering also more complicated things. Without Jennifer organization of typical Swiss Apéro events for the EPFL, Valais Campus life would not have been so rich during the pre-COVID times.

I also received assistance from people outside the university that I would like to thank. Clemens and Helgard have provided me with a spacious home during COVID confinement. Their support was a great help during this difficult time and allowed me to continue my studies smoothly. I am also thankful for Martin, who continuously supported me every day also in difficult times and who introduced me to my new favorite

dish, Ramen. A profound thanks go, of course, go to my parents, Margarete and Werner, and my two brothers, Lukas and Sven, for their support and encouragement throughout this time. Their numerous trips to Switzerland helped me discover the mountains more and take some relaxing time off from my research work. Without my friends Lisa, Simon, Isaac, Jordi, Hamza, and Jocelyn, my days would have been less colorful. I will always think back on the wonderful times we have spent together in the mountains, enjoying all the different seasons, especially in Valais.

Thank you, everyone, who helped make my Ph.D. one of the best experiences in my life!

Nadja Klipfel, Sion, January 2022



# Abstract

A new and promising technology has emerged to compete with traditional silicon photovoltaic semiconductors. The low material and processing costs and high-power conversion efficiencies of organic-inorganic metal halide perovskites make these a promising technology for the future. Despite record efficiencies for small-area devices, stability remains challenging. Due to rapid progress in the field, avenues for large-area commercial production are being explored. One approach is *via* thermal evaporation, which is presented in this work. The focus is on the vacuum-deposition method itself, the interface engineering of perovskite layers, and the study of a family of low-cost hole-transporting materials (HTM).

To improve reproducibility among research groups in vacuum-deposition processes, a better understanding and control of the crystal formation is essential. Of the experimental parameters, two were investigated that were not yet considered in-depth or combined: deposition speed and underlayer material. It was shown that perovskite growth rate changes affect preferred crystal orientation. In addition, it was found that the final perovskite composition is influenced by its underlayer chemistry.

Multi-source vacuum deposition of perovskite layers is complex due to the laborious calibration process necessary for proper stoichiometry. Single-source evaporation of pre-synthesized perovskite powders can reduce effort and time. The feasibility of obtaining pure phase films was demonstrated and confirmed by multiple analysis methods.

Interfaces in contact with the perovskite can be a source of defects with a deteriorating effect on stability and efficiency. The charge transport processes at the interface of electron transport material (ETM) and perovskite were investigated. The results showed a synergistic effect between  $c\text{TiO}_2$  and  $\text{C}_{60}$  and the importance of  $\text{C}_{60}$  as a charge extraction layer. The perovskite-hole transporting material (HTM) interface was also systematically studied. Monitoring of dopants showed, for the first time in literature,

TFSI anion migration through grain boundaries to the perovskite surface. It was further shown that non-radiative recombination pathways are reduced, indicating self-passivating of crystal defects during migration processes.

The state-of-the-art HTM 2,2',7,7'-tetrakis (N,N-di-p-methoxyphenylamine)-9,9'-spirofluorene (spiro-OMeTAD) is widely employed in spin-coated PSCs. Developing a less costly manufacturing alternative to this material that retains similar properties is a key challenge. A new class of Zn (II) and Cu (II)-based phthalocyanine HTMs functionalized with butyl- and ethylhexyl- groups in the periphery was investigated. Devices fabricated with the Zn (II)-based HTM (*n*-butyl functionalization) demonstrated the best performance. The device architecture with the highest stability maintained 80% of its initial power conversion efficiency (PCE) over 20h of illumination. At 20.2%, the perovskite architecture with the highest PCE also was the least stable, indicating a trade-off between these two characteristics for this HTM class.

**Keywords:** Perovskite, thermal evaporation, single-source evaporation, spin-coating, highly oriented, dopant migration, surface passivation, impedance spectroscopy, Cu/Zn-phthalocyanines



# Résumé

Une nouvelle technologie prometteuse est apparue pour concurrencer les semi-conducteurs photovoltaïques traditionnels à base de silicium. Les faibles coûts de matériaux et de traitement et les rendements élevés de conversion de puissance des pérovskites d'halogénures métalliques organiques-inorganiques en font une technologie prometteuse pour l'avenir. Malgré des rendements records pour les dispositifs de petite surface, la stabilité reste un défi. En raison des progrès rapides dans ce domaine, des solutions pour une production commerciale à grande échelle sont actuellement étudiées. L'une de ces approches est l'évaporation thermique, qui est présentée dans ce travail. L'accent est mis sur la méthode de dépôt sous vide elle-même, l'ingénierie de l'interface des couches de pérovskite, et l'étude d'une famille de matériaux de transport de trous (HTM) à faible coût.

Pour améliorer la reproductibilité entre les groupes de recherche sur les procédés de dépôt sous vide, il est essentiel de mieux comprendre et contrôler la formation des cristaux. Parmi les paramètres expérimentaux, deux ont été étudiés qui n'avaient pas encore été considérés en profondeur ou combinés : la vitesse de dépôt et le matériau de la sous-couche. Il a été démontré que les changements de vitesse de croissance de la pérovskite affectent l'orientation préférentielle des cristaux. En outre, il a été constaté que la composition finale de la pérovskite est influencée par la chimie de sa sous-couche.

Le dépôt sous vide à sources multiples de couches de pérovskite est complexe en raison du processus laborieux de calibrage nécessaire à une stœchiométrie correcte. L'évaporation à source unique de poudres de pérovskite pré-synthétisées peut réduire les efforts et le temps. La faisabilité de l'obtention de films de phase pure a été démontrée et confirmée par de multiples méthodes d'analyse.

Les interfaces en contact avec la pérovskite peuvent être une source de défauts ayant un effet détériorant sur la stabilité et le rendement. Les processus de transport de charge à l'interface du matériau de transport d'électrons (ETM) et de la pérovskite ont été étudiés. Les résultats ont montré un effet synergique entre  $c\text{TiO}_2$  et  $\text{C}_{60}$  et l'importance du  $\text{C}_{60}$  comme couche d'extraction de charge. L'interface pérovskite/HTM a

également été systématiquement étudiée. Le suivi des dopants a montré, pour la première fois dans la littérature, la migration des anions TFSI à travers les joints de grains vers la surface de la pérovskite. Il a également été démontré que les voies de recombinaison non radiative sont réduites, ce qui indique une auto-passivation des défauts cristallins pendant les processus de migration.

Le HTM spiro-OMeTAD est largement utilisé dans les PSCs à revêtement par centrifugation. Le développement d'une alternative de fabrication moins coûteuse à ce matériau et conservant des propriétés similaires est un défi majeur. Une nouvelle classe de HTM à base de complexes de phtalocyanine coordonnés par un métal a été étudiée. Les dispositifs fabriqués avec la HTM à base de Zn (II) (fonctionnalisation n-butyle) ont montré les meilleures performances. L'architecture du dispositif avec la plus grande stabilité a maintenu 80% de son efficacité de conversion de puissance initiale (PCE) sur 20h d'illustration. À 20,2 %, l'architecture pérovskite présentant le meilleur PCE était également la moins stable, ce qui indique un compromis entre ces deux caractéristiques pour cette classe de HTM.

**Mots clés :** Pérovskite, évaporation thermique, évaporation à source unique, revêtement par centrifugation, très orienté, migration de dopants, passivation de surface, spectroscopie d'impédance, phtalocyanines de Cu/ Zn

# Table of Contents

Acknowledgments .....	v
Abstract.....	ix
Résumé.....	11
Table of Contents.....	13
List of Figures .....	16
List of Tables .....	21
Symbols and Abbreviations.....	23
Introduction .....	31
1.1 Metal Halide Perovskite Material .....	33
1.2 Different Deposition Methods of Perovskite Films.....	35
1.2.1 Solution-Processed Perovskite Materials .....	36
1.2.2 Vacuum based Deposition of Perovskite Materials.....	38
1.3 Perovskite Solar Cells.....	42
1.3.1 Working Principle of p-n junction Solar Cells.....	42
1.3.2 Device Architectures of PSCs .....	47
1.3.3 PSCs Characterization.....	49
1.4 General Limiting Factors in Perovskite Solar Cells .....	51
1.4.1 Toxicity.....	51
1.4.2 Cost.....	53
1.4.3 Stability .....	53
1.4.4 Towards Shockley-Queisser Limit .....	56
Advantages and Limiting Factors of Vacuum-deposited Perovskite Layers .....	59
1.5 Controlling the Perovskite Composition .....	61
1.5.1 Controlling the Perovskite Morphology.....	61
1.6 Interface Engineering in Perovskite Solar Cells.....	62
1.6.1 Interface Engineering in Thermally Evaporated Perovskite Cells.....	65
Motivation and Strategy .....	69

Crystallographically Oriented Perovskites via Thermal Vacuum Codeposition .....	73
1.7 Introduction .....	74
1.8 Results and Discussion .....	76
1.9 Conclusions .....	90
Structural and Optoelectrical Characterization of Single-Source Evaporation of Phase Pure CsFAPbI <sub>3</sub> and FAPbI <sub>3</sub> Perovskite Thin Films.....	93
1.10 Introduction.....	94
1.11 Results and Discussion .....	96
1.12 Conclusion .....	105
C60 Thin Films in Perovskite Solar Cells: Efficient or Limiting Charge Transport Layer? .....	107
1.13 Introduction.....	108
1.14 Results and Discussion .....	109
1.15 Conclusions.....	121
Mechanistic Insights into the Role of the Bis(trifluoro-methanesulfonyl)imide Ion in Co-Evaporated p-i-n Perovskite Solar Cells.....	123
1.16 Introduction.....	124
1.17 Results and Discussion .....	126
1.18 Conclusion .....	136
Zn(II) and Cu(II) tetrakis(diarylamine)phthalocyanines as Hole-Transporting Materials for Perovskite Solar Cells.....	137
1.19 Introduction.....	138
1.20 Results and Discussion .....	141
1.21 Conclusion .....	155
Conclusions and Outlook.....	157
References.....	161

Table of Contents

---

Appendix A: Supplementary Information to Chapter 4 .....	191
Appendix B: Supplementary Information to Chapter 5.....	209
Appendix C: Supplementary Information to Chapter 6 .....	227
Appendix D: Supplementary Information to Chapter 7 .....	243
Appendix E: Supplementary Information to Chapter 8.....	263
Curriculum Vitae .....	290
List of Publications .....	293

# List of Figures

Figure 1.1. 3D perovskite crystal structure of hybrid organic-inorganic perovskite MAPbI <sub>3</sub> . The inorganic lead iodide-based framework encloses the organic methylammonium cation. ....	34
Figure 1.2: Schematics illustrating the spin-coating process of the one-step perovskite deposition process. ....	36
Figure 1.3. Schematics illustrating the spin-coating process of the two-step perovskite deposition process. ....	37
Figure 1.4. Schematics illustrating the spin-coating process of the antisolvent deposition process. ....	38
Figure 1.5: Schematics displaying the two different evaporation set-ups a) dual-source evaporation of MAPbI <sub>3</sub> b) single-source evaporation of pre-synthesized perovskite powder. ....	39
Figure 1.6: Schematics of the general working principle of the perovskite solar cell....	42
Figure 1.7: Schematic of radiative recombination. ....	43
Figure 1.8: Schematic of defect or trap assisted recombination a) donor type and b) acceptor type trap, $r_1$ = electron capture from the CB, $r_2$ = electron emission from the CB, $r_3$ = hole capture from the VB, $r_4$ = hole emission from the VB.....	44
Figure 1.9: Schematic of Auger recombination a) involving two electrons b) two holes. ....	45
Figure 1.10: Schematic of surface recombination.....	45
Figure 1.11: Schematic of the different device architectures: a) normal ( <i>n-i-p</i> ) planar configuration b) normal ( <i>n-i-p</i> ) mesoscopic configuration c) inverted ( <i>p-i-n</i> ) planar configuration .....	47
Figure 1.12: <i>J-V</i> characteristics of solar cells in light and dark conditions. ....	49
Figure 1.13: Illustration of transition between $\delta$ -FAPbI <sub>3</sub> and $\alpha$ -FAPbI <sub>3</sub> . ....	54
Figure 1.14: Illustration of transition between $\delta$ -CsFAPbI <sub>3</sub> and $\alpha$ -CsFAPbI <sub>3</sub> . ....	55
Figure 1.15: Shockley Queisser limit for maximum PCE in relation with the bandgap, considering AM 1.5G illumination at 25°C. The data was plotted from the reference data reported by Sven Rühle. <sup>[152]</sup> .....	57

- Figure 2.1 Illustration of the defects in the perovskite lattice: a) non-defect lattice b) B-site vacancy c) X-site vacancy d) B-X antisite substitution, e) interstitial of A f) interstitial of X g) dangling bonds h) grain boundary. .... 64
- Figure 4.1: Dual-source evaporation process and device configuration. a) Co-evaporation of MAPbI<sub>3</sub> from PbI<sub>2</sub> and MAI precursors at several deposition rates (from C-4C) and substrate architecture. b) p- and n-type semiconductors (HTM and ETM, respectively) employed as underlying charge transport materials.....77
- Figure 4.2: MAPbI<sub>3</sub> films grown on NiOx. a) Energy levels extracted from UPS measurements of films grown at several deposition rates (from C to 4C). b) UV-visible absorption and c) PL spectra of films shown in an (excitation wavelength  $\lambda = 450$  nm) d) WAXS images of films shown in a. e) Integration of the azimuthal intensity along the 220 reflex in WAXS. Inset: schematic of 220 lattice plane orientation showing out-of-plane orientation relative to the substrate (cubes in different brown shading: 220 lattice plane tilted 78° (C), 75° (2C), 80° (3C) from the substrate). Note the apparent trend in 4C of intensity between 80-90°. Fewer white cubes indicate a more preferred orientation. d) UV-visible absorption and PL spectra of films (excitation wavelength  $\lambda = 450$  nm)..... 80
- Figure 4.3: MAPbI<sub>3</sub> films grown on spiro-OMeTAD. a) Integration of the azimuthal intensity along the 220 reflex ( $2.0 \text{ \AA}^{-1}$ ) in WAXS for films crystallized at different deposition rates (from C to 4C). Inset: schematic of grains with 220 lattice plane showing out-of-plane orientation (indicated by cubes with purple shading: tilted 76° (C), 72° (2C), 72° (3C) from the substrate). Grains with 004 lattice plane showing in-plane orientation (indicated by cubes with grey shading: tilted 72° (C), 76° (2C), 76° (3C) from the substrate). Note the apparent trends for peak intensity angles between 70-90° of 220-lattice plane (4C). Fewer white cubes indicate more preferred orientation b) Cross-section and top-view (inset) SEM images of MAPbI<sub>3</sub> formed on spiro-OMeTAD substrates. c) Estimated grain-size distribution of the perovskite layers..... 82

Figure 4.4: MAPbI<sub>3</sub> films deposited on several semiconductors. a) Energy levels extracted from UPS data of perovskites formed on top of n- and p-type underlayers prepared under the same evaporation condition (3C). b) Compositional data extracted from XPS for the elements lead (Pb 4f), nitrogen (N 1s), and iodide (I 3d). c) PL spectra recorded for all conditions. d) Integration of the azimuthal intensity distribution of the 220 reflex in the WAXS data. Inset: schematic of grains with 220 lattice plane showing out-of-plane alignment relative to the substrate (for perovskite on meso-TiO<sub>2</sub>, red cube 220 lattice plane 80° from the substrate; for perovskite on PEDOT: PSS, blue cube 220 lattice plane 90° from the substrate)..... 84

Figure 4.5: Evolution of vacuum deposited MAPbI<sub>3</sub> layers. a) WAXS images of 35 nm films grown on NiO<sub>x</sub>, spiro-OMeTAD, and PEDOT: PSS. Diffractions related to FTO and PbI<sub>2</sub> are indicated in the label. b) Evolution of XRD patterns with increasing film thickness. .... 87

Figure 4.6: Influence of deposition rate on crystallization and device performance. a) Scheme of *p-i-n* architecture employed for the PSCs. b) 2D-detector images of 500 nm MAPbI<sub>3</sub> grown on spiro-OMeTAD at different deposition rates (from C to 4C). The spots indicate preferred out-of-plane orientation. c) Top- and cross-section SEM of MAPbI<sub>3</sub> films (3C). Scale bar: 1 μm. d), J-V curves, and d) EQE spectra of typical devices, including absorption spectra for underlayer spiro-OMeTAD containing films shown in a and b..... 90

Figure 5.1 a) Schematic for single-source evaporation of presynthesized α-CsFAPbI<sub>3</sub> and δ-FAPbI<sub>3</sub> perovskite powder, b,c) diffractograms of CsFAPbI<sub>3</sub> thin films on glass b) as-deposited and c) annealed at 60°C for 3 min, d,e) diffractograms of FAPbI<sub>3</sub> thin films on glass d) as-deposited and e) annealed at 200°C for 10s. .... 97

Figure 5.2 GIWAXS images taken at an angle of 0.12 of a) CsFAPbI<sub>3</sub> film as deposited b) CsFAPbI<sub>3</sub> film annealed at 60°C. Integrated q-data of the GIWAXS images for c) as-deposited CsFAPbI<sub>3</sub> film and d) CsFAPbI<sub>3</sub> film after post-annealing at 60°C. .... 100



Figure 5.3 Storage stability of the perovskite layers. a,b) diffractograms over two weeks for a) CsFAPbI<sub>3</sub> and b) FAPbI<sub>3</sub> layers stored under dry air. Planes labeled in black correspond to  $\alpha$ -phase and in brown to  $\delta$ -phase..... 102

Figure 6.1. a) Schematic representation of the device architectures used in this study. b) *JV* characteristics of the most efficient device per condition using b) FTO/C<sub>60</sub> with C<sub>60</sub> thickness being: 5 nm, 10 nm, 15 nm, 20 nm, and 30 nm and c) FTO/cTiO<sub>2</sub>/C<sub>60</sub> as ETMs with C<sub>60</sub> thickness being: 0 nm, 5 nm, 10 nm, 15 nm, 20 nm, and 30 nm, respectively. d) Energy level diagram for different C<sub>60</sub> thicknesses deposited on FTO/cTiO<sub>2</sub>. .....111

Figure 6.2. a) Film structure of co-evaporated MAPbI<sub>3</sub> thin films deposited on top of glass/C<sub>60</sub> or glass/cTiO<sub>2</sub>/C<sub>60</sub>, b) and c) steady-state PL spectra ( $\lambda_{exc}=475$  nm) and time-resolved PL decay ( $\lambda_{exc} = 655$  nm) of glass/cTiO<sub>2</sub>/C<sub>60</sub>/MAPbI<sub>3</sub> samples and d) cross-sectional SEM images of co-evaporated MAPbI<sub>3</sub> thin films deposited on top of FTO/cTiO<sub>2</sub>/C<sub>60</sub> and FTO/C<sub>60</sub> with the C<sub>60</sub> thicknesses being 15 nm. .... 115

Figure 6.3. a) and b) Impedance Spectroscopy response measured under illumination at 900 mV for the different thicknesses of C<sub>60</sub>-layer on perovskite solar cells with (filled dots) and without (empty dots) cTiO<sub>2</sub> layer. c) Equivalent circuit used to fit the impedance spectra composed by: series resistance (R<sub>S</sub>), geometrical capacitance (C<sub>g</sub>), transfer resistance (R<sub>tr</sub>), recombination resistance (R<sub>rec</sub>), internal capacitance (C<sub>int</sub>), extra recombination resistance (R<sub>L</sub>), and inductance (L). .....116

Figure 6.4. Results of the fitting of the impedance responses a) series resistance (R<sub>S</sub>) and transport resistance (R<sub>tr</sub>) in dependence of C<sub>60</sub> thickness b) recombination resistance (R<sub>rec</sub>) and extra recombination resistance (R<sub>L</sub>) in dependence of C<sub>60</sub> thickness c) geometrical capacitance (C<sub>g</sub>) and internal capacitance (C<sub>int</sub>) in dependence of C<sub>60</sub> thickness d) are plotted the characteristic times: transport ( $\tau_{tr}$ ), recombination ( $\tau_{rec}$ ), and extra recombination ( $\tau_L$ ). .....119

Figure 7.1: Co-evaporated MAPbI<sub>3</sub> thin films deposited on top of glass or glass/HTM (tBP, Li-tBP, Co-tBP, 3Co-tBP and Li-Co-tBP): a) absorbance spectra, b) steady-state PL spectra ( $\lambda_{exc}=475$  nm) and c) time-resolved PL decay ( $\lambda_{exc}=655$  nm). .... 127

Figure 7.2: a) F<sub>1s</sub> XPS spectra of 500 nm perovskite film deposited on top of doped-HTM. b) F<sub>1s</sub>/Pb<sub>4f</sub> atomic ratio calculated by XPS at the perovskite surface with different perovskite thicknesses deposited on ITO/HTM. c) F atomic concentration detected by EDX in 500 nm perovskite bulk. d) Schematic representation of the TFSI migration process. .... 131

Figure 7.3: a) Energy level diagram of the fabricated *p-i-n* solar cells. b) *J-V* characteristics of the most efficient devices. c) Long-term stability of the unencapsulated solar cells under 1 sun illumination at 25°C in nitrogen atmosphere. .... 135

Figure 8.1. Molecular structure of Zn(II) and Cu(II) phthalocyanines bearing bis(4-alkoxyphenyl)amino substituents. ....141

Figure 8.2. UV-Vis spectra of tetrasubstituted MPCs in THF solution. .... 143

Figure 8.3. a) Steady-state photoluminescence spectra ( $\lambda_{exc}=475\text{nm}$ ), b) time-resolved PL decay ( $\lambda_{exc}=640\text{nm}$ ,  $\lambda_{em}=760\text{nm}$ ). GIWAXS pattern of the films coated on a silicon wafer: c) spiro-OMeTAD and d) Zn-BL54..... 145

Figure 8.4. a) Energy level diagram of the device containing doped HTMs (HOMO values for the HTMs, double and triple cation perovskite from their corresponding UPS measurements), b) *J-V* curves of the most efficient devices based on triple cation perovskite, c) long-term stability of unencapsulated triple cation-based devices measured under continuous light illumination at 25°C in a nitrogen atmosphere and with inset water contact angle of spiro-OMeTAD and Zn-BL54 deposited on top of the perovskite layer and d) *J-V* curves of the most efficient solar cells containing double cation-based perovskite. .... 150

# List of Tables

Table 2.1: Advantages and disadvantages of the vacuum-deposition method.....	60
Table 4.1: Compositional analysis of MAPbI <sub>3</sub> deposited on p- and n-type semiconductors. Atomic ratios extracted from the XPS data are shown in Figure A.15 (Appendix A). .....	85
Table 6.1. PV parameters extracted from the corresponding <i>JV</i> curves of the most efficient devices.....	112
Table 7.1: PV parameters extracted from the corresponding <i>J-V</i> curves of the most efficient devices and lateral conductivity of dopant-free and doped spiro- OMeTAD layers.....	134
Table 8.1. Photovoltaic parameters extracted from the corresponding <i>J-V</i> curves for triple cation and double cation-based most efficient devices.....	151



# Symbols and Abbreviations

°C	degree Celsius
0D	zero-dimensional
1D	one-dimensional
2D	two-dimensional
3D	three-dimensional
Å	angstrom
AFM	atomic force microscopy
AM	air mass
cTiO <sub>2</sub>	compact-TiO <sub>2</sub>
C <sub>60</sub>	fullerene
CB	conduction band
CBM	conduction band minimum
CdTe	cadmium telluride
CdS	cadmium sulfide
C <sub>g</sub>	geometrical capacitance
C <sub>int</sub>	internal capacitance
CIGS	cadmium indium gallium selenide
CoTFSI	cobalt- bis(trifluoromethanesulphonyl) imide
CV	cyclic voltammetry

DFT	density functional theory
DMF	dimethylformamide
DMSO	dimethyl sulfoxide
DSC	dye synthesized solar cell
$E_b$	electron binding energy
EBSD	electron backscatter diffraction
$E_g$	bandgap
EQE	external quantum efficiency
ETL	electron-transporting layer
ETM	electron-transporting material
eV	electron volt
$E_{VB}$	valence band value
FAI	formamidinium iodide
$FF$	fill factor
FTO	fluorine-doped tin oxide
GBL	$\gamma$ -butyrolactone
$h$	Planck constant
h	hour
HI	hydrogen iodide
HOMO	highest-occupied molecular orbital

HTL	hole-transporting layer
HTM	hole-transporting material
$I$ - $V$	current-voltage
$I_{in}$	incident power
IP	ionization potential
$I_{ph}$	photocurrent
IS	impedance spectroscopy
ITO	indium-doped tin oxide
$J$ - $V$	current density-voltage
$J_o$	saturation current density
$J_{ph}$	photogenerated current density
$J_{sc}$	short-circuit current density
K	kelvin
$k_B$	Boltzmann constant
kWh	kilo watt-hour
LiTFSI	li-bis(trifluoromethanesulphonyl) imide
LUMO	lowest-unoccupied molecular orbital
M	molar
MA	methylammonium
MABr	methylammonium bromide

MAI	methylammonium iodide
MAPbI <sub>3</sub>	methylammonium lead iodide
mbar	millibar
mg	milligram
mL	milliliter
min	minute
mM	millimolar
mmol	millimole
MOF	metal-organic framework
mp-TiO <sub>2</sub>	mesoporous-TiO <sub>2</sub>
MPP	maximum power point
MPPT	maximum power point tracking
MS	mass spectrometry
NiO <sub>x</sub>	nickel-oxide
<i>n-i-p</i>	negative-intrinsic- positive
nm	nanometer
NMR	nuclear magnetic resonance
ns	nanosecond
OFET	organic field-effect transistor
OLED	organic-light-emitting device



OPV	organic photovoltaics
PCE	power conversion efficiency
PEDOT:PSS	poly(3,4-ethylenedioxythiophene) polystyrene sulfonate
<i>p-i-n</i>	positive-intrinsic-negative
PL	photoluminescence
$P_{max}$	maximum power
PSC	perovskite solar cell
PTAA	poly[bis(4-phenyl)(2,4,6-trimethylphenyl)amine]
PV	Photovoltaic
PVD	physical vapor deposition
$q$	elementary charge
QCM	quartz crystal microbalances
$q_{xy}$	scattering observed in the plane of the substrate
$q_z$	scattering observed out-of-plane to the substrate
$r$	radius
R	large organic cation
RMS	root-mean-square
$R_{rec}$	recombination resistance
$R_{tr}$	transport resistance
PV	photovoltaics

r.p.m	rotation per minute
s	second
series resistance	$R_s$
SEM	scanning electron microscopy
spiro-OMeTAD	2,2,7,7-tetrakis( <i>N,N</i> -di- <i>p</i> -methoxyphenylamine)-9,9-spirobifluorene
SRH	Schockley-Read-Hall
STC	standard test condition
$T$	temperature
TAA	titanium diisopropoxide bis(acetylacetonate)
t	time
$\tau_L$	characteristic extra recombination time
$\tau_{tr}$	characteristic time for transport of the charges
$\tau_{rec}$	characteristic time for recombination of the charges
TaTm	$N_4, N_4, N_4'', N_4''$ -tetra([1,1'-biphenyl]-4-yl)-[1,1':4',1''-terphenyl]-4,4''-diamine
tBP	4- <i>tert</i> -butylpyridine
TCO	transparent conducting oxide
TEM	transmission electron microscopy
$t_G$	Goldschmidt tolerance factor

TrPL	time-resolved photoluminescence
UPS	ultraviolet photoelectron spectroscopy
UV	ultraviolet
UV-vis	ultraviolet-visible
$\nu$	frequency
V	volt
VB	valence band
VBM	valence band maximum
$V_{MPP}$	voltage at maximum power point
$V_{OC}$	open-circuit voltage
W	watt
WAXS	wide-angle x-ray scattering
XPS	x-ray photoelectron spectroscopy
XRD	x-ray diffraction
$\theta$	diffraction angle
$\lambda$	wavelength
$\mu$	mobility
$\mu\text{L}$	microliter
$\mu\text{m}$	micrometer
$\phi$	work function

$\Psi_{ph,\lambda}$  spectral photon flow incident on the solar cell

# Introduction

In combination with a steadily rising world population, global warming entails new challenges to provide humankind with energy in an environmentally friendly, sustainable, and cost-efficient way. The world population will reach 9 billion by 2040, and the living standards are expected to increase in highly populated countries like China or India, which contain more than a third of the world population.<sup>[1,2]</sup> In a society still highly dependent on fossil fuels, cost-efficient and environmentally friendly alternatives are mandatory.<sup>[3]</sup>

Global warming is not anymore only a theoretical description. Scientific reports describe with evidence the effect of industrialization on the wellbeing of our environment.<sup>[4]</sup> The atmospheric carbon dioxide levels raised from 300 ppm to over 400 ppm within the last 70 years through human-made emissions. Especially the last 35 years mark the time where most of the global warming happened, which resulted in an average increase of the earth's surface temperature around 0.9°C.<sup>[5]</sup> Warming oceans, decrease in arctic ice sheets, glacial retreat, shrinking snow coverage, rising sea levels, and mass extinctions are all results of the current human way of living. Rethinking our economic approaches to prevent further damage to the environment is crucial to avoid further damage. A circular economy is a new buzzword to describe an alternative to the traditional linear economy, which aims to extract the maximum value of each product by keeping it as long as possible in use. At the same time, at the end of each service life, materials are recovered or regenerated. Fundamental research at Universities or Institutes gives direction for innovations, which can later lead to new products on the market. Is it, therefore, not also the responsibility of the researchers, which are standing at the foundation of innovation, to keep the concept of circular economy in mind when exploring new ideas, especially in applied science, to contribute towards a more sustainable world?

Sun, wind, and water are natural sources that can transform natural energy into electricity. In Switzerland, 60% of the domestic electricity is generated by renewable energy, mainly from hydropower stations.<sup>[6]</sup> Switzerland consumes 58.46 billion kWh per year, which results in a total energy consumption per person of 6768 kWh per year.<sup>[3]</sup>

Swisstopo and MeteoSwiss showed that 80% of the Swiss energy consumption could be generated if solar panels covered all roofs in Switzerland.<sup>[7]</sup>

Solar energy indeed is the only unlimited energy source on earth. The sun's surface has a temperature of 6000 K and emits an irradiance of 1361 W/m<sup>2</sup>.<sup>[8]</sup> After passing through the atmosphere, it still has an irradiance power of 1000 W/m<sup>2</sup> that could be transformed into valuable energy.<sup>[9]</sup> At present, silicon modules dominate the photovoltaic market due to their feasible cost, stability, and efficiency. For mono-crystalline silicon wafer-based technology, a power conversion efficiency (PCE) of 26.7% can be achieved,<sup>[10]</sup> and for multi-crystalline silicon, a PCE of 22.3% is reported for a typical panel on the market.<sup>[11]</sup> Nevertheless, several drawbacks require the development of new generation solar cells. Up to now, the photovoltaic market has been controlled by a 95% total production share by silicon-wafer-based technology.<sup>[12]</sup> However, highly pure silicon crystals are required during manufacturing as small impurities cause deleterious effects on the performance.<sup>[13]</sup> Additionally, their heavyweight and rigid substrates cannot everywhere be installed, and their efficiency can reach at best the Shockley-Queisser limit (max. 30%).<sup>[14]</sup> To be competitive or even outperform silicon solar cells, the new generation must meet requirements that cannot be reached with today's conventional ones. Especially needs such as lower production costs, higher efficiencies, lightweight (flexible), and lower material consumption (thin-film technology) should be met. The second generation of solar cells included amorphous Si-based thin-film solar cells, Cadmium Telluride/Cadmium Sulfide (CdTe/CdS) solar cells, and Copper Indium Gallium Selenide (CIGS) solar cells. Compared to the first generation, these solar cells could be produced more cost-efficient, are in visual aesthetics more appealing, but have lower efficiencies approaching 20%.<sup>[14]</sup>

Consequently, the third generation of solar cells was developed to improve further. Dye-sensitized solar cells (DSSC) and organic photovoltaics (OPV) were developed in this generation. These solar cells are solution-processable and seem to meet all the requirements mentioned above. However, with efficiencies, only between 11-14%, and problems in the upscaling and commercialization, these solar cells have never reached

the market so far.<sup>[14]</sup> In 2009 a new generation of solar cells based on the DSSC technology emerged from the research community. Perovskite solar cell (PSC) technology was developed within the last 11 years so far that efficiencies of 25.6% at lab-scale were already reported, which displays the immense potential of the 4<sup>th</sup> generation solar cell technology.<sup>[15]</sup> It is thought that PSC can compete with crystalline and thin-film photovoltaic systems, mainly because they demonstrated many advantages when considering photovoltaic applications. PSCs can be fabricated by different fabrication methods, such as solution-process (e. g. inkjet-printing, screen printing, slot-die coating, spin-coating, spray-coating) and vacuum-based processes, such as physical vapor deposition (PVD) (thermal evaporation) or chemical vapor deposition (CVD).<sup>[16-18]</sup> The processing methods' versatility enables perovskites to be considered for large-scale fabrication processes. Also, the possibility of using different deposition methods enables the deposition also on multiple substrates, including flexible substrates, used in wearable devices.<sup>[19,20]</sup> The color-tuning of the perovskite through small changes in the chemical composition enables the colorful perovskite films,<sup>[21]</sup> precise control of the thickness while still obtaining considerable efficiencies plus the possibility of fabricating semi-transparent devices,<sup>[22]</sup> make perovskite an attractive technology for building integration like windows, roofs, or building facades.<sup>[21,23,24]</sup>

## 1.1 Metal Halide Perovskite Material

The metal halide perovskite's crystal structure has the unique advantage of tuning possibilities, resulting in different dimensional crystal structures, such as zero- (0D), one- (1D), quasi-two- and two-(2D), and three- (3D).<sup>[25-27]</sup> In this thesis, my main focus is the 3D perovskite structure.

Perovskites belong to a broad class of crystalline materials with the general formula  $ABX_3$ .<sup>[28]</sup> This simplest crystal structure consists of a 3D network of corner-sharing  $BX_6$  octahedra (Figure 1.1). The B atom (red in Figure 1.1) is a metallic cation (such as  $Pb^{2+}$  or  $Sn^{2+}$ ), X represents a monovalent anion (blue), typically a halide ( $I^-$ ,  $Br^-$ ,  $Cl^-$ ).<sup>[29-31]</sup> A represents a small cation (A, yellow) that fits into the empty gaps between the

octahedra. It can be an organic one (methylammonium ( $\text{CH}_3\text{NH}_3^+$ ), formamidinium ( $\text{NH}_2\text{CH}=\text{NH}_2^+$ ), or an inorganic cation such as cesium  $\text{Cs}^+$ .<sup>[32]</sup>

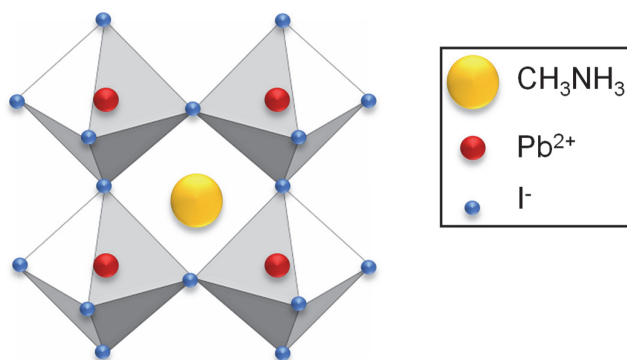


Figure 0.1. 3D perovskite crystal structure of hybrid organic-inorganic perovskite  $\text{MAPbI}_3$ . The inorganic lead iodide-based framework encloses the organic methylammonium cation.

The Goldschmidt tolerance factor ( $t$ ) is an empirical measure to describe the fit of the A-site cation into the cubic corner-sharing  $\text{BX}_6$  octahedra, considering that the lattice is an array of closed-packed spheres.<sup>[33]</sup> The factor is a measure to predict the stable crystal structure of the perovskite material in terms of ionic packing.

$$t = \frac{r_A + r_X}{\sqrt{2} (r_B + r_X)} \quad (1)$$

Where  $r_A$ ,  $r_B$ , and  $r_X$  are the ionic radii of A, B, X. Cubic crystal structure is preferred if the  $t$  value is between 0.8 and 1.0. If the  $t$ -value is higher than 1.0 and smaller than 0.8, no perovskite structure is formed.<sup>[34-37]</sup>

If considering the simplest perovskite structure methylammonium lead iodide ( $\text{MAPbI}_3$ ), the perovskite structure was shown to have three different thermodynamically stable crystal phases depending on the temperature.<sup>[38]</sup> Cubic crystal phase above 330K, the tetragonal crystal phase from 160K to 330 K and orthorhombic crystal phase below 160K.<sup>[38]</sup>

Hybrid organic-inorganic perovskites contain in a single material highly desirable properties for optoelectronic applications: they are direct bandgap semiconductors with a high hole and electron mobility, large charge carrier diffusion length, and a high



absorption coefficient, all combined with an incredibly low density of trapping states, even if they are processed via solution-based methods.<sup>[32,39-43]</sup> The first solution-processed perovskite solar cell was reported by Miyasaka *et al.* in 2009, reaching a power conversion efficiency of 3.8%.<sup>[44]</sup> After spending over one decade optimizing the perovskite solar cells through compositional engineering,<sup>[45,46]</sup> solvent engineering,<sup>[47]</sup> optimization of charge transport layers,<sup>[48,49]</sup> defect passivation,<sup>[50,51]</sup> interface modifications<sup>[52,53]</sup> and morphology modulation,<sup>[54]</sup> 25.6%<sup>[15]</sup> efficiency was finally reached for small-area cells.

The perovskite optical bandgap ( $E_g$ ) can be easily tuned over the whole visible spectrum *via* different approaches, like using organic cations with varied sizes or other halide atoms. Lead (Pb) halide (X) perovskites have a valence band maximum (VBM) formed through an antibonding Pb s/X p combination. In contrast, the conduction band minimum (CBM) is determined through empty Pb p orbitals.<sup>[55]</sup> For example, expansion of the unit cell via incorporation of larger atoms,<sup>[55]</sup> or incorporation of different halide anions by ionic engineering can quickly shift the bandgap, allowing a change from 1.55 eV for I<sup>-</sup> anion to 3.2 eV with a simple Cl<sup>-</sup> substitution.<sup>[56], [57]</sup> Consequently, the bandgap is defined by the Pb-X bond and the Pb-X-Pb bond-angle, and small changes in the lattice parameters can lead to bandgap variations. Besides, the bandgap can also be modified through an external stress field, leading to structural deformation of the crystal and changes in the Pb-X and Pb-X-Pb bond lengths.<sup>[57]</sup>

## 1.2 Different Deposition Methods of Perovskite Films

In literature, different deposition methods have been reported employing either solution-based techniques or vacuum-based ones. Studies have shown that the perovskite film significantly depends on the technique used, in such an extension, that the concept “same compound, different material” can be applied.<sup>[58]</sup> Therefore, it is important to clearly describe the method used and the environmental conditions (such as dry air, humidity, vacuum, dry nitrogen) during the deposition process, as they

influence the perovskite layer and its properties.<sup>[58]</sup> In this thesis, I have used vacuum-based processing methods and solution-based ones for the perovskite layer.

### 1.2.1 Solution-Processed Perovskite Materials

Organic solvents are used to dissolve the perovskite precursors, and the solution is deposited via coating or printing methods such as spin-coating, inject-printing, or slot-die coating.<sup>[59]</sup>

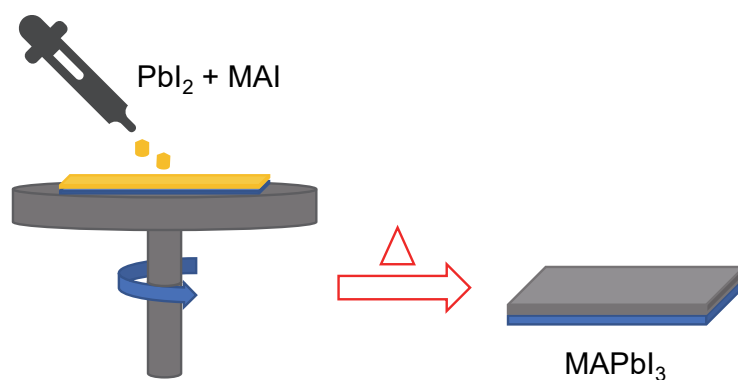


Figure 0.2: Schematics illustrating the spin-coating process of the one-step perovskite deposition process.

The most utilized device fabrication technique at lab scale is spin-coating due to its easy handling and low costs. Therefore, a small amount of the precursor solution is added onto a substrate and rotated at high speed. The deposition of the solution can either be static (substrate is not rotating) or dynamic (solution is dropped after a few seconds on the rotating substrate). The solution is spread during the high-speed rotation due to centrifugal force while the solvent simultaneously evaporates, resulting in a semi-dry uniform film thickness.<sup>[59]</sup>

There are three different solution-processing methods that can be distinguished:

- One-step deposition
- Two-step deposition
- Antisolvent deposition

In the first method, the perovskite solution of the precursors is directly deposited. Mostly high-boiling polar solvents are therefore used, such as dimethylsulfoxide (DMSO), dimethylformamide (DMF),  $\gamma$ -butyrolactone (GBL) are used in the solution preparation.<sup>[60]</sup> Typically, the perovskite is deposited by spin-coating, followed by a post-annealing treatment (Figure 1.2). This deposition method is not used often anymore, as the layer deposited is inhomogeneous, with high roughness, due to uncontrolled crystal growth.<sup>[61]</sup>

Two-step deposition method

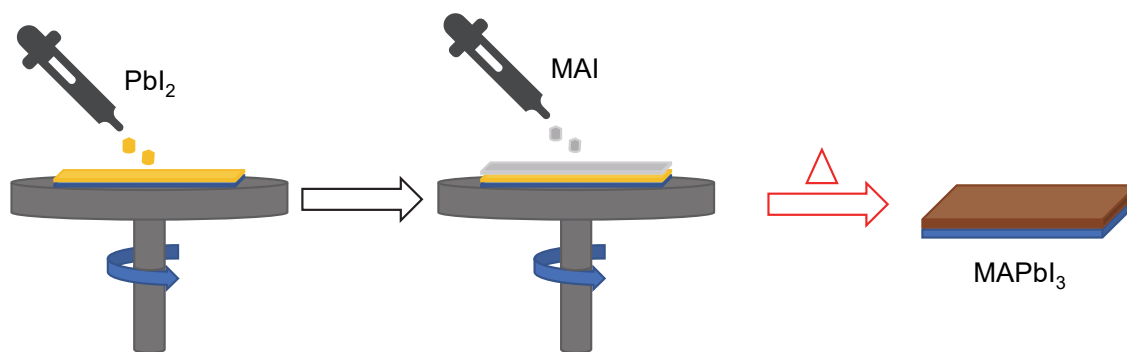


Figure 0.3. Schematics illustrating the spin-coating process of the two-step perovskite deposition process.

Two steps are used in this method to obtain the perovskite film. In the simplest perovskite  $\text{MAPbI}_3$  first, a  $\text{PbI}_2$  layer is spin-coated, followed by either dipping or spin-coating of the cation/organic salt (MAI) solution (Figure 1.3), which is consequently resulting in a subsequent conversion into perovskite. The diffusion of MAI determines the reaction rate in the  $\text{PbI}_2$  lattice, and the morphology of the spin-coated  $\text{PbI}_2$  film determines the final film morphology. Post-annealing of the samples leads to the completion of the crystallization. This method showed better potential in reaching highly efficient

perovskite films, but a rough morphology and incomplete  $\text{PbI}_2$  conversion are challenges that could not be overcome.<sup>[62-64]</sup>

### Antisolvent deposition method

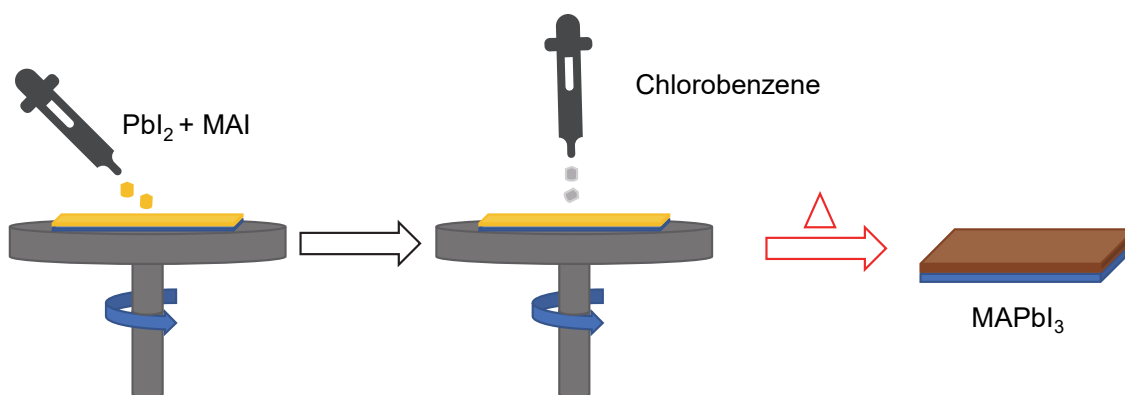


Figure 1.4. Schematics illustrating the spin-coating process of the antisolvent deposition process.

Another approach adopted by most groups nowadays adds one additional step to the fabrication process. Seok's group introduced the antisolvent method in 2014<sup>[47]</sup>, which remained up to date as the best method to achieve highly efficient solar cells. First, the perovskite precursor solution is deposited in one step on the substrate. Then during the last few seconds of the spin-coating process, an antisolvent such as chlorobenzene, toluene, or diethyl ether, is dropped onto the film, promoting crystallization. Finally, a heating step is added to complete perovskite crystallization (Figure 1.4).<sup>[47]</sup> This method was proven to achieve films with large grains and smooth morphology.<sup>[47,65,66]</sup>

### 1.2.2 Vacuum based Deposition of Perovskite Materials

Vacuum-based deposition of perovskite material allows the fabrication of perovskite films with high control of the thin film formation. The films are prepared in a high vacuum chamber ( $10^{-5}$  to  $10^{-6}$  mbar), where the perovskite or perovskite precursors are loaded in one or separate crucibles (single- or dual-source (co-evaporation) evaporation, respectively) and then heated to their corresponding sublimation temperature. At

the same time, the substrate is often maintained at room temperature.<sup>[67]</sup> A thin quartz crystal microbalance (QCM) is sandwiched between two metal electrodes, inducing an electric field that causes the crystal to vibrate in its resonance frequency. Mass accumulation on the crystal is monitored due to the change in oscillation frequency, allowing to control the film thickness at a nanometre scale.<sup>[68]</sup>

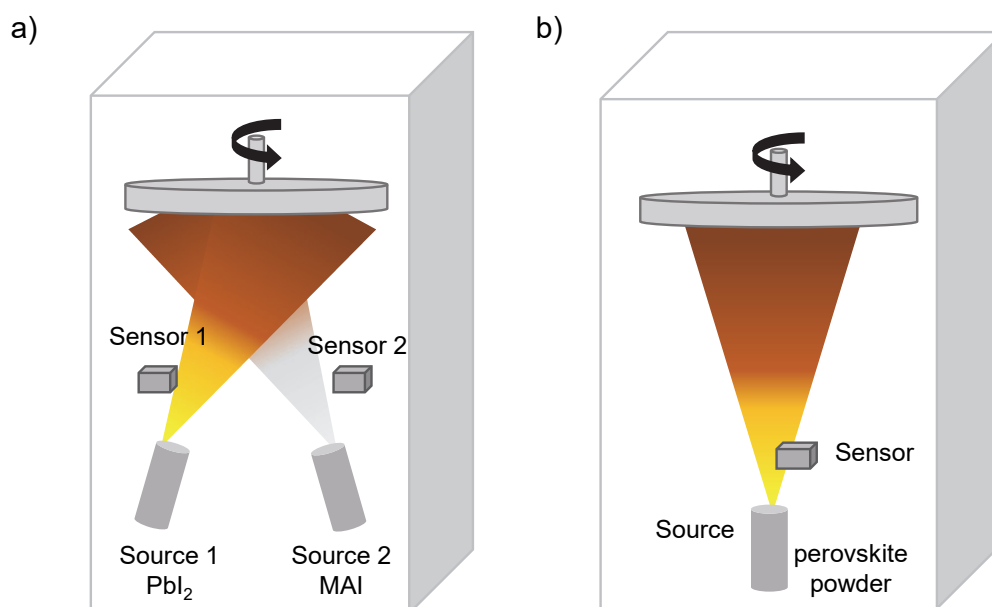


Figure 0.5: Schematics displaying the two different evaporation set-ups a) dual-source evaporation of  $MAPbI_3$  b) single-source evaporation of pre-synthesized perovskite powder.

For the dual-source evaporation (Figure 1.5 a), calibration of each precursor individually is essential before the perovskite deposition. Therefore, the tooling factor for each material must be evaluated first. The tooling factor is a correction factor that considers the differences between the material deposited on the substrate versus the material deposited on the QCM by taking into account the different source-to-QCM and source-to-substrate distances.<sup>[69]</sup> Therefore, a film of the material to calibrate is deposited on a flat substrate while recording the apparent thickness measured by the QCM, with a previous tooling factor value ( $Tooling_i$ ). After the deposition process, the actual thickness of deposited material on the flat substrates is determined by cross-section SEM or surface profilometer and compared to the apparent thickness read by the QCM.

The following linear relationship provides the new tooling factor ( $\text{Tooling}_2$ ) for the material of interest.<sup>[69]</sup>

$$\text{Tooling}_2 = \text{Tooling}_1 \times (\text{thickness}_{\text{actual}} / \text{thickness}_{\text{QCM}}) \quad (2)$$

The material's density ( $\rho$ ), the acoustic impedance (or Z-ratio), and the tooling factor are necessary to determine the correct thickness and the evaporation rate ( $\text{\AA}/\text{s}$ ) of the sublimed material. Therefore, these factors are set in the evaporation system to ensure that the evaporation rates of the precursors can correctly control the stoichiometry (chemical deposition) of the deposited film. Different precursors can be simultaneously evaporated under precise regulation of their molar ratio (composition) through monitoring the deposition rate.<sup>[70-73]</sup>

Another approach is the single source evaporation of pre-synthesized perovskite powder (schematics Figure 1.5 b). The same evaporator setup described above is used, but only one source is filled with the pre-synthesized perovskite powder.<sup>[74]</sup> The evaporation rate and the average power supply must be held stable throughout the process to maintain good perovskite crystallization conditions.

The successful control of all the above-described parameters, in addition to the high purity of the films, raise thermal evaporation as one of the most versatile and exciting technique to fabricate and investigate perovskites.

In 1997, Era *et al.* deposited a Pbl-based perovskite quantum well, the first attempt using dual-source vapor deposition.<sup>[73]</sup> Then in 2013, a PCE of 15.4% could be reported by Liu *et al.* for the first time for a planar PSC of co-evaporated  $\text{CH}_3\text{NH}_3\text{PbI}_{3-x}\text{Cl}_x$  deposited on top of a metal oxide layer.<sup>[67]</sup> Malinkiewicz *et al.* published in 2014 the evaporation of perovskite solar cells on organic hole-transporting layers<sup>[75]</sup>, which was followed shortly by an article by Roldán-Carmona *et al.* used the advantage of vapor-deposition, that the substrate temperature is at RT, to co-evaporate perovskite on top of rigid and flexible substrates.<sup>[75,76]</sup> Yang *et al.* (2015) and Momblona *et al.* (2016) both used in their studies the advantage that multilayer devices can be fabricated without any chemical

modifications or orthogonal solvents. Yang *et al.* alternated  $\text{PbCl}_2$  and  $\text{CH}_3\text{NH}_3\text{I}$  precursors in a bilayer deposition reaching a PCE of 16.03%<sup>[77]</sup>, and Momblona *et al.* fabricated fully sublimed *p-i-n* and *n-i-p* devices containing the same materials and layers. Inverted deposition order of the materials led to efficiencies of 16.5% for *p-i-n* and 20% for *n-i-p*.<sup>[78]</sup> Understanding the influence and the importance of the underlayer on the perovskite formation during the sublimation process is essential. Olthof *et al.* demonstrated in their research that the underlayer determines which precursor is sticking to the substrate first, starting the crystallization of the perovskite layer.<sup>[79]</sup> In 2019, the field moved from the more simple perovskite  $\text{MAPbI}_3$  towards more complicated systems, with large  $\text{MAPb}(\text{Br}_{0.2}\text{I}_{0.8})_3$  and narrow bandgap perovskites  $\text{FAPb}_{0.5}\text{Sn}_{0.5}\text{I}_3$ , reaching 15.9% and 13.98%, respectively.<sup>[80,81]</sup> Since 2020, the publications employing co-evaporation as the primary fabrication technique have been rising. Lead-free bismuth perovskites were approached for the first time,<sup>[82]</sup> and multi-source evaporation of  $\text{FA}_{0.7}\text{Cs}_{0.3}\text{Pb}(\text{I}_{0.9}\text{Br}_{0.1})_3$  was approached by Chiang *et al.*, reaching 18.2% efficiency.<sup>[83]</sup> In 2021, Abib *et al.* tried the single source evaporation of pre-synthesized  $\text{CsPbBr}_2$  powder for the first time and achieved solar cells with max. PCE of 8.95%.<sup>[74]</sup> The industrialization/commercialization of the vacuum-based fabrication method was demonstrated by Wang *et al.*, reaching 20.28% ( $21 \text{ cm}^2$ ) with mini-modules.<sup>[84]</sup> Currently, the highest efficiency of 20.6% for the small area was reported by Li *et al.*<sup>[85]</sup> and with efficiencies now over 20% even in mini-modules<sup>[84]</sup> combined with the advantages of the vacuum-deposition process, including avoidance of toxic solvents, give sublimed perovskite devices the promise for real applications.

## 1.3 Perovskite Solar Cells

### 1.3.1 Working Principle of $p$ - $n$ junction Solar Cells

The working principle of the perovskite solar cell is demonstrated in Figure 1.6. It can be simplified into the following steps:

- 1) *Charge Generation*
- 2) *Charge Separation*
- 3) *Charge Transport and Collection*

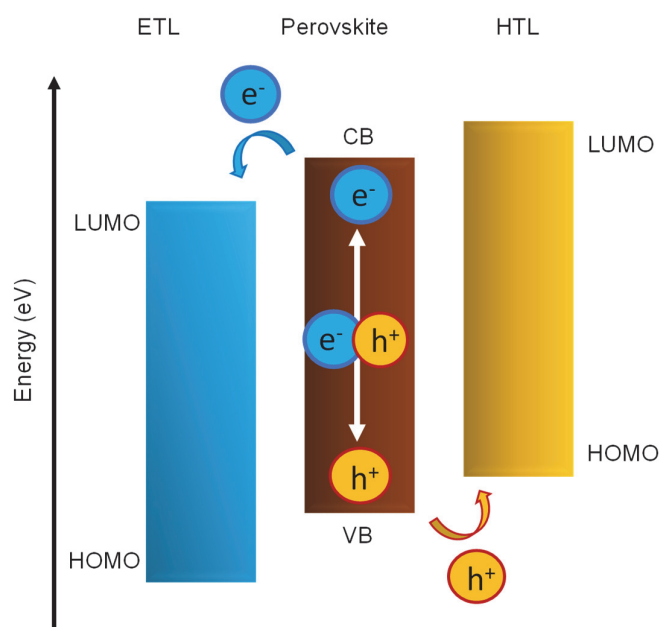


Figure 1.6: Schematics of the general working principle of the perovskite solar cell.

#### 1.) *Charge Generation*

The perovskite material is the light-collecting material in the solar cell. The more incoming light the perovskite can absorb, the more photogenerated charges are created. Therefore, the absorption coefficient is the most important property of the material itself. The remarkable absorption coefficient compared to other materials makes the perovskite material a good candidate for solar cell applications.<sup>[86]</sup> Only photons with the



same or higher energy than the bandgap ( $E_g$ ) can be absorbed by the light-collecting material. Therefore, the bandgap is essential for the charge generation process.<sup>[87]</sup> Additionally, the wavelength that can be absorbed by the perovskite is also attributed to the  $E_g$ .<sup>[9]</sup> Photons with higher energy than the perovskite's  $E_g$  further excite the electrons an energy level higher than the conduction band (CB) of the perovskite. These electrons relax back to the CB by releasing the excess energy in the form of heat.<sup>[9,88]</sup>

Different types of recombination processes can occur in the light harvester during the charge generation process, affecting the solar cell performance.<sup>[9,88]</sup> These four recombination processes can be distinguished with the following explanations:

#### 1. Radiative recombination

Radiative recombination (Figure 1.7), or band-to-band recombination, is the primary recombination process of direct bandgap semiconductors.<sup>[89,90]</sup> During the recombination process, the excited electron in the CB combines with the hole in the valence band (VB), and a photon equal to the energy of the semiconductor's bandgap is released.<sup>[88-90]</sup> For very high-quality semiconductors, this recombination process, it the limit of the solar cell's efficiency. However, in perovskite solar cells also non-radiative recombination processes limit the efficiency.<sup>[88-90]</sup>

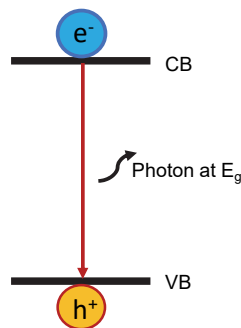


Figure 0.7: Schematic of radiative recombination.

## 2. Shockley-Read-Hall recombination

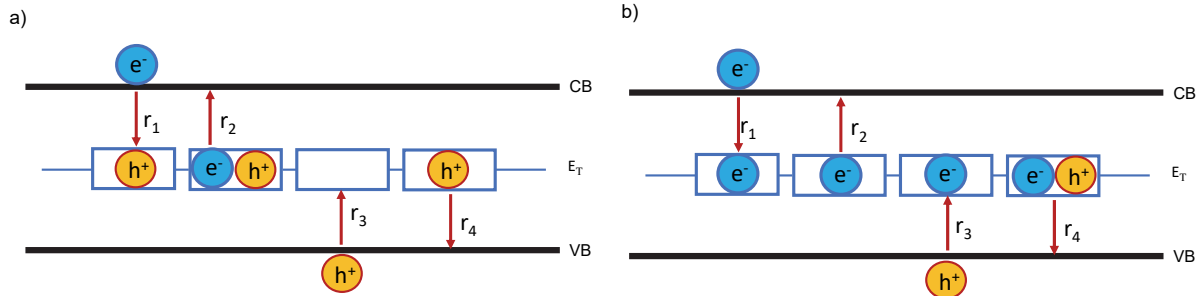


Figure 1.8: Schematic of defect or trap assisted recombination a) donor type and b) acceptor type trap,  $r_1$ = electron capture from the CB,  $r_2$ = electron emission from the CB,  $r_3$ = hole capture from the VB,  $r_4$ = hole emission from the VB.

Shockley-Read-Hall (SRH), named after William B. Shockley, T. Read, and Robert N. Hall, also known as a defect- or trap- assisted recombination, was discovered in 1952.<sup>[9]</sup> In this case, the non-radiative process of the recombination of electrons and holes does not happen directly from the bandgap (Figure 1.8). Instead, it is caused by impurities in the lattice defects in the semiconductor, leading to new recombination centers within the bandgap, referred to as trap states.<sup>[9]</sup> There are two primary types of trap states or recombination centers: donor-type and acceptor-type. The donor-type trap states trap a hole, followed by the capture of an electron from the CB, while in acceptor-type recombination, the electron is trapped, followed by a hole capture of the VB. This non-radiative recombination releases the excess energy as phonons (lattice vibration).<sup>[9,9]</sup>

## 3. Auger recombination

In the non-radiative Auger recombination, the energy of the recombining hole and electron is transferred to another electron or hole (Figure 1.9). Suppose the energy is transferred to an electron. In that case, the electron is excited to the higher level of the CB, followed by a relaxation process back to the CB, while releasing its energy in phonons and finally in thermal energy (Figure 1.9a). If the particle is a hole, it will be

excited to a lower level of the VB, followed by transferring the energy in phonon (Figure 1.7b).<sup>[9,92]</sup> Auger recombination generally occurs in semiconductors with indirect bandgap, where the direct band to band recombination is limited or impossible.<sup>[9,93]</sup> Auger recombination is the dominant process in indirect bandgap semiconductors, limiting the efficiency in high purity solar cells, such as silicon (Si) and germanium (Ge).<sup>[88,93]</sup>

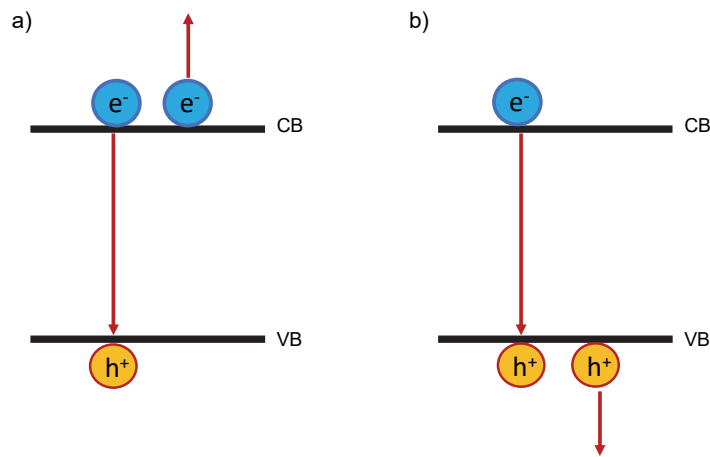


Figure 0.9: Schematic of Auger recombination a) involving two electrons b) two holes.

#### 4. Grain boundaries, surface, and interface recombination

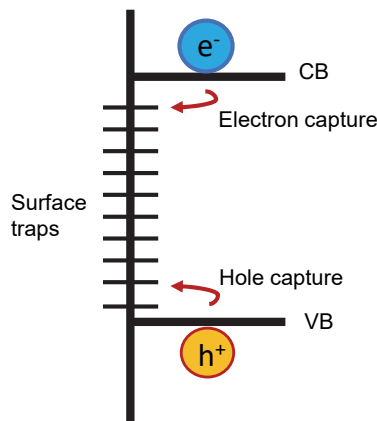


Figure 0.10: Schematic of surface recombination.

Trap states and recombination occur not only within the bulk of the semiconductor but also due to impurities, dangling bonds, or surface defects on the material's surface (Figure 1.10). They also occur between interfaces of two semiconductors or at high-angle grain boundaries in polycrystalline materials, leading to a recombination process similar to the SRH described before.<sup>[9,88]</sup>

### 2) Charge Separation

Before the photogenerated charges (excitons or free carriers, depending on material permittivity) can be extracted and collected, they need to be separated into electrons (negative charges) and holes (positive charges). The pre-condition for generating free electrons and holes is that the photogenerated charges overcome the exciton binding energy ( $E_b$ ). Low  $E_b$  ( $E_b=2$  meV-75 meV at RT) is preferred in PV applications to obtain an efficient charge dissociation of free carriers. The grain size influences the  $E_b$  value of the simplest perovskite MAPbI<sub>3</sub>, for example. Single crystals, for example, exhibit the highest  $E_b$  value.<sup>[43,94]</sup>

### 3) Charge Transportation and Collection

The generated free charges, electrons, and holes will move towards the selective contacts within the semiconductors. The electrons selective contact named electron-transport layer (ETL) will selectively transport the electrons and block the holes, and the hole selective layer, named hole-transporting layer (HTL), will transport the holes and block the electrons. The perovskite layer in device applications is always sandwiched between the ETL and HTL. The alignment of the energy levels between the perovskite and the charge transporting layers is hence critical to ensure efficient charge transport. Therefore, if considering the ETL, the lowest-occupied molecular orbital (LUMO) must be deeper than the conduction band (CB) of the perovskite to assure efficient electron extraction. The highest occupied molecular orbital (HOMO) should be low enough, so the holes are blocked. For the HTL, the HOMO should be higher than the perovskite valence band (VB), so the holes can be efficiently transferred. The LUMO should be high enough to block the electrons efficiently. Other important parameters

that need to be considered are electron and hole mobility. The conductivity of the material describes the product of the number of charges times the mobility of the charges. Therefore, electron and hole mobility define how fast the electrons and holes can be transported through the selective contact layer. After transporting the charges through HTL and ETL, they are collected at the corresponding electrode.

### 1.3.2 Device Architectures of PSCs

Generally, the perovskite layer is sandwiched between the charge carrier selective layers (electron-transporting and hole transporting layer) and the electrodes in a solar cell. Two main architectures can be distinguished, depending on how the perovskite is in contact with the ETL or HTL.<sup>[40]</sup>

#### 1) Normal (*n-i-p*) Configuration

#### 2) Inverted (*p-i-n*) Configuration

#### 3) Other PSCs configurations

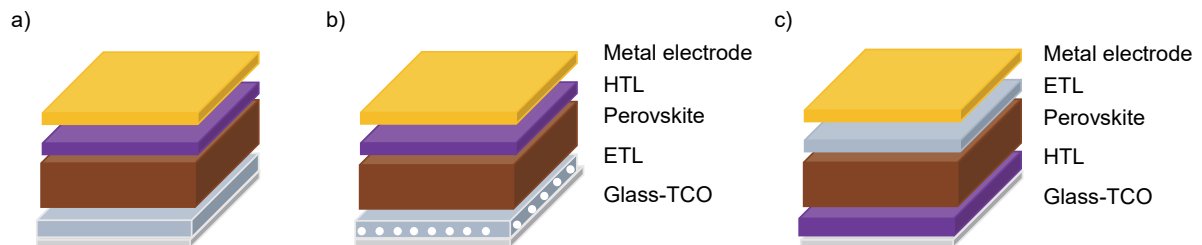


Figure 0.11: Schematic of the different device architectures: a) normal (*n-i-p*) planar configuration b) normal (*n-i-p*) mesoscopic configuration c) inverted (*p-i-n*) planar configuration

#### 1) Normal (*n-i-p*) configuration

The normal structure is defined through the contact of the ETL with the front transparent conducting oxide (TCO), such as fluorine-doped tin oxide (FTO) or indium-doped tin oxide (ITO) or (Figure 11 a). The perovskite is sandwiched between the ETL and HTL, where the HTL is in contact with the metal top electrode, such as silver (Ag) or gold (Au).<sup>[95]</sup> The light needs to pass first through the ETL in the normal structure

before reaching the perovskite layer. It, therefore, is necessary to choose a transparent  $n$ -type semiconductor, which commonly used are  $\text{SnO}_2$  or  $\text{TiO}_2$ .<sup>[96]</sup> The simpler device architecture is the planar structure.<sup>[97]</sup> The mesoscopic architecture is derived from the dye-synthesized solar (DSSCs) cell structure (Figure 1.11b). An additional layer of nanoparticles, for example,  $\text{TiO}_2$ , is scaffolded on top of the planar ETL, allowing improvement of the electron collection and reducing the hysteresis effect of the PSCs.<sup>[47,98]</sup>

### 2) *Inverted (p-i-n) configuration*

The inverted configuration inverts the structure when considering the normal structure. Here the HTL is in contact with the transparent front electrode, and the ETL is in contact with the metal electrode (Figure 1.11 c).<sup>[97]</sup> Normally transparent  $p$ -type semiconductor layers are employed in this configuration. The light first needs to pass this layer before reaching the perovskite layer, without any parasitic absorption, which might lead to losses. Typical HTLs are e.g. nickel-oxide ( $\text{NiO}_x$ ), poly[bis(4-phenyl)(2,5,6-trimethylphenyl)amine (PTAA), or poly(3,4-ethylene dioxythiophene) polystyrene sulfonate (PEDOT:PSS).<sup>[99,100]</sup> The inverted configuration is more versatile. It opens the possibility of processing the charge selective layers using low-temperature methods, such as vacuum deposition, enabling the cells to be processed on flexible substrates.

### 3) *Other PSCs configurations*

Other device configurations that are reported in the literature are based on the two conventional ones ( $n-i-p$  and  $p-i-n$ ) described above. Mostly they were explored to simplify the architecture towards a more cost-efficient fabrication process. An ETL-free PSC was reported with a power-conversion efficiency (PCE) of 21% by interface engineering.<sup>[101]</sup> An HTL-free device was also demonstrated by passivating the perovskite-gold interface sufficiently to reach a PCE of 15%.<sup>[102]</sup> Another approach is the use of carbon-based material instead of a metal back electrode, which enables depositing of the solar cell with large-scale methods, such as doctor blade or printing method.<sup>[103]</sup>

## 1.3.3 PSCs Characterization

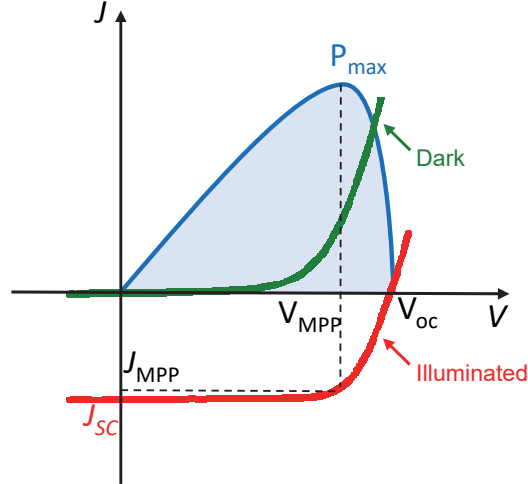


Figure 0.12:  $J$ - $V$  characteristics of solar cells in light and dark conditions.

The photovoltaic characteristics are determined by the parameters of the PSCs measured under light and dark conditions. Pre-condition of the measuring setup in light is that the spectrum of the light source (often xenon) is matching the air mass (AM) of 1.5 spectra (defined as the sun is tilted  $37^\circ$  to the horizontal plane) and that the measurement is carried out under the standard test conditions (STC). This includes calibrating the light source before measuring to  $1000 \text{ W/cm}^2$  and keeping the cell at room temperature ( $25^\circ\text{C}$ ) throughout the measurement.<sup>[9]</sup>

The main parameters that define the  $J$ - $V$  characteristics are short-circuited current density ( $J_{sc}$ ), open-circuit voltage ( $V_{oc}$ ), fill factor ( $FF$ ), and power conversion efficiency (PCE) (Figure 1.12).<sup>[94]</sup> The  $J_{sc}$  is obtained using a mask with a fixed aperture typically used to comply with the STC. The  $J_{sc}$  is a measure that describes the current density flowing through the external circuit when the electrodes are shorted. The  $V_{oc}$  is a measure for the maximum voltage the solar cell can reach, and it is defined as the voltage when no current is flowing. The  $V_{oc}$  is linked to the saturation current density ( $J_o$ ) and the photogenerated current density ( $J_{ph}$ ).  $J_o$  is affected by the recombination processes and can change in magnitude, whereas the  $J_{ph}$  typically only shows slight variation. The  $V_{oc}$  is defined following the equation:<sup>[9,94]</sup>

$$V_{oc} = \frac{k_B T}{q} \ln\left(\frac{J_{ph}}{J_o}\right) \quad (3)$$

$k_B$  is the Boltzmann constant,  $T$  is the temperature, and  $q$  is the elemental charge.

The  $FF$  is a measure that describes the ratio between the maximum power ( $P_{max}$ ) and the product of the  $V_{oc}$  and  $J_{sc}$  as described in the following equation:

$$FF = \frac{P_{max}}{V_{oc} J_{sc}} = \frac{V_{MPP} J_{MPP}}{V_{oc} J_{sc}} \quad (4)$$

$V_{MPP}$  and  $J_{MPP}$  are voltage and current at maximum power point (MPP), defined as the  $J$ - $V$  curve where the maximum power output is reached. The power conversion efficiency (PCE) is calculated based on the parameters defined above.<sup>[9]</sup>

The PCE is defined to be the ratio between *the*  $P_{max}$  generated at the incident power ( $I_{in}$ ) by the solar cell, which is incident light with AM 1.5 spectrum as defined above:<sup>[9]</sup>

$$PCE = \frac{P_{max}}{I_{in}} = \frac{V_{oc} J_{sc} FF}{I_{in}} \quad (5)$$

External Quantum Efficiency (EQE)

The external quantum efficiency is defined by the number of incident photons converted into electron-hole pairs that are collected at the electrodes. The EQE is measured by illuminating the solar cell with monochromatic light at a specific wavelength ( $\lambda$ ), while the photocurrent ( $I_{ph}$ ) is recorded and expressed as a function of a wavelength ( $\lambda$ ).<sup>[104]</sup> The EQE is also defined by  $q$ , the elementary charge,  $\Psi_{ph,\lambda}$  the spectral photon flow, which is obtained by measuring the EQE of a calibrated diode under the same light source.<sup>[9]</sup>

$$EQE(\lambda) = \frac{I_{ph}(\lambda)}{q\Psi_{ph,\lambda}} \quad (6)$$

The EQE spectrum gives information about the optical and electrical losses of the solar cell due to parasitic absorption and recombination. It can be used to calculate the  $J_{sc}$  of the solar cell, and if the measurement was performed under short circuit conditions, the EQE can also be used to calculate the  $J_{sc}$  value obtained from the  $J$ - $V$



measurement. The  $J_{sc}$  from the EQE can be obtained by integrating the EQE with respect to the photon flux of the AM 1.5 spectrum across all wavelengths.<sup>[9,104]</sup>

$$J_{sc} = -q \int_{\lambda_1}^{\lambda_2} EQE(\lambda) \phi_{ph,\lambda}^{AM 1.5} d\lambda \quad (7)$$

## 1.4 General Limiting Factors in Perovskite Solar Cells

Contemporarily, although hybrid lead halide perovskites are considered one of the most prominent alternatives for optoelectronics, many milestones still need to be achieved to realize the full potential of hybrid perovskite absorbers. The Shockley-Queisser limit (see Figure 1.15) indicated that the highest possible efficiency is 31% for direct bandgap materials.<sup>[105]</sup> Besides, the material toxicity and the long-term stability are challenges that still need to be solved. When analyzing the solar cells, they are tested in a strictly controlled environment. The cells reported with the highest PCE are at a laboratory scale. When considering upscaling the laboratory scale to a solar panel working in actual conditions, not operating in a controlled environment, one must consider the stability, environmental impact, and commercialization process in all weather conditions. These factors go beyond solving all the questions about toxicity, stability, costs, and the theoretical efficiency limit after Shockley-Queisser.

### 1.4.1 Toxicity

The hybrid inorganic perovskite material employed in today's most efficient perovskite solar cell has one disadvantage.  $PbI_2$ , one of the precursor materials, is highly toxic for human health and the environment. Its water solubility makes it extremely dangerous when leaching from a solar cell into the environment.<sup>[106]</sup> Lead is so toxic that the European Union has recently decreased the maximum lead content in drinking water to 5 mg/L, ten times less than the lethal doses in the blood, indicating lead poisoning.<sup>[107]</sup> Lead poisoning leads to severe illnesses such as kidney damage or neurological disorders, especially in children and pregnant women.<sup>[108]</sup> Antonio Abate has studied the impact of perovskite by monitoring the uptake of lead into plants. Interestingly, he

could demonstrate that the cation and the  $\text{PbI}_2$  act as an amplifier for this reaction. The cation first changes the pH of the soil, which then leads to higher absorption of  $\text{PbI}_2$  into the plants.<sup>[106]</sup> As one hindrance of commercialization is the risks involved with lead, researchers are exploring different options to either replace the lead in the material crystal structure or find other ways to prevent lead leakage into the environment from solar panels. Therefore, lead-free perovskite solar cells seem to be an alternative. However, lead-free perovskites based on other metals such as silver (Ag)<sup>[109,110]</sup>, indium (In)<sup>[111,112]</sup>, bismuth (Bi)<sup>[113]</sup>, or germanium (Ge)<sup>[114,115]</sup> have not yet shown sufficient efficiencies to be considered as an option for replacing lead-based perovskite solar cells. When employed in perovskite, the only metal showing good PCE values is tin (Sn). Tin-based perovskite has shown 10.6% efficiencies.<sup>[116]</sup> However, this material class is not entirely harmless, considering  $\text{SnI}_2$ , the precursor used, forms hydrogen iodide (HI) under acidic conditions, which is even more toxic. Nevertheless, tin-based perovskites have one advantage. The oxidation from  $\text{Sn}^{2+}$  to  $\text{Sn}^{4+}$  and later tin-oxide ( $\text{SnO}_2$ ) is fast, making them less toxic than Pb-based perovskites but more sensitive towards degradation in ambient air conditions.<sup>[117,118]</sup> The Abate's group demonstrated this by treating the soil with Sn-perovskite. They could conclude that only a minimal amount of Sn is absorbed by the plants, probably due to the fast degradation from  $\text{Sn}^{4+}$  to  $\text{Sn}^{2+}$ . As tin-based perovskite solar cells are not yet comparable in their performance, other solutions to solve the toxicity challenges were explored. The uptake of lead by a porous scaffold, like a metal-organic framework, was investigated by Huckaba *et al.*. They demonstrated that contaminated water with lead can be cleaned by metal organic frameworks (MOF) treatment, resulting in drinking water following the regulations.<sup>[119]</sup> Another approach is also to encapsulate the perovskite module with a self-healing polymer, reducing the leakage from the module upon breakage.<sup>[120]</sup> The perfect solution to prevent environmentally harm by lead leakage is not yet found, but will if the safety aspect is already considered during the design process.

### 1.4.2 Cost

Bringing perovskite solar panels to the market needs competitive pricing compared to other technologies. Up-scaling is more complicated if the material costs are high, as these materials will dominate the pricing range. The typical metal electrode employed in highly efficient solar cells is gold (1g= 58.74).<sup>[121]</sup> Gold has excellent electrical conductivity, appropriate work function, and superior long-term stability compared to other metal options.<sup>[122]</sup> These less expensive options, such as silver, copper, chromium, and aluminum, have high conductivity and low stability. For example, silver<sup>[123,124]</sup> and aluminum<sup>[122,125]</sup> react with the halides of the perovskite,<sup>[126–129]</sup> inducing a halide, mainly iodide deficiency in the perovskite layer. These metal halide species additionally hinder charge transfer from the adjacent layer.<sup>[130]</sup> Replacing, therefore, the metal electrode is essential for the upscaling of the perovskite solar cells. Therefore, employing carbon-based electrodes is not only cheaper but also more environmentally friendly, a promising alternative, given that efficiencies of 19.2% could already be achieved.<sup>[131]</sup>

Another cost factor at the moment is the state-of-the-art hole-transporting material spiro-OMeTAD (1g=403 CHF) or PTAA (1g=2550 CHF), which are both very expensive.<sup>[132–134]</sup> Therefore, several attempts were made to find new comparable performing HTMs with shorted synthesis pathways and low-cost starting materials.<sup>[135,136]</sup> A more detailed study on alternative cost-effective HTMs will be explored in Chapter 7 of this thesis.

### 1.4.3 Stability

One remaining challenge in the commercialization of perovskite solar modules is the stability of the material itself, intrinsically, and the stability of the layer in ambient air. One, therefore, needs to consider photostability, thermal stability, and moisture stability when designing a solar cell. I will focus only on thermal stability and moisture stability because I have further evaluated them in my research.

### Thermal stability

In operating conditions, a solar panel should be able to restrain high temperatures over  $85^{\circ}\text{C}$  or even shallow temperatures up to  $-40^{\circ}\text{C}$  depending on the location of the solar module installations.<sup>[130,137]</sup> These extreme temperatures should not impact any solar cell material, preventing loss in performance over a short time. The simplest perovskite structure,  $\text{MAPbI}_3$ , is known to degrade under heat and stress at  $85^{\circ}\text{C}$ , even in  $\text{N}_2$  atmosphere. Hydroiodic acid HI and gaseous methylamine (MA) are produced during degradation, leaving a pure  $\text{PbI}_2$  film behind.<sup>[138]</sup> Therefore, usage of  $\text{MAPbI}_3$  in large-scale applications is less suitable, and more stable materials under these harsh conditions are desired. Therefore, replacing the organic cation  $\text{MA}^+$  with the heavier organic formamidinium cation  $\text{FA}^+$  is suitable, as  $\text{FAPbI}_3$  has improved stability under thermal stress.<sup>[139]</sup>

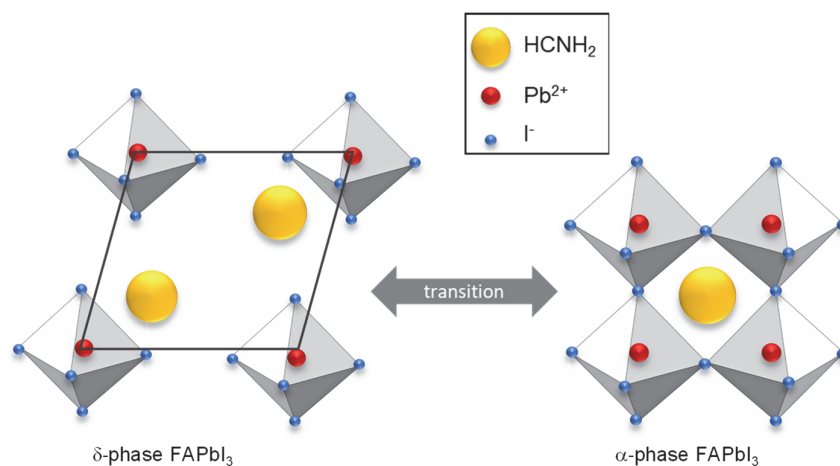


Figure 0.13: Illustration of transition between  $\delta\text{-FAPbI}_3$  and  $\alpha\text{-FAPbI}_3$ .

The lower bandgap of this material at 1.47 eV in comparison to  $\text{MAPbI}_3$  with a bandgap of 1.6 eV enables the material to absorb a broader wavelength range, leading to enhanced PV performance compared to  $\text{MAPbI}_3$ .<sup>[140,141]</sup> Nevertheless, also  $\text{FAPbI}_3$  has some drawbacks. At room temperature, the  $\delta$ -phase, is not photoactive. Only the high-temperature  $\alpha$ -phase is photoactive but only stable at temperatures between  $150^{\circ}\text{C}$ - $180^{\circ}\text{C}$  (Figure 1.13).<sup>[142,143]</sup> The equilibrium reaction will always convert the perovskite

material to the  $\delta$  phase at room temperature. Introduction of multiple cations in the A site of the crystal structure, such as double cation ( $\text{MA}^+$  and  $\text{FA}^+$ )<sup>[144]</sup>, triple cation ( $\text{MA}^+$ ,  $\text{FA}^+$ ,  $\text{Cs}^+$ )<sup>[145]</sup> quadruple cation ( $\text{FA}^+$ ,  $\text{MA}^+$ ,  $\text{Cs}^+$ ,  $\text{Rb}^+$ )<sup>[146]</sup> has been proven to stabilize the back phase of  $\text{FAPbI}_3$ , also leading to better PV performance (Figure 1.14). In Chapter 5, I will study the single-source evaporation of pre-synthesized  $\text{FAPbI}_3$  and  $\text{CsFAPbI}_3$  more thoroughly, highlighting if the structures can be stabilized by vacuum sublimation techniques.

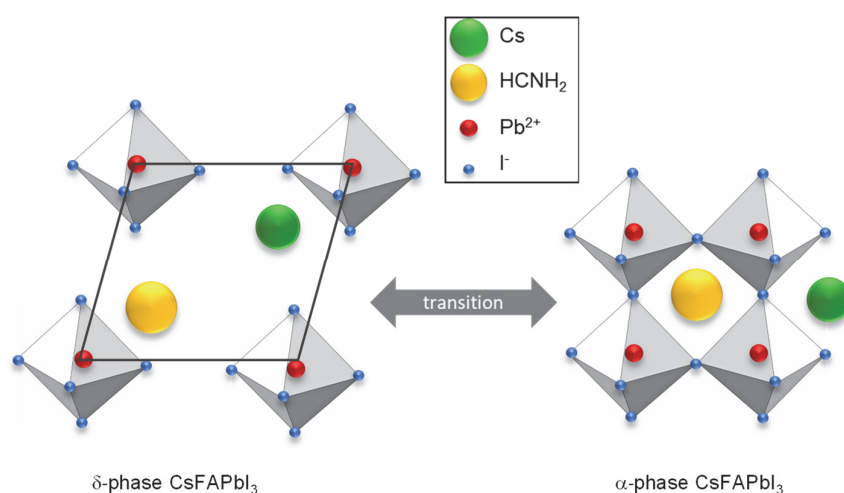


Figure 1.14: Illustration of transition between  $\delta$ - $\text{CsFAPbI}_3$  and  $\alpha$ - $\text{CsFAPbI}_3$ .

### Moisture stability

Moisture is present in the ambient air and is one of the external influences that degrades the perovskite material fast. Therefore, moisture influences the most the long-term stability of the perovskite solar cells.<sup>[128]</sup> Nevertheless, encapsulation technologies that are mature for perovskite solar cells were developed throughout the last years, even though when compared with silicon modules, challenges are still to be solved due to the unstable properties of the perovskite material in moisture.<sup>[147]</sup> Moisture can penetrate the perovskite, leading to the formation of a hydrated phase, further dissolving the organic species, leading to the evaporation of the volatile species, which finally decomposes the material.<sup>[130]</sup> However, the moisture influences the perovskite layer negatively and the hole-transporting material, especially when the state-of-the-art dopant such as

Li-bis(trifluoromethansulphonyl) imide (Li-TFSI) is used to improve the hole mobility and conductivity of the HTM spiro-OMeTAD.<sup>[148,149]</sup> Its hygroscopic nature attracts moisture which interacts with Li-TFSI resulting in the formation of pinholes. These pinholes enable water to penetrate the perovskite layers, leading to degradation.<sup>[148]</sup> In Chapter 7, a more detailed study is described to understand the role of the dopants in spiro-OMeTAD and their influence on *p-i-n* co-evaporated perovskite layers. The design of hydrophobic hole-transporting layers can also be an option to prevent moisture damage to the perovskite solar cells. For example, Zheng *et al.* has demonstrated an oligothiophene with a contact angle of  $107.4^\circ$ , successfully repelling moisture from the solar cell.<sup>[150]</sup> In Chapter 8, I am introducing a class of HTM materials showing exceptional hydrophobic properties, leading to good device stability.

#### 1.4.4 Towards Shockley-Queisser Limit

The most critical limit that cannot be overcome by a single junction solar cell is the Shockley-Queisser limit. William Shockley and Hans-Joachim Queisser defined this limit for the first time for a *p-n* junction cell in 1961.<sup>[151]</sup> It describes the maximum PCE a solar cell can achieve when considering a single junction solar cell under a specific light illumination spectrum.<sup>[152]</sup> To simplify the definition of the maximum PCE, several assumptions were made.

- Only radiative recombination is considered, which therefore determines the upper limit of the minority carrier lifetime<sup>[153]</sup>
- Only photons with an energy higher than the bandgap will be converted into electron-hole pairs, while photons with energy lower than the bandgap will not be considered<sup>[153]</sup>

Following these assumptions, a max PCE of 31% can be reached for solar cells, having a bandgap around 1.4-1.6 eV (for example, for FAPbI<sub>3</sub> and MAPbI<sub>3</sub>), considering the standard AM 1.5G illumination.<sup>[154,155]</sup> See bandgap max PCE dependence summarized in Figure 1.15.<sup>[152]</sup> Nevertheless, other factors that limit the solar cell's performance are not

considered in the Shockley-Queisser limit, like non-radiative recombination through a defect, or trap sites are, for example.<sup>[156-160]</sup>

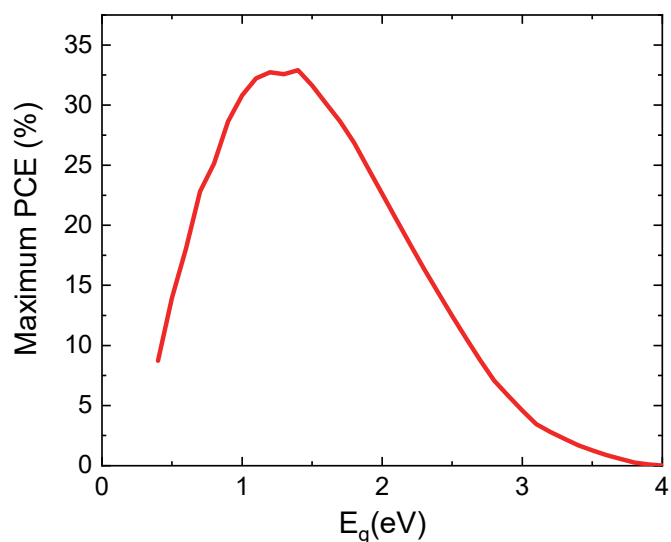


Figure 0.15: Shockley Queisser limit for maximum PCE in relation with the bandgap, considering AM 1.5G illumination at 25°C. The data was plotted from the reference data reported by Sven Rühle.<sup>[152]</sup>

Defect passivation was demonstrated as an efficient technique, and it has become a popular approach within the research community. Interface passivation can be achieved in various ways, such as adding small organic molecules, polymers, introducing an interlayer, and constructing a gradient perovskite layer.<sup>[159,160]</sup> Further discussion on interface engineering will be presented in Chapter 2, and insight into the role of fullerene ( $C_{60}$ ) as an interlayer will be explored in Chapter 6.





## Advantages and Limiting Factors of Vacuum-deposited Perovskite Layers

Vacuum deposition is an available industry technique that has many advantages compared to the solution process. Toxic organic solvents are used in perovskite precursor solutions, and operating these toxic solvents at an industrial scale would impose negative impacts on human health and environmental balance. Recent studies on the human health and environmental impacts of solvents used in PSCs fabrication showed that the solvents strongly impact human health and the environment.<sup>[161,162]</sup> In this context, the minimal chemical wastage, solvent-free processing, large scale compatibility, thickness precision in the nm range, lower intermixing of different layers at the interfaces, and the low-temperature annealing of thin films, highlights vacuum deposition as an energy-efficient green contender for well-explored solution-process technique.<sup>[163,164]</sup> In vacuum deposition, the materials are heated in high vacuum conditions ( $p \leq 10^{-6}$  Pa) and sublimed on substrates. When heated in the source, the evaporated particles move away in a deposition cone to reach the substrate. The longer the mean free pathway from source to substrate, the more uniform the deposition, but also the more parasitic material deposition in the vacuum chamber walls. The variety of materials that can be evaporated is wide. Metals and organic materials are only limited by the molecular weight and size or the required sublimation temperature.<sup>[165]</sup> Another advantage is the possibility of depositing multilayers of perovskite materials in combination with electron/hole-transporting materials without intermixing the different layers.<sup>[166]</sup> Additionally, thermal annealing of the layers is unnecessary, making the method suitable for the fabrication of flexible electronics.<sup>[167]</sup> Vacuum deposition is also suitable for large-scale applications, demonstrated by its successful usage in the OLED industry.<sup>[168]</sup> Hence, it is also suitable for tandem applications, and it can be used for more complex perovskite compositions.<sup>[169]</sup> Nevertheless, evaporation from more than two sources simultaneously is challenging due to the complex composition and stoichiometry that must be reached in the final film.<sup>[170]</sup> However, different challenges in vacuum-

deposition still need a solution. First, vacuum deposition cannot be performed in any laboratory as it needs an expensive and complex vacuum system.<sup>[171]</sup> Second, the fabrication of the perovskite solar cells is far slower, with a low throughput method due to substrate holder limitations. Even with identical conditions, it is challenging to reproduce and achieve the same results, as the precursor material on the walls may lead to trace contamination during the process.<sup>[172]</sup> Only a handful of groups are dedicated to the thermal deposition of perovskites, which still leaves a lot of room for improvement, optimization, and research.<sup>[172]</sup> Vacuum deposition can be used for perovskites in different ways: by co-evaporation of different precursors, evaporation from a single source, flash evaporation, or sequential evaporation. In my work, I have focused mainly on the co-evaporation and single-source evaporation of perovskites. I address in Chapters 4 and 5 the issue of morphology, composition, and irreproducibility by advising new standards that should be considered in the evaporation community.

Table 0.1: Advantages and disadvantages of the vacuum-deposition method

Advantages	Disadvantages
✓ uniform deposition	✗ ultra-high vacuum (costs intensive)
✓ evaporation of a large range of materials	✗ parasitic condensation at chamber walls
✓ no post-annealing step necessary	✗ difficult to control vapor pressure of MAI
✓ coating on flexible substrates	✗ challenging if more than two sources are used simultaneously
✓ thickness control in the nm range	✗ few research reported for perovskites
✓ highly pure layers	
✓ large-area compatible	
✓ adequate for the tandem application	
✓ toxic solvent-free	
✓ no intermixing of different layers	

## 1.5 Controlling the Perovskite Composition

The composition of the perovskite material cannot be readily determined, especially when considering multi-source evaporation. Tuning of the perovskite composition can be made by selecting the evaporation rates carefully for each of the perovskite precursors. Nevertheless, especially for mixed halide perovskite, these experiments require multiple reference experiments to determine and calibrate each precursor. Essential for the calibration is to know the density, acoustic impedance, and geometric factors for each material as above-mentioned, which are not always available.<sup>[173]</sup> Another difficulty, especially for the perovskites using methylammonium iodide as a precursor, is the uncontrollable and reproducible evaporation of methylammonium iodide due to its high vapor pressure.<sup>[165]</sup> Easy deprotonation during the evaporation to HI and CH<sub>3</sub>NH<sub>3</sub><sup>[174]</sup> and low sticking coefficient on different substrates, or even decomposing to CH<sub>3</sub>I and NH<sub>4</sub><sup>[175]</sup>, are challenges one must consider. During the first few nanometres, non-stoichiometric thin layers can be formed, which block the charge extraction and result in lower device performance.<sup>[79]</sup> In principle, the evaporation of small molecules as additives in parallel to the evaporation of the perovskite could be feasible, but not many reports have been so far made. Therefore the positive effect seen with additives in spin-coating considering defect passivation, stabilization of the perovskite crystal phase, or elimination of hysteresis effect, which all lead to superior device performance has not yet been investigated deeper in the community.<sup>[176,177]</sup> Only one report in this direction was made by Wu et al., who co-evaporated fullerenes with perovskite precursors demonstrating a significant improvement in device performance.<sup>[178]</sup>

### 1.5.1 Controlling the Perovskite Morphology

Controlling the grain sizes and the morphology is more complicated in thermally evaporated perovskite layers than in solution-processed ones. Contrary to previous studies of solution-processed perovskite, Lohmann *et al.*, Kim et al., and Jiang *et al.* reported that the sublimation technique results in smaller crystal sizes which can also lead to high efficient perovskite devices.<sup>[179-181]</sup> Parott *et al.* published in 2019 the first

study, describing the perovskite growth modes on glass substrates, reporting that the perovskite layer is first formed by crystalline islands of 8 nm in height before full coverage is achieved.<sup>[182]</sup> Johnston *et al.* has shown that the perovskite grains can be controlled by varying the substrate temperature from tens of nanometres (nm) to micrometers ( $\mu\text{m}$ ). They also found that the grain size depends on the substrate used in the evaporation.<sup>[179]</sup> The same was confirmed by Albrecht *et al.*, who investigated the effect of substrate temperature and hole-transporting material on the microstructure of the perovskite layer. They have observed a subtler change in microstructure than what was reported by Johnston *et al.* but also concluded that the perovskite's morphology influences the device performance.<sup>[183]</sup> Understanding, therefore, the crystallization process on a more profound and standardized level is important when considering vacuum deposition as the technique for upscaling.

## 1.6 Interface Engineering in Perovskite Solar Cells

Interface engineering is important for improving the stability and the device performance of perovskite solar cells. Perovskite solar cells are constructed of a multilayer structure (see Chapter 1.3.2), with a minimum of 5 layers, resulting in 4 different interfaces within the device. Any imperfection between the contact of two layers or on the surface of each layer can lead to the formation of defects. The introduction of these non-radiative recombination centers is disadvantageous to the photovoltaic performance. The introduction of a new interlayer between two surfaces has been used to relieve the surface defects in PSCs. The introduction of an additional passivation layer on top of the perovskite surface to encapsulate the perovskite layer can be an interesting approach to stabilize the perovskite at ambient air.<sup>[184]</sup> Therefore, the ideal interfacial layer will improve the device efficiency through the passivation of non-radiative recombination centers and also the stability. Interface engineering will be discussed in this thesis for devices in *p-i-n* and *n-i-p* architecture for vacuum-deposited perovskite.

### *Photovoltaic Performance Improvement*

Perovskite layers have shown to have a high defect tolerance compared to other light-collecting materials.<sup>[87]</sup> However, defects are produced during the fabrication process of the layers. As described above, many parameters can influence the perovskite crystallization when deposited *via* vacuum deposition. Therefore, the formation of defects cannot be excluded during the evaporation process. The most common defects include halide or Pb vacancy, antisite substitution of halide or Pb, interstitial halide or Pb-site defect, dangling bonds, and grain boundary defects (see Figure 2.1).<sup>[184,185]</sup> All defects introduce a non-radiative recombination process, leading to lower PCE performance of the cell. In addition, the interface between the perovskite and an adjunct layer has been proven to be the most likely for defect formation. This is especially critical, as the interface itself has a very important role in the device.<sup>[186]</sup> All charge dynamics such as charge separation, charge collection, charge injection, and charge recombination processes are happening at the interface after the charge generation in the perovskite layer.<sup>[187]</sup> The interface between the perovskite/HTM is especially vulnerable, as the presence of defects at this interface have a direct influence on the hole extraction process, which with increasing series resistance, results in lower  $J_{sc}$  and  $FF$  values.<sup>[184]</sup> Defects at interfaces are more deep-level defects, which give a larger contribution to the non-radiative recombination than shallow-level defects in the bulk of the perovskite.<sup>[187]</sup> It is, therefore, necessary to suppress the interfacial defects by interface engineering of the perovskite/HTM interface to boost the efficiency and stability.

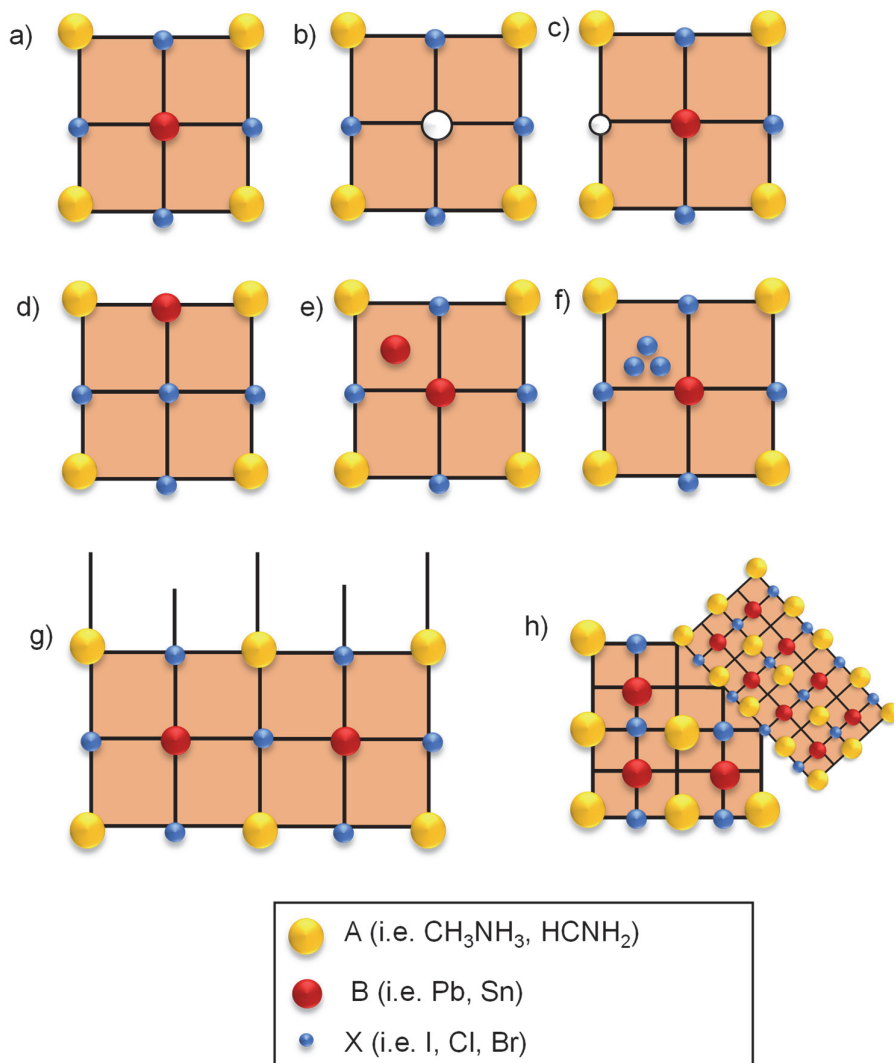


Figure 0.1 Illustration of the defects in the perovskite lattice: a) non-defect lattice b) B-site vacancy c) X-site vacancy d) B-X antisite substitution, e) interstitial of A f) interstitial of X g) dangling bonds h) grain boundary.

The common term used in the solar cell community, which describes the elimination of non-radiative recombination centers, is called passivation. Different materials have been explored as passivation materials, for example, excess  $\text{PbI}_2$ , organic ammonium salts, Lewis base, Lewis acid, organic molecules with improved hydrophobicity, wide bandgap materials, and low-dimensional perovskites.<sup>[159,184,187]</sup>

### *Stability Improvement*

The degradation processes of the perovskite have been reported to start at grain boundaries and the interface. The presence of both types of defects are therefore influencing the stability in a negative way, especially as the interaction between the perovskite layer and the adjunct layer is contributing to the device stability.<sup>[187]</sup> Unwanted kinetic processes such as ion or molecule migration can be triggered by defects and are not desirable when considering the long-term stability, as an accumulation of ions or charges at the interfaces is not favorable for the device's stability and performance.<sup>[187]</sup> Therefore, the passivation of these defects is essential for the improvement of the perovskite device.

The device stability is also influenced negatively by the moisture from ambient air, which also accelerates the degradation mechanism. Interface engineering is recently also used to provide a hydrophobic barrier on top of the perovskite layer. Therefore, the idea to create both a passivating later and a moisture resistive layer has attracted a lot of attention in the field. Organic passivation materials such as hydrophobic molecules and low-dimensional perovskite have been developed to enhance efficiency and stability.<sup>[184]</sup>

#### 1.6.1 Interface Engineering in Thermally Evaporated Perovskite Cells

Interfaces are essential in perovskite solar cells, as efficient extraction layers and passivated interfaces<sup>[188,189]</sup> are leading to the suppression of ion migration,<sup>[190,191]</sup> interfacial reactions<sup>[192-194]</sup>, and compensations for unfavoured energetic alignment.<sup>[194,195]</sup> However, most strategies for interface engineering used in the solution process cannot be adopted in thermal evaporation because of the lack of molecules that are efficient transport layers and that can be evaporated. Small molecular weight molecules usually have a low conductivity, and therefore are not suitable as efficient charge transport layers. One strategy for interfacial engineering is the introduction of dopants into the hole-transporting layers. Polander *et al.* were the first to implement spiro-OMeTAD derivatives as hole-transporting materials in fully vacuum-deposited perovskite devices, who

doped the materials with F<sub>6</sub>-TCNNQ which was leading to a PCE of 10.6%.<sup>[196]</sup> In another strategy a combination of the intrinsic and molecularly doped charge transport layers was used by Momblona *et al.* in 2016. They reported the combination of a thin, pristine layer of the hole-transporting material N<sub>4</sub>, N<sub>4</sub>, N<sub>4</sub>'', N<sub>4</sub>''-tetra([1,1'-biphenyl]-4-yl)-[1,1':4',1''-terphenyl]-4,4''-diamine (TaTm) with a thicker layer of doped HTM, TaTm: F<sub>6</sub>-TCNNQ, where F<sub>6</sub>-TCNNQ oxidizes the hole-transporting layer. They also employed first a thin electron-transport layer C<sub>60</sub> combined with a thicker doped layer of C<sub>60</sub> with PhIm. Both doping strategies enhanced the conductivity of the layers significantly, reaching in *p-i-n* configuration as PCE of 15% and *n-i-p* configuration a PCE of 18%.<sup>[78]</sup> Pérez-del-Rey *et al.* reported highly efficient perovskite solar cells using an intrinsic MoO<sub>3</sub> layer in combination with the HTM TaTm.<sup>[197]</sup>

There are not many options for highly conductive charge-transport layers currently available. Therefore, most studies in thermal evaporation use a mixture of spin-coated charge extraction layers and vacuum-deposited perovskite layers. Olthof *et al.* reported in 2017 an extensive work analyzing the interface between the hybrid perovskite MAPbI<sub>3</sub> and various substrates, including solution-processed ones.<sup>[79]</sup> She demonstrated that before the perovskite growth, an induction period is present where volatile compounds catalyzed by the substrate are formed. The length of this period of time is dependent on the nature of the substrate. For inorganic materials, this period can take up to 20-30nm of precursor deposition before the surface is passivated, for organic substrate, the period is shorter, and perovskite formation can be observed already after 3nm of precursor deposition. They also found that the composition of the 2-3 nm thin passivation layer is different from the expected perovskite composition, mainly being decomposition products of the organic cation. The regular growth of the perovskite also shows a deviation from the commonly assumed one. Band bending and dipole formation dominate the interface. Therefore, the substrate does not only influence the energy levels of the perovskite but can also introduce gap states and influence the composition and perovskite morphology.<sup>[79]</sup> Therefore, careful selection of the underlayer is necessary to provide an interface suitable for fast perovskite formation during the evaporation process. The



importance of the interface will be discussed further in Chapters 4 and 6, where a more deep investigation of the influence of interfaces is carried out.<sup>[79]</sup>



## Motivation and Strategy

Perovskite material is a fascinating technology that could be implemented in future applications such as light-emitting diodes<sup>[198]</sup>, photodetectors<sup>[199]</sup>, solar cells, quantum lasers<sup>[200]</sup>, or transistors<sup>[201]</sup>. Overcoming the challenges mentioned in chapter 2.1 is crucial for the up-scaling and commercialization of the technology. In the first part of my thesis, I tackle some challenges the vacuum-deposition method still faces: reproducibility of the perovskite crystallization and ensuring the correct composition.

Vacuum deposition is already used in the organic light-emitting device (OLED) technology, and it can also be used when up-scaling perovskite solar cells.<sup>[168]</sup> Nevertheless, as explained in chapters 1.4 and 2.1, the perovskite material has different limitations that must be overcome; therefore, optimization of the deposition method is crucial for commercialization. I focused on understanding the reproducibility challenges in co-evaporated perovskites, using the most straightforward structure MAPbI<sub>3</sub>, a benchmark. Perovskite films commonly form polycrystalline films with multiple grain sizes and surface defects. The evaporation of homogenous, defect-free large-area films is, therefore, a challenge. Understanding on a deeper level the perovskite crystallization and how crystal growth can be controlled is therefore interesting. Hence, this work is focused on two different variables that influence crystallization: evaporation speed and underlayer selection (interface engineering). Interestingly, we could observe that the preferred crystal orientation is substantially affected by the evaporation speed. Further, we found that different underlayers' chemistry greatly influences the composition and energy level of the perovskite material formed. Combining these two factors helped us fabricate a reproducible and highly oriented perovskite film with a micrometer-sized grain feature.

However, the simplification of the multi-source evaporation process is significant when considering the vacuum-deposition processes for up-scaling. I have described in Chapter 2 that the vacuum deposition method is work-intensive, especially if evaporating from simultaneously multi-sources. Each material must be calibrated independently

first and later in the perovskite to obtain the correct stoichiometry. Evaporating, therefore, a pre-synthesized perovskite material from a single source could shorten the effort in the evaporation processes and could be interesting for commercial application, especially as toxic solvents could be completely avoided. Therefore, in my subsequent work, I focused on the single-source evaporation of CsFAPbI<sub>3</sub> and FAPbI<sub>3</sub>, both attractive perovskite candidates due to their lower bandgap and stable high-temperature phase. In this work, I demonstrate the preparation of  $\alpha$ -phase perovskite thin films from pre-synthesized  $\alpha$ -CsFAPbI<sub>3</sub> and  $\delta$ -FAPbI<sub>3</sub> powders, indicating the feasibility of this approach.

In my subsequent research, I focused on understanding the dopants' influence in the state-of-the-art HTM spiro-OMeTAD on the co-evaporated perovskite material. For the first time, I identified that bis(trifluoromethanesulfonyl)imide (TFSI<sup>-</sup>), an anion employed in *p*-type dopants for spiro-OMeTAD, is migrating through the perovskite material via the grain boundaries and finally accumulating at the interface to the electron-transporting material. Interestingly, the migrating TFSI<sup>-</sup> is self-passivating the crystal defects in the perovskite layer and reduces non-radiative recombination pathways. In addition, the TFSI<sup>-</sup> anion is also leading to enhanced stability, retaining 90% of the device performance after 1600h of testing.

Interface engineering is still very limited in vacuum deposition. So far, the only engineering that can be applied is by selecting the chemical groups of the underlayer carefully to ensure good interaction with the perovskite layer. To better understand the interface's importance between the electron-transport layers and the perovskite, I chose to analyze the effect of the thermally evaporated electron-transport layer C<sub>60</sub> via impedance spectroscopy. In this work, it was found that selecting the optimum C<sub>60</sub> layer thickness is essential for the charge extraction resulting in improvement of the short circuit current ( $J_{sc}$ ).

After investigating the stability and performance improvements of co-evaporated solar cells by interface engineering, I was curious to explore the option of stability improvement from a solution-process point of view. A new class of HTM materials was

used to investigate their influence on the device's long-term stability of solution-processed perovskite devices. Implementing phthalocyanines with Zn (II) and Cu (II) coordination metals (ZnPcs and CuPcs) and differing in the alkyl side chains in devices was investigated. Interestingly in comparison to spiro-OMeTAD, ZnPcs featuring four *n*-butoxy side chains molecules demonstrated superior long-term stability under continuous 1-sun-illumination.



# Crystallographically Oriented Perovskites via Thermal Vacuum Codeposition

As discussed in Chapter 2, one limiting factor of the vacuum deposition method is the reproducibility of the perovskite quality. In this chapter, I focus on the reasons behind this challenge by first investigating the influence of the evaporation speed on perovskite crystallization. Second, I investigate the influence of the underlayer on the perovskite composition and energetic profile. It could be shown that the evaporation speed influences the perovskite morphology as well as the preferred crystallization. Further, varying the underlayer interfaces greatly influences the composition of the final perovskite and again in its energetic profile. We highlight that the correct combination of these two factors, speed, and underlayer, lead to the reproducible fabrication of vertically aligned and micrometer-sized grain features.

*This chapter is based on the following published article: Nadja Klipfel, Cristina Momblona, Hiroyuki Kanda, Naoyuki Shibayma, Yuiga Nakamura, Mounir Driss Mensi, Cheng Lui, Cristina Roldan-Carmona, Mohammad Nazeeruddin “Crystallographically Oriented Perovskites via Thermal Vacuum Deposition” Sol. RRL 5.8 (2021):2100191. DOI: 10.1002/solr.202100191.*

*In this work, I conceptualized the idea, designed the experiments, and performed the fabrication as well as characterization of perovskite thin films and solar cells. H. Kanda carried out the PL analysis; the WAXS experiments were carried out in collaboration with Prof. Dr. N. Shibayama and Dr. Y. Nakamura. Dr. M. Mensi measured the XPS and UPS, C. Liu. helped with the revision, and Dr. C. Momblona, Dr. C. Roldan-Carmona, help with finalizing the manuscript.*

## 1.7 Introduction

Organic-inorganic perovskite materials have emerged as powerful alternatives for low-cost, highly efficient third-generation solar cells. The combination of optimal optoelectronic properties, low processing costs, and high tolerance to crystal defects could overcome current limits on photovoltaic manufacturing by using a large variety of solution and vapor-based routes.<sup>[40,41,43,202–204]</sup> To date, the leading limitation of perovskite technology is the high instability under heat and light soaking conditions. Although early studies neglected the effect of crystal defects in highly efficient formulations, recent investigations on trap-mediated decomposition indicate a different scenario in which bulk and surface defects strongly impact long-term stability.<sup>[205–207]</sup> This opens the question of the role of crystallization and processing routes on operational stability and the possibility of fine-tuning the film deposition towards low-defect crystals. Unfortunately, techniques targeting film morphology and orientation to improve stability without sacrificing efficiency are still insufficient. The efficiency records achieved so far use fast depositions *via* solution-based processing at laboratory scales.<sup>[10]</sup> Consequently, there is a considerable lack of understanding of crystal formation obtained from non-conventional processes, which might become crucial to producing efficient and stable devices. In this context, thermal co-evaporation is a technique with great potential. Using a solvent-free methodology allows precise monitoring of the precursor's stoichiometry, film thickness, and the crystal-growth rate at the nanometre scale. Vacuum deposition was first employed in the perovskite field in 2013 when Liu *et al.* demonstrated for the first time a planar PSC of  $\text{CH}_3\text{NH}_3\text{PbI}_{3-x}\text{Cl}_x$  deposited on top of a metal oxide layer reaching a power conversion efficiency (PCE) of 15.4%.<sup>[67]</sup> In 2014 Malinkiewicz *et al.* and Roldán-Carmona *et al.* demonstrated the versatility of the co-evaporation method by evaporating  $\text{MAPbI}_3$  sandwiched between both organic charge transport layers on top of rigid and flexible substrates.<sup>[75,76]</sup> Yang *et al.* developed an alternating vacuum deposition method by alternating  $\text{PbCl}_2$  and  $\text{CH}_3\text{NH}_3\text{I}$  precursor layers, reaching a PCE of 16.03%.<sup>[77]</sup> Then, in 2016, Momblona *et al.* presented a direct comparison between fully sublimed *n-i-p* and *p-i-n* devices, containing the same materials and layers but with



inverted deposition order leading to efficiencies exceeding 16.5% for *p-i-n* and 20% for *n-i-p*.<sup>[78]</sup> Also, in 2019, the group of Lohmann *et al.* published a first study targeting the crystal growth modes in the co-evaporation of MAPbI<sub>3</sub>.<sup>[179]</sup> Vacuum-deposition techniques are not limited to MAPbI<sub>3</sub>-based perovskites. In 2017, Borchert *et al.* used the scalable co-evaporation method to fabricate formamidinium- based perovskite devices reaching efficiencies of 14.2% (8 cm<sup>2</sup>).<sup>[124]</sup> Zhu *et al.* demonstrated co-evaporated CsMAPbI<sub>3</sub> devices reaching efficiencies as high as 20.13%.<sup>[208]</sup> Hutter *et al.* reported in the same year the sequential vapor-deposition of all inorganic CsPbI<sub>3</sub>, reaching a PCE of 8%.<sup>[209]</sup> Multi-cation and multi-halide perovskite has been demonstrated to be deposited by vacuum-based techniques. For example, large bandgap perovskite devices of MAPb(Br<sub>0.2</sub>I<sub>0.8</sub>)<sub>3</sub> were for the first time demonstrated in 2018 from the group of Bolink *et al.*, reaching 15.9%, which was followed then by the demonstration of narrow-bandgap FAPb<sub>0.5</sub>Sn<sub>0.5</sub>I<sub>3</sub> reaching a PCE of 13.98% in 2019.<sup>[80,81]</sup> In 2020, the publications employing co-evaporation as the primary fabrication technique was significantly rising. In 2020 Momblona *et al.* demonstrated that co-evaporation is also an interesting method for fabricating lead-free perovskites, such as methylammonium bismuth iodide.<sup>[82]</sup> In the same year, Chiang *et al.* demonstrated the multisource evaporation of *p-i-n* FA<sub>0.7</sub>Cs<sub>0.3</sub>Pb<sub>(10.9Br<sub>0.1</sub>)<sub>3</sub></sub> reaching 18.2% efficiency.<sup>[83]</sup> Wang *et al.* demonstrated the fabrication of mini-modules reaching efficiencies of 20.28% (21 cm<sup>2</sup>).<sup>[84]</sup>

Unfortunately, reproducing this level of performance exceeding 20% remains elusive. Indeed, a deeper understanding of the evaporation process and resulting perovskites is still limited compared to those reported from the solution. For example, it is unclear if thermally co-evaporated methylammonium lead iodide (MAPbI<sub>3</sub>) can crystallize in the cubic phase with alternating PbI<sub>2</sub> amount, therefore altering the thermodynamic equilibrium established for the crystal phase.<sup>[210]</sup> Ávila *et al.* also reported unusual values in the refractive index, suggesting optical properties distinct from those prepared from solution.<sup>[211]</sup> In addition, contrary to previous studies of solution-based processes, Lohmann *et al.*, Kim *et al.*, and Jiang *et al.* observed that smaller crystals prepared *via* sublimation have a positive impact on device efficiency.<sup>[179-181]</sup> Additionally, little

attention has been given to the surface of deposition and the possible interactions occurring via sublimation.<sup>[79,212,213]</sup> Therefore, despite the apparent simplicity and increasing effort to understand the deposition process, thermal co-evaporation of hybrid perovskites remains unclear, and only a limited number of research teams report satisfactory results<sup>[78,84,179,182,208]</sup>, which could be due to the influence of the substrate co-evaporated perovskite that Olthof *et al.* described for the first time.<sup>[79]</sup>

Here, we present a systematic study investigating fundamental aspects in the thermal co-evaporation of MAPbI<sub>3</sub>, the benchmark system with the simplest hybrid organic-inorganic composition. While many variables influence the vacuum deposition (film thickness, chamber pressure, substrate temperature, or precursors ratio), they are very well established within the field and considered in every deposition process.

However, here we investigate the crystallization speed and surface chemistry and their effect on perovskite work function, morphology, and crystal orientation. Our results demonstrate that these two variables, often neglected, are critical to obtaining reproducible results. They determine the crystal formation, orientation, and film morphology, having an outsized impact on the structural and optoelectronic features. This enables the fine-tuning of crystal formation towards vertically monolithic crystals, providing for the first-time high control on crystal growth and orientation on a large-area compatible technique, which is an imperative requirement to move forward towards commercialization.

## 1.8 Results and Discussion

Figure 4.1 provides a schematic overview of the dual evaporation process and the different charge transport materials used in this study (HTM, for holes-, and ETM, for electrons-). In brief, MAPbI<sub>3</sub> films were prepared by co-evaporating the two starting precursors, CH<sub>3</sub>NH<sub>3</sub>I and PbI<sub>2</sub>, in a 1:1 molar ratio, forming the typical 3D perovskite with tetragonal phase (Figure A.1, Appendix A).<sup>[124]</sup> We investigated the effect of the evaporation rate and, therefore, the speed of crystal growth on perovskite formation.

The evaporation rate for  $\text{PbI}_2$  was monitored by a quartz crystal microbalance situated above the  $\text{PbI}_2$  source. A perovskite growth-rate of  $0.18 \text{ \AA}\cdot\text{s}^{-1}$  (see specifications in device fabrication) was initially fixed as reference (C), and increased by a factor of two ( $2C = 0.36 \text{ \AA}\cdot\text{s}^{-1}$ ), three ( $3C = 0.54 \text{ \AA}\cdot\text{s}^{-1}$ ) and four ( $4C = 0.72 \text{ \AA}\cdot\text{s}^{-1}$ ) (Figure 4.1a).

$\text{MAPbI}_3$  films were deposited under different deposition rates while maintaining the same precursor ratio in all cases (Figure A2, Appendix A). State-of-the-art semiconductors were employed as charge transport materials. 2,2',7,7'-Tetrakis[N,N-di(4-methoxyphenyl)amino]-9,9'-spirobifluorene (spiro-OMeTAD), poly(3,4-ethylene dioxythiophene)-poly(styrene sulfonate) (PEDOT:PSS) and  $\text{NiO}_x$  were chosen as HTMs, and  $\text{TiO}_2$  (planar- or mesoporous) were used as ETMs (Figure 4.1b).

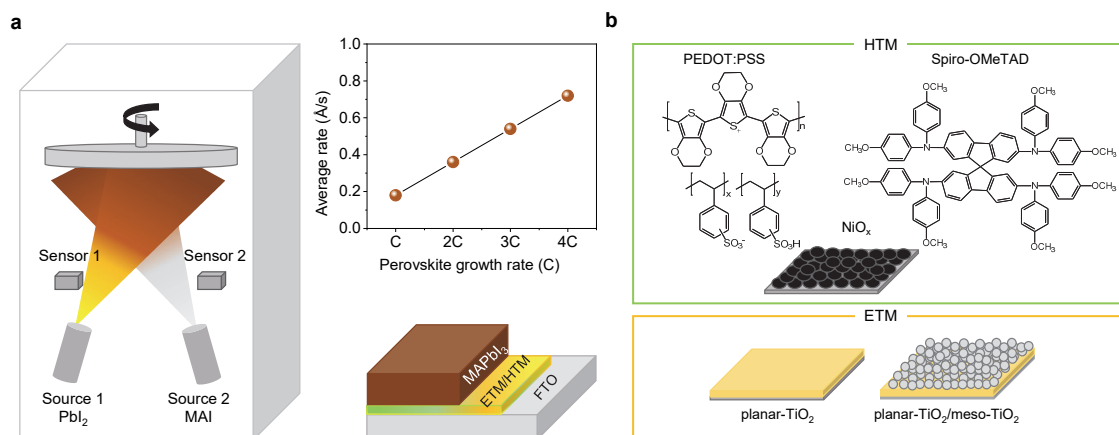


Figure 0.1: Dual-source evaporation process and device configuration. a) Co-evaporation of  $\text{MAPbI}_3$  from  $\text{PbI}_2$  and MAI precursors at several deposition rates (from C-4C) and substrate architecture. b) p- and n-type semiconductors (HTM and ETM, respectively) employed as underlying charge transport materials.

To initiate the study, we employed FTO substrates covered with  $\text{NiO}_x$  as HTM and deposited  $\text{MAPbI}_3$  films ( $\sim 1 \mu\text{m}$  thick) at increasing crystal growth rates, ranging from C to 4C. We analyzed the film morphology, surface coverage, and roughness using scanning electron microscopy (SEM) and atomic force microscopy (AFM). The SEM images, illustrated in Figure A.3 (Appendix A), show a polycrystalline morphology, with the estimated grain size distribution varying slightly according to the perovskite growth

rate (Figure A.4, Appendix A). Films deposited at a low rate (C) show homogeneous SEM features along with the entire film, with an average value of  $\sim 237$  nm. Similar grain distribution has typically been reported for vacuum co-evaporated perovskites.<sup>[78]</sup> Yet, using faster deposition rates (4C) increases the mean value to  $\sim 340$  nm and induces the formation of prominent grains over  $1 \mu\text{m}$  in diameter (see top-surface SEM, Figure A3a, Appendix A). A similar trend is observed for the film roughness, as the root-mean-square (RMS) value increases from  $\sim 58$  to  $78$  nm under faster growing rates (C to 4C) (Figure A5, Appendix A). This suggests that the roughness of vacuum-deposited perovskites is not necessarily similar to the underlayer, as would generally be expected from a conformal deposition of the film (see also Figure A12, Appendix A). Still, it rather depends on the growing condition selected for the process.

We further investigated the electronic structure by using ultraviolet photoelectron spectroscopy (UPS) (Figure A.6, Appendix A). This technique is a powerful tool to access the electronic profile providing relevant information like work function ( $\phi$ ) or injection barrier between specific materials. The results, summarized in the energetic profile illustrated in Figure 4.2 a, reveal pronounced changes in the perovskite's electronic levels motivated by the different sublimation speeds. As we increase the perovskite growth rate, a small shift in the Fermi level occurs of up to  $0.07$  eV for 3C, and a prominent change in the valence band values ( $E_{\text{VB}}$ ) from  $-5.37$  eV (C) to  $-5.54$  eV (3C) (Figure A.6, Appendix A). Given that  $\text{MAPbI}_3$  has a bandgap value of  $1.6$  eV, this implies that the perovskite gradually changes from p-type to an intrinsic semiconductor character as the growth rate increases from C to 3C. A faster growth rate (4C) induces a reverse valence band shift of  $0.11$  eV, towards higher binding energy, making the material gain more p-type characteristics. Note that such differences, emerging exclusively from the various deposition speeds, are paramount for achieving optically aligned electronic levels and efficient charge extraction within the device. We also characterized the materials by UV-visible absorption and photoluminescence (PL) spectroscopy. Contrary to UPS, these techniques are less sensitive to surface effects and instead provide rich information about the bulk material, facilitating a more complete picture of the

layer. The results, shown in Figures 4.2b and 4.2c, reveal significant changes in the shape of the spectra and a tiny shift in the absorption onset consistent with the UPS trend (see full spectra in Figure A.7, Appendix A). In particular, we highlight the strong redshift occurring in the PL emission for faster depositions, from 1.65 eV (C) to 1.59 eV (3C), which again reverses for very fast crystallization (4C). We note here that in literature, perovskite is co-evaporated at a fixed precursor rate and on top of underlayers with similar functional structures such as PTAA, MoO<sub>3</sub>/TaTm so that such differences that we observe could not be noted before. Therefore similar effects have been previously ascribed to small changes altering the lattice strain and orbital hybridization of the inorganic skeleton.<sup>[57,78,83,214–217]</sup> In our case, the crystallization dynamics during crystal formation affect the photophysical scenario, which may alter factors such as charge dissociation, charge transport, diffusion length, and consequently, device performance.<sup>[218]</sup>

To shed light on the origin of such variations, we further explored the crystallinity of the perovskites by X-ray diffraction (XRD) measurements. Figure A.8 Appendix A contains the diffraction patterns of NiOx/MAPbI<sub>3</sub> films grown at increasing crystallization speeds. All films exhibit intense diffraction signals typical from the crystalline tetragonal MAPbI<sub>3</sub> phase (theoretical pattern is included for reference). Still, there are strong differences in the relative intensity between peaks for the different growing conditions, e.g. (200) crystal plane disappears with increasing perovskite growth rate in 2C, 3C, and 4C. This phenomenon denotes a non-uniform distribution of the crystallites in the angular space, suggesting plausible film growth along preferred crystal orientations. We verified the out-of-plane reflections by using wide-angle X-ray scattering (WAXS), which allows the investigation of crystal planes not accessible by conventional powder XRD.<sup>[219]</sup> In the WAXS 2D images, illustrated in Figure 4.2d, the azimuthal intensity distribution correlates to the orientation of the planes, therefore uniform intensity along the Debye-Scherrer ring (e.g., 4C at  $q_z = 1.0, 2.0 \text{ \AA}^{-1}$ ) indicates no preferred crystal orientation. By contrast, the high intensity red-spots at  $q_z = 1.0, 2.0 \text{ \AA}^{-1}$  for C, 2C and 3C suggest specific out-of-plane orientations. To better visualize these changes, we selected the Debye-Scherrer ring corresponding to (220) lattice plane at  $q_z = 2.0 \text{ \AA}^{-1}$  (Figure 4.2e)

and integrated the intensity along the azimuthal angle between  $q_z = 2.00\text{--}2.03 \text{ \AA}^{-1}$  (see Supplementary Notes). The intensity profile, shown in Figure 4.2e, consists of an intense peak for C, 2C, and 3C, suggesting a large portion of crystals oriented along with  $\chi$  values of  $75^\circ - 78^\circ$  (see specific values in the inset).

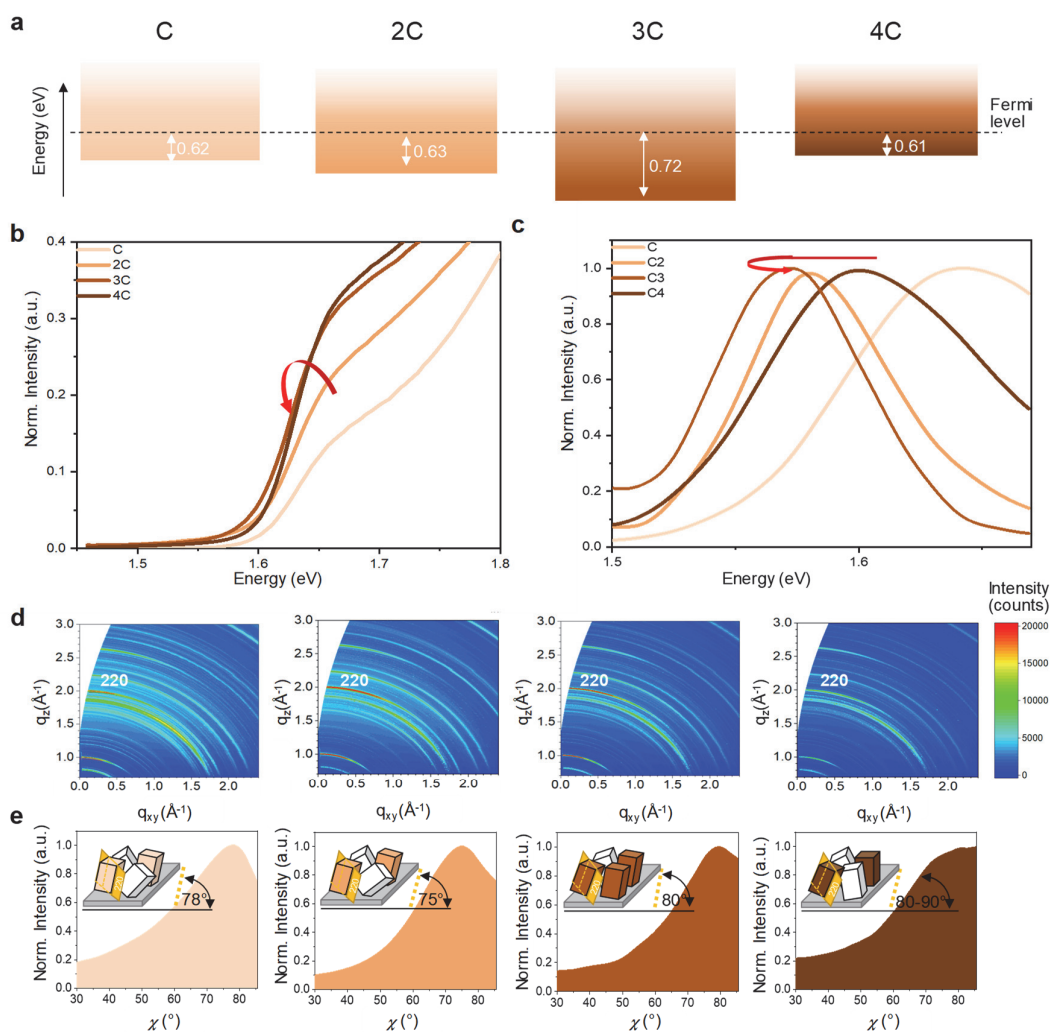


Figure 4.2: MAPbI<sub>3</sub> films grown on NiOx. a) Energy levels extracted from UPS measurements of films grown at several deposition rates (from C to 4C). b) UV-visible absorption and c) PL spectra of films shown in a (excitation wavelength  $\lambda = 450 \text{ nm}$ ). d) WAXS images of films shown in a. e) Integration of the azimuthal intensity along the 220 reflex in WAXS. Inset: schematic of 220 lattice plane orientation showing out-of-plane orientation relative to the substrate (cubes in different brown shading: 220 lattice plane tilted  $78^\circ$  (C),  $75^\circ$  (2C),  $80^\circ$  (3C) from the substrate). Note the apparent trend in 4C of intensity between  $80^\circ$ – $90^\circ$ . Fewer white cubes indicate a more

preferred orientation. d) UV-visible absorption and PL spectra of films (excitation wavelength  $\lambda = 450$  nm).

Contrary to that expected from crystal growth theory,<sup>[220]</sup> faster perovskite growth rates (3C) decreases peak broadness and induce more prominent orientations up to 4C, the latest with broader distribution of crystals aligning between  $70^\circ - 90^\circ$  (see the schematic number of brown (oriented) versus white (non-oriented) cubes in the inset). Interestingly, the changes in orientation follow a similar trend to that observed for the UPS, suggesting strong correlations between the optical properties and the crystallization kinetics.

We performed similar experiments on perovskite films deposited on  $\text{TiO}_2$  to compare with a metal oxide semiconductor with a very different work function value. Figures A.9 and A10, Appendix A, demonstrate similar changes to those observed in NiOx for the optoelectronic properties after varying perovskite growth rate, providing strong variations in the Fermi level bandgap and PL peak position. It can also be noted that a varying deposition rate on both metal oxides, NiOx and  $\text{TiO}_2$ , promotes a similar change in the orientation of the 220-lattice plane and could potentially induce specific crystal orientations. Such effects, promoted by the deposition speed, have not been previously observed and point out the perovskite growth rate as a key parameter affecting vacuum-deposited perovskites. We note that given that vacuum deposition allows easy control of this parameter, it could be plausibly used to minimize the morphological and energetic disorder of the films. Interestingly, spiro-OMeTAD, the archetypal organic HTM employed in PSCs, showed a rather different behavior (Figure 4.3a). We fabricated films using the same conditions as described before (C to 4C) and integrated the azimuthal intensity of the Debye-Scherrer ring at about  $2.0 \text{ \AA}^{-1}$  of the WAXS data. The crystal orientation was barely affected by the perovskite growth rate (Figure 4.3a, from C to 4C), and films exhibit pronounced out-of-plane crystal-alignments centered at  $\chi = 72^\circ$  (see inset). Similar to the previous results, increasing growth rate produces a sharper peak for the 220-lattice plane, providing the strongest preferred orientations for perovskites grown at 3C. Interestingly, a second Debye-Scherrer ring at  $1.97\text{-}2.00 \text{ \AA}^{-1}$  (corresponding to (004) lattice plane, Figure A11, Appendix A) revealed an additional

orientation appearing only for 2C and 3C, which is perpendicular to the prior. We note that the tetragonal (220) diffracts at very close  $2\theta$  angles than that of (004), and therefore both peaks frequently overlap. This is the situation observed in Figure 4.2 for films grown on NiOx. However, if we inspect the  $q_z \sim 2.0 \text{ \AA}^{-1}$  region in Figure A.11, diffraction lines always appear at either  $1.99 \text{ \AA}^{-1}$  or  $2.01 \text{ \AA}^{-1}$ , or both of them, depending on the growing conditions. These lines are assigned to (220) and (004), respectively, and can be used to identify the planes in the 2D-WAXs images.

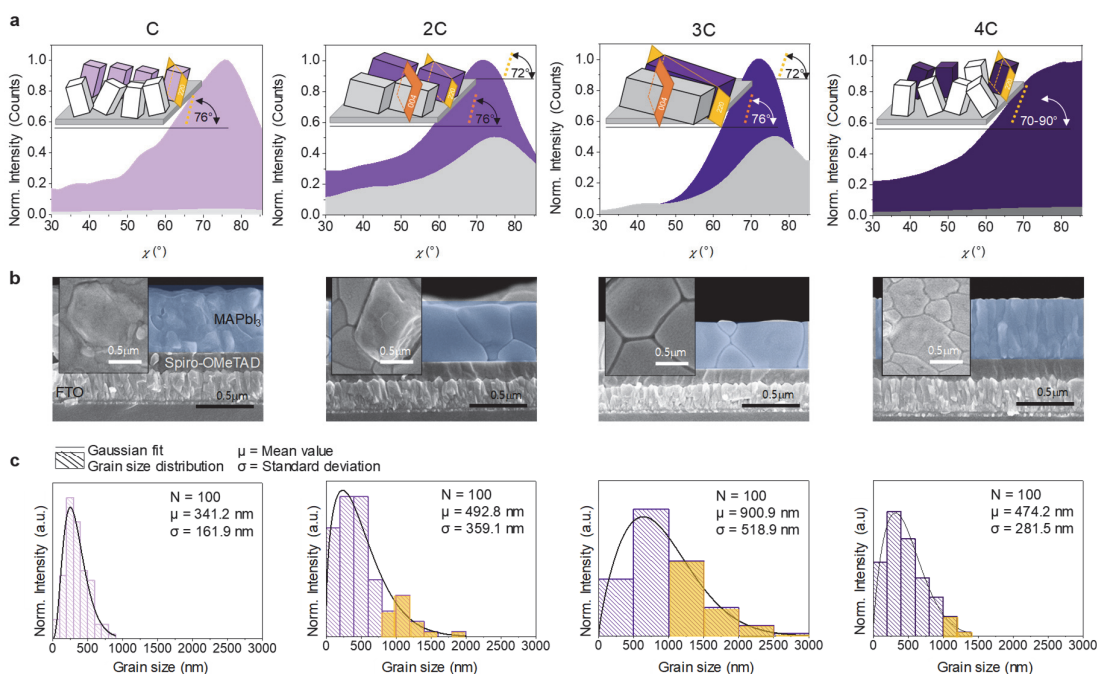


Figure 0.3: MAPbI<sub>3</sub> films grown on spiro-OMeTAD. a) Integration of the azimuthal intensity along the 220 reflex ( $2.0 \text{ \AA}^{-1}$ ) in WAXS for films crystallized at different deposition rates (from C to 4C). Inset: schematic of grains with 220 lattice plane showing out-of-plane orientation (indicated by cubes with purple shading: tilted  $76^\circ$  (C),  $72^\circ$  (2C),  $72^\circ$  (3C) from the substrate). Grains with 004 lattice plane showing in-plane orientation (indicated by cubes with grey shading: tilted  $72^\circ$  (C),  $76^\circ$  (2C),  $76^\circ$  (3C) from the substrate). Note the apparent trends for peak intensity angles between  $70$ - $90^\circ$  of 220-lattice plane (4C). Fewer white cubes indicate more preferred orientation b) Cross-section and top-view (inset) SEM images of MAPbI<sub>3</sub> formed on spiro-OMeTAD substrates. c) Estimated grain-size distribution of the perovskite layers.

Therefore, films made under such conditions exhibit highly oriented crystals with both out-of-plane and in-plane crystal orientations at  $\chi_{220} = 72^\circ$  and  $\chi_{004} = 76^\circ$ . Noteworthy, the top and cross-section SEM images (Figure 4.3b) also show strong



variations in film morphology and grain size, according to the speed of crystallization. Despite a deeper analysis *via* electron backscatter diffraction (EBSD) or transmission electron microscopy (TEM) has not been performed, in the following lines, we will refer as grains to the features observed in SEM, as commonly used in literature. Therefore, the grain sizes here are estimations used to describe a general trend that we see in morphology. Starting with smaller grains (C), a striking difference appears for 2C and 3C, providing uniform and large crystals of over  $\sim 1 \mu\text{m}$  diameter (see Figure 4.3c). In particular, we highlight the monolithic growth of the crystal in the out-of-plane direction, especially remarkable for layer 3C, in which the grains align perfectly in the vertical direction (see Figure 4.3b, rate 3C). Only at the highest speed (4C) do grain sizes become smaller and more randomly oriented, forming a uniform nano rod-like morphology lined up along the substrate (see grain size distribution in Figure 4.3c). We note that obtaining such morphology and homogeneous distribution is challenging in vacuum co-deposited films, and comparable morphologies have only been acquired under very severe temperature treatments ( $-2^\circ\text{C}$ ).<sup>11</sup> The AFM measurements, shown in Figure A.12, Appendix A, also showed different roughness according to the deposition rate (1C, RMS= 63.08nm; 2C, RMS=50.05nm; 3C, RMS= 38.62nm; 4C, RMS=46.81nm), differing substantially from that of the underlayer (RMS = 2.96 nm). These changes reveal for the first time the dual impact of crystal growth rate and interfacial chemistry on vacuum-deposited perovskites, which calls for deeper analysis to explore their origin and repercussions on thin films.

To specifically target the effects induced by the interface, we investigated the crystallization dynamics on several underlying materials under fixed deposition rate and thickness (3C =  $0.54 \text{ \AA}\cdot\text{s}^{-1}$ , 500 nm) and extended the investigation to alternative state-of-the-art semiconductors like PEDOT: PSS and meso-TiO<sub>2</sub>. Due to the versatility of thermal evaporation, several substrates could be targeted in single evaporation, therefore ensuring that the interface is the unique variable between films. The electronic structure, optical properties, and elemental composition of the resulting films are summarized in Figure 4.4. Results show that perovskites undergo pinning in the Fermi level

with the valence band onset determined by the substrate, but contrary to previous reports using different semiconductors, the changes barely deviate according to the p- or n-type character, while they mostly do according to the chemical nature of the contacting material (see values for metal oxides in Figure 4.4a).<sup>[221–223]</sup> Specifically, perovskites grown on p-type semiconductors with similar  $\phi$  values but different surface chemistry (Figure 4.4a) exhibit large changes on the Fermi level and valence band onset even for 500 nm films. We observed values of  $\phi_{\text{Per/NiO}_x} = 4.82$  eV,  $\phi_{\text{Per/spiro-OMeTAD}} = 4.67$  eV,  $\phi_{\text{Per/PEDOT:PSS}} = 4.88$  eV, showing differences of  $> 0.2$  eV between spiro-OMeTAD and PEDOT:PSS (see  $\phi$  values for the bare underlayer in Figure A.13, Appendix A). Similarly, the valence band onsets shift by 0.72, 0.81, and 0.69 eV to the Fermi level for NiO<sub>x</sub>, spiro-OMeTAD, and PEDOT:PSS, respectively.

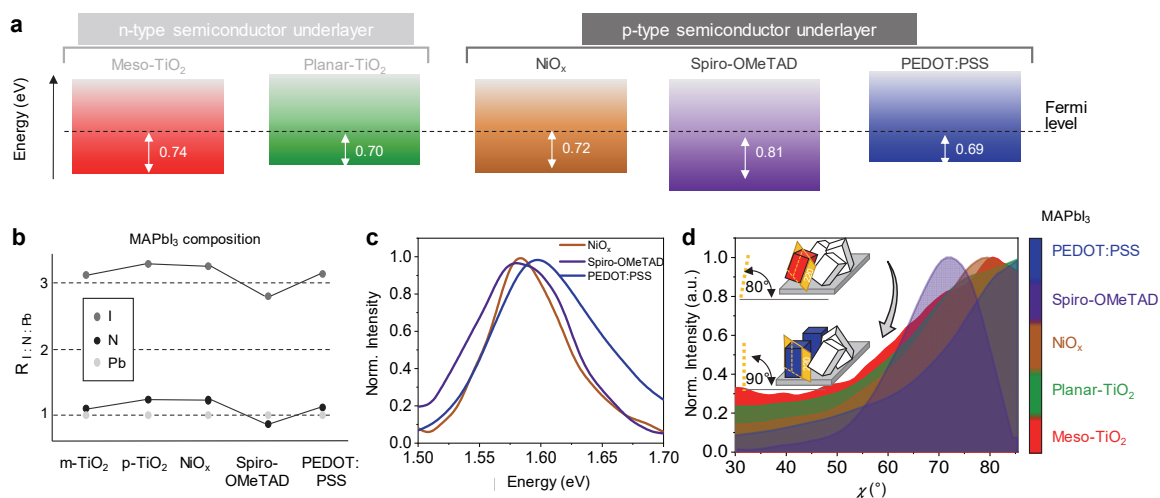


Figure 4.4: MAPbI<sub>3</sub> films deposited on several semiconductors. a) Energy levels extracted from UPS data of perovskites formed on top of n- and p-type underlayers prepared under the same evaporation condition (3C). b) Compositional data extracted from XPS for the elements lead (Pb 4f), nitrogen (N 1s), and iodide (I 3d). c) PL spectra recorded for all conditions. d) Integration of the azimuthal intensity distribution of the 220 reflex in the WAXS data. Inset: schematic of grains with 220 lattice plane showing out-of-plane alignment relative to the substrate (for perovskite on meso-TiO<sub>2</sub>, red cube 220 lattice plane 80° from the substrate; for perovskite on PEDOT:PSS, blue cube 220 lattice plane 90° from the substrate).

Such strong variations are in line with previous reports describing plausible chemical interactions at the perovskite/metal-oxide interface.<sup>[79]</sup> However, these

interactions are expected to affect the first 30 nm of the seeding layer, leading to identical perovskite composition and crystal growth over 30 nm exclusively. In our case, the effects extend to the whole perovskite material (500 nm), thus affecting also the bulk optical and electronic features (Figure 4.4c and Figure A.14, Appendix A). We further investigated the chemical environment of nitrogen (N 1s), iodine (I 3d<sub>5/2</sub>), and lead (Pb 4f<sub>7/2</sub>) signals by X-ray photoelectron spectroscopy (XPS) (Figure A.15, Appendix A). To avoid any surface contamination, we transferred the fresh samples directly from the glovebox into the XPS machine via a transfer vessel. We observe the typical photoemission peak attributed to NH<sub>3</sub><sup>+</sup> group in methylammonium (402.6 eV), sharp double peaks assigned to I 3d (~ 619.5 eV for I 3d<sub>5/2</sub>, ~ 631 eV for I 3d<sub>3/2</sub>) and Pb<sup>+2</sup> (~ 138.6 eV for Pb 4f<sub>7/2</sub>, ~ 143.4 eV for Pb 4f<sub>5/2</sub>) which confirm the formation of Pb–I bonds. No metallic lead (~136.5 and ~141.5 eV) is detected on any layer. Despite this confirmation, the perovskite composition at the surface shows significant changes with respect to the underlayer: while perovskites form similarly on metal-oxides, big differences appear in those grown on organic p-type layers (Figure 4.4b, Table 1).

Table 0.1: Compositional analysis of MAPbI<sub>3</sub> deposited on p- and n-type semiconductors. Atomic ratios extracted from the XPS data are shown in Figure A.15 (Appendix A).

Type of Under-layer	Atomic Ratio			
	I: Pb		N: Pb	
	Experimental	Theoretical	Experimental	Theoretical
Meso-TiO <sub>2</sub>	3.05		0.99	
Planar-TiO <sub>2</sub>	3.29		1.19	
NiO <sub>x</sub>	3.24	3	1.19	1
Spiro-OMeTAD	2.86		0.87	
PEDOT: PSS	3.13		1.08	

Comparing the three types of HTMs presented in Figure 4.4 (organic and inorganic), the relative I: Pb ratio varies by 3.24, 3.13, and 2.86 for NiO<sub>x</sub>, PEDOT: PSS, and spiro-OMeTAD, respectively, suggesting an excess of PbI<sub>2</sub> dominating the perovskite on spiro-OMeTAD. As perovskites crystallize in the same evaporation process with a 1:1

fixed precursor ratio, it is the underlayer, which determines the final chemical composition and energetic features of the co-evaporated perovskite. We note that in other techniques, like vacuum flash evaporation or layer-by-layer precursor deposition, such strong changes in perovskite composition were not observed on top of different underlayers as the perovskite crystallized in stoichiometric ratios.<sup>[224,225]</sup>

Such results, which could stem from the various crystallographic changes and surface properties induced by each underlayer, have important implications in device optimization and upscaling of fabrication, as well as device reproducibility from different laboratories.<sup>[226]</sup>

Indeed, strong variations in crystal orientation (500 nm) are detected from the azimuthal integration of the 220 lattice plane for each underlayer (Debye-Scherrer ring at  $2.0 \text{ \AA}^{-1}$ ) (Figure 4d). While the meso-TiO<sub>2</sub> favors a uniform random crystal distribution, few preferred orientations emerge on planar metal-oxides but do become apparent on the organic semiconductors. As discussed in Figure 4.3, such preferred crystal orientations observed for spiro-OMeTAD and PEDOT: PSS does not heavily depend on the perovskite growth rate, denoting a key role of the surface chemistry of the underlayer on dictating specific crystal alignments, paramount to controlling the crystallization via thermal co-evaporation (see also Figure A16, Appendix A). Interestingly, strong interactions at the interfaces with methoxy anchors (present in spiro-OMeTAD) (Figure 4.1b) and thiophene derivatives (present in PEDOT: PSS) (Figure 4.1b) have been previously reported for perovskites processed via solution.<sup>[227]</sup> We, therefore, believe that such interfacial interactions could become crucial on vacuum-deposited perovskites, providing an effective tool to fine-tune the crystal growing into specific lattice orientations.

To gain insight into this phenomenon, we investigated the WAXS images for perovskite seeding layers of 35 nm, exclusively targeting the region in direct contact with the interface. Figure 4.5a (and Figure A.17a, Appendix A) show evidence of ring patterns without preferred crystal orientations for layers grown on metal-oxides but a clear out-of-plane orientation for the two organic interfaces. Importantly, a single crystalline

orientation emerges on spiro-OMeTAD, denoting a very consistent crystal growth induced by methoxy groups. We note that having such strong out-of-plane crystal orientation remains to date of high interest for many optoelectronics, offering the opportunity to more closely approach the Shockley-Queisser limit in photovoltaics, as compared to polycrystalline layers.<sup>[43,204,227-230]</sup> This also provides additional support to our previous assessment, demonstrating interfacial-guided orientations induced by the underlying surface.

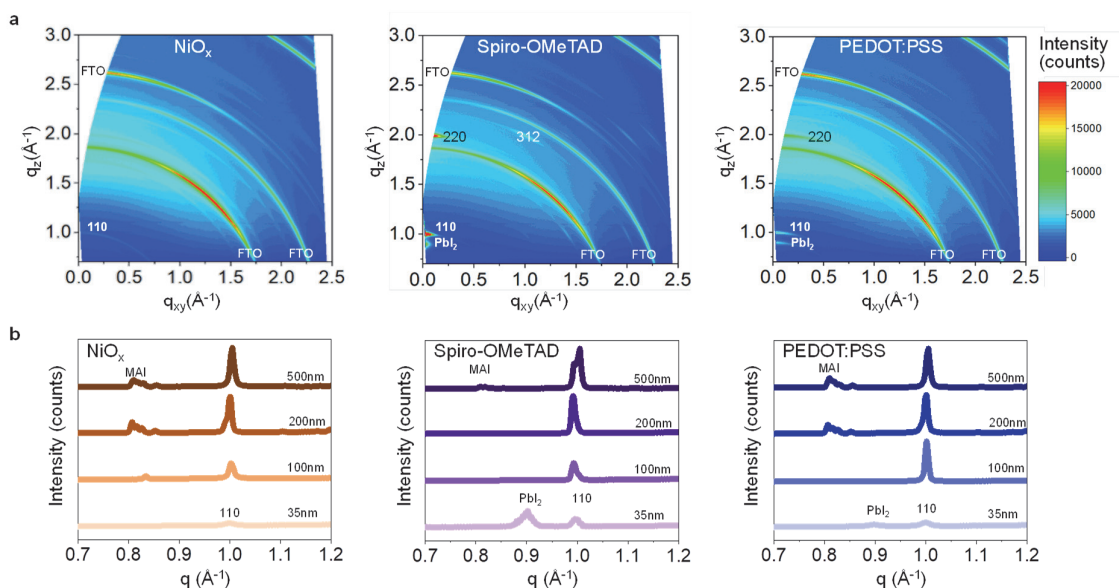


Figure 0.5: Evolution of vacuum deposited MAPbI<sub>3</sub> layers. a) WAXS images of 35 nm films grown on NiO<sub>x</sub>, spiro-OMeTAD, and PEDOT: PSS. Diffractions related to FTO and PbI<sub>2</sub> are indicated in the label. b) Evolution of XRD patterns with increasing film thickness.

Our data also suggests that the seeding composition highly depends on the type of underlayer, showing preferential accumulation of PbI<sub>2</sub> precursor on the organic interlayers. Moreover, these seeding layers will determine the upcoming crystal growth and film composition obtained during the deposition process, as also revealed by the  $q$ -pattern evolution in Figure 4.5b. We note that previous reports based on glass surfaces have proposed initial nucleation of MAPbI<sub>3</sub> islands (with 8nm height) via Volmer-Weber type growth, which explains the formation of multiple small grain sizes in the film.<sup>[182]</sup> However, here we see that small-grains are not the unique possible morphology in

evaporated films, and instead, it is highly influenced by the type of underlayer and rate of evaporation, resulting in films with different properties and grain sizes (Figure A.4, Figure 4.3c). We further observe that the initial accumulation of  $\text{PbI}_2$  on organic substrates, absent for metal-oxide substrates, rapidly vanishes as the layer evolves from 35–500 nm, maintaining a stoichiometric film for organic underlayers  $\leq 200$  nm thick. This is concomitant to a gradual accumulation of MAI occurring for perovskites grown on metal-oxides ( $q = 0.8 \text{ \AA}^{-1}$ ) (Figure A.17a, b, Appendix A), which is only detected at  $\geq 200$  nm in PEDOT: PSS (almost absent for those grown on spiro-OMeTAD, 500 nm). Given that the films crystallized under the same sublimation process, the surface chemistry of the underlayer might determine which precursor adsorbs first, resulting in different seeding centers from where the perovskite evolves. In addition, as the final stoichiometry is substantially influenced by the two parameters here discussed, it is no longer adequate to generalize with a specific precursor ratio to achieve an optimal perovskite, as this must be independently optimized with the specific underlayer and deposition rate.

We verified the impact of the several crystallizations on device performance by selecting spiro-OMeTAD as template underlayer and fine-tuning the crystal arrangements via the deposition rate. We embodied 500 nm layers into *p-i-n* devices, using  $\text{C}_{60}$ /BCP as ETM and chromium/gold as a metallic electrode (see device configuration in Figure 4.6a). We note that this simple approach enabled the preparation of perovskite films with micrometer-sized grains of identical orientation, as demonstrated in 2D-XRD and SEM images presented in Figure 4.6. Such results underline the high potential of tuning the deposition rate in controlling the crystal formation towards perfect crystal orientation.

Figure 4.6d, e and Figure A.18, Appendix A, summarize the main photovoltaic parameters obtained for each type of layer, confirming a direct relation between crystallization and device performance, providing the best results for the highest oriented films. Indeed, the short current density ( $J_{sc}$ ) gradually increases when changing the perovskite growth rate from C to 3C ( $J_C = 18.45 \text{ mA}\cdot\text{cm}^{-2}$ ;  $J_{2C} = 18.90 \text{ mA}\cdot\text{cm}^{-2}$ ;  $J_{3C} = 19.94 \text{ mA}\cdot\text{cm}^{-2}$ ) but strongly reduces for 4C ( $J_{4C} = 17.66 \text{ mA}\cdot\text{cm}^{-2}$ ) (Table S1, Supporting Information), in

agreement to the external quantum efficiency (EQE) spectra (Figure 4.6e). A similar trend is observed for the fill factor (FF), which improves by 33% when shifting from C to 3C, boosting the PCE from 9.46–15.19%. Notably, despite high photon-to-current conversion efficiency of ~ 80 % is observed in the visible range (resulting in an integrated current of 17.74, 19.02, 19.52, and 18.21 mA·cm<sup>-2</sup> for C to 4C, respectively), no signal is detected in the region below 400 nm. We explain this by considering the high absorption of spiro-OMeTAD in the blue spectral region below 450 nm, which limits the photogeneration of carriers in the high-energy zone. We note that this absorption further extends up to 700 nm (see Figure 4.6e), behaving as an optical filter for the incoming light. This partially explains the moderate PCE values observed for this specific *p-i-n* configuration and invites for designing more transparent alternatives containing methoxy-enriched interfaces, such as spiro-OMeTAD. The devices where the perovskite was grown at 2C and 3C crystallization speed also showed improved stability when measured at maximum power point (MPP) tracking and continuous light illumination, as illustrated in Figure A.19, Appendix A.

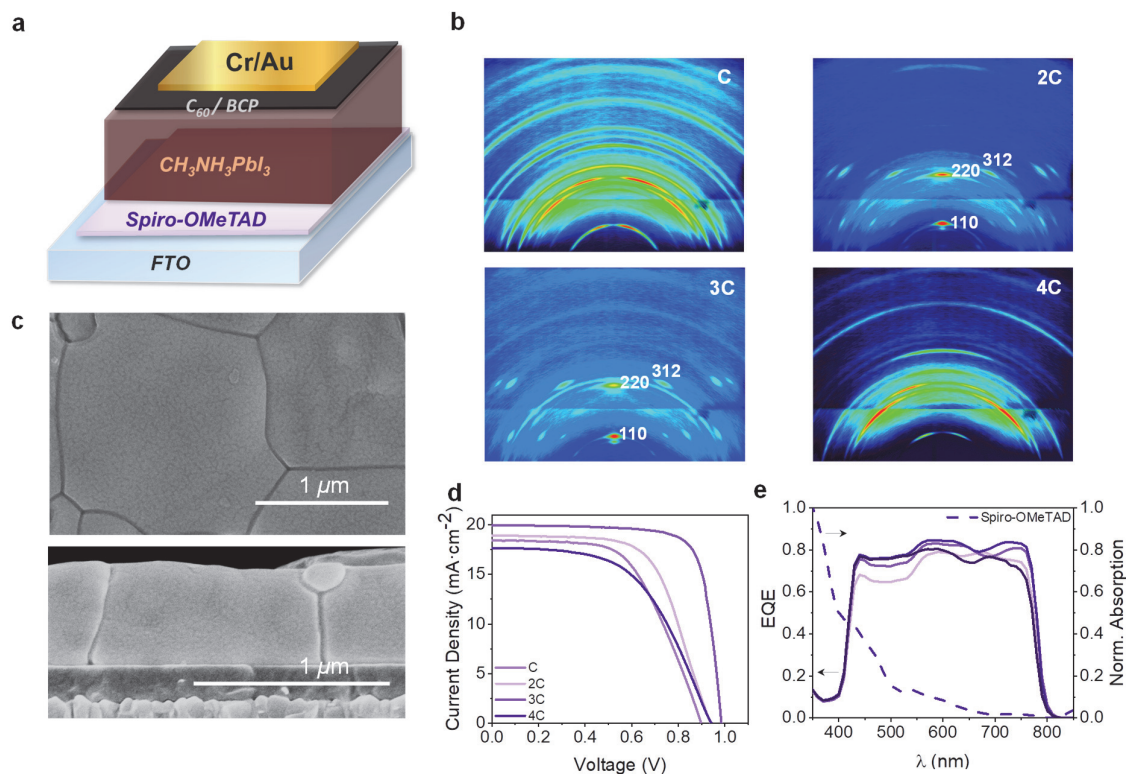


Figure 0.6: Influence of deposition rate on crystallization and device performance. a) Scheme of *p-i-n* architecture employed for the PSCs. b) 2D-detector images of 500 nm MAPbI<sub>3</sub> grown on Spiro-OMeTAD at different deposition rates (from C to 4C). The spots indicate preferred out-of-plane orientation. c) Top- and cross-section SEM of MAPbI<sub>3</sub> films (3C). Scale bar: 1 μm. d), J-V curves, and d) EQE spectra of typical devices, including absorption spectra for underlayer Spiro-OMeTAD containing films shown in a and b.

## 1.9 Conclusions

A proper combination of surface chemistry of the underlayer and speed of sublimation in vacuum-deposited perovskites allows, for the first time, full control over morphology, chemical composition, and crystal alignment. To date, this has been difficult to achieve. These variables, usually neglected in the literature, may be a major source of irreproducibility when not carefully chosen and must therefore be explicitly indicated in all future publications. However, when properly combined, these parameters provide an opening for fine-tuning perovskite films towards specific crystal quality and orientation. This enables the fabrication of monolithic micrometer-sized crystals with perfect crystal alignment via thermal co-evaporation, pushing forward the understanding of



irreproducibility sources in a large-area compatible technique, which is a prerequisite for any future attempt of commercializati



# Structural and Optoelectrical Characterization of Single-Source Evaporation of Phase Pure CsFAPbI<sub>3</sub> and FAPbI<sub>3</sub> Perovskite Thin Films

Thermal vacuum deposition is an exciting technique when scaling up perovskite solar cells. However, time-consuming calibration of the different precursor sources are necessary when evaporating from multiple sources simultaneously to prepare more complex perovskite compositions. Replacing, therefore, the more complicated multi-source evaporation with single-source evaporation could be interesting. In this work, I am elaborating on the feasibility of evaporating pre-synthesized perovskite powders directly from a single source to simplify the process. I demonstrate the preparation of  $\alpha$ -phase perovskite thin films from pre-synthesized  $\alpha$ -CsFAPbI<sub>3</sub> and  $\delta$ -FAPbI<sub>3</sub> powders, indicating the feasibility of this approach.

*This chapter is based on the following article currently in preparation: Nadja Klipfel, Harris Muhammed, Albertus Adrian Sutanto, Naoyuki Shibayama, Hiroyuki Kanda, Abdullah M. Asiri, Cristina Momblona, Ahmad Shahzada, Mohammad Khaja Nazeeruddi "Structural and Optoelectronic Characterization of Phase Pure CsFAPbI<sub>3</sub> and FAPbI<sub>3</sub> Perovskite Thin Films."*

*In this work, I and H. Muhammed conceptualized the idea together. I designed the experiments and performed the fabrication and characterizations of perovskite thin films and solar cells, including the writing of the manuscript. H. Muhammed prepared the synthesized perovskite powders and measured the DSC. Dr. A. Sutanto measured the SEM top-view and cross-section images, Dr. H. Kanda helped measure the PL, TrPL data and helped with the analysis of the GIWAXS data, Prof. Dr. N. Shibayama measured the GIWAXS data, and Dr. C. Momblona also helped with the SEM images as well as with finalizing the manuscript.*

## 1.10 Introduction

The power conversion efficiency (PCE) of perovskite solar cells (PSCs) improved over the last decade, from 3.8% in 2009 to over 25% today.<sup>[44,231]</sup> This increase in efficiency is remarkable and makes perovskite solar cells a promising technology toward reducing carbon emissions.<sup>[232]</sup> Perovskites are considered inexpensive,<sup>[233]</sup> easy to process, and recyclable,<sup>[234]</sup> factors contributing to achieving sustainability goals.<sup>[235]</sup> Nevertheless, commercialization is still challenging due to the instability of the overall device and the perovskite's material intolerance to environmental stresses<sup>[236-239]</sup>, complicating large-scale production. To overcome these difficulties, various strategies such as compositional- and process engineering have been adopted. The degradation-prone methylammonium lead triiodide (MAPbI<sub>3</sub>) was replaced by formamidinium lead triiodide (FAPbI<sub>3</sub>) due to its reduced optical bandgap and higher thermal stability.<sup>[240]</sup> However, the critical phase transition ( $\alpha$ - to  $\delta$ -phase) of FAPbI<sub>3</sub> at room temperature hindered its application. Further extension of compositional engineering using the FA-site doping with smaller cations and anions such as methylammonium (MA<sup>+</sup>), cesium (Cs<sup>+</sup>), bromine (Br<sup>-</sup>), chloride (Cl<sup>-</sup>) helped to stabilize the perovskite phase.<sup>[241,242]</sup> Through process engineering, various thin film fabrication methods such as the two-step sequential spin-coating method, a one-step spin-coating method, vapor-assisted solution process, and the vacuum deposition method emerged. While solution-processed PSCs possess low-cost and higher efficiencies at the lab scale, the technique is not yet fully optimized for large-scale PSCs fabrication.<sup>[243-245]</sup> Moreover, toxic organic solvents are used in perovskite precursor solutions. Employing these at an industrial scale could severely impact human health and the environment.<sup>[161,162]</sup> In this context, vacuum deposition techniques provide a solvent-free alternative to solution processing. Advantages include large-scale compatibility, nanometer-scale precision, and prevention of intermixing of different layers.<sup>[163,164]</sup>

In conventional vacuum deposition methods (also known as multi-source vacuum deposition (MSVD)), precursor powders are sublimed simultaneously from different crucibles.<sup>[243]</sup> In literature, MSVD was first reported by Borchert *et al.* in 2017,

describing the large-area (16 cm<sup>2</sup>) fabrication of FAPbI<sub>3</sub> films with a stabilized efficiency of 14.2%<sup>[164]</sup> Inspired by solution-process techniques, MAI<sup>[246]</sup>, Cs<sup>+</sup>,<sup>[247]</sup> PbBr<sub>2</sub><sup>[248]</sup>, and excess FAI<sup>[249]</sup> were co-sublimed to stabilize the  $\alpha$ -FAPbI<sub>3</sub> layer, leading to two-, three- or four-source vacuum deposition processes. Controlling the stoichiometric ratio in MSVD-fabricated thin films is difficult for mixed anion or mixed cation perovskites. Each material must be calibrated independently first and later in the perovskite to obtain the correct stoichiometry. Evaporating, therefore, a pre-synthesized perovskite material from a single source could shorten the effort in the evaporation processes and could be interesting for commercial application. Moreover, high vapor pressure and low decomposition temperatures of organic ammonium halides challenge compositional tuning of the final thin film.<sup>[250]</sup> Single-source vapor deposition technique (SSVD), where the presynthesized perovskite powder is sublimed instead of individual precursors, has emerged as one possible solution to overcome such barriers. Fan *et al* was the first to report the SSVD for halide perovskite thin films and deposited a 400 nm thick MAPbI<sub>3</sub> layer leading to a 10% PCE.<sup>[245]</sup> Later Ajjouri *et al.* fabricated inorganic CsPbX<sub>3</sub> thin films employing SSVD. They observed that their thin films showed improved crystallinity relative to MSVD.<sup>[251]</sup> It was suggested that during SSVD, at least a portion of perovskite powder gets sublimed in the form of CsPbX<sub>3</sub> instead of undergoing a complete decomposition to CsX+PbX<sub>2</sub> as observed for the MSVD process. The simple and quick operational procedure made SSVD superior over MSVD. Recently, Crane *et al* employed the SSVD technique for the ball-milled (FA<sub>0.81</sub>MA<sub>0.14</sub>Cs<sub>0.05</sub>) Pb(Cl<sub>0.02</sub>Br<sub>0.14</sub>I<sub>0.84</sub>)<sub>3</sub> perovskite powder observing PbI<sub>2</sub> excess in the deposited film. Excess use of FAI and MABr in the ball-milled powder led to proper perovskite formation.<sup>[250]</sup>

Thus, the simplification of the vacuum deposition technique is paramount, especially when considering the up-scaling of this future technology. Herein, we have successfully employed the SSVD technique to fabricate CsFAPbI<sub>3</sub> and FAPbI<sub>3</sub> thin films from pre-synthesized perovskite powders for the first time. To avoid the stoichiometric differences between precursor powder and thin film, we used our synthesized  $\alpha$ -CsFAPbI<sub>3</sub> and  $\delta$ -FAPbI<sub>3</sub> powders instead of ball-milled powders. The structural and

optoelectronic studies confirmed the phase-pure thin films with commendable stability, and the perovskite layer compatibility with different underlayers was studied.

## 1.11 Results and Discussion

The  $\alpha$ -CsFAPbI<sub>3</sub> and  $\delta$ -FAPbI<sub>3</sub> powders (referred later in text with CsFAPbI<sub>3</sub> powder and FAPbI<sub>3</sub> powder) (Appendix B, Figure B.1) were synthesized as detailed in the experimental section. The  $\delta$ -FAPbI<sub>3</sub> powder was synthesized without post-heating treatment,<sup>[252]</sup> while the  $\delta$ -CsFAPbI<sub>3</sub> powder was converted to  $\alpha$ -CsFAPbI<sub>3</sub> by heating the  $\delta$ -CsFAPbI<sub>3</sub> at 150 °C for 1 hour in a tube furnace.<sup>[252]</sup> We characterized the perovskite powders using X-ray photon spectroscopy (XPS). The elemental composition and the nature of chemical bonding for both perovskite powders was evaluated first by XPS analysis. The XPS signals corresponding to Cs 3d<sub>5/2</sub> and Cs 3d<sub>3/2</sub> at 721.8 and 735.77 eV (Figure S3a), respectively, are visible for CsFAPbI<sub>3</sub> powder and a small shift in the I 3d<sub>3/2</sub>= 615.38 eV I 3d<sub>5/2</sub>= 626.88 eV (Figure B.2b) and Pb 4f<sub>7/2</sub>= 134.50 eV Pb 4f<sub>5/2</sub>= 139.40 eV (Figure B.2c). The XPS signals for FAPbI<sub>3</sub> powder (Figure B.3) are I 3d<sub>3/2</sub>= 615.75 eV I 3d<sub>5/2</sub>= 627.25 eV, for I 3d and Pb 4f<sub>7/2</sub>= 134.99 eV Pb 4f<sub>5/2</sub>= 139.92 eV for Pb 4f (Figure B.3b and Figure B.3c, respectively).<sup>[252]</sup> Compared to the core level signals of FAPbI<sub>3</sub> a small shift can be observed, which emerges from the inclusion of the Cs.<sup>[252,253]</sup> As depicted in the diffractograms (Figure B.4), the powders exhibited exceptional phase purity with no traces of residual components. The values for thermogravimetric (TGA) and DSC of the FAPbI<sub>3</sub> powder were reported by Yong *et al.* describing that the synthesized  $\delta$ -phase FAPbI<sub>3</sub> loses FAI at 304-363°C, according to the TGA result. In a mixture of the precursors (FAI and PbI<sub>2</sub>), FAI starts to evaporate at a lower temperature (234°C) due to decomposition of unreacted FAI to FA and outgassing of HI.<sup>[254,255]</sup> DSC reveals two endothermic peaks along with multiple endothermic peaks for the synthesized FAPbI<sub>3</sub> powder, while for precursor mixture, indicating a nonstoichiometric reaction forming  $\delta$  and  $\alpha$  phases.<sup>[254,256]</sup> These findings and the low phase-transition temperature of both presynthesized perovskite powder suggested that solvent-free single-source evaporation could be possible. This opened the pathway of replacing the complicated multi-source

evaporation with single-source evaporation of presynthesized perovskite powders. It is worth noting that we have not used any precursor materials (like FAI or CsX) in excess as usually reported in the literature for mix-perovskites.<sup>20</sup>

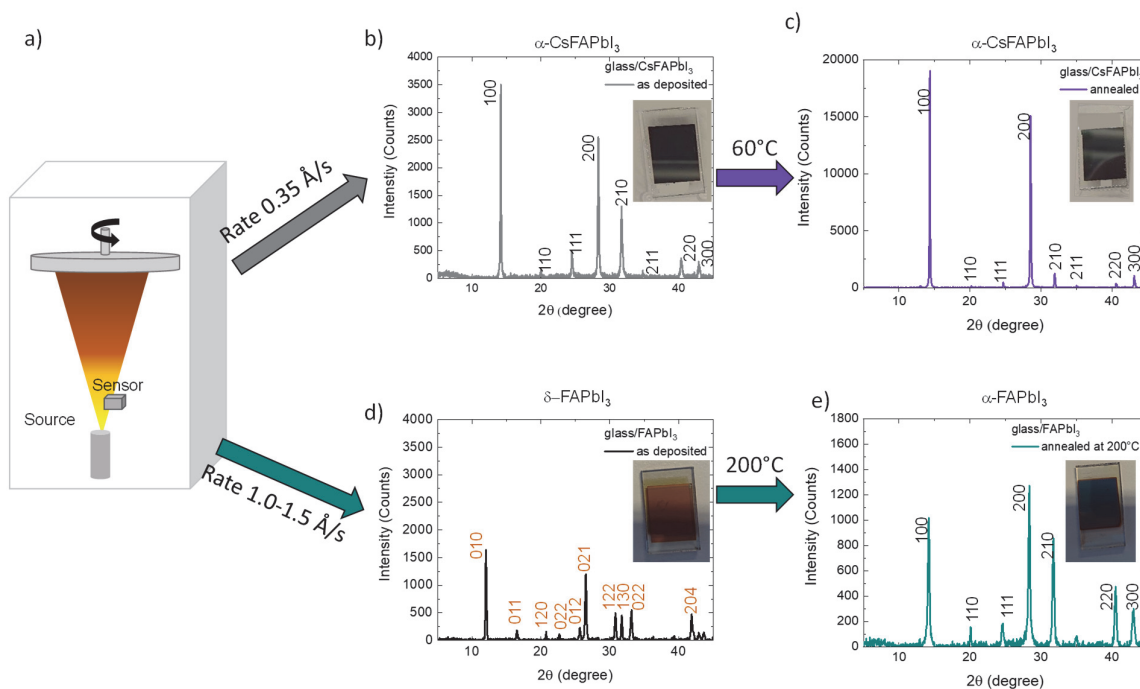


Figure 5.1 a) Schematic for single-source evaporation of presynthesized  $\alpha$ -CsFAPbI<sub>3</sub> and  $\delta$ -FAPbI<sub>3</sub> perovskite powder, b,c) diffractograms of CsFAPbI<sub>3</sub> thin films on glass b) as-deposited and c) annealed at 60°C for 3 min, d,e) diffractograms of FAPbI<sub>3</sub> thin films on glass d) as-deposited and e) annealed at 200°C for 10s.

Figure 5.1a shows the schematic description of the single-source evaporation process used to sublime the two perovskite powders. As reported earlier, the phase-transition temperature for CsFAPbI<sub>3</sub> powder (130 °C) is lower than for FAPbI<sub>3</sub> powder (150 °C).<sup>22</sup> This finding limited the temperature and, therefore, the sublimation power and the evaporation rate applied during the deposition process. To analyze the effect of the sublimation temperature on the composition and degradation, thermal evaporation at subsequent evaporation rates was performed to optimize the thin film deposition process for CsFAPbI<sub>3</sub> and FAPbI<sub>3</sub> powders (Table B.1). It must be noted that the rate applied directly relates to the applied temperature used during the deposition process. The higher the rate, the higher the sublimation power applied. To simplify, we will describe

the deposition process by rate. The CsFAPbI<sub>3</sub> powder was sublimed at three different deposition rates, i.e., 0.25 Å/s, 0.35 Å/s, and 1.0-1.05 Å/s, and the phase purity of deposited thin films were probed using PXRD measurements. As shown (Figure B.5, Appendix B), the diffractogram of the as-deposited CsFAPbI<sub>3</sub> at 0.35 Å/s reveals the characteristic  $\alpha$ -phase diffractions i.e., (100), (110), (111), (200), (210), (211), (220) and (300).<sup>[252]</sup> A faster deposition at 1.0-1.05 Å/s leads to  $\delta$ -phase perovskite. The XRD reflexes confirm the presence of the  $\delta$ -CsFAPbI<sub>3</sub> perovskite phase with two major reflexes at (022) and (211). Further, the slower deposition at 0.25 Å/s did lead to a mixed-phase perovskite. The XRD diffractogram identified the presence of (100), (111), and (211) reflections indicating the  $\alpha$ -phase along with the (022) and (211) reflections indicating the  $\delta$ -phase. Hence, we have identified a moderate deposition rate of 0.35 Å/s as the optimum for the deposition  $\alpha$ -CsFAPbI<sub>3</sub> thin films. Similarly, the FAPbI<sub>3</sub> powder was sublimed at two different rates, i.e., 1.0-1.05 Å/s and 3.0-3.05 Å/s. At 1.0-1.05 Å/s deposition, diffractograms indexed with (010), (011), (120), (022), (012), (021), (122), (130), (022) and (204) reflections indicating the  $\delta$ -phase. Whereas deposition at 3.0-3.05 Å/s lead to a mixed-phase perovskite layer which includes the  $\alpha$ - and  $\delta$ -phases along with excess PbI<sub>2</sub> (Figure B.6). We attribute the intense PbI<sub>2</sub> presence to the FAI decomposition at a faster deposition rate, which agrees with previous reports.<sup>[249]</sup> Annealing the thin film deposited at 3.0-3.05 Å/s did not convert the mixed-phase perovskite to pure  $\alpha$ -FAPbI<sub>3</sub> (Figure B.6b, Appendix B). Therefore, we found the optimum rate for the deposition of FAPbI<sub>3</sub> powder at 1.0-1.05 Å/s. Ultraviolet photon spectroscopy was performed to verify the crystal phase formed. The UV-Vis absorbance spectra (Figure B.7) confirm the formation of pure  $\alpha$ -phase of FAPbI<sub>3</sub> perovskite after annealing the film deposited at 1.0-1.05 Å/s. The XRD pattern (Figure B.6b, Appendix B) supports these findings by displaying the typical reflexes for the pure  $\alpha$ -phase FAPbI<sub>3</sub> ((100), (110), (111), (200), (210), (220), (300)).<sup>[252]</sup> To secure full conversion of the already as-deposited CsFAPbI<sub>3</sub> perovskite film, we annealed the film at 60°C for 5s. The absorbance spectra is shown (Figure B.8, Appendix B). The XRD spectra of the annealed film at 60 °C reveal more high intense reflections indicating an improved crystallinity of the  $\alpha$ -CsFAPbI<sub>3</sub> perovskite (Figure 5.1c). In addition, the full width at half



maximum for the 100 reflex in as-deposited  $\alpha$ -CsFAPbI<sub>3</sub> film was calculated to be 0.14°, and for annealed  $\alpha$ -CsFAPbI<sub>3</sub> was calculated to be 0.11° (Supporting Figure B.9). This decrease in FWHM for the annealed  $\alpha$ -CsFAPbI<sub>3</sub>, in addition to the increase of intensity for 100 reflex indicates the higher crystallinity of the thin films prepared. The comparison of the XRD pattern of confirmed this by the indication of a small shift of the 100 reflex towards higher angles (Appendix B.9b). We further investigated the effect of the annealing process on the preferred crystal orientation of the perovskite films and performed 2D grazing incidence wide-angle X-ray scattering (2D GIWAXS) with an angle of 0.12° (Figure 5.2). The analysis of the integrated q-data of these images revealed slight differences between the CsFAPbI<sub>3</sub> film as-deposited and the annealed one. A small amount of  $\delta$ -CsFAPbI<sub>3</sub> is present in the as-deposited film (Figure 5.2c, d,  $q = 0.9 \text{ \AA}^{-1}$ ), which was not detected in PXRD. After annealing the film at 60 °C, this peak disappeared, and the pure  $\alpha$ -CsFAPbI<sub>3</sub> film was formed (Figure 5.2d). The azimuthal integration of the GIWAXS films at 100 reflexes ( $q = 1.0 \text{ \AA}^{-1}$ ) revealed for the as-deposited films a preferred crystal orientation with both in-plane and out-of-plane at  $\chi_{100} = 16^\circ$  and  $\chi_{100} = 79^\circ$  (Figure B.10a,b, Appendix B). However, the annealing of the films at 60 °C leads to a restructuring of the film resulting in a less-preferred in- and out-of-plane orientation (Figure B.10b, more flat part). We also made GIWAXS analysis for the annealed  $\alpha$ -FAPbI<sub>3</sub> films (Figure B.11, Appendix B). The q-integration of the image revealed traces of  $\delta$ -FAPbI<sub>3</sub> in the film after annealing at 200 °C ( $q = 0.8\text{-}0.9 \text{ \AA}^{-1}$ ). The azimuthal integration of the GIWAXS 100 reflex ( $q = 1.0 \text{ \AA}^{-1}$ ) shows a preferred crystal orientation with both in- and out-of-plane at  $\chi_{100} = 16^\circ$  and  $\chi_{100} = 79^\circ$ , similar to the one already described for the as-deposited  $\alpha$ -CsFAPbI<sub>3</sub> film (Figure B.11 a and B.11 c, Appendix B). The GIWAXS also confirmed the exceptional phase purity for the CsFAPbI<sub>3</sub> thin film.

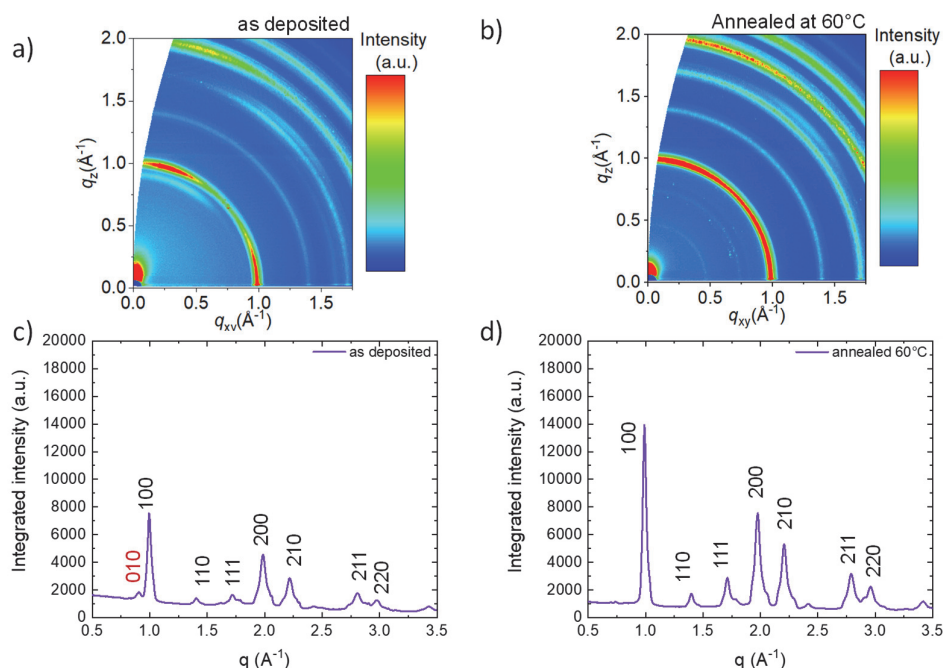


Figure 0.2 GIWAXS images taken at an angle of  $0.12^\circ$  of a) CsFAPbI<sub>3</sub> film as deposited b) CsFAPbI<sub>3</sub> film annealed at  $60^\circ\text{C}$ . Integrated  $q$ -data of the GIWAXS images for c) as-deposited CsFAPbI<sub>3</sub> film and d) CsFAPbI<sub>3</sub> film after post-annealing at  $60^\circ\text{C}$ .

### Photophysics:

The photophysical properties were compared for the annealed films evaporated at  $0.35 \text{ \AA/s}$  for the CsFAPbI<sub>3</sub> and  $1.0\text{-}1.05 \text{ \AA/s}$  for FAPbI<sub>3</sub> (Figure B.12, Appendix B). The comparison of the steady-state photoluminescence (PL) spectra of the CsFAPbI<sub>3</sub> and FAPbI<sub>3</sub> film after annealing revealed a slight change in the PL maximum CsFAPbI<sub>3</sub> ( $PL_{60^\circ\text{C}} \sim 800\text{nm}$ ), and for FAPbI<sub>3</sub> ( $PL_{200^\circ\text{C}} \sim 810\text{nm}$ ) (Figure B.12a). The blue shift in the fluorescence spectra indicates the inclusion of the smaller Cs cations into the FAPbI<sub>3</sub>.<sup>[252]</sup> To evaluate further the photophysical properties of the vacuum-deposited perovskite thin films, time-resolved photoluminescence (TRPL) measurements were performed (Figure B.12b, c, Appendix B). Therefore, the samples were measured with an excitation wavelength of  $640 \text{ nm}$ . The corresponding decays were fitted to a double exponential equation, where the fast component ( $\tau_1$ ) is related to trap-assisted recombination at defect sites and the slow component ( $\tau_2$ ) to radiative recombination inside the grains (see the fitted values in Table B.2, Appendix B).<sup>[257,258]</sup> As observed, the as-

deposited perovskite CsFAPbI<sub>3</sub> film exhibits  $\tau_1$  and  $\tau_2$  values of 3.12 ns and 24.07 ns, and the as-deposited FAPbI<sub>3</sub> film exhibits  $\tau_1$  and  $\tau_2$  values of 20.26 ns and 76.95 ns, respectively. These values decrease significantly after annealing of the films, resulting in  $\tau_1$  and  $\tau_2$  values for CsFAPbI<sub>3</sub> of 18.98 ns and 61.61 ns and  $\tau_1$  and  $\tau_2$  values for FAPbI<sub>3</sub> of 1.09 ns and 27.03 ns, respectively. This data indicates that the as-deposited films exhibit a slightly slower process than the annealed ones, indicating slower charge recombination processes.<sup>[259]</sup> When comparing the values extracted from the experimental data to the ones observed in the literature, the characteristic times for  $\tau_1$  and  $\tau_2$  for both perovskite layers are very low compared to the literature reports. Typical values for  $\alpha$ -CsFAPbI<sub>3</sub> are  $\tau_1=23.75$  ns and  $\tau_2=18.33$  ns<sup>[260]</sup>, and for  $\alpha$ -FAPbI<sub>3</sub> are  $\tau_1=68.8$  ns and  $\tau_2=234.6$  ns.<sup>[261]</sup> Our deposited SSVD thin films have short lifetimes than that of the solution-processed perovskites and could be due to the presence of more trap-assisted recombination.<sup>[262]</sup> However, the vapor deposition techniques typically display short lifetimes<sup>[164,263]</sup> and which indicates that further optimization of the lifetimes is required in the future.

The stability of fabricated perovskite layers is important for their implementation. The dry-air storage stability of the annealed  $\alpha$ -CsFAPbI<sub>3</sub> (Figure 5.3a) and  $\alpha$ -FAPbI<sub>3</sub> (Figure 5.3b) films on glass substrates were monitored by PXRD measurements over a two week time period. Contrary to the solution process method, the  $\alpha$ -FAPbI<sub>3</sub> film showed superior storage stability than the  $\alpha$ -CsFAPbI<sub>3</sub> film. Upon dry-air storage for seven days, the CsFAPbI<sub>3</sub> layer showed a significant decrement in the (100) reflection intensity and the emergence of new reflections, which belong to the  $\delta$ -phase (black markings Figure 5.3a). Remarkably the annealed FAPbI<sub>3</sub> thin films did not show any sign of degradation within these two weeks, indicating superior film stability (Figure 5.3b). An in-depth analysis is necessary for the future to track the underlying mechanisms.

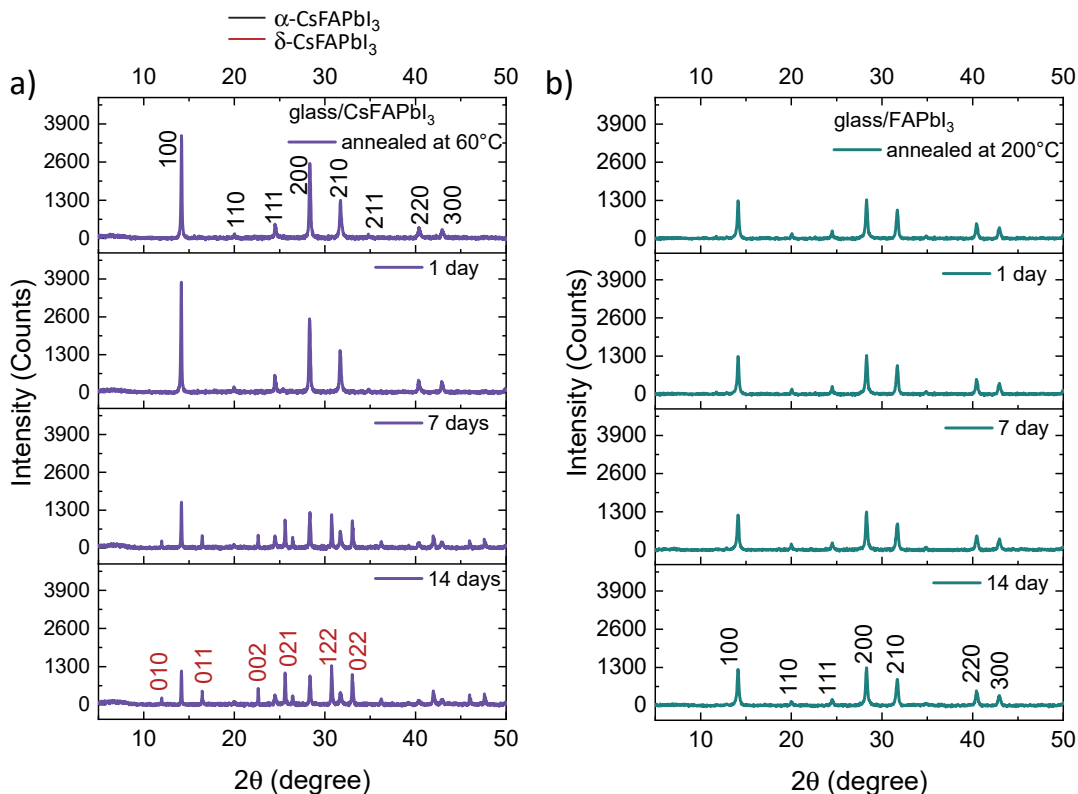


Figure 0.3 Storage stability of the perovskite layers. a,b) diffractograms over two weeks for a) CsFAPbI<sub>3</sub> and b) FAPbI<sub>3</sub> layers stored under dry air. Planes labeled in black correspond to  $\alpha$ -phase and in brown to  $\delta$ -phase.

The ultimate aim of the SSVD technique is to fabricate the PSCs on an industrial scale; therefore, the sublimation of compact layers with good interfaces is crucial. It has been widely reported that the chemical groups influence the perovskite formation and stability,<sup>[264]</sup> we, therefore, investigated the formation of the perovskite layer on different organic and inorganic materials. We extended our study to the state-of-the-art used underlayers. MoO<sub>3</sub>/TaTm (TaTm= N<sub>4</sub>,N<sub>4</sub>,N<sub>4</sub>'',N<sub>4</sub>''-tetra([1,1'-biphenyl]-4-yl)-[1,1':4,1''-terphenyl]-4,4''-diamine), MoO<sub>3</sub>/spiro-OMeTAD (N<sup>2</sup>,N<sup>2</sup>,N<sup>2'</sup>,N<sup>2'</sup>,N<sup>7</sup>,N<sup>7</sup>,N<sup>7'</sup>,N<sup>7'</sup>-octakis(4-methoxyphenyl)-9,9'-spirobi[9H-fluorene]-2,2',7,7'-tetramine), cTiO<sub>2</sub>/SnO<sub>2</sub> and MeO-2PACz ([2-(3,6-dimethoxy-9H-carbazole-9-yl)-ethyl]phosphonic) acid. The underlayer chosen were of interest due to their different chemical nature and functional groups. TaTm has only benzene-groups, spiro-OMeTAD methoxy-groups, MeO-2PACz phosphonic acid groups, and SnO<sub>2</sub>, inorganic oxide groups. In literature, TaTm<sup>[78]</sup>, spiro-

OMeTAD<sup>[264]</sup>, and MeO-2PACz<sup>[249]</sup> have already been incorporated as underlayers in vacuum-deposited underlayers before, and the positive effect of their functional groups was mentioned. Marcel Ross et al.<sup>[249]</sup>, reported the positive effect of phosphonic groups in MeO-2PACz on the perovskite formation of FAPbI<sub>3</sub> during the MSVD process, and our group described a positive effect of MeO-groups on the perovskite crystallization, leading to micrometer-sized crystal features.<sup>[264]</sup>

Microstructure analysis was made by performing scanning electron microscopy (SEM). Top-view SEM images of the post-annealed  $\alpha$ -CsFAPbI<sub>3</sub> and  $\alpha$ -FAPbI<sub>3</sub> thin films deposited by SSVD (Figure B.13, Appendix B) were made to analyze the morphology of the perovskite layers. The top view images reveal the formation of perovskite crystals with a homogeneous coverage without pinholes for both types of perovskite. The top-view images for  $\alpha$ -CsFAPbI<sub>3</sub> reveal that on top of the underlayer MoO<sub>3</sub>/spiro-OMeTAD and MoO<sub>3</sub>/TaTm, agglomerates of grain like feature were formed. Grain size distribution (Figure B.14, Figure B.15, Appendix B) reveals that the perovskite formed on MoO<sub>3</sub>/TaTm has larger grain sizes with an average grain size of ~358 nm than the grains on MoO<sub>3</sub>/spiro-OMeTAD (~333 nm). On SnO<sub>2</sub> and MeO-2PACz, the perovskite grains were in their average size larger (~455nm and ~404nm) and could be distinguished by their grain-like features. The top-view SEM images (Appendix B. Figure B.13) for  $\alpha$ -FAPbI<sub>3</sub> show agglomerates of gain-like features for the perovskite on MoO<sub>3</sub>/TaTm (~324 nm) and MoO<sub>3</sub>/spiro-OMeTAD, pyramid-like grain features (~484 nm). For the underlayer SnO<sub>2</sub> and MeO-2PACz, the same can be observed for  $\alpha$ -FAPbI<sub>3</sub> as for  $\alpha$ -CsFAPbI<sub>3</sub>, the grains formed with clear grain boundaries, indicating the grain sizes better. Larger grains can be observed for the perovskite on SnO<sub>2</sub> (~530 nm) than for the perovskite on MeO-2PACz (~398 nm). By comparing the crystal size of  $\alpha$ -CsFAPbI<sub>3</sub> with  $\alpha$ -FAPbI<sub>3</sub> (excluding perovskite on top of MoO<sub>3</sub>/TaTm due to not apparent grain-like features), one can observe that the total crystal sizes are smaller for the  $\alpha$ -CsFAPbI<sub>3</sub> than for  $\alpha$ -FAPbI<sub>3</sub>. This confirms our findings from above, where we observe an XRD shift towards higher angels upon incorporating Cs into the crystal structures and higher crystallinity by increased intensity. In literature, Cs is known to reduce the

grain sizes by increasing the density of crystal nuclei during the film formation, leading to reduced grain sizes and the absence of agglomerations.<sup>[265]</sup> The SEM cross-section images (Figure B.16, Appendix B) for CsFAPbI<sub>3</sub> show that the perovskite layer is not well crystallized on the underlayers MoO<sub>3</sub>/spiro-OMeTAD and MoO<sub>3</sub>/TaTm. On MeO-2PACz and SnO<sub>2</sub>, the perovskite crystallization is better, revealing big crystals (~450 nm for MeO-PACz and ~400 nm for SnO<sub>2</sub>). However, pinholes are dominating at the interface. The same observations can be made for the cross-section images for FAPbI<sub>3</sub>. The perovskite generally shows a better crystalline layer than the one in CsFAPbI<sub>3</sub>, but the perovskite layers are not fully attached to the substrate, revealing either complete separation (MoO<sub>3</sub>/spiro-OMeTAD and MoO<sub>3</sub>/TaTm) or pinholes (MeO-2PACz and SnO<sub>2</sub>). Unfortunately, no typical perovskite crystallization was possible on MoO<sub>3</sub>/TaTm and MoO<sub>3</sub>/spiro-OMeTAD, suggesting a negative effect of methoxy and benzene-groups on the perovskite crystallization when deposited by SSVD methods, as described above.

Interestingly, the cross-section images for both perovskites reveal different layer thicknesses when considering the underlayers SnO<sub>2</sub> and MeO-2PACz, where the perovskite crystallized with large grain features. We note at this point that the samples with the same type of perovskite were fabricated during the same evaporation process. Differences in thickness cannot be explained due to inconsistencies between the evaporation processes. Nevertheless, the cross-sectional images show large deformity in the perovskite at the interface and reveal a difference in perovskite thickness when comparing the samples deposited on the metal oxide SnO<sub>2</sub> (~400 nm thickness) and the organic underlayer MeO-2PACz (~450 nm thickness). The difference in thickness can be explained by the interaction of the perovskite powder with the underlayer. Metal oxides are known to have a catalytic surface. Olthof *et al.* reported that a passivation layer of 30 nm of degradation products is deposited first until the perovskite formation starts. For organic underlayers, the perovskite formation starts earlier already after 3nm of deposition.<sup>[79]</sup> In earlier studies, we have found the influence of the underlayer on the co-evaporated methylammonium lead iodide perovskite formation. Oxides were found to be especially hindering due to their catalytic nature, promoting only after 100nm

precursor deposition perovskite growth.<sup>[264]</sup> In the case of the underlayer SnO<sub>2</sub>, large holes can be observed independently of the perovskite deposited. The same large holes are observed for the  $\alpha$ -CsFAPbI<sub>3</sub> and  $\alpha$ -FAPbI<sub>3</sub> films on the underlayer MeO-2PACs. In both cases, the compact perovskite layers show big crystal sizes; however, further optimization of the SSVD process is necessary to prevent the formation of pinholes at the interface. Nevertheless, our data suggests the underlayer MeO-2PACz and SnO<sub>2</sub> are good candidates to continue optimization for implementing into *p-i-n* or *n-i-p* device structures.

### 1.12 Conclusion

In summary, we demonstrated successful employment of the SSVD technique to fabricate CsFAPbI<sub>3</sub> and FAPbI<sub>3</sub> thin films without the excess usage of FAI or CsI. PXRD, UV-Vis absorption, PL and GIWAXS analyses were employed to confirm the high phase purity for the deposited films. We have additionally analyzed the feasibility of device fabrication from these layers and establish that impairment of the perovskite can be seen on all of the state-of-the-art underlayers except on SnO<sub>2</sub> and MeO-2PACz. These findings suggest that an optimization of the composition of the perovskite powder is crucial when following up on the single-source evaporation as an upgraded technique towards large-scale application in the future.





## C<sub>60</sub> Thin Films in Perovskite Solar Cells: Efficient or Limiting Charge Transport Layer?

Interfacial engineering is necessary but challenging in vacuum-deposited perovskite devices. Not many charge-transport layers have efficient conductivity and well-aligned energy levels to match the perovskite. Therefore, understanding the charge-transport processes of state-of-the-art electron-transport material could help find new underlayers for better efficient perovskite devices. In this chapter, I investigate the function and the importance of the electron-transport layers cTiO<sub>2</sub> and C<sub>60</sub> at the interface of vacuum-deposited perovskite. Both layers in combination are beneficial for the device efficiencies, as they show a synergetic effect. When considering the optimum C<sub>60</sub> thickness, it could be demonstrated that the energy levels of C<sub>60</sub> change with thickness, leading to better charge extraction at 15 nm than for thicker or thinner layer, indicating C<sub>60</sub> as a limiting factor in the efficient device fabrication.

*This chapter is based on the based on the following published article.: Nadja Klipfel, Agustin O. Alvarez, Hiroyuki Kanda, Albertus Adrian Sutanto, Cansu Igci, Cristina Roldan-Carmona, Cristina Momblona, Francisco Fabregat-Santiago, Mohammad Khaja Nazeeruddin “C<sub>60</sub> thin films in perovskite solar cells: efficient or limiting charge transport layer” in ACS Appl. Energy Mater. 2022, XXXX, XXX, XXX-XXX. DOI:10.1021/acsaem.1c03060.*

*In this work, I conceptualized the idea, designed the experiments, and performed the fabrication as well as characterization of perovskite thin films and solar cells, A. Alvarez, helped with the analysis of the impedance data, Dr. H. Kanda carried out the PL analysis, Dr. A. Sutanto analyzed the SEM images, and Dr. C. Momblona, Dr. C. Roldan-Carmona, help with finalizing the manuscript.*

### 1.13 Introduction

Hybrid organic-inorganic perovskites are an exciting class of materials with the potential to replace silicon photovoltaics (PV) in the future. Despite their unique semi-conducting properties, which caught the attention of scientists in the 1970s and 1990s [266,267], it was not until 2009 that they were first employed, showing a power conversion efficiency (PCE) of  $\sim 4\%$ . [268] Remarkably, the PCE of spin-coated perovskite solar cells (PSCs) rapidly improved in the last decade from 3.8% to a certified value of 25.5%. [10] Moreover, their efficiency is now rivaling silicon-based cells for small and large area scales. In 2013, Jeng *et al.* reported for the first time the concept of integrating a perovskite/fullerene structure into a spin-coated perovskite solar cell, and in 2014 Sun *et al.* demonstrated that also PC<sub>61</sub>BM can be used as a suitable layer in low-temperature processable bilayer solar cells. [86,269] Since 2013, Liu *et al.* demonstrated the first vacuum-deposited PSCs, with an efficiency of 15.4%. [208] The field of vacuum deposition steadily grew. It is now shown by several groups [75–78,83,270,271] that vacuum deposition can be used as an alternative fabrication method, reaching a maximum efficiency of 20.13% for co-evaporated CsMAPbI<sub>3</sub> devices. [208] Nevertheless, despite these fast improvements in PCE, understanding PSCs' working principles is still a challenge. Nowadays, vacuum deposition is broadly used within the community. It allows a solvent-free, fully controlled deposition of sequential layers, enabling combinations of device architectures not accessible by solution processing methods. [13–18] Understanding the role of each layer in PSCs and, in particular, of electron transport layers (ETLs) beyond metal oxide-based ETLs, is important to obtain efficient and long-term stable perovskite solar cells. [278] Fullerenes are commonly integrated into spin-coated perovskite devices, especially in inverted configurations (*p-i-n* configuration), as they are known to extract the electrons efficiently from the perovskite as well as eliminate hysteresis and passivate trap states. [279] On top of that, the easy fabrication of fullerene-based layers by vacuum deposition or spin-coating at low temperatures makes fullerene an excellent electron transport layer for PSCs. [280],[281] In literature, the use of an ultrathin layer of 1 nm C<sub>60</sub> as an electron-selective material in a *p-i-n* device demonstrated that even ultrathin films

of fullerenes could be used to aid electron extraction and collection.<sup>[282]</sup> The thickness dependence of fullerene on MAPbI<sub>3</sub> perovskite was investigated by Wang *et al.* in 2015, where they found an interface dipole between the perovskite and the C<sub>60</sub> layer.<sup>[283]</sup> It was also shown that a compact C<sub>60</sub> layer can replace the cTiO<sub>2</sub> in n-i-p devices, leading to negligible hysteresis and enhanced stability.<sup>[239]</sup> In addition, Arivazhagan *et al.* investigated the C<sub>60</sub> growth on FTO, finding that at low C<sub>60</sub>-thickness, the physical defects at the FTO/C<sub>60</sub> interface lead to surface roughness and Ohmic behavior similar to bare FTO. Once further increasing the C<sub>60</sub> thickness, the FTO/C<sub>60</sub> interface defects are reduced and enhanced the electron extraction.<sup>[281]</sup> In another approach, a C<sub>60</sub>/ultrathin-TiO<sub>x</sub> compact ETL layer was applied in n-i-p perovskite solar cells, enhancing perovskite crystallization due to better surface energy.<sup>[284]</sup> Nevertheless, little research was so far conducted to understand the influence of fullerenes when deposited as ETLs under the perovskite in solar cells with n-i-p configuration, mainly if the perovskite was fabricated through co-evaporation. Only one report in literature can be found that described the integration of a thin-film of intrinsic fullerene C<sub>60</sub> layer between the perovskite and the compact-TiO<sub>2</sub> (cTiO<sub>2</sub>) layer improves the efficiency from 4% to 14% for evaporated solar cells.<sup>[285]</sup> The influence of C<sub>60</sub> at the interface of co-evaporated perovskite and the underlying processes associated with the efficiency boost could not yet be fully understood. To further advance the efficiency of the devices, identification and understanding of these limiting processes are necessary.

Here, we investigate the influence of the fullerene C<sub>60</sub> thickness as an electron-transporting layer (ETL) on the perovskite charge transport processes in co-evaporated PSCs.

## 1.14 Results and Discussion

Methylammonium lead iodide (MAPbI<sub>3</sub>) perovskite devices were fabricated by thermally co-depositing MAPbI<sub>3</sub> on top of FTO/C<sub>60</sub> or FTO/cTiO<sub>2</sub>/C<sub>60</sub> containing four different C<sub>60</sub> thicknesses (Figure 6.1a). In summary, C<sub>60</sub> was introduced with *i*) 5 nm, *ii*) 10 nm, *iii*) 15 nm, *iv*) 20 nm, and *v*) 30 nm. As a reference, MAPbI<sub>3</sub> perovskite devices,

which do not contain the  $C_{60}$  layer (FTO/ $cTiO_2$ /MAPbI<sub>3</sub>/spiro-OMeTAD/Au), were also fabricated. We would like to note that all samples described in this manuscript were prepared with the same fabrication procedure obtaining samples with the same MAPbI<sub>3</sub> thickness, which allows a direct comparison. The current density-voltage ( $J$ - $V$ ) characteristics of the best-performing devices are shown in Figures 6.1b and 1c, and their characteristic parameters are listed in Table 1. Statistical data for each  $C_{60}$  thickness is provided in Figure C.1 and Table C.1 in Appendix C. For FTO/ $C_{60}$ -based devices, we find that the highest device efficiency could be achieved for the devices integrating a 15 nm  $C_{60}$  layer, reaching PCE of 15.3%, with an open-circuit voltage ( $V_{OC}$ ) of 1.002 V, fill factor (FF) of 0.74 and a short-circuit current density ( $J_{SC}$ ) of  $-20.61 \text{ mA cm}^{-2}$ . With increasing  $C_{60}$  thickness, the  $J_{SC}$ , FF, and  $V_{OC}$  values increase until the optimum thickness of 15 nm  $C_{60}$  is reached, mainly attributed to a decrease of defects at the FTO/ $C_{60}$  interface that will enhance the charge extraction and reduce the recombination in the interface at increasing  $C_{60}$  thickness.<sup>[28]</sup> For the devices containing thicker  $C_{60}$  layers (20 and 30 nm), all the PV parameters are detrimentally affected, suggesting charge transport/extraction issues through the device. For FTO/ $cTiO_2$ / $C_{60}$ -based devices, the device performance is even more enhanced until achieving the highest efficiency of 16.1% at 15 nm  $C_{60}$  thickness. Compared with the FTO/ $C_{60}$  counterpart device, this enhancement is due to a slight increase in  $J_{SC}$  from  $-20.61$  to  $-21.70 \text{ mA cm}^{-2}$ . Using a thicker  $C_{60}$  layer ( $>20$  nm) again induces charge transport/extraction issues in the device.

The trend in the device performance is supported by the statistical data presented in Figure C.1 and Table C.1, Appendix C. The PCE distribution for the devices fabricated with FTO/ $cTiO_2$ / $C_{60}$  is narrower than those containing FTO/ $C_{60}$ . The use of  $cTiO_2$  might avoid direct contact between the  $C_{60}$  and the FTO, preventing the devices from shorting. In addition, the synergetic effect between  $cTiO_2$  and  $C_{60}$  produces more efficient devices than their equivalent FTO/ $C_{60}$ -based ones. Moreover, using  $C_{60}$  with an optimized thickness seems to be essential for a better charge extraction, resulting in higher PV characteristics.

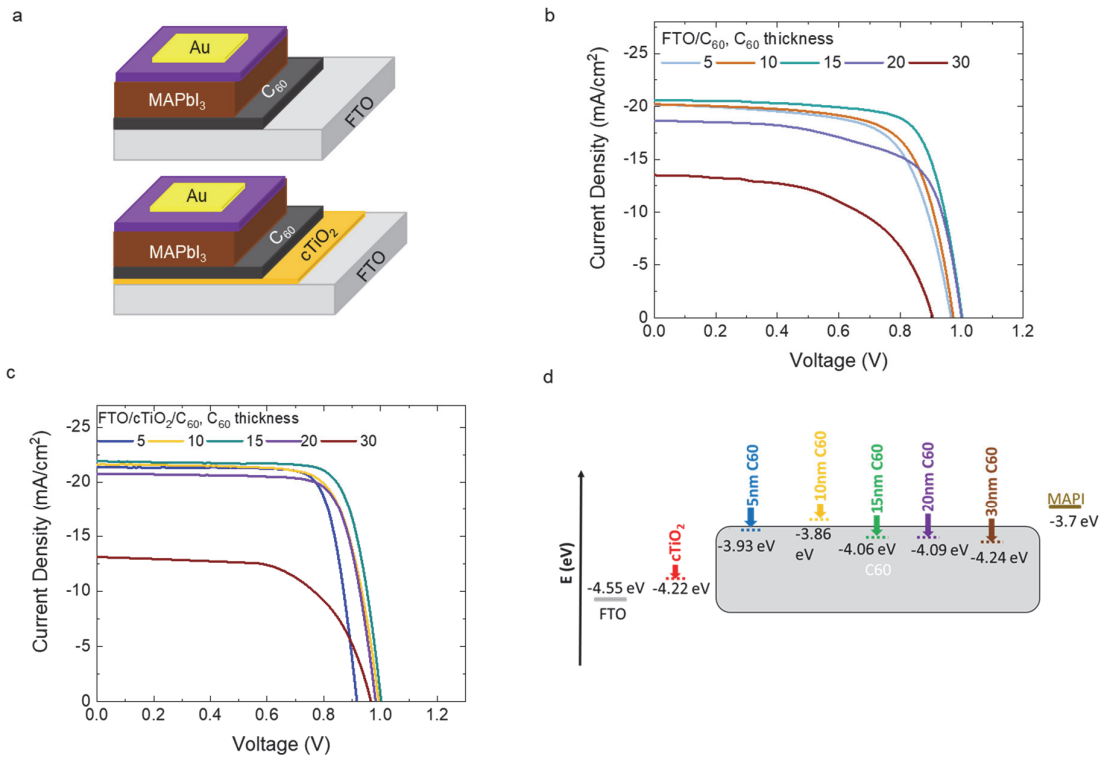


Figure 0.1. a) Schematic representation of the device architectures used in this study. b) *JV* characteristics of the most efficient device per condition using b) FTO/C<sub>60</sub> with C<sub>60</sub> thickness being: 5 nm, 10 nm, 15 nm, 20 nm, and 30 nm and c) FTO/cTiO<sub>2</sub>/C<sub>60</sub> as ETMs with C<sub>60</sub> thickness being: 0 nm, 5 nm, 10 nm, 15 nm, 20 nm, and 30 nm, respectively. d) Energy level diagram for different C<sub>60</sub> thicknesses deposited on FTO/cTiO<sub>2</sub>.

Table 0.1. PV parameters extracted from the corresponding  $JV$  curves of the most efficient devices.

	$C_{60}$ thickness (nm)	$J_{SC}$ ( $\text{mA cm}^{-2}$ )	$V_{OC}$ (V)	FF	PCE (%)
FTO/ $C_{60}$	5	-20.18	0.965	0.67	13.0
	10	-20.19	0.972	0.70	13.7
	15	-20.61	1.002	0.74	15.3
	20	-19.67	0.988	0.64	12.4
	30	-14.02	0.974	0.48	7.0
	0	-12.62	0.867	0.21	2.3
FTO/ $cTiO_2$ / $C_{60}$	5	-21.37	0.926	0.79	15.6
	10	-21.91	0.993	0.72	15.9
	15	-21.70	1.000	0.74	16.1
	20	-20.77	0.992	0.77	15.9
	30	-12.15	0.961	0.68	7.9

In both device layouts, a  $C_{60}$  layer is placed at the front contact, and the light absorption produced at the fullerene layer can result in absorption losses in the devices. The absorption spectra of the different thicknesses of  $C_{60}$  layers deposited in glass were measured and depicted in Figure C.2, Appendix C. The absorption of the  $C_{60}$  layer increases linearly with the deposited thickness; however, it does not strongly affect the device performance as the  $J_{SC}$  values remains similar at  $C_{60}$  thickness from 5nm to 20nm (FTO/ $C_{60}$ :  $J_{SC}$ : -20.18 – -19.67  $\text{mA cm}^{-2}$  from 5 to 20 nm  $C_{60}$  and FTO/ $cTiO_2$ / $C_{60}$ :  $J_{SC}$ : -21.37 – -20.77  $\text{mA cm}^{-2}$  from 5 to 20 nm  $C_{60}$ ). Therefore, depth analysis of underlying processes in the devices will be evaluated by impedance spectroscopy (IS).

The external quantum efficiency (EQE) was measured for both device architectures and is depicted in Figure C.3, Appendix C. The EQE is higher and flatter for the samples employing  $cTiO_2$  as an additional layer. In both cases, the absorption of the  $C_{60}$  layers decreases the photon-to-current efficiency between 400-450 nm for the samples

FTO/cTiO<sub>2</sub>/C<sub>60</sub> and FTO/C<sub>60</sub>, denoting the absorbance losses/extraction issues at the front contact under low-intensity illumination, which becomes very relevant at C<sub>60</sub> thickness of 30 nm.

To look into the reasons for the differences in the device efficiency more closely, ultraviolet photoelectron spectroscopy (UPS) measurements were performed for all different C<sub>60</sub> thicknesses employed in the two structures, FTO/cTiO<sub>2</sub>/C<sub>60</sub> and FTO/C<sub>60</sub>. Matching energy levels between the ETL and perovskite are important to ensure efficient charge extraction in the device. The cut-off region and the valence band region for the different fullerene thicknesses are displayed in Figures C.4 and C.5, Appendix C. The ionization potential (IP) was calculated from the energy cut-off, and work function (WF) was extracted from the data (Table C.2, Appendix C). The LUMO (lowest-unoccupied molecular orbital) level for the different C<sub>60</sub> thicknesses deposited on top of FTO or FTO/cTiO<sub>2</sub> was calculated by subtracting the reported bandgap of 1.86 eV<sup>[286]</sup> from the ionization potential. The energy diagram is depicted in Figure 6.1d and Figure C.6 for FTO/C<sub>60</sub> and FTO/cTiO<sub>2</sub>/C<sub>60</sub>-based devices. Interestingly, the LUMO of C<sub>60</sub>'s energy level changes with the thickness independent of the underlayer. On cTiO<sub>2</sub> (Figure 6.1d), the values for the LUMO are higher (5 nm = -3.93 eV, 10 nm = -3.86 eV, 15 nm = -4.06 eV, 20 nm = -4.09 eV and 30 nm = -4.24 eV) than the energy levels for C<sub>60</sub> directly on FTO, which are -4.02 eV for 5 nm, -4.0 eV for 10 nm, -3.96 eV for 15 nm, -4.21 eV for 20 nm C<sub>60</sub> and -4.28 eV for 30 nm). These values are in good agreement with the LUMO values for C<sub>60</sub> reported in the literature (-3.9 – -4.2 eV).<sup>[287]</sup> The better the energy level of C<sub>60</sub> matches the energy level of MAPbI<sub>3</sub>, the better the charge extraction. These findings support our device data, where we found that the devices with a C<sub>60</sub> thickness of 15 nm perform best.

The JV curves were measured in dark conditions to further evaluate our devices for the devices FTO/cTiO<sub>2</sub>/C<sub>60</sub>/MAPbI<sub>3</sub>/spiro-OMeTAD/Au (Appendix C, Figure C.7) and FTO/C<sub>60</sub>/MAPbI<sub>3</sub>/spiro-OMeTAD/Au (Appendix C, Figure C.7b). We observe that the integration of cTiO<sub>2</sub> results in a decrease in leakage current compared to the devices employing only C<sub>60</sub> as an additional layer (Appendix C, Figure C.7b).<sup>[288]</sup> This supports

that the presence of  $c\text{TiO}_2$  reduces defects at the front contact and enhance charge extraction due to a synergetic effect of both ETLs being produced. To analyze the dominant recombination process, the values of ideality factor were extracted from the dark  $JV$  curves (Appendix C, Figure C.8). The ideality factor is typically used to conclude the dominant recombination process by making the following assumptions: an ideality factor close to 1 signifies a band-to-band recombination process is dominating the device, and an ideality factor close to 2 corresponds to bulk Shockley-Read-Hall (SRH) trap assisted recombination.<sup>[289]</sup> The ideality factors for our data were calculated by fitting an exponential equation to the steep part in the curve between the range of 0.9-1.0 V (Appendix C, Figure C.7a,b), and the ideality factor is shown in Figure C.8. Upon integrating  $\text{C}_{60}$  into the device structure, the recombination changes from band-to-band recombination to trap-assisted recombination, indicating defects within the device.<sup>[289]</sup>

The charge extraction properties of the different architectures used in this work were evaluated by steady-state photoluminescence (PL) and time-resolved photoluminescence (TRPL). Thin films of co-evaporated  $\text{MAPbI}_3$  on glass/ $\text{C}_{60}$  and glass/ $c\text{TiO}_2/\text{C}_{60}$  with increasing  $\text{C}_{60}$  thickness (from 0 to 30 nm) were fabricated and analyzed by PL (Figure 6.2b for glass/ $c\text{TiO}_2/\text{C}_{60}$  and S9 for glass/ $\text{C}_{60}$ ) and TRPL (Figure 6.2c for glass/ $c\text{TiO}_2/\text{C}_{60}$  and S9 for glass/ $\text{C}_{60}$ ). To ensure the excitation of the first  $\sim 200$  nm from the perovskite interface,<sup>[290]-[291]</sup> we employed excitation wavelengths with a small penetration depth (475 nm and 640 nm). All samples were excited from the top of the perovskite side. All samples present the same  $\text{PL}_{\text{max}}$  of 760 nm. The quenching ability increases with  $\text{C}_{60}$  thickness for both samples' layouts. Remarkably, the PL intensity follows the trend:  $\text{MAPbI}_3 > c\text{TiO}_2/\text{MAPbI}_3 > \text{C}_{60}/\text{MAPbI}_3 > c\text{TiO}_2/\text{C}_{60}/\text{MAPbI}_3$ . In addition, the samples with more extraction ability are formed by the bilayer  $c\text{TiO}_2/\text{C}_{60}$ .

The TRPL decays were fitted to a double exponential equation, and the corresponding fitted values are shown in Table S3. The longest decay values  $\tau_1$  and  $\tau_2$  values ( $\tau_1 = 27.8$  ns and  $\tau_2 = 92.2$  ns) were observed for the perovskite on glass with no  $\text{C}_{60}$  interlayer, which is directly followed by a small decrease for these values for the sample



cTiO<sub>2</sub>/MAPbI<sub>3</sub> ( $\tau_1 = 23.3$  ns and  $\tau_2 = 81.7$  ns). Surprisingly, this data reveals that the addition of cTiO<sub>2</sub> does not change the carrier lifetime a lot, which means that cTiO<sub>2</sub> does not significantly influence the dynamics of the photoexcited carriers. The addition of increasing C<sub>60</sub> thickness into these configurations leads to a faster charge carrier dynamic resulting in a further decrease of  $\tau_1$  and  $\tau_2$ . Therefore, C<sub>60</sub> induces faster charge carrier dynamics in the samples and lately in the device.

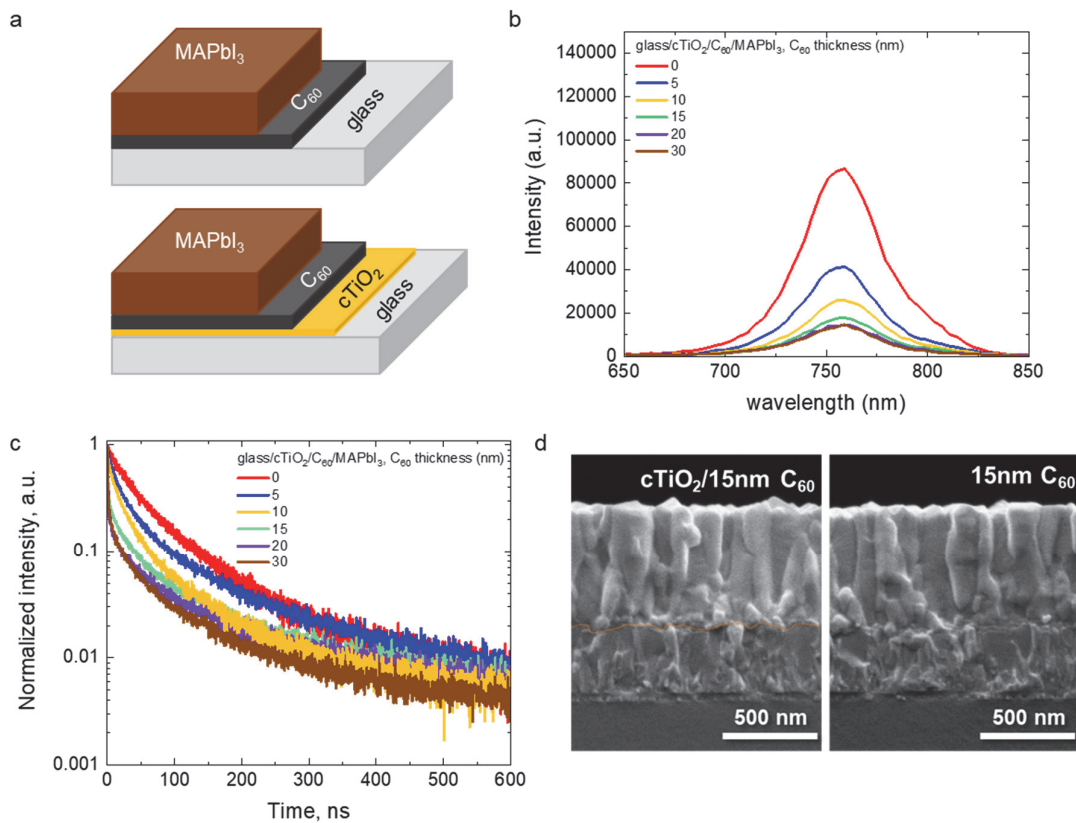


Figure 6.2. a) Film structure of co-evaporated MAPbI<sub>3</sub> thin films deposited on top of glass/C<sub>60</sub> or glass/cTiO<sub>2</sub>/C<sub>60</sub>, b) and c) steady-state PL spectra ( $\lambda_{\text{exc}}=475$  nm) and time-resolved PL decay ( $\lambda_{\text{exc}} = 655$  nm) of glass/cTiO<sub>2</sub>/C<sub>60</sub>/MAPbI<sub>3</sub> samples and d) cross-sectional SEM images of co-evaporated MAPbI<sub>3</sub> thin films deposited on top of FTO/cTiO<sub>2</sub>/C<sub>60</sub> and FTO/C<sub>60</sub> with the C<sub>60</sub> thicknesses being 15 nm.

To understand changes in the crystallinity of the different perovskite, a more detailed understanding of the X-ray diffraction (XRD) pattern shown in Figure C.10, Appendix C is necessary. The crystalline tetragonal MAPbI<sub>3</sub> was formed in all cases.

However, the reference sample containing no  $C_{60}$  interlayer showed a diffraction pattern with higher intensities than the perovskite grown on the organic  $C_{60}$  layer. This increase in intensity gives first hints that the perovskite formation on top of different underlayers is different. Indeed, previous reports have demonstrated that the perovskite formation on inorganic oxides or organics is different when the perovskite is sublimed.<sup>[79]</sup>

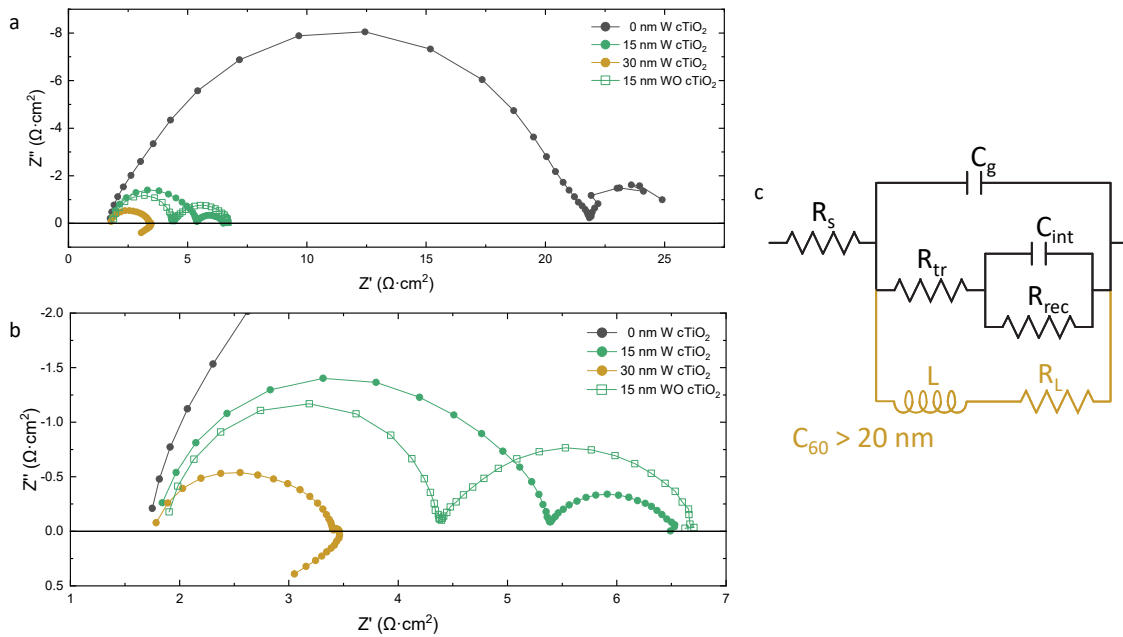


Figure 0.3. a) and b) Impedance Spectroscopy response measured under illumination at 900 mV for the different thicknesses of  $C_{60}$ -layer on perovskite solar cells with (filled dots) and without (empty dots)  $c\text{TiO}_2$  layer. c) Equivalent circuit used to fit the impedance spectra composed by: series resistance ( $R_s$ ), geometrical capacitance ( $C_g$ ), transfer resistance ( $R_{tr}$ ), recombination resistance ( $R_{rec}$ ), internal capacitance ( $C_{int}$ ), extra recombination resistance ( $R_L$ ), and inductance ( $L$ ).

In a previous report, our group highlighted this observation and the differences in chemical composition concerning the underlayer.<sup>[141]</sup> This explains that the XRD pattern for each  $C_{60}$  thickness is identical and independent of  $c\text{TiO}_2$  or FTO. Only the XRD pattern of the sample FTO/ $C_{60}$  with a  $C_{60}$  thickness of 20 nm exhibits an excess of  $\text{PbI}_2$  ( $2\theta \sim 12.7^\circ$ ). We also verified the perovskite morphology formed by analyzing the cross-section and top-view scanning electron microscopy (SEM) images presented in Figure 6.2d and Appendix C in Figures C.11 and C.12. The films show uniform and dense

coverage with very similar crystalline grains in their shape and size. For example, the perovskite on top of 5 nm  $C_{60}$  (Appendix C, Figure C.11b, Figure C.12b) shows cube-shaped perovskite grains ranging in size between 25 to 100 nm, which is typical for vacuum-deposited perovskite films.<sup>[78],[288],[272]</sup> The only perovskite sample that shows a slightly different morphology is the sample employing 20 nm  $C_{60}$  on FTO. Here small round particles in a whiter color and more elongated grains can be observed, which might be attributed to  $PbI_2$  excess, also observed in the XRD pattern (see Figure C.10, Appendix C).

There are no significant changes observed in the XRD pattern or the morphology of the perovskite between the different samples. We, therefore, focus our further analysis on getting more insight into the charge transport processes within the device. We use impedance spectroscopy (IS) to clarify what we have observed earlier in the device data. We conclude that incorporating the  $cTiO_2$  improves the performance of the devices, but only to a small extent. When there is no  $C_{60}$  (with and without  $cTiO_2$ ), the current is much lower, which seems to be related to a poorly conducting interface, translated into a bad extraction. The performances of the cells improve when the  $C_{60}$ -layer increases until 15 nm, then with thicker  $C_{60}$  layer decreases again.

Figures 6.3a and b show the Impedance Spectroscopy (IS) response at 900mV under illumination for the different thicknesses of the  $C_{60}$ -layer on the perovskite solar cells (PSCs) with (filled dots) and without (empty dots) integrating the  $cTiO_2$  layer. For thicknesses up to 20 nm of the  $C_{60}$ -layer, two arcs can be distinguished. With increasing  $C_{60}$  layer thickness, a low-frequency arc appears in the bottom quadrant (see Figure 6.3a, b). For perovskite solar cells, IS spectra with two arcs have been commonly observed, and they are usually analyzed with the equivalent circuit shown in black in Figure 6.3c. Figure C.13 shows a typical schematic of an impedance response, highlighting the effect of the different processes in the observed spectroscopy. The high-frequency arc is generally related to a transfer resistance ( $R_{tr}$ ) and the geometrical capacitance ( $C_g$ ), while the low-frequency arc is related to the recombination resistance ( $R_{rec}$ ) and the internal

capacitance ( $C_{\text{int}}$ ).<sup>[292,293]</sup>  $C_{\text{int}}$  has been associated with interfacial effects producing charge accumulation at perovskite interfaces from which electronic accumulation is the only one able to produce the giant capacitances observed in many perovskite systems.<sup>[294]</sup>  $R_{\text{tr}}$  is generally related to charge transfer resistance at the perovskite interfaces and transport resistance both in the perovskite and other layers in the device.<sup>[295],40</sup> However, it has also been reported that it also contains contributions to recombination from high-frequency phenomena not included in  $R_{\text{rec}}$ .<sup>37,[295]</sup> This model has the same behavior as similar proposed options that locate the  $R_{\text{rec}}$  in parallel to the  $C_{\text{g}}$  instead of its present position.<sup>[296]</sup> The main difference with the proposed model is that their recombination resistance contains the sum of our  $R_{\text{tr}}$  and  $R_{\text{rec}}$ , while capacitances remain the same. Conclusions we obtain are not affected by the use of one or the other.

In addition to the typical two arcs, further features have been observed in IS responses of PSCs, including inductive loops and arcs in the bottom quadrant (as also observed in our data, Figure 6.2b).<sup>[297-299]</sup> These features are generated by the presence of a negative capacitance (or induction), which has been identified as a deleterious effect for the resulting performance in the device.<sup>[300]</sup> Recently, this has been related to the presence of an extra recombination process.<sup>[301,302]</sup> To study all the features observed in the IS of our perovskite devices, the EC, was extended and a parallel branch containing a recombination resistance ( $R_{\text{L}}$ ) together with an inductance ( $L$ ) is incorporated additionally, see Figure 6.3c (brown). This change was necessary to analyze the low-frequency arc for devices with a thicker  $C_{60}$  layer (>20nm).

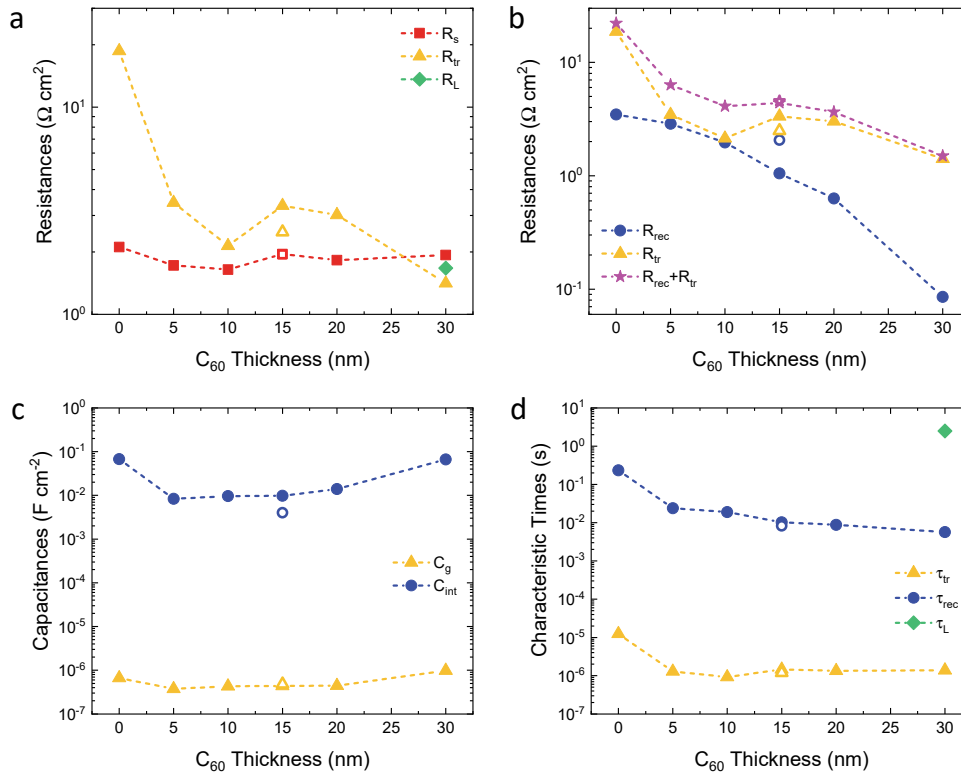


Figure 6.4. Results of the fitting of the impedance responses a) series resistance ( $R_s$ ) and transport resistance ( $R_{tr}$ ) in dependence of  $C_{60}$  thickness b) recombination resistance ( $R_{rec}$ ) and extra recombination resistance ( $R_L$ ) in dependence of  $C_{60}$  thickness c) geometrical capacitance ( $C_g$ ) and internal capacitance ( $C_{int}$ ) in dependence of  $C_{60}$  thickness d) are plotted the characteristic times: transport ( $\tau_{tr}$ ), recombination ( $\tau_{rec}$ ), and extra recombination ( $\tau_L$ ).

The results of the analysis of the IS spectra (Figures 6.3a and b) with the equivalent circuit (Figure 6.3c) are shown in Figure 6.4, and Table C.4, where the filled dots represent the devices with  $c\text{TiO}_2$ , and the empty dots represent the devices without  $c\text{TiO}_2$ , respectively. First, we would like to notice that the series resistance ( $R_s$ ) in red squares in Figure 6.4a is approximately the same for all the devices independently of the incorporation of  $c\text{TiO}_2$ . This implies that neither the  $c\text{TiO}_2$  nor the  $C_{60}$  layers contribute significantly to this resistance. Also, in Figure 6.4a, it can be observed that the addition of the  $C_{60}$ -layer leads to an abrupt decrease of the transfer resistance (yellow triangles), which indicates a better extraction of the photogenerated charges and results consequently in a better device performance (compare 0 nm with 5 nm in Figure 1 and Table

1). This improvement in charge extraction (decrease in  $R_{tr}$ ) explains the also abrupt increase of  $J_{SC}$ ,  $V_{OC}$ , and FF. It is known that perovskite has certain difficulties in transferring charge to  $cTiO_2$ . This result suggests that  $C_{60}$  is playing the role of buffering the interface and that some energy realignment favors the extraction occurs.

For 10 nm thick  $C_{60}$ -layers, we can observe that the  $R_{tr}$  is further reduced, but for 15 and 20 nm, the resistance of the first arc peaks. This fact, together with the peak of  $V_{OC}$  (see Figure C.14 and Tables 1 and C.1) and the decrease in the recombination resistance ( $R_{rec}$ , see Figure 6.4b) for increasing  $C_{60}$  thickness, make us think that the peak in the resistance in Figure 6.4a is associated with recombination process occurring at high frequencies and not included in  $R_{rec}$  so that the total recombination resistance is larger, see Figure 6.4b, and thus  $V_{OC}$  increases.<sup>[393]</sup> In fact, if we compare the sum of  $R_{tr}$  and  $R_{rec}$  in Figure 6.4b with the evolution of  $V_{OC}$ , with  $C_{60}$  thickness see Figure C.14, we observe that from 10nm, both parameters match perfectly, confirming that from this threshold thickness, recombination processes dominate both  $V_{OC}$  and cell performance, while the gross of charge transfer limitations found at 0 and 5 nm become of lesser importance.

For the thicker  $C_{60}$ -layer (i.e., 30 nm), an extra impedance feature is present, as the IS data penetrates the fourth quadrant data in the Nyquist plot. This is associated with new recombination paths and the apparition of negative capacitance and, linked to it, associated inverted hysteresis in the cyclic voltammetry. Traces of this behavior are observed for  $C_{60}$  layers with a thickness of 15 nm and 20 nm, which can be related to the peak observed for total recombination resistance and  $V_{OC}$ . Overall, the final consequence of these trends observed by impedance is that when the  $C_{60}$  becomes too thick (> 20 nm), the total recombination increases due to these inductive effects, and therefore performance reduces (see Tables 1 and S1).

From these data, we can conclude that in the devices, there is a competition between the charge extraction and the recombination processes that depend on the  $C_{60}$ -thickness. The optimum performance occurs for devices with a  $C_{60}$  layer around 15nm

Figure 6.4c describes the dependence of the geometrical capacitance ( $C_g$ ) on the  $C_{60}$  thickness. It can be noted that  $C_g$  is constant, independently of the  $C_{60}$  thickness. The geometrical capacitance is directly related to the perovskite layer. As the value observed is constant, it indicates that the perovskite layer was successfully kept unchanged in composition among the different devices. In this figure, the relation between the internal capacitance ( $C_{int}$ ) and the  $C_{60}$  thickness is also plotted. Between 5 nm and 20 nm thick  $C_{60}$  layer,  $C_{int}$  is nearly constant. In the extremes 0 and 30 nm,  $C_{int}$  is significantly larger. In the first case, we can attribute this change to the insertion of the relatively low dielectric constant of  $C_{60}$  (10-22) with respect to  $cTiO_2$  (~80). For the 30 nm  $C_{60}$ , the apparition of the negative capacitance strongly affects the precision to estimate  $C_{int}$ .

Figure 6.4d shows the calculated characteristic times. As a result of the resistances and capacitances observations, the transfer characteristic-time ( $\tau_g = R_{tr} \cdot C_g$ ) has a mayor reduction when the  $C_{60}$ -layer is added but keeps approximately constant for the different thicknesses, while the recombination characteristic-time ( $\tau_{rec} = R_{rec} \cdot C_{int}$ ) associated to the low-frequency phenomena, constantly decreases with increasing  $C_{60}$ -thickness. These two processes are separated in the time scale, and both can be distinguished from the extra recombination characteristic-time ( $\tau_L = L / R_L$ ) associated with the inductive process in the thickest film. Interestingly this time (2.5 seconds) is in the time range that has been related to large interactions between accumulated ions/vacancies and the surface.<sup>[301]</sup> Finally, the result of the device without the  $cTiO_2$  layer (empty dots in Figures 6.3 and 6.4) are very similar to the devices with the  $cTiO_2$  layer (filled dots), as expected when comparing their device efficiencies in Table 1. Again, the higher  $R_{ec}$  yields to a larger  $V_{OC}$ .

## 1.15 Conclusions

In summary, we have investigated the role of  $cTiO_2$  and  $C_{60}$  as electron transport layers by analyzing the underlying working principles of perovskite devices. We used impedance spectroscopy to describe the response of the different arcs in the spectra and how they contribute to the cell performance. We observed that neither the  $cTiO_2$  nor

the  $C_{60}$  layers provided a significant contribution to the high-frequency series resistance ( $R_s$ ). We could prove that  $cTiO_2$  combined with an optimum  $C_{60}$  layer improves the charge extraction, resulting in an enhanced short circuit current ( $J_{SC}$ ) and, simultaneously, reduces recombination what increases  $V_{OC}$ . The thicker layers of  $C_{60}$  have two detrimental effects on the performance of the samples. On one side, thick  $C_{60}$  absorbs light, decreasing charge generation in the perovskite and thus  $J_{SC}$ . Conversely, the thickest  $C_{60}$  samples show a low-frequency inductive behavior (also known as negative capacitance) in impedance spectroscopy. This implies a delay in extracting photogenerated charge that lately increases recombination and reduces all performance parameters in the solar cells. Our analysis gives first-time insight into the working principles of the  $C_{60}$  layer in a perovskite solar cell and explains its contribution to the device performance.



# Mechanistic Insights into the Role of the Bis(trifluoro-methanesulfonyl)imide Ion in Co-Evaporated *p-i-n* Perovskite Solar Cells

Doping of hole-transporting materials, especially  $N^2,N^2,N^2',N^2',N^7,N^7,N^7',N^7'$ -octakis(4-methoxyphenyl)-9,9'-spirobi[9H-fluorene]-2,2',7,7'-tetramine (spiro-OMeTAD) with Li (II)-bis(trifluoromethanesulfonyl)imide (Li-TFSI), 4-*tert*-butylpyridine (tBP), and Co (III)-bis(trifluoromethanesulfonyl)imide (Co-TFSI), leads in *n-i-p* devices generally to a decrease in the long-term stability (see Chapter 1.4.4). Understanding the influence of these dopants of vacuum-deposited perovskite in *p-i-n* configuration is therefore attractive. In this work, interestingly, we could find that bis(trifluoromethanesulfonyl)imide (TFSI<sup>-</sup>) migrates through the grain boundaries on top of the perovskite surface accumulating at the interface with the electron-transporting layer (ETL). We have used x-ray photon spectroscopy XPS and energy-dispersive x-ray spectroscopy (EDX) to monitor the mobile dopant species to clarify the mechanism. Our results indicate that TFSI<sup>-</sup> passivates the crystal defects during the migration process, reducing non-radiative recombination pathways. Interestingly, and contrary to expected, our findings reveal that the migration of TFSI<sup>-</sup> enhances the device performance and stability, especially for cells containing only TFSI<sup>-</sup> from Co (III)-complex. They retained 90% of the initial performance after 1600 h of testing.

*This chapter is based on the following published article: Nadja Klipfel, Hiroyuki Kanda, A. Sutanto, Mounir Mensi, Cansu Igci, Klaus Leifer, Keith Brooks, Sachin Kinge, Cristina Roldan-Carmona, Cristina Momblona, Paul J. Dyson, Mohammad Khaja Nazzeeruddin "Mechanistic insights into the role of the bis(trifluoro-methanesulfonyl)imide ion in co-evaporated p-i-n perovskite solar cells" in ACS Appl. Mater. Interfaces 2021, 13, 44, 5245-52460, DOI: 10.1021/acsami.1c10117.*

*In this work, I conceptualized the idea, designed the experiments, and performed the fabrication as well as characterization of perovskite thin films and solar cells. Dr. H. Kanda carried out the PL analysis, Dr. A. Sutanto analyzed the SEM images, Dr. M. Mensi*

*measured the XPS and UPS, Dr. C. Igci helped with the analysis of the conductivity, and Dr. C. Momblona, Dr. C. Roldan-Carmona, help with finalizing the manuscript.*

## 1.16 Introduction

Perovskite solar cells (PSCs) have recently reached power conversion efficiencies (PCE) exceeding 25%, which are comparable to the well-established commercial silicon-based technologies.<sup>[10]</sup> Improving the stability of the perovskite under heat and light soaking is one of the current challenges which still hinders commercialization. The stability of perovskite films is influenced by extrinsic and intrinsic factors. The former generally consist of environmental oxygen and moisture and can be minimized by encapsulation methods or via integration of 2D/3D perovskite bilayers.<sup>[304-307]</sup> However, the latter are more challenging as they involve crystal defects, ion migration, or molecular dissociation.<sup>[304]</sup> Among them, under-coordinated  $\text{Pb}^{2+}$  at the grain boundaries is especially common and induces the formation of trap sites at the perovskite layer, affecting charge recombination.<sup>[308]</sup> There are numerous works reported in the literature which successfully control the formation of crystal defects using additives or post-deposition treatments.<sup>[309]</sup> Hence the defects are passivated through the neutralization of the under-coordinated  $\text{Pb}^{2+}$  by negatively-charged species.<sup>[310,311]</sup> Some examples contain ionic liquids or small Lewis base molecules such as thiophene or benzylamine derivatives.<sup>[312],[313,314]</sup>

Other factors influencing the device stability are related to the chemical doping of the hole-transporting layers (HTL),<sup>[315-317]</sup> which mostly entails lithium bis(trifluoromethanesulfonyl)imide (LiTFSI), tris(2-(1H-pyrazol-1-yl)-4-tert-butylpyridine)cobalt(III) tri[bis(trifluoromethane)sulfonimide] (CoTFSI) and tert-butylpyridine (tBP). This is the case for the state-of-the-art 2,2',7,7'-tetrakis (N,N-di-p-methoxyphenylamine)-9,9'spirofluorene (spiro-OMeTAD), the most widely used hole transporting material (HTM) for highly efficient PSCs.<sup>[318-320]</sup> Although LiTFSI is necessary to improve the hole conductivity,<sup>[319-323]</sup>  $\text{Li}^+$  ions easily migrate towards the film surface, which given its high hydrophilic nature, results in higher infiltration of oxygen and moisture and

accelerated degradation.<sup>[318,319,324,325]</sup> Similarly, tBP increases the LiTFSI solubility<sup>[319]</sup> and reduces phase segregation, ensuring a better film quality, but its corrosive nature harms the perovskite material.<sup>[326,327]</sup> These drawbacks are only partially palliated by the formation of  $\text{Li}^+ - \text{tBP}$  complex,<sup>19</sup> while similar degradation effects can be observed by doping the HTM via chemical oxidization of CoTFSI and tBP.<sup>[328],[329]</sup> To minimize these drawbacks, different approaches have been developed in the last years. For example, the synthesis of dopant-free HTMs<sup>[132]</sup> is attracting great attention, as well as the use of inert interlayers preventing interfacial reactions from happening.<sup>[78,183,330,331]</sup> Yet comparable results in device performance to those obtained with doped spiro-OMeTAD are still missing. In addition, little attention has been paid to the counterions neutralizing the dopants and their possible role, if any, on the evolution of device operation. In particular, TFSI<sup>-</sup> is a common ion in CoTFSI and LiTFSI dopants, which is also used in various additives proposed in the literature for the bulk perovskite material.<sup>[328]</sup> Unfortunately, there are no specific studies targeting these species, nor a general consensus, to understand their effect in the pristine films and their embodiment in a device.

Here we present a systematic study targeting the most employed ionic dopants, LiTFSI and CoTFSI, and the specific interplay of TFSI<sup>-</sup> as beneficial passivate incorporated via migration to the perovskite material. We note that spiro-OMeTAD is generally deposited as the top layer in n-i-p device configurations, as it easily dissolves and degrades by the perovskite solution in *p-i-n* configurations.<sup>[332]</sup> Therefore, in solution-processed *p-i-n* devices, the infiltration of the HTL solution through the perovskite layer and grain boundaries cannot be avoided, hindering the proper discrimination of any plausible dopant migration through the layer. To avoid these phenomena, here we employ spiro-OMeTAD in *p-i-n* device configurations but using perovskite layers deposited via thermal co-evaporation. This vacuum-based technique enables the deposition of different materials without damaging the underneath layer; hence we can ensure the formation of clean interfaces between sequentially deposited materials and avoid any cross-contamination due to the solvent infiltration. By using as main techniques photoluminescence (PL) decay, X-ray photoelectron spectroscopy (XPS), and energy-

dispersive X-ray spectroscopy (EDX), we have evaluated the migration of ionic species originated from the doped HTL and their influence on both the bulk and the surface perovskite properties. Our study reveals a strong correlation between the type of dopant employed in the HTL and the structural and optical features of the perovskite, which is also reflected in the device's stability and efficiency. These findings, revealed here for the first time, are relevant for understanding the several processes occurring on the multi-stack devices, calling for deeper investigations to clarify the specific role and behavior of every ionic species in cell performance.

### 1.17 Results and Discussion

Methylammonium lead iodide ( $\text{MAPbI}_3$ ) films were thermally co-deposited on top of FTO/spiro-OMeTAD substrates containing five different dopant compositions. In summary we mixed the HTL with: i) LiTFSI, CoTFSI and tBP dopants (named hereafter **Li-Co-tBP**) in the same concentration as usually employed for state-of-the-art devices (used as reference); ii) containing only tBP (**tBP**); iii) containing a combination of LiTFSI and tBP (**Li-tBP**); iv) containing a combination of CoTFSI and tBP (**Co-tBP**) and v) the same as iv but containing 3 times higher ( $3n\text{-TFSI}(\text{Co})$ ) concentration of CoTFSI (**3Co-tBP**). Given that the ionic stoichiometry is different for LiTFSI and CoTFSI (1:1 and 1:3 respectively), we use the conditions described in (v) to enable a direct comparison between films with equal TFSI<sup>-</sup> concentration but different counter-cation (either  $\text{Co}^{3+}$  or  $\text{Li}^+$ ).

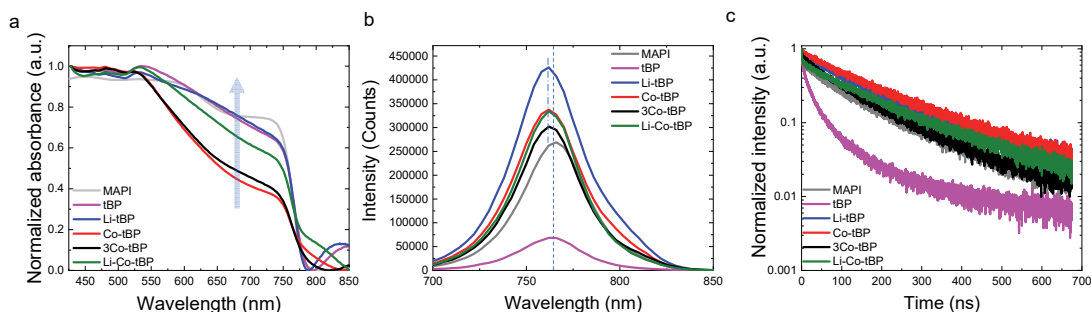


Figure 7.1: Co-evaporated  $\text{MAPbI}_3$  thin films deposited on top of glass or glass/HTM (tBP, Li-tBP, Co-tBP, 3Co-tBP and Li-Co-tBP): a) absorbance spectra, b) steady-state PL spectra ( $\lambda_{\text{exc}}=475$  nm) and c) time-resolved PL decay ( $\lambda_{\text{exc}}=655$  nm).

The UV-visible spectroscopic characterization of the as-deposited  $\text{MAPbI}_3$  films is displayed in Figure 7.1. Because the samples were prepared in the same deposition process under holder rotation, the film evaporation and thickness are exactly the same, which enables a direct comparison between their optical features and their correlation to the underlayer material. As presented in Figure 7.1a, all films exhibit a broad absorption in the whole visible spectra and a similar absorbance onset located at 783 nm. However, important differences appear in the absorption intensity along the 550-750 nm region, showing reduced values for those samples grown on CoTFSI containing HTMs. Given that previous reports have demonstrated a strong correlation between the perovskite formed in vacuum conditions and the layer underneath,<sup>[79]</sup> a detailed understanding of the structure-property relationship via X-ray diffraction (XRD) is highly recommended. According to the diffractograms reported in Figure D.1 (Appendix D), all HTM compositions induce the formation of crystalline  $\text{MAPbI}_3$  in the tetragonal phase and preferential orientation along with the (110) and (220) directions. However, those films grown on doped layers are independent of the dopant chemical nature (LiTFSI or CoTFSI) but contain unreacted  $\text{PbI}_2$  ( $2\theta \sim 12.7^\circ$ ).<sup>[333]</sup> This  $\text{PbI}_2$  is absent for those grown on the dopant-free spiro-OMeTAD (tBP) underlayer. This indicates that the type of dopant and concentration employed in the HTM influences the perovskite crystal deposited on top. In particular, we observe a significant drop in the diffraction intensity when the spiro-OMeTAD contains CoTFSI complex, consistent with the lower UV-Visible

absorbance previously observed. We additionally verified the morphology of the films by analyzing the top-view and cross-section scanning electron microscopy (SEM) images presented in Figure D.2, Appendix D. The films show uniform and dense coverage but also important differences in the shape and size of the crystalline grains. For example, MAPbI<sub>3</sub> deposited on top of **tBP** exhibits columnar-shaped grains with 100-250 nm size. This shape is maintained for those deposited on LiTFSI, but the grain size reduces to 100 nm. Similarly, the layers were grown on films containing CoTFSI (**Co-tBP**, **3Co-tBP**, and **Li-Co-tBP**) form stacks of small grains with sizes ranging from 25 to 100 nm, consistent with the previous vacuum-deposited perovskite reports.<sup>[78],[288],[272]</sup> To evaluate the changes induced by the dopants, we used steady-state photoluminescence (PL) and time-resolved photoluminescence (TrPL) spectroscopy (Figure 7.1b and 1c). The PL and TrPL spectra were collected while the samples were excited from the top perovskite side. We employed excitation wavelengths with small penetration depth (475 nm and 655 nm, respectively), which ensured that we were targeting the first ~ 200 nm from the perovskite interface exclusively.<sup>[290]-[291]</sup> Interestingly, the PL intensity reduced for samples deposited on non-doped **tBP**, while it increased for films grown on doped HTMs. Such results, related to reduced defect-mediated recombination, suggest a different perovskite trap density<sup>[334]</sup> induced by the underlayer additives. In particular, films were grown on HTMs containing only LiTFSI exhibit higher PL than those containing Co-salts (either **Li-Co-tBP**, **Co-tBP**, or **3Co-tBP** samples). In addition, we observed a PL blue-shift when using doped underlayers compared to perovskites deposited on dopant-free HTMs. This effect plausibly originated from the smaller perovskite grains grown on doped HTMs,<sup>[80]</sup> calls for a deeper analysis to clarify the real origin of the perovskite optical changes. The TrPL decays, shown in Fig. 1c, were fitted to a double exponential equation, in which the fast component is generally related to trap-assisted recombination at the defect sites, whereas the slow decay is related to radiative recombination inside the grains (see calculated parameters in Table S1).<sup>[335]</sup> As observed in Table S1, the bare MAPbI<sub>3</sub> film exhibits  $\tau_1$  and  $\tau_2$  values of 4.36 ns and 122.54 ns, respectively. These values increase considerably for perovskites grown on doped HTMs, showing values of

45.7 ns and 177.3 ns for **Li-tBP**, or 53.6 ns and 185.78 ns for **Co-tBP**, respectively. There is, however, a reversed behavior for larger dopant amounts, and the process accelerates, reducing  $\tau_1$  and  $\tau_2$  values to 32.1 ns and 136.2 ns (for **3Co-tBP**) and 1.28ns and 151.8ns (**Li-Co-tBP**) respectively. This implies that the dopants initially incorporated into the HTM film delay the electron-hole recombination in the perovskite given an optimum molar concentration, and therefore might induce inferior defect-density within the perovskite material. Interestingly, this could be related to the dopants behaving as effective passivates, affecting the formation process during the perovskite crystallization.

To shed light on the origin of such observations, we further explored the surface chemistry of the samples by X-ray photoelectron spectroscopy (XPS). The F, Pb, and I atomic concentrations were calculated from the integration of the corresponding XPS signals and divided by the sensitivity factors using CasaXPS software<sup>[336]</sup> (see results summarized in Figure D.3-D.8 and Table D2, Appendix D). Contrary to expected, we observed strong signals corresponding to F1s (689 eV) and C1s peaks (293 eV) attributed to -F and -CF<sub>3</sub> groups, denoting the existence of fluorine-containing species at the very top perovskite surface.<sup>[337]</sup> Such strong signals, originated merely from the TFSI<sup>-</sup> in Li-TFSI and Co-TFSI dopants added to the HTL (Figure D.3, Appendix D), are systematically observed when using doped underlayers, but their intensities are strongly dependent on the nature and type of dopants. Because the F1s signal shows a very intense single peak (Figure 7.2a), we used it for further analysis comparing several perovskite thicknesses. The XPS signals corresponding to LiTFSI and CoTFSI powder are depicted in Figure D.3 (Appendix D), used here for reference. We investigated with XPS the F signal of perovskite films having a thickness of 30 nm and 500nm deposited on the different doped HTM layers. We observed for films grown on **Co-tBP** stronger F peaks than for the films grown on the underlayer **Li-tBP**. We note that both underlayers, **3Co-tBP** and **Li-tBP**, contain the same TFSI<sup>-</sup> concentration (see Figure 7.2a), and therefore the larger concentration observed in MAPbI<sub>3</sub> for the **Co-tBP** sample gives evidence of a much faster TFSI<sup>-</sup> migration through the perovskite layer. Given the large ionic size and the absence of any peak shift or emergence in the XRD patterns (Figure D.1, Appendix D),

we can exclude the incorporation of TFSI<sup>-</sup> in the perovskite lattice during ion migration, and therefore it must plausibly move through the perovskite grain boundaries. A schematic representation of the suggested mechanism is presented in Figure 7.2d. We note that, different from previous studies reporting Li migration across the device and TFSI<sup>-</sup> ion remaining in the spiro-OMeTAD layer,<sup>[324]</sup> we find that TFSI ion migrates through the absorber layer and accumulates at the perovskite top surface, self-modifying the bulk and opposite interface. From an electronic perspective, this might be advantageous for passivating the Pb defects and halide vacancies,<sup>[338]</sup> which provides additional support to the previous photoluminescence results. In particular, we highlight the increased  $\tau_1$  values obtained from trPL decays for all samples deposited on doped HTMs. To further corroborate these observations, we investigated the TFSI dynamics by performing XPS analysis in thinner perovskite samples (30 nm) (Figure 7.2b and D4-D7). The atomic concentration for F, Pb, I are calculated from the corresponding spectra and the F1s signal are shown in Figure D.7, Table D2, Appendix D. We note that the F1s peaks exhibit higher intensity for **3Co-tBP**, **Co-tBP**, and **Li-Co-tBP**, compared to those of 500 nm, and therefore a faster accumulation of TFSI at the surface for thinner perovskite layers occurs (Appendix D, Figure D.4 and D5). Interestingly, the trend is reversed for **Co-tBP** and **Li-tBP** in addition to a less pronounced difference in TFSI ions on the surface of thicker perovskite.

To provide additional evidence of the TFSI migration, we performed bulk-sensitive Energy-dispersive X-ray spectroscopy (EDX) measurements (see Appendix D, Figure D.9, D10). We first fabricated solution-processed MAPbI<sub>3</sub> films containing intentional incorporation of different LiTFSI concentrations to the bulk with the aim to obtain a calibration curve for the interpolation of our experimental results. A minimum detection limit of 0.5 % at. concentration was found for fluorine elements. Later, the co-evaporated MAPbI<sub>3</sub> samples were analyzed at the same experimental conditions as in the standard samples. The samples were deposited on top of indium tin oxide ITO to avoid additional F sources, ensuring that the F detected originates only from the HTM layer. The XPS spectra of the as-deposited 500 nm MAPbI<sub>3</sub> films, fitted and compared



to the standard samples, showed  $F < 1\%$  at. concentration in all the samples (Figure 7.2c). This implies that the amount of TFSI<sup>-</sup> within the bulk is considerably lower than that detected at the perovskite surface (see Table S2).

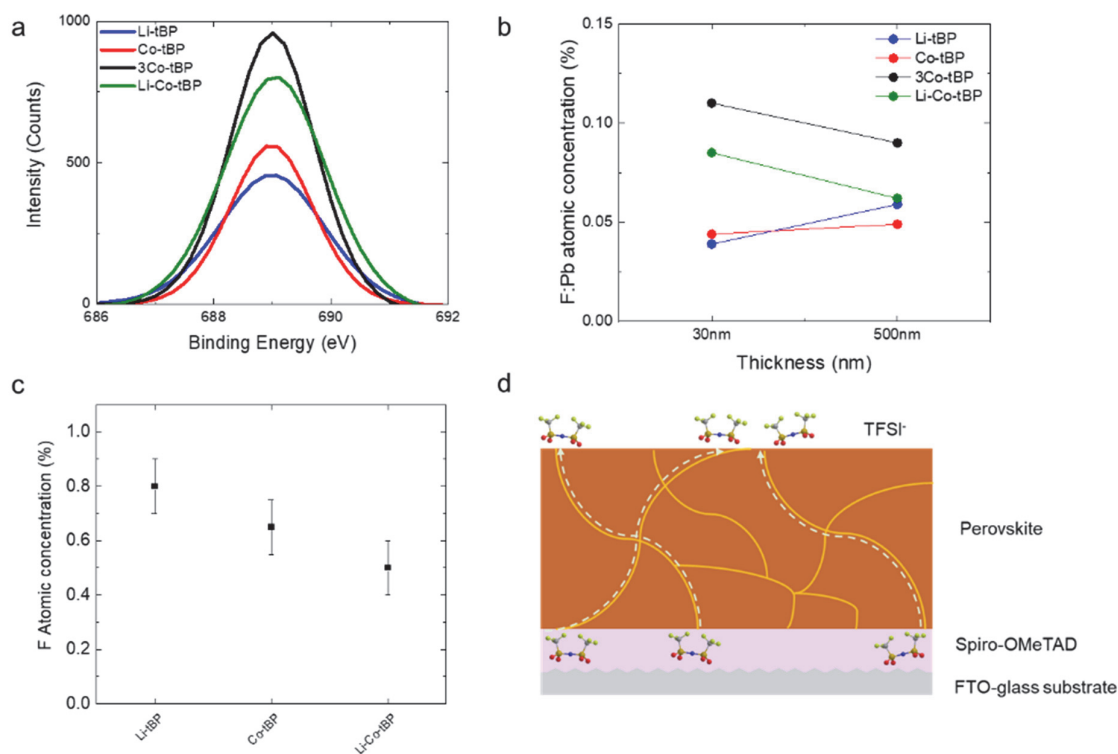


Figure 7.2: a) F<sub>1s</sub> XPS spectra of 500 nm perovskite film deposited on top of doped-HTM. b) F<sub>1s</sub>/Pb<sub>4f</sub> atomic ratio calculated by XPS at the perovskite surface with different perovskite thicknesses deposited on ITO/HTM. c) F atomic concentration detected by EDX in 500 nm perovskite bulk. d) Schematic representation of the TFSI<sup>-</sup> migration process.

We further investigated the influence of the dopants in the electronic properties at the MAPbI<sub>3</sub> by ultraviolet photoelectron spectroscopy (UPS). Since the UPS probing depth is smaller than that of XPS, the electronic properties are expected to be modified by the presence of the TFSI<sup>-</sup> ions at the perovskite surface. The work function (WF) is estimated as the difference between the source photon energy (21.22 eV) and the intercept of the secondary electron cutoff (SECO) and the zero-intensity y-axis (Figure D11, Appendix D). The WF values for perovskite samples are presented in Table S3 and with values of -4.62, -4.72, -4.82, -4.52 and -4.92 eV for the **tBP**, **Li-tBP**, **Co-tBP**, **3Co-tBP**

and **Li-Co-tBP**, respectively. The valence band maximum (VBM) was calculated from the intercept between the linear fitting of the valence band onset and the zero-intensity y-axis (Figure D.11c, Appendix D), and are located for the perovskite samples at 0.9 eV for **tBP** and **Li-tBP**, 1.0 eV for **Co-tBP** and **Li-Co-tBP** and 1.6 eV for **3Co-tBP** below the Fermi level, respectively. The ionization potential was calculated as the difference between the WF and the energy cut-off and was assumed to be equal to the valence band energy level ( $E_{VB}$ ).<sup>[339]</sup> Hence, the obtained values are -5.52, -5.62, -5.82, -6.12 and -5.92 eV, for **tBP**, **Li-tBP**, **Co-tBP**, **3Co-tBP** and **Li-Co-tBP**, respectively. The  $E_{VB}$  for co-evaporated  $\text{MAPbI}_3$  is -5.52 eV, in good agreement with reported values for  $\text{MAPbI}_3$  (-5.5 – -5.7 eV).<sup>[340],[341]</sup> However, we found that the surface passivation of the perovskite with TFSI anions results in a downward shift with respect to the Fermi level, from -5.52 eV (**tBP**) to deeper values (-6.12 eV for **3Co-tBP**). A correlation is shown between the shifted energy level and the F atomic concentration detected by XPS (Table S2), which indicates that the interaction between the  $\text{TFSI}^-$  and perovskite impacts the energetics of the perovskite surface and therefore will influence the energy alignment with the contact layer on top of it.<sup>[342],[343]</sup>

Prior to the device preparation, the stability of the co-evaporated  $\text{MAPbI}_3$  was evaluated (Figure D.12, Appendix D). The intensity ratio of the (001)  $\text{PbI}_2$  reflection to the (110)  $\text{MAPbI}_3$  reflection was used as an indicator to follow the perovskite decomposition process with time. After three weeks, the  $\text{MAPbI}_3$  degradation is evidenced by the lower intensity of the perovskite reflections. The degradation process in all the samples leads to higher  $\text{PbI}_2$  contribution in the thin film accompanied most likely by a release of methylammonium gas.<sup>[344]</sup> Moreover, the main perovskite reflection undergoes changes. The perovskite peak is split into a minor peak/shoulder at  $14.1^\circ$  (002 plane) and  $14.2^\circ$  (110 plane) for the samples **tBP** and **Li-tBP**. This indicates that during the degradation process, a crystal reorientation process is produced in CoTFSI-free samples, and grains with (002) direction normal to the substrate surface can be detected.<sup>43</sup> Note that this splitting is not observed in samples containing CoTFSI, which could indicate a beneficial effect in the perovskite stabilization.

The temporal changes of the chemical composition were monitored by analyzing changes of the F, Pb, and I atoms in the perovskite film by XPS. The XPS spectra are presented in Appendix D, Figure D.13-16, and the corresponding atomic concentration extracted and listed in Table B2. The time-dependent F/Pb ratio analysis is depicted in Figure D.17 (Appendix D) and shows different behaviors. The F concentration still increases during two weeks for all samples except **3Co-tBP**. However, after three weeks, the F concentration in all cases decreases, indicating its reorganization through the sample or its solubility at ambient conditions due to its hydrophilic nature.<sup>[345]</sup> The Pb/I ratio is modified due to the degradation of MAPbI<sub>3</sub> and further formation of excess PbI<sub>2</sub>, as confirmed by XRD (Figure D.1, Appendix D).

These findings are of great interest to further explore their impacts on PV performance. Spiro-OMeTAD, especially after doping, may cause parasitic absorption, which results in absorption loss of the front contact. The absorbance of the dopant-free and doped spiro-OMeTAD layers, deposited with the same experimental conditions as in the device, was measured, and it is depicted in Figure D.18a, Appendix D. The films containing LiTFSI or CoTFSI show the characteristic peak at 520 nm (HOMO→LUMO transition), indicating the formation of mono-cation radical partially oxidized spiro-OMeTAD. The increased absorption intensity implies an increase in the concentration of the oxidized spiro-OMeTAD.<sup>[346]-[347]</sup> The oxidation is, to a greater extent, on the Co-doped thin film than the LiTFSI-doped one. This fact will contribute to higher parasitic absorption in the device. In addition, the use of p-type dopants provides the necessary electrical conductivity for the insulating spiro-OMeTAD. The lateral thin-film conductivity of the dopant-free and doped spiro-OMeTAD layers was measured on OFET substrates (see Figure D.18b, Appendix D). The conductivity of pristine spiro-OMeTAD was determined to be  $1.3 \times 10^{-7} \text{ S cm}^{-1}$ . On the other hand, the conductivity of the oxidized spiro-OMeTAD layers increases by 3 orders of magnitude following the trend: **Li-tBP** < **Co-tBP** < **Li-Co-tBP** < **3Co-tBP** with conductivity values of  $4.56 \times 10^{-4}$ ,  $4.82 \times 10^{-4}$ ,  $5.54 \times 10^{-4}$  and  $5.99 \times 10^{-4} \text{ S cm}^{-1}$ , respectively. The impact of these factors will be taken into consideration in the PV performance in the corresponding PSCs (Table 1).

Table 0.1: PV parameters extracted from the corresponding J-V curves of the most efficient devices and lateral conductivity of dopant-free and doped spiro-OMeTAD layers.

	Device performance				HTM
	$J_{sc}$ (mA cm <sup>-2</sup> )	$V_{oc}$ (V)	$FF$	PCE (%)	thin film $\sigma$ (S cm <sup>-1</sup> )
<b>tBP</b>	-10.95	0.903	0.45	4.52	$1.3 \cdot 10^{-7}$
<b>Li-tBP</b>	-20.12	0.991	0.75	15.17	$4.56 \cdot 10^{-4}$
<b>Co-tBP</b>	-19.00	1.082	0.75	15.39	$4.82 \cdot 10^{-4}$
<b>3Co-tBP</b>	-14.46	0.982	0.51	7.30	$5.99 \cdot 10^{-4}$
<b>Li-Co-tBP</b>	-20.18	0.985	0.67	13.14	$5.54 \cdot 10^{-4}$

The energy band diagram of the *p-i-n* devices is depicted in Figure 7.3a, indicating the different valence band values for the TFSI-modified perovskite. J-V characteristics of the most efficient devices are depicted in Figure 7.3b, and the corresponding PV parameters are extracted and presented in Table 7.1. The external quantum efficiency spectra and the calculated short circuit current density are presented in Figure D.19, Appendix D.

The device statistics are depicted in Appendix D, Figure D.20, and tabulated in Table D4 for PSCs with different spiro-OMeTAD dopants. The devices containing dopant-free spiro-OMeTAD presented the lowest efficiencies of the series. The photogenerated charges produced at the perovskite layer will not be able to be transported to the electrode due to the low conductivity of the dopant-free spiro-OMeTAD layer. The charges will be accumulated and recombined at the spiro-OMeTAD/ MAPbI<sub>3</sub> interface, as observed for the lowest open-circuit voltage observed for the samples. The charge extraction is enhanced by the higher conductivity in doped spiro-OMeTAD, but it is important to keep in mind that at higher doped spiro-OMeTAD content, more parasitic absorption will occur at the device, negatively affecting the charge generation in perovskite. In addition, the deeper valence band values for the modified perovskite layers will lead to reduced interfacial potential energy losses due to lower trap density.

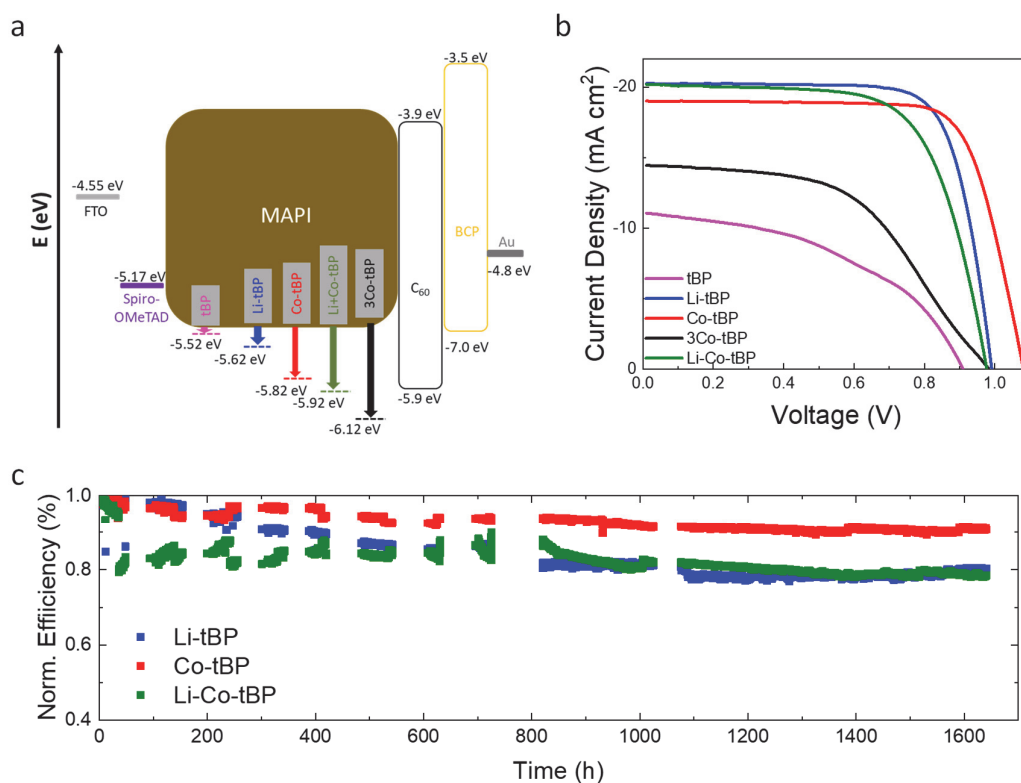


Figure 0.3: a) Energy level diagram of the fabricated *p-i-n* solar cells. b) J-V characteristics of the most efficient devices. c) Long-term stability of the unencapsulated solar cells under 1 sun illumination at 25°C in nitrogen atmosphere.

The trade-off between parasitic absorbance and conductivity lead to the devices containing LiTFSI or CoTFSI the highest efficiencies of the series. In both cases, the devices present the highest  $V_{oc}$  and FF values of the series, indicating lower charge recombination in the device and good charge extraction through the device. The average values are listed in Table S5.

The long-term stability measurements were evaluated under continuous 1 sun illumination (Figure 7.3c). During the study, the devices were kept at the maximum power point tracking (mppt) in N<sub>2</sub> atmosphere at 25°C. Devices containing CoTFSI present the highest stability of the series, retaining 90% of its initial PV performance up to 1600 h under continuous illumination. **Li-tBP** and **(Li-Co-tBP)** present lower device stability than the Co-based counterpart, retaining 79% of its initial PV performance after

1600 h under operation at continuous illumination. The former continuously decreases while the latter presents a fast decay in the first 20 operating hours and then stabilizes. The higher stability for the devices containing CoTFSI is in good agreement with the higher stability observed for the perovskite layers.

### 1.18 Conclusion

In conclusion, we have detected the TFSI anion at the co-evaporated perovskite surface, indicating that the mobile dopants in their spiro-OMeTAD layer must migrate through the grain-boundaries to the perovskite surface. Consequently, the presence of TFSI anions detected at the perovskite surface is advantageous for defect passivation. We show in our systematic study that the migration of the TFSI<sup>-</sup> coming from the Co (III) complex shows higher mobility than the TFSI anion from the other sources, and are a highlight that the migration of TFSI<sup>-</sup>, contrary to current knowledge, is beneficial for device stability and performance.

# Zn(II) and Cu(II) tetrakis(diarylamine)phthalocyanines as Hole-Transporting Materials for Perovskite Solar Cells

Finding new hole-transporting materials (HTMs) suitable for replacing the state-of-the-art spiro-OMeTAD is still challenging. In this work, newly synthesized diarylamine-substituted metal phthalocyanines (MPcs, M = Zn(II) or Cu(II)) functionalized with either linear or branched alkoxy chains are evaluated as HTMs in perovskite solar cells. We investigate how the nature of the alkoxy chains and of the coordinated metal species is influencing the photophysical properties of the perovskite thin films and the device efficiency stability.

*This chapter is based on the following article currently under review: Nadja Klipfel, Jianxing Xia, Pavel Čulík, Simonetta Orlandi, Marco Cavazzini, Naoyuki Shibayama, Hiroyuki Kanda, Cansu Igci, Abdullah M. Asiri, Cristina Momblona, Gianluca Pozzi, Mohammad Khaja Nazeerudin “Zn(II) and Cu(II) tetrakis(diarylamine)phthalocyanines as hole-transporting materials for perovskite solar cells.”*

*In this work, I designed the experiments and performed the characterization of perovskite thin films and solar cells, as well as the writing of the manuscript Dr. S. Orlandi and Dr. M. Cavazzini synthesized the hole-transporting materials. J. Xia and P. Čulík and I spin-coated the devices and characterized the devices. Dr. H. Kanda helped measure the PL, TrPL data and helped with the analysis of the GIWAXS data, J. Xia did the DFT calculations, Prof. Dr. N. Shibayama measured the GIWAXS data, Dr. C. Igci helped with the CV measurements, and Dr. C. Momblona helped with the conductivity measurements and with finalizing the manuscript.*

## 1.19 Introduction

The power conversion efficiency (PCE) of perovskite solar cells (PSCs) increased over the last decade, from 3.8% to over 25%,<sup>[44,231]</sup> making PSCs a promising technology toward reduced carbon emissions,<sup>[232]</sup> with additional benefits in terms of sustainability goals, such as low cost,<sup>[233]</sup> ease of fabrication, and recyclability.<sup>[234]</sup> The remarkable increase in PSCs efficiency was achieved by carefully optimizing the perovskite composition and improving the electron-<sup>[52,348]</sup> hole-<sup>[259,349]</sup> transporting layers. Nevertheless, the commercialization of PSCs is still challenging due to the instability of the overall device and the material itself towards heat, stress humidity, light illumination, and oxygen.<sup>[236-239]</sup> Some instability can also be originated from the chemical doping of the hole-transporting material (HTM). In *n-i-p* PSCs, the HTM is typically sandwiched between the perovskite layer and the metal top electrode. Therefore, the energy-alignment between the highest occupied molecular orbital (HOMO) and the perovskite valence band (VB) is essential for an efficient hole-extraction, ensuring good transport towards the electrode.<sup>[350,351]</sup> Despite the effort to find new hole-transporting materials that improve the perovskite solar cell in stability and efficiency, 2,2',7,7'-Tetrakis[N, N-di(4-methoxyphenyl)amino]-9,9'-spirobifluorene (**spiro-OMeTAD**) is still the benchmark HTM, even though drawbacks such as high costs, low intrinsic conductivity, and hole-mobility and stability are well known and limit the potential in up-scaling of the technology.<sup>[349,352,353]</sup>

Phthalocyanines (Pcs) are structurally related to porphyrins, which are photo- and electrochemically stable.<sup>[354]</sup> Several transition metal complexes of phthalocyanines (MPcs) endowed with semiconducting properties in the solid-state have been investigated in recent years as HTMs in PSCs.<sup>[355]</sup> The unsubstituted CuPcs complex was vacuum-deposited and employed as HTM in PSCs, leading to device efficiencies ranging from 5.0% to 15.4%.<sup>[356,357]</sup> However, the structure of MPcs can be modified at will easily. Structural modifications of the Pc macrocyclic ligand in the peripheral and non-peripheral positions and the choice of the core metal cation can tune essential properties like the electronic and optical properties and its solubility, which will later influence the



final device performance.<sup>[358]</sup> Different strategies have been followed in the literature to improve the intrinsic low solubility of MPcs, in particular the incorporation of alkyl-,<sup>[359]</sup> thiophene-,<sup>[360]</sup> or arylamine (triphenylamine) groups,<sup>[361]</sup> among others, at various positions.<sup>[362], [363]</sup> On the other hand, the presence of Pcs substituents can be used to influence the self-assembly behavior of MPcs through the modulation of  $\pi$ - $\pi$  intermolecular interactions between Pcs rings<sup>[364]</sup> with possible consequences on intermolecular charge transport processes.<sup>[358]</sup>

Arylamine groups, in particular triphenylamine (TPA) or diphenylamine (DPA) derivatives, have been widely employed as components of small molecule-based HTMs due to their excellent hole-transporting properties, electron-donor ability, high stability, and solubility.<sup>[365]</sup> In the case of Pc-based HTMs, molecular structure modifications by the insertion of arylamine substituents have been much less explored. In 2016, we demonstrated the use of doped DPA-tetrasubstituted ZnPcs as HTMs in PSCs, with a PCE of 11.75%. Two other Zn-Pcs bearing carbazole derivatives as substituents were also investigated, shedding some light on the impact of steric effects and aggregation of Pcs derivatives on their charge-transport properties.<sup>[366]</sup> Later on, we reported the synthesis of Zn(II) and Cu(II)-based phthalocyanines with eight secondary aromatic amines directly linked to the peripheral positions of the macrocycle by the C-N bond. These MPcs proved to be promising HTMs in PSCs, allowing PCEs ranging from 4.93% to 18.10%.<sup>[367]</sup> Sfyrí *et al.* also implemented ZnPcs bearing four peripheral TPA substituents in PSCs, and its use as HTM led to device efficiencies of 5.6%.<sup>[368]</sup> In another recent example, Feng *et al.* compared the photovoltaic performance of PSCs fabricated with OMe-DPA-CuPcs and OMe-TPA-CuPcs, featuring four bis-(4-methoxyphenyl)amino substituents and four *N,N*-bis(4-methoxyphenyl)benzenamino substituents, respectively. OMe-DPA-CuPcs showed a lower PCE than OMe-TPA-CuPc (16.73% vs. 19.67%). This fact was ascribed to the lower HOMO energy level of OMe-TPA-CuPcs and its lower recombination rate and more efficient hole transport properties.<sup>[369]</sup> The limited data shows that arylamine-substituted MPcs have a great potential as HTMs in PSCs, which can be fully unleashed through the rational design of novel compounds of this class.

Alkyl side chains in organic semiconductors are insulating units and do not directly contribute to charge transport in organic electronic devices. Nevertheless, alkyl side-chains can have a noticeable impact on charge transport for polymer and small molecule semiconductors, including MPcs, by influencing intermolecular interactions and/or film morphology in solid-state due to two competing effects: steric hindrance and intermolecular dispersive attraction.<sup>[370]</sup> Therefore, even subtle alterations on chain length, branching position, odd-even effect, and stereochemistry of alkyl chains can significantly affect charge mobility.<sup>[359]</sup> Thus, L. Calió *et al.* reported the use of two MPcs (M = Cu(II) or Zn(II)) with 4-*tert*-octylphenoxy substituents as HTMs in PSCs, achieving PCEs of 8.33% and 7.25% for the Cu(II) and the Zn(II) complex, respectively.<sup>[371]</sup> More importantly, we could prove that MPcs featuring bis(4-alkoxyphenyl)amino substituents were superior HTMs with respect to their 9*H*-carbazol-9-yl and diphenylamino analogs, with subtle yet clear differences elicited by the nature of the alkoxy chains.<sup>[366],[367]</sup> In that context, the best photovoltaic performance was obtained with ZnPcs **BL40** (Figure 8.1) bearing eight bis(4-*n*-butoxyphenyl)amino substituents. This prompted us to evaluate further the effects of the alkoxy chain length and branching on the behavior of diarylamine-substituted MPcs. To this end, we have now synthesized and tested ZnPcs complexes **Zn-BL54**, **Zn-BL58**, and CuPcs complexes **Cu-BL57**, **Cu-BL61** (Figure 8.1).

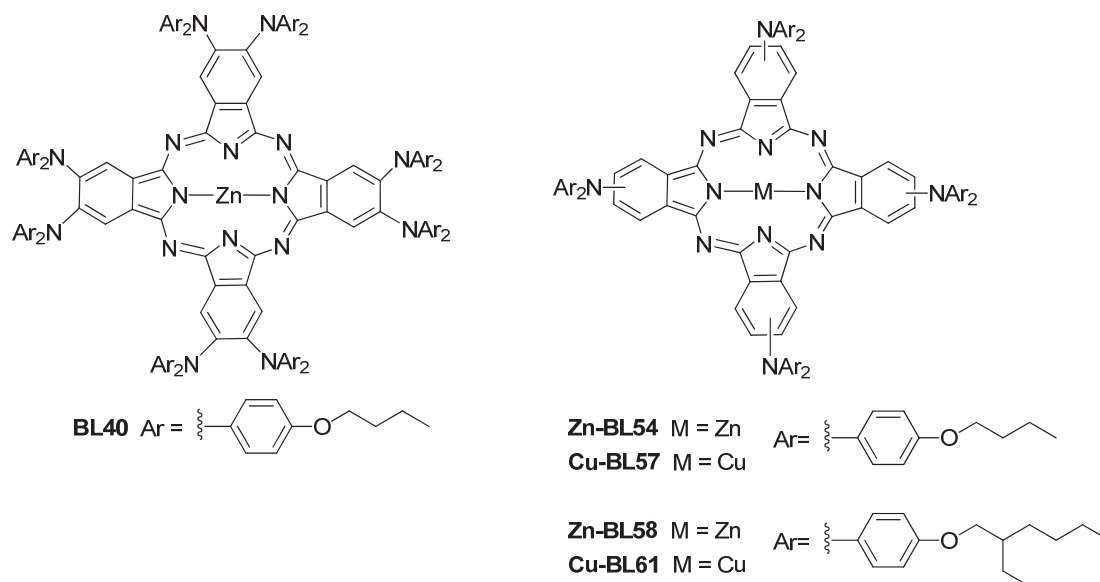
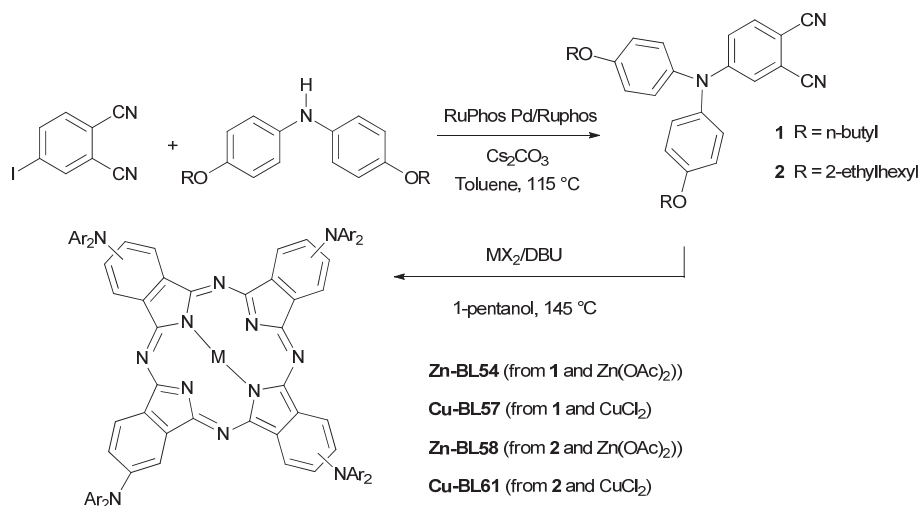


Figure 0.1. Molecular structure of Zn(II) and Cu(II) phthalocyanines bearing bis(4-alkoxyphenyl)amino substituents.

## 1.20 Results and Discussion

### *Synthesis of tetrasubstituted MPcs*

Metal-templated cyclotetramerization of suitable phthalonitrile precursors provides convenient access to MPcs bearing either four or eight bis(4-alkoxyphenyl)amino substituents.<sup>[366,367]</sup> However, preparing the 4,5-disubstituted phthalonitriles required to synthesize octasubstituted MPcs such as **BL40** is a rather cumbersome multi-step process. On the contrary, phthalonitriles **1** and **2**, the starting materials for the preparation of MPcs **Zn-BL54**, **Cu-BL57** and **Zn-BL58**, **Cu-BL61**, respectively, were readily obtained in excellent yields (88–93%) by Palladium-catalyzed amination reaction between 4-iodophthalonitrile and the corresponding secondary aromatic amine (**Scheme 8.1**). MPcs **Zn-BL54**, **Cu-BL57**, **Zn-BL58**, **Cu-BL61** were subsequently obtained as mixtures of positional isomers by cyclotetramerization reaction of these phthalonitriles in the presence of 1,8-diaza-bicyclo[5.4.0]undec-7-ene (DBU) and a metal salt (**Scheme 8.1**). Analytical data of **Zn-BL54**, **Cu-BL57**, **Zn-BL58**, **Cu-BL61** were in complete agreement with the proposed structures.



Scheme 8.1. Synthesis of tetrasubstituted MPcs.

The new octasubstituted MPcs are soluble in common organic solvents such as THF or DCM. However, NMR characterization could not be performed on the paramagnetic CuPcs **Cu-BL57** and **Cu-BL61**. The chemical structure of these two compounds was nonetheless confirmed by UV-Vis, FTIR, and HRMS data (see experimental methods, Appendix E).

## 2.2 Photophysical, electrochemical, and 2D GIWAXS characterization of MPcs

Typical B and Q bands of MPcs in the near UV region and Vis region, respectively, characterize the UV-Vis spectra of the new compounds (Figure 8.2), which also show broad bands of low intensity in the 450-550 nm region. These bands are distinctive of MPcs with aromatic secondary amine substituents.<sup>[366,367]</sup> The energy required for the  $\pi \rightarrow \pi^*$  transition ( $\text{a}_{1u} \rightarrow \text{e}_{g^*}$ ) from HOMO to lowest unoccupied molecular orbital (LUMO) of the Pcs ring, which is responsible for the Q band, is significantly lower for most peripherally-substituted Cu- and ZnPcs tested so far as solution-processable HTMs in PSCs, including ZnPcs bearing four diaryl amino substituents without alkoxy side chains.<sup>[367]</sup> For example, a bathochromic effect in the order of +20 nm is observed for the Q bands of ZnPcs **Zn-BL54,58** (739 nm, THF solution) with respect to their analogue ZnPcs **BL25** (720 nm, THF solution) depleted of alkoxy side-chains.<sup>[367]</sup> An

additional, although much smaller, red-shift of the absorption maxima is triggered by changing the coordinated metal species from Zn(II) to Cu(II). Thus, CuPcs **Cu-BL57** and **Cu-BL61** show absorption maxima at 744 nm and 745 nm, respectively. These data also show that the influence of branching and elongation of the alkoxy side chains on UV-Vis absorption is negligible. On the other hand, the energy required for the  $\pi \rightarrow \pi^*$  transition in MPcs bearing four peripheral bis(4-alkoxyphenyl)amine substituents is higher than that required for their octa substituted analogue, as exemplified by comparison between **Zn-BL54** and **BL40** (758 nm, THF solution).

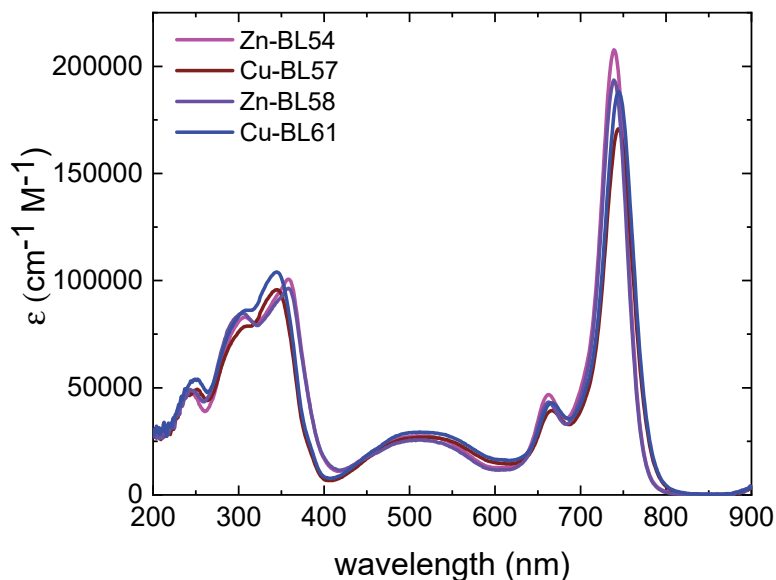


Figure o.2. UV-Vis spectra of tetrasubstituted MPcs in THF solution.

Cyclic voltammetry (CV) measurements were performed with a standard three-electrode configuration to experimentally investigate the highest occupied molecular orbital (HOMO) energy levels ( $E_{\text{HOMO}}$ ) of the undoped HTM materials **Zn-BL54**, **Cu-BL57**, **Zn-BL58**, and **Cu-BL61** (Appendix E, Figure E.1, Table E.1). The compounds were tested in dichloromethane solution containing 0.1 M *n*-Bu<sub>4</sub>NPF<sub>6</sub> as a supporting electrolyte, and the oxidation potential was calibrated against ferrocene used as an internal standard. The  $E_{\text{HOMO}}$  values were calculated to be -5.37, -5.48, -5.36, and -5.46 eV vs.

vacuum for **Zn-BL54**, **Cu-BL57**, **Zn-BL58**, and **Cu-BL61**, respectively (Table S1). Slightly deeper HOMO levels were observed for Cu(II) based phthalocyanines **Cu-BL57** and **Cu-BL61** compared to Zn(II)based phthalocyanines **Zn-BL54** and **Zn-BL58**. The electron-donating effect of the longer branched alkoxy chains of **Zn-BL58** and **Cu-BL61** resulted in relatively higher HOMO levels than **Zn-BL54** and **Cu-BL57**.<sup>[372]</sup>

Quantum chemical calculations were performed with the Gaussian 09W program to establish the most probable molecular geometry and energy levels in solid-state for the HTMs. The density functional theory (DFT) method B3LYP/6-311G was used for geometry optimization.<sup>[373]</sup> The optimized structures highlight the nonplanar conformation of the arylamine moiety and the twists between the core nitrogen and phenyl groups (Figure E.2, Appendix E). The electron density distributions for the highest occupied molecular orbital HOMO-1, HOMO, LUMO, and LUMO+1, are presented with their corresponding energy levels (Figure E.3, Appendix E). The values extracted from the DFT calculations are shown in Table E (Appendix E). The bandgap ( $E_g$ ) was calculated following:  $E_g = E_{LUMO} - E_{HOMO}$ , see Appendix E Figure E.3. The energy level for the frontier molecular orbitals for LUMO and HOMO are shown in the schematics Figure E.4 (Appendix E). The trend of the calculated HOMO values follows the energy levels obtained from cyclic voltammetry.  $E_{HOMO, DFT}$  for **Zn-BL54**= -4.52, **Cu-BL57**= -4.55, **Zn-BL58**=-4.53, **Cu-BL61**= -4.54 eV.

The photogenerated hole extraction efficiency of the new HTMs was evaluated by performing steady-state PL measurements. Therefore, triple cation perovskite films were deposited on glass, and the PL spectra were recorded under wavelength excitation at 475 nm. The new HTMs were then deposited in the same ways as during the device fabrication, and the PL emission spectra were again recorded. Interestingly, a stronger quenching effect can be observed compared to the **spiro-OMeTAD** spectra (Figure 8.3a). The most substantial quenching effect can be observed for **Zn-BL54** and **Cu-BL57** HTMs (98, 99 quenching %, respectively, see Table E3, Appendix E), with the *n*-butoxy side chain in their structure. Less quenching can be observed for **Zn-BL58** and **Cu-BL61** (83 and 89 % quenching, respectively (Table E3, Appendix E), which bear 2-

ethylhexyloxy chains. This indicates that the *n*-butoxy-substituted MPCs have an enhanced hole extraction as observed in the zoom-in Figure 8.3a compared to their 2-ethylhexyloxy-based Pcs counterparts. The PL quenching trend **Cu-BL57**>**Zn-BL54**>**Cu-BL61**>**Zn-BL58**>**spiro-OMeTAD** indicates the best hole-transfer between **Cu-BL57** and the perovskite<sup>[374]</sup>

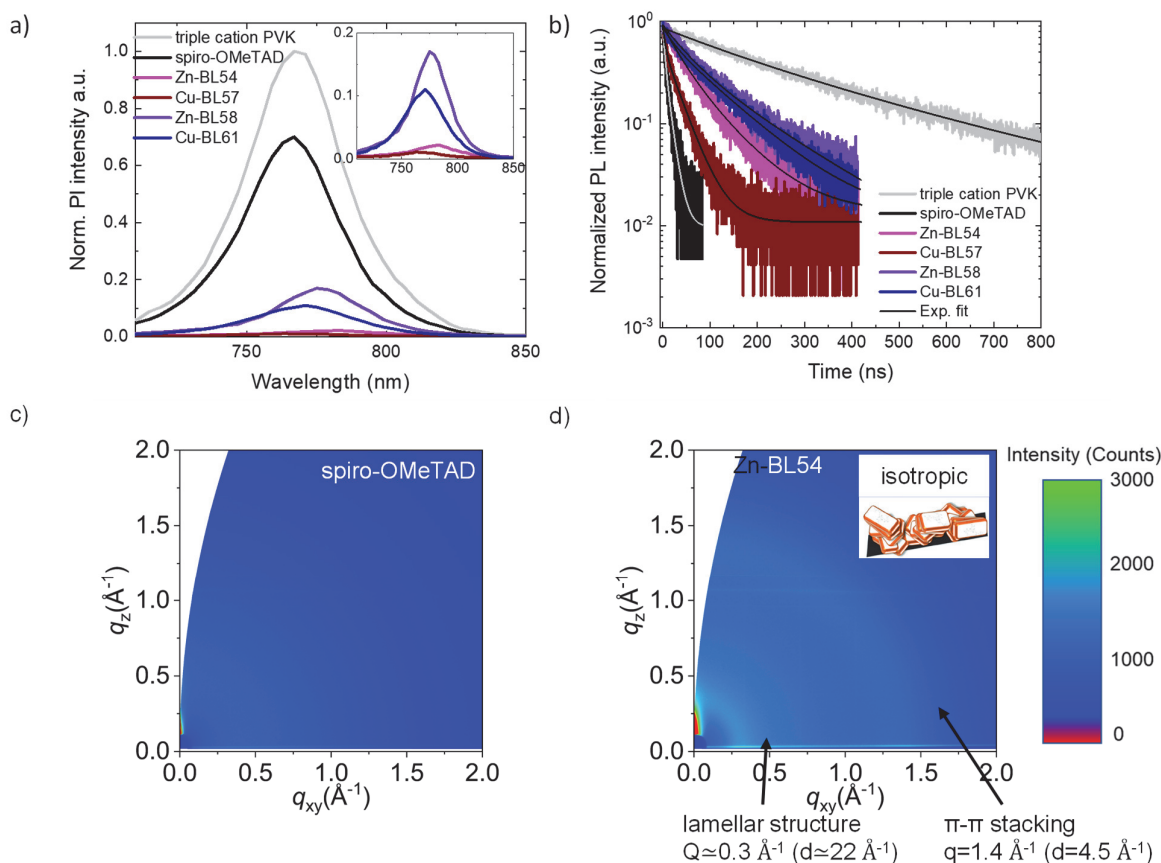


Figure 8.3. a) Steady-state photoluminescence spectra ( $\lambda_{\text{exc}}=475\text{nm}$ ), b) time-resolved PL decay ( $\lambda_{\text{exc}}=640\text{nm}$ ,  $\lambda_{\text{em}}=760\text{nm}$ ). GIWAXS pattern of the films coated on a silicon wafer: c) spiro-OMeTAD and d) Zn-BL54.

The observation follows the general trend where the bulkier alkoxy groups seem less optimal for the charge transfer. Interestingly, the decrease in PL intensity suggests a good hole-extraction between the VB of the perovskite and the HOMO of the HTMs, probably due to a good perovskite/HTM interface.<sup>[375]</sup> In addition to the quenching, we

also observed a red-shift in the  $PL_{\max}$  for the HTMs **Zn-BL54** ( $PL_{\max}= 783\text{nm}$ ) and **Cu-BL58** ( $PL_{\max}= 776\text{nm}$ ) compared to the HTMs **Zn-BL57** ( $PL_{\max}= 764\text{nm}$ ) and **Cu-BL61** ( $PL_{\max}= 770\text{nm}$ ). To evaluate further the HTMs, time-resolved photoluminescence (TrPL) measurements were performed (Figure 8.3b). Therefore, the samples were prepared in the same manner as described for the steady-state PL measurements and measured with an excitation wavelength of 640 nm. The corresponding decays were fitted to a double exponential equation, where the fast component ( $\tau_1$ ) is related to trap-assisted recombination at defect sites and the slow component ( $\tau_2$ ) to radiative recombination inside the grains (see the fitted values in Table S4). As observed, the bare perovskite film exhibits  $\tau_1$  and  $\tau_2$  values of 139 ns and 336 ns, respectively. These values decrease significantly after depositing the HTM following the trend perovskite>**Zn-BL58**>**Cu-BL61**>**Zn-BL54**>**Cu-BL57**>**spiro-OMeTAD**. This data indicates that all new HTMs exhibit a slightly slower process than **spiro-OMeTAD**, indicating slower charge recombination processes for the new HTMs than the reference containing **spiro-OMeTAD**.<sup>[259]</sup> It also indicates that the HTMs employing the less bulky alkoxy chains (**Zn-BL54** and **Cu-BL57**) extract the charges faster than those employing more bulky alkoxy chains (**Zn-BL58** and **Cu-BL61**).

2D grazing incidence wide-angle X-ray scattering (2D GIWAXS) was performed to investigate the crystallization and the  $\pi\rightarrow\pi$  stacking of the reference HTM (**spiro-OMeTAD**) and the novel HTMs with a different alkoxy group and central metal (Figure 8.3c, d, and Appendix E Figure E.5).<sup>[374,376]</sup> The samples were prepared by spin-coating the corresponding HTM solutions on silicon wafers. No  $\pi\text{-}\pi$  stacking or lamella structure can be observed for the **spiro-OMeTAD** (Figure 8.3c). For the four new HTMs, two diffractions rings appeared corresponding to the  $\pi\text{-}\pi$  stacking structure ( $q \approx 1.4 \text{ \AA}^{-1}$ ) and the lamellar structure ( $q \approx 0.3 \text{ \AA}^{-1}$ ) (Figure 8.3d and Appendix E Figure E.5, E.6). The lamellar structure can be more dominantly observed on the samples **Cu-BL57** and **Cu-BL61** than the samples with Zn(II) metal core (Appendix E Figure E5). The azimuthally integrated intensity profile was calculated from 2D GIWAXS spectra (Appendix E Figure E7). The d-spacings for the  $\pi\text{-}\pi$  stacking structure was  $4.6 \text{ \AA}$  for all the HTMs, while the



intercolumnar organization and distance were different for all HTMs: **Zn-BL54**=18.9 Å, **Zn-BL58**= 22.3 Å, **Cu-BL57**= 22.3 Å, and **Cu-BL61**= 24.1 Å. Interestingly, the lamellar distance increases by exchanging Zn(II) with Cu(II) and exchanging the *n*-butoxy with the 2-ethylhexyloxy side chain. The calculated angular dependence of the peak intensity at  $q = 1.4 \text{ \AA}^{-1}$  corresponds well to d-spacings of  $\pi$ - $\pi$  stacking (4.6 Å) from the MM2 simulation (Appendix E Figure E.8). To investigate if there is a preferred crystal orientation, the set-up was the following: theta ( $\theta$ ) is the angle to the  $q_z$  axis (out-of-plane), whereas  $\theta = 90^\circ$  is  $q_{xy}$  axis (in-plane). Regarding the 2D GIWAXS patterns, all four HTMs show  $\pi$ - $\pi$  stacking interaction and random orientation (Figure 8.3). Since the intensity of each HTM shows no change as a function  $\theta$ , all HTMs are isotropic (Figure 8.3d inset and Appendix E E9). The  $\pi$ - $\pi$  stacking peak at  $1.6 \text{ \AA}^{-1}$  shows isotropic orientation, and its stacking phase is randomly arranged according to the broad peak at  $0.3 \text{ \AA}^{-1}$ . Notably, the simulated molecular size of HTMs is consistent with the GIWAXS data (Appendix E E10) and confirms the trend of the lamellar size structure. At equal side chains, the HTMs incorporating Cu(II) are more significant than those incorporating Zn(II).

#### *Photovoltaic performance of solution-processed PSCs*

The new octasubstituted MPcs were evaluated as doped-HTMs in *n-i-p* PSCs. Solar cell devices were fabricated with the following device layout: FTO/c-TiO<sub>2</sub>/m-TiO<sub>2</sub>/SnO<sub>2</sub>/perovskite/HTM/Au. All layers were deposited by solution process except for the thermally-evaporated gold electrode. The “so-called” triple cation perovskite [(FAPbI<sub>3</sub>)<sub>0.87</sub> (MAPbBr<sub>3</sub>)<sub>0.13</sub>]<sub>0.92</sub>(CsPbI<sub>3</sub>)<sub>0.08</sub> was used for initial screening as a light absorber. **Spiro-OMeTAD** and octasubstituted MPcs HTM layers were doped with cobalt (III)- tris(bis-(trifluoromethylsulfonyl)imide) (CoTFSI) and (trifluoromethylsulfonyl) imide lithium salt (LiTFSI). To increase the LiTFSI solubility and the HTM thin film morphology, *tert*-butylpyridine (TBP) was added to the HTM solution.<sup>[319]</sup> Top-view and cross-section scanning electron microscopy (SEM) were performed to determine the morphology and thickness of the HTMs (Appendix E Figure E.11). The cross-section images show a compact and uniform layer with a thickness of ~247 nm for **spiro-**

OMeTAD-based devices and a thickness of ~170 nm for devices containing **Zn-BL54**, **Cu-BL57**, and **Zn-BL58** and **Cu-BL61**, respectively. The top-view images show complete and homogeneous coverage of the perovskite by the HTM without aggregating the material and/or pinholes (Appendix E Figure E.11).

Figure 8.4a displays a schematic of the energy level diagram of the fabricated devices. The solid-state ionization potential of the doped HTMs was extracted from ultraviolet photoelectron spectroscopy (UPS) measurements (Appendix E Figure E.12), and the energy cut-off, work function (WF), and ionization potential (IP) values are presented in Table E.1. The ionization potential values of the doped HTMs layers are -5.29 eV for **spiro-OMeTAD** and -5.51, -5.61, -5.44 and -5.57 eV for **Zn-BL54**, **Cu-BL57**, **Zn-BL58** and **Cu-BL61**, respectively. The trend observed in the UPS measurement agrees with the one observed by CV. The HOMO levels align well with the valence band energy level of the typical lead iodide-based perovskites (-5.70 eV) (Appendix E E13, Table E5).

The best-performing devices fabricated with the triple cation perovskite and the **BL**-series HTMs and **spiro-OMeTAD** are compared in Figure 8.4b, and the corresponding photovoltaic parameters are extracted and displayed in Table 8.1. The reference device employed **spiro-OMeTAD** as HTM showed the highest efficiency with a PCE of 17.72%. **Zn-BL54** provided the best results in the **BL**-series with a PCE of 13.85%, followed by **Cu-BL57** (11.36%), featuring *n*-butoxy chains. The two HTMs characterized by the presence of bulkier 2-ethylhexyloxy chains, **Cu-BL61** (10.15%) and **Zn-BL58** (9.92%), provided lower PCE values than **Zn-BL54** and **Cu-BL57**. This finding indicates that the alkoxy side chains are more relevant than the coordinated metal species in determining the photovoltaic performance of these octasubstituted MPcs. The PCE trend can be related to the conductivity values obtained for the HTMs (Appendix E Figure E.14, Table E6). Indeed, the HTMs with the branched, sterically hindering 2-ethylhexyloxy chain (**Zn-BL58** =  $3.22 \times 10^{-6}$  cm<sup>2</sup>/Vs and **Cu-BL61** =  $7.3 \times 10^{-6}$  cm<sup>2</sup>/Vs) show lower conductivity compared to the HTMs with linear and shorter *n*-butoxy chain (**Zn-BL54** =  $1.96 \times 10^{-5}$  cm<sup>2</sup>/Vs and **Cu-BL57** =  $7.97 \times 10^{-5}$  cm<sup>2</sup>/Vs). It must be noted that even though **Cu-BL57**

has the highest conductivity of the **BL**-series, the efficiency is only the second-best, which indicates that also the coordination metal is playing a role. The reference HTM **spiro-OMeTAD** shows the highest conductivity with  $3.4 \times 10^{-4} \text{ cm}^2/\text{Vs}$ , which can be related to the highest efficiency.

A deeper analysis of the photovoltaic characteristics for the triple cation perovskite devices can be found in Table 1. **Zn-BL54** and **Cu-BL57** have different short-circuit current densities ( $J_{sc}$ ) values, ranging from  $-21.72 \text{ mA cm}^{-2}$  for **Zn-BL54** to  $-20.69 \text{ mA cm}^{-2}$  for **Cu-BL57**. Substitution of the *n*-butoxy chains present in these two MPcs with 2-ethylhexyloxy chains leads to lower  $J_{sc}$  values for **Zn-BL68** ( $J_{sc} = -20.01 \text{ mA cm}^{-2}$ ) and **Cu-BL61** ( $J_{sc} = -20.13 \text{ mA cm}^{-2}$ ). Both factors, the kind of alkoxy chain and coordinated metal, seem to play a role here. The influence of the MPcs at the rear part of the device is observed in the corresponding external quantum efficiency (EQE) spectra (Appendix E Figure E.15). The integrated current densities values are in good agreement (5% deviation) with the measured values from *J-V* characteristics.

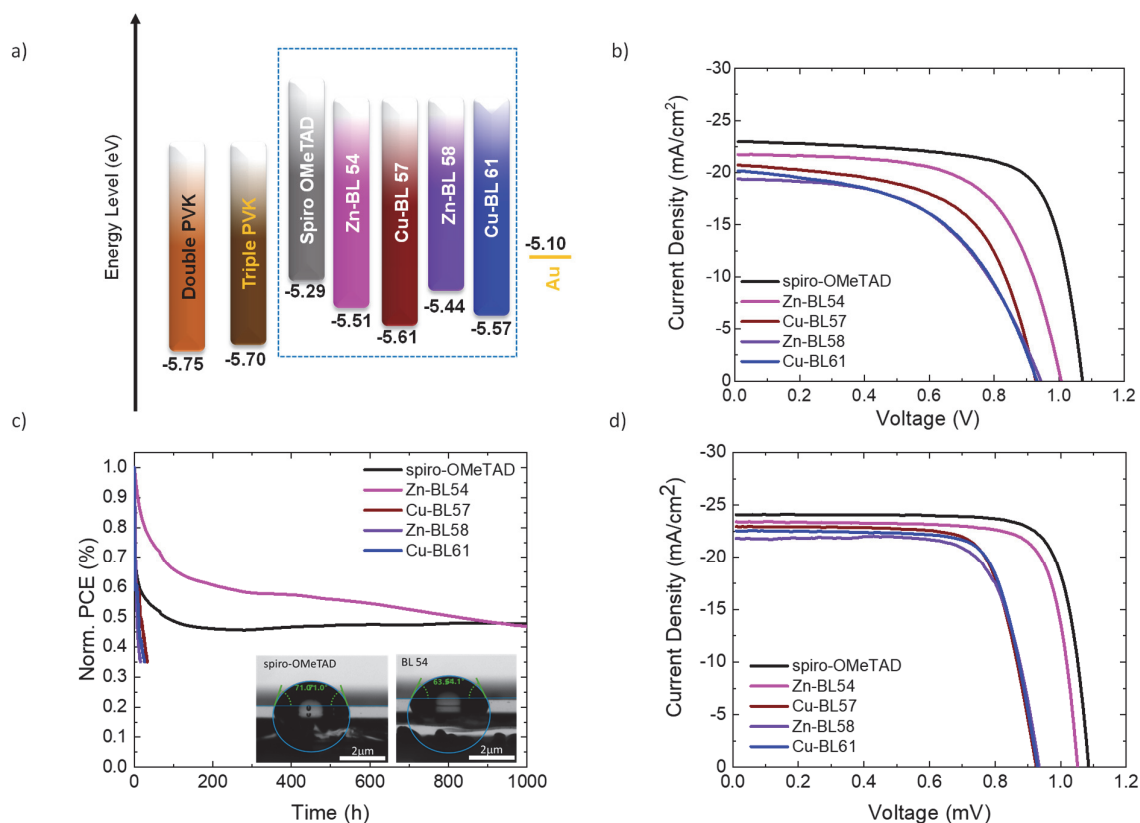


Figure 8.4. a) Energy level diagram of the device containing doped HTMs (HOMO values for the HTMs, double and triple cation perovskite from their corresponding UPS measurements), b)  $J$ - $V$  curves of the most efficient devices based on triple cation perovskite, c) long-term stability of unencapsulated triple cation-based devices measured under continuous light illumination at 25°C in a nitrogen atmosphere and with inset water contact angle of spiro-OMeTAD and Zn-BL54 deposited on top of the perovskite layer and d)  $J$ - $V$  curves of the most efficient solar cells containing double cation-based perovskite.

At high energy wavelengths, the EQE observed is very similar for all HTMs, staying close to 90%. Nevertheless, above 600nm, a substantial decrease in the EQE can be observed for all HTMs of the **BL**-series, in agreement with the strong absorption band of the octasubstituted MPCs from 450nm to 790nm, which can be appreciated in the absorbance spectra of doped **BL**-HTM thin films from 400nm to 800nm (Appendix E Figure E.16). This absorption can considerably reduce the fraction of current generated by the second pass of reflected light from the gold electrode. As the perovskite film exhibits a higher absorption coefficient at a shorter wavelength, this effect can only be observed for low-energy photons. Compared to the reference cell with **spiro-OMeTAD**,

which is transparent in the visible range, octasubstituted MPCs absorb part of this light, causing a decrease in the incident photon-to-current conversion efficiency above 590nm.<sup>[377]</sup>

The behavior of the devices under forward and reverse bias at AM 1.5 illumination in the ambient atmosphere was tested. The calculated hysteresis index,<sup>[98]</sup> is similar for **spiro-OMeTAD** 0.05 and **Zn-BL54** 0.05 but slightly higher for the rest of the HTMs, **Cu-BL57** 0.07, **Zn-BL58** 0.14, and **Cu-BL61** 0.16, following the trend of device efficiencies. The lower the efficiency, the higher the hysteresis index (see Appendix E Figure E.17 and Table E.7). This behavior can most likely be linked to the not well-aligned energy levels, which results in an unbalanced separation and extraction of the electrons and holes.<sup>[378]</sup>

The fill factor (FF) values for **Zn-BL58** and **Cu-BL61**, the HTMs with 2-ethylhexyloxy side chains, are lower than those measured for **Zn-BL54** and **Cu-BL57**. This trend in FF can be related to the enhanced conductivity of MPCs with *n*-butoxy chains (**Zn-BL54** and **Cu-BL57**) discussed before. When comparing further the parameters of device performance of the **BL** series to **spiro-OMeTAD**, then another main parameter leading to lower performance is the open-circuit voltage ( $V_{oc}$ ). The best performing cell with **spiro-OMeTAD** has a  $V_{oc}$  value of 1.07 V, while the cells containing the BL HTM series **Zn-BL54**, **Cu-BL57**, **Zn-BL58**, and **Cu-BL61** exhibit lower  $V_{oc}$  values (1.01, 0.93, 0.93, 0.92 V, respectively). Changes in  $V_{oc}$  can be attributed to differences in the energy alignment between the perovskite conduction band and the octasubstituted MPCs.

Table 0.1. Photovoltaic parameters extracted from the corresponding  $J$ - $V$  curves for triple cation and double cation-based most efficient devices

Perovskite	HTM	$J_{sc}$ (mA/cm <sup>2</sup> )	$V_{oc}$ (V)	FF	PCE (%)
triple cation	<b>spiro-OMeTAD</b>	-22.99	1.07	0.72	17.72
	<b>Zn-BL54</b>	-21.72	1.01	0.63	13.85

	<b>Cu-BL57</b>	-20.69	0.93	0.59	11.36
	<b>Zn-BL58</b>	-20.01	0.93	0.53	9.92
	<b>Cu-BL61</b>	-20.13	0.92	0.55	10.15
	<b>spiro-OMeTAD</b>	-24.86	1.09	0.79	21.30
double cation	<b>Zn-BL54</b>	-23.87	1.07	0.79	20.18
	<b>Cu-BL57</b>	-23.00	0.94	0.74	16.00
	<b>Zn-BL58</b>	-22.12	0.95	0.73	15.34
	<b>Cu-BL61</b>	-22.57	0.94	0.75	15.91

LUMO levels inducing recombination at the interface. The ionization potential values for the thin films of the new HTMs (-5.51, -5.61, -5.44, and -5.57 eV for **Zn-BL54**, **Cu-BL57**, **Zn-BL58**, and **Cu-BL61**, respectively) are suitable for perovskite energy matching, but to a lower degree in comparison to **spiro-OMeTAD** (-5.29 eV. See Supporting Information Table S1). Higher energy levels of the HTMs could prevent  $V_{oc}$  losses would be preferable for a better charge extraction.<sup>[379]</sup>

Finally, the long-term stability of the non-encapsulated devices with triple cation perovskite was measured under 1 sun illumination and in an  $N_2$  atmosphere. The device lifetime was evaluated based on the 80% retention of its initial photovoltaic performance (Figure 8.4c and Appendix E Figure E.18). Interestingly, the nature of the alkoxy chains affects the device performance and displays a strong influence on long-term device stability. In the **BL**-series, the presence of 2-ethylhexyloxy chains (**Zn-BL58** and **Cu-BL61**) deteriorated the long-term stability, while the device based on **Zn-BL54** presents the highest long-term stability under light illumination; such behavior suggests that the degradation of the layer is enhanced with bulkier insulating chains. On the other hand, the device based on **Cu-BL57**, the Cu(II) analogue of **Zn-BL54**, displayed much lower

stability, thus pointing out a negative effect of Cu(II) coordination. Additionally, for the first 700h, **Zn-BL54** showed outstanding good light stability compared with the most widely used HTM in PSC, **spiro-OMeTAD**, whose efficiency is reduced to 45% from its initial performance after 1000 h under constant light illumination. **Zn-BL54** is more stable until it reached 80% of its initial efficiency after 20h, which from that point slowly decreased until 45% of its efficiency at 1000h.

Water contact angle measurements were performed on top of glass/perovskite/doped HTMs to investigate the hydrophobicity of the HTMs (Figure 8.4c, Appendix E Figure E.19). The following trend could be observed: **Zn-BL54**<**Cu-BL57**<**spiro-OMeTAD**<**Zn-BL58**<**Cu-BL61**, with contact angles of 63°, 69°, 71°, 72°, and 81° respectively. **Cu-BL61** showed a significantly higher hydrophobicity than all the other HTMs, agreeing with the presence of coordinated Cu (II) and lipophilic 2-ethylhexyloxy chains in its structure. MPCs with branched, bulkier alkoxy chains displayed a higher hydrophobic nature concerning those bearing *n*-butoxy chains, but this did not translate in improved device stability, as expected based on increased repelling moisture during the operation. [380] Quite surprisingly, despite its pretty average hydrophobicity, **Zn-BL54** ensured superior device stability among the HTMs examined, resulting from a combination of factors besides water repellency. The results so far show that the combination of Zn(II) with a shorter alkoxy chain is more beneficial when considering the device's performance.

To improve the efficiency further, we have evaluated the doped octasubstituted MPCs HTMs in perovskite solar cells containing a different perovskite composition. The double cation perovskite (FAMAPb(IBr)) was integrated into the following device structure: FTO/c-TiO<sub>2</sub>/ SnO<sub>2</sub>/PCBM/perovskite/HTM/Au. The solid-state ionization potential of the double cation perovskite layer was extracted from UPS measurements. The work function, the energy-cut off, and the ionization potential are presented in Appendix E Figure E.20 and Table E.8. It can be observed that the energy level of the double cation perovskite is -5.75 eV, slightly deeper than the triple cation perovskite. The *J-V* curves for the best performing device with double cation perovskite are shown in Figure

8.4d. The corresponding device parameters necessary for a deeper analysis of the photovoltaic parameters are shown in Table 1. The same efficiency trend can be observed for double cation than for triple cation perovskite (see Figure 8.4d, Table 8.1). The reference device employed **spiro-OMeTAD** as HTM showed the highest efficiency with a PCE of 21.30%. **Zn-BL54** provided the best results in the **BL**-series with a PCE of 20.18%, followed by **Cu-BL57** (16.00%), both featuring *n*-butoxy chains. The two HTMs characterized by the presence of bulkier 2-ethylhexyloxy chains, **Cu-BL61** (15.91%) and **Zn-BL58** (15.34%), provided lower PCE values than **Zn-BL54** and **Cu-BL57**.

The  $J_{sc}$  value for the double cation devices is higher than triple cation devices. This might be due to the better crystallization of the perovskite, influenced positively by adding MAI into the solution.<sup>[381]</sup> Several reports stated before that the addition of MAI into the perovskite solution leads to a better morphology and crystallinity, resulting in better photophysical properties leading to higher efficiency.<sup>[381-383]</sup>

However, the same trend for the  $J_{sc}$  values is observed with the triple cation perovskite devices. The exchange of the coordination metal Zn(II) to Cu(II) reduces the  $J_{sc}$ , and the addition of longer alkoxy chains reduces the  $J_{sc}$  even further. The  $J_{sc}$  is the highest for **Zn-BL54** ( $-23.87 \text{ mA cm}^{-2}$ ), followed by **Cu-BL57** ( $-23.00 \text{ mA cm}^{-2}$ ). The substitution of the *n*-butoxy with 2-ethylhexyloxy chains leads to lower  $J_{sc}$  values for **Zn-BL68** ( $J_{sc} = -22.12 \text{ mA cm}^{-2}$ ) and **Cu-BL61** ( $J_{sc} = -22.57 \text{ mA cm}^{-2}$ ). The reference cell containing **spiro-OMeTAD** exhibits a  $V_{oc}$  value of 1.09 V, the highest one, while the cells containing the BL HTM series **Zn-BL54**, **Cu-BL57**, **Zn-BL58**, and **Cu-BL61** exhibit lower  $V_{oc}$  values (1.07, 0.94, 0.95, and 0.94 V, respectively). The small changes observed in  $V_{oc}$  values between the different HTMs can be attributed to differences in the energy alignment between perovskite and the HTM.

The influence of the MPCs at the rear part of the device is again observed in the corresponding EQE spectra (Appendix E, Figure E.21). The EQE reveals the same trend and features described before for the triple cation. The EQE and the integrated  $J_{sc}$  values are slightly higher than the triple cation, resulting in the different perovskite



compositions. The maximum power point tracking (MPPT) for the 90s was preliminary data for their device stability. Despite the substantial increase in performance, we observe lower stability for the double cation devices compared to the triple cation ones (see the comparison in Appendix E, Figure E.22). This shows that there is a trade-off between high efficiency and long-stability, where the perovskite and HTM both play an important role. To further enhance the whole device performance in terms of efficiency and stability, special attention must be paid to both materials, perovskite composition, and MPcs HTM.

### 1.21 Conclusion

In summary, we have reported four new metal phthalocyanines, incorporating either Zn(II) or Cu(II) with *n*-butoxy or 2-ethylhexyloxy side chains used as HTMs in perovskite solar cells. We found that the coordinated transition metal cation is not only driving the differences in device performance. The steric hindrance of the alkoxy side chain is the factor that primarily determines the properties of the HTMs and the device performance. Our result demonstrates that the nature of the alkoxy side chains affects HTM properties. These influence charge carrier transport and recombination at the interface. Two device architectures were tested, and their advantages and disadvantages were evaluated. A more stable device could be obtained using the triple cation perovskite, maintaining 80% of its original PCE until 20 h of illumination but reaching only 13.85%. Changing the perovskite composition resulted in a PCE of 20.18% for the best performing HTM, **Zn-BL54**, while exhibiting lower device stability.



## Conclusions and Outlook

The main goal of my thesis was to work first on solving the main challenges of vacuum deposition for the fabrication of highly reproducible perovskite solar cells. As a relatively unexplored method in PSCs, extensive research could not be reported due to a small evaporation community.

In my first work, I focused on understanding if the reproducibility of the evaporation process itself could be optimized. Therefore, two different parameters were investigated: First, the evaporation speed by understanding how it influences the perovskite crystallization, and second, the influence of the underlayer on the perovskite composition and its electronic properties. My research could show that the evaporation speed substantially influences the perovskite crystallization and orientation. I could also highlight that the composition and perovskite growth differ depending on the underlayer, which influences the optoelectronic properties of the perovskite layers.

Vacuum deposition especially, when considering multi-source deposition, has the disadvantage that all precursor materials have to be individually calibrated, and several layer depositions with different perovskite ratios are needed before reaching a working perovskite layer. Another disadvantage is that slight changes in evaporation rate between the precursors lead to changes in the composition. I, therefore, chose a different approach in this project to simplify these challenges. Pre-synthesized perovskite materials (FAPbI<sub>3</sub> and CsFAPbI<sub>3</sub>) were evaporated from a single source. In this work, I demonstrated the feasibility of the direct evaporation of  $\alpha$ -phase CsFAPbI<sub>3</sub> without any addition of additives or post-annealing treatment. I could also demonstrate that  $\alpha$ -phase FAPbI<sub>3</sub> was formed after a short annealing process. A Series of structural and optoelectronic investigations were carried out to optimize the phase purity and storage stability of the thin films. Furthermore, we probed the perovskite layer compatibility with various underlayers, and we noted the organic underlayer displayed superiority over the metal oxide layer, suggesting its suitability of *p-i-n* devices over the *n-i-p*

Next, I moved in my thesis more towards understanding more profound interface engineering of vacuum-deposited perovskite solar cells. I choose to work with commonly integrated state-of-the-art charge transport layers and to investigate the charge transport processes at the interface.

In my first work on understanding the influence of interfaces, I focused on the commonly integrated electron-transporting materials  $C_{60}$  and  $cTiO_2$ . The goal of this study was to understand on a deeper level the charge transport processes when these two layers are employed in the solar cell. Impedance Spectroscopy was performed to help get more profound insight. A synergetic effect between  $cTiO_2$  and  $C_{60}$  when extracting the charges was found. Additionally, an optimal thickness of  $C_{60}$  was proven to be essential for enhancing the device's performance.

In my next work, I investigated the influence of the dopants Li-TFSI and Co-TFSI, typically employed in the spin-coated spiro-OMeTAD HTM layer. Interestingly, I found that the TFSI anion is migrating through the grain boundaries to the surface of the perovskite layers when employed in a *p-i-n* configuration. A passivation effect could be attributed to the TFSI anion on the surface of the perovskite layer, leading to better device performance and improved stability.

After focusing on the interface engineering of the state-of-the-art hole and electron-transporting materials, I moved my research towards exploring a new HTM material family, which could be explored further to improve the long-term stability of spin-coated perovskite devices. Spiro-OMeTAD is commonly used as the state-of-the-art hole-transporting material, even though it is widely known to be expensive due to its low synthesis yields and poor stability in long-term stability experiments. Finding a comparable performing different class of HTMs is attractive, mainly when they can be produced at low cost and show good stability.

I consequently expanded my work towards Zn (II) and Cu (II) complexes of phthalocyanines functionalized with butyl or 2-ethylhexyl side chains. The four different HMTs were compared by metalcore and by their functionalization. Surprisingly, we

found that the coordinated transition metal cation is not only driving the differences in device performance. Still, the steric hindrance of the alkoxy side chain is the factor that primarily determines the properties of the HTMs and the device performance. Our result demonstrates that the nature of the alkoxy side chains influences the molecular packing of the HTMs, which results in direct consequences in the charge carrier transport and charge recombination at the interface. It could be found that the best performing HTM was BL 54, which incorporated the Zn (II) as coordination metal and butyl functionalization. Two device architectures were tested, and their advantages and disadvantages were evaluated. A more stable device could be obtained using the triple cation perovskite, maintaining 80% of its original PCE until 20 h of illumination but reaching only 13.85%. Changing the perovskite composition could achieve a much higher PCE of 20.18% for the best performing HTM Zn-BL54, exhibiting much lower device stability.

To summarize, I have extensively investigated first the thermal-evaporation process and second the reasons behind the improvement of photovoltaic performance and stability of PSCs by interface engineering.

Nevertheless, when considering the vacuum-deposition method as the primary method for commercialization, different challenges need to be solved. At the moment, the community does not know the exact composition of the evaporated perovskite films, as one of the components is organic in nature which is unstable under certain measuring conditions, making it difficult to be quantified. Hence, other optical and crystallographic techniques are used for its characterization and compositional identification. However, an analytical method where the composition could be easily and precisely analyzed would make a difference in the community. When considering interface engineering and charge-transport layers for fully evaporated perovskite solar cells, the topic of additives should be explored further. Additives highly improve solution-processed films and could therefore also improve the vacuum-deposited perovskite layers. Therefore, understanding which small organic molecules could be co-evaporated during the

perovskite deposition for passivation of defects would be great in moving one step close towards commercialization.

Additionally, more research efforts should be conducted in the field of charge-transport layers. So far only very few well-working combinations of sublimable/evaporated/vacuum-deposited charge transport layers are known. Exploring other options that might have already found application in the field evaporated organic devices such as OLEDs could be interesting. Despite the challenges that still need to be solved on commercializing perovskite solar cells, I believe that the work carried out in this thesis gives a fundamental understanding of the intelligent fabrication methods necessary to design high performance, stable performance, and low costs PSCs.

# References

- [1] J. Hawks, K. Hunley, S. H. Lee, M. Wolpoff, *Mol. Biol. Evol.* **2000**, *17*, 2–22.
- [2] B. R. Mitchell, *International Historical Statistics*, Palgrave Macmillan UK, London, **1998**.
- [3] E. Sugawara, H. Nikaido, *Antimicrob. Agents Chemother.* **2014**, *58*, 7250–7257.
- [4] “Climate change widespread, rapid, and intensifying – IPCC,” can be found under <https://www.ipcc.ch/2021/08/09/ar6-wg1-20210809-pr/>, visited 10.11.2021.
- [5] U.S. Global Change Research Program, *U.S. Glob. Chang. Res. Progr.* **2018**, *1*, 470.
- [6] “Energy consumption in Switzerland,” can be found under <https://www.worlddata.info/europe/switzerland/energy-consumption.php>, visited 15.11.2021.
- [7] “Do Swiss roofs have the potential to produce over 80% of the country’s electricity? — Born to Engineer,” can be found under <https://www.borntoengineer.com/do-swiss-roofs-have-the-potential-to-produce-over-80-of-the-countrys-electricity>, 15.12.2021.
- [8] C. F. Ropelewski, P. A. Arkin, *Climate Analysis*, Cambridge University Press, Cambridge, **2019**.
- [9] A. Smets, K. Jäger, I. Olindo, R. Van Swaaij, M. Zeman, *Solar Energy The Physics and Engineering of Photovoltaic Conversion Technologies and Systems*, UIT Cambridge Ltd, Cambridge, **2016**.
- [10] “NREL Research Cell Record Efficiency Chart,” can be found under [http://www.nrel.gov/pv/assets/images/efficiency\\_chart.jpg](http://www.nrel.gov/pv/assets/images/efficiency_chart.jpg), 15.10.2021..
- [11] D. M. Chapin, C. S. Fuller, G. L. Pearson, *J. Appl. Phys.* **1954**, *25*, 676–677.
- [12] P. R. I. F. O. R. S. E. S. ISE, “Photovoltaics Report,” can be found under <https://www.ise.fraunhofer.de/en/press-media/press-releases/2021/photovoltaics-report-delivers-facts-about-solar-energy->

worldwide.html, 11.11.2021.

- [13] S. R. Wenham, M. a Green, *Prog. Photovolt Res. Appl.* **1996**, *4*, 3–33.
- [14] P. K. Nayak, S. Mahesh, H. J. Snaith, D. Cahen, *Nat. Rev. Mater.* **2019**, *4*, 269–285.
- [15] J. Jeong, M. Kim, J. Seo, H. Lu, P. Ahlawat, A. Mishra, Y. Yang, M. A. Hope, F. T. Eickemeyer, M. Kim, et al., *Nature* **2021**, *592*, 381–385.
- [16] M. I. H. Ansari, A. Qurashi, M. K. Nazeeruddin, *J. Photochem. Photobiol. C Photochem. Rev.* **2018**, *35*, 1–24.
- [17] Z. Saki, M. M. Byranvand, N. Taghavinia, M. Kedia, M. Saliba, *Energy Environ. Sci.* **2021**, *14*, 5690–5722.
- [18] G. Kim, S. An, S. K. Hyeong, S. K. Lee, M. Kim, N. Shin, *Chem. Mater.* **2019**, *31*, 8212–8221.
- [19] G. Lee, M. C. Kim, Y. W. Choi, N. Ahn, J. Jang, J. Yoon, S. M. Kim, J. G. Lee, D. Kang, H. S. Jung, et al., *Energy Environ. Sci.* **2019**, *12*, 3182–3191.
- [20] X. Hu, F. Li, Y. Song, *ACS Energy Lett.* **2019**, *4*, 1065–1072.
- [21] H. Wang, H. A. Dewi, T. M. Koh, A. Bruno, S. Mhaisalkar, N. Mathews, *ACS Appl. Mater. Interfaces* **2020**, *12*, 484–493.
- [22] A. J. Bett, K. M. Winkler, M. Bivour, L. Cojocar, Ö. Kabakli, P. S. C. Schulze, G. Siefert, L. Tutsch, M. Hermle, S. W. Glunz, et al., *ACS Appl. Mater. Interfaces* **2019**, *11*, 45796–45804.
- [23] M. Batmunkh, Y. L. Zhong, H. Zhao, *Adv. Mater.* **2020**, *32*, 2000631.
- [24] A. Roy, A. Ghosh, S. Bhandari, S. Sundaram, T. K. Mallick, *Buildings* **2020**, *10*, 1–33.
- [25] H. Lin, C. Zhou, Y. Tian, T. Siegrist, B. Ma, *ACS Energy Lett.* **2018**, *3*, 54–62.



- [26] P. P. Boix, S. Agarwala, T. M. Koh, N. Mathews, S. G. Mhaisalkar, *J. Phys. Chem. Lett.* **2015**, *6*, 898–907.
- [27] B. Saparov, D. B. Mitzi, *Chem. Rev.* **2016**, *116*, 4558–4596.
- [28] G. E. Eperon, S. D. Stranks, C. Menelaou, M. B. Johnston, L. M. Herz, H. J. Snaith, *Energy Environ. Sci.* **2014**, *7*, 982–988.
- [29] T. Miyasaka, A. Kojima, K. Teshima, Y. Shirai, *J. Am. Chem. Soc.* **2009**, *131*, 6050–6051.
- [30] H. S. Kim, C. R. Lee, J. H. Im, K. B. Lee, T. Moehl, A. Marchioro, S. J. Moon, R. Humphry-Baker, J. H. Yum, J. E. Moser, et al., *Sci. Rep.* **2012**, *2*, 1–7.
- [31] Woon Seok Yang, Byung-Wook Park, Eui Hyuk Jung, Nam Joong Jeon, Young Chan Kim, Dong Uk Lee, Seong Sik Shin, Jangwon Seo, Eun Kyu Kim, Jun Hong Noh, et al., *Science (80-. )*. **2017**, *356*, 1376–1379.
- [32] C. C. Stoumpos, C. D. Malliakas, M. G. Kanatzidis, *Inorg. Chem.* **2013**, *52*, 9019–9038.
- [33] V. M. Goldschmidt, *Naturwissenschaften* **1926**, *14*, 477–485.
- [34] L. Liang, L. Wencong, C. Nianyi, *J. Phys. Chem. Solids* **2004**, *65*, 855–860.
- [35] W. Travis, E. N. K. Glover, H. Bronstein, D. O. Scanlon, R. G. Palgrave, *Chem. Sci.* **2016**, *7*, 4548–4556.
- [36] G. Kieslich, S. Sun, A. K. Cheetham, *Chem. Sci.* **2014**, *5*, 4712–4715.
- [37] G. Kieslich, S. Sun, A. K. Cheetham, *Chem. Sci.* **2015**, *6*, 3430–3433.
- [38] P. S. Whitfield, N. Herron, W. E. Guise, K. Page, Y. Q. Cheng, I. Milas, M. K. Crawford, *Sci. Rep.* **2016**, *6*, 1–16.
- [39] S. D. Stranks, S. D. Stranks, G. E. Eperon, G. Grancini, C. Menelaou, M. J. P. Alcocer, T. Leijtens, L. M. Herz, A. Petrozza, H. J. Snaith, *Science (80-. )*. **2013**, *342*,

341–344.

- [40] V. Gonzalez-pedro, E. J. Juarez-perez, W. Arsyad, E. M. Barea, F. Fabregat-santiago, I. Mora-sero, J. Bisquert, *Nano Lett.* **2014**, *14*, 888–893.
- [41] W. J. Yin, T. Shi, Y. Yan, *Adv. Mater.* **2014**, *26*, 4653–4658.
- [42] D. Shi, V. Adinolfi, R. Comin, M. Yuan, E. Alarousu, A. Buin, Y. Chen, S. Hoogland, A. Rothenberger, K. Katsiev, et al., *Science (80-. )*. **2015**, *347*, 519–522.
- [43] Q. Dong, Y. Fang, Y. Shao, P. Mulligan, J. Qiu, L. Cao, J. Huang, *Science (80-. )*. **2015**, *347*, 967–970.
- [44] A. Kojima, K. Teshima, Y. Shirai, T. Miyasaka, *J. Am. Chem. Soc.* **2009**, *131*, 6050–6051.
- [45] J. P. Correa-Baena, M. Saliba, T. Buonassisi, M. Grätzel, A. Abate, W. Tress, A. Hagfeldt, *Science (80-. )*. **2017**, *358*, 739–744.
- [46] M. Saliba, T. Matsui, J. Y. Seo, K. Domanski, J. P. Correa-Baena, M. K. Nazeeruddin, S. M. Zakeeruddin, W. Tress, A. Abate, A. Hagfeldt, et al., *Energy Environ. Sci.* **2016**, *9*, 1989–1997.
- [47] N. J. Jeon, J. H. Noh, Y. C. Kim, W. S. Yang, S. Ryu, S. Il Seok, *Nat. Mater.* **2014**, *13*, 897–903.
- [48] S. Ma, X. Liu, X. Zhang, R. Ghadari, Y. Ding, M. Cai, S. Dai, *Chem. Commun.* **2020**, *56*, 14471–14474.
- [49] M. M. Byranvand, M. Saliba, *Matter* **2021**, *4*, 1758–1759.
- [50] J. Ye, M. M. Byranvand, C. O. Martínez, R. L. Z. Hoye, M. Saliba, L. Polavarapu, *Angew. Chemie - Int. Ed.* **2021**, *60*, 21636–21660.
- [51] H. Kanda, N. Shibayama, A. Huckaba, Y. Lee, S. Paek, N. Klipfel, C. Roldán Carmona, V. I. E. Queloz, G. Grancini, Y. Zhang, et al., *Energy Environ. Sci.* **2019**,

- 1–502.
- [52] M. Abuhelaiqa, S. Paek, Y. Lee, K. T. Cho, S. Heo, E. Oveisi, A. J. Huckaba, H. Kanda, H. Kim, Y. Zhang, et al., *Energy Environ. Sci.* **2019**, *12*, 1910–1917.
- [53] W. Zhang, J. Song, D. Wang, K. Deng, J. Wu, L. Zhang, *J. Mater. Chem. C* **2018**, *6*, 13034–13042.
- [54] W. Nie, H. Tsai, R. Asadpour, A. J. Neukirch, G. Gupta, J. J. Crochet, M. Chhowalla, S. Tretiak, M. A. Alam, H. Wang, **2015**, *347*, 522–526.
- [55] F. Brivio, A. B. Walker, A. Walsh, *APL Mater.* **2013**, *1*, 1–5.
- [56] T. Forsyth, *Int. Encycl. Geogr.* **2009**, 2163–2157.
- [57] L. Zhang, W. Geng, C. J. Tong, X. Chen, T. Cao, M. Chen, *Sci. Rep.* **2018**, *8*, 1–9.
- [58] C. C. Stoumpos, M. G. Kanatzidis, *Acc. Chem. Res.* **2015**, *48*, 2791–2802.
- [59] Z. Saki, M. M. Byranvand, N. Taghavinia, M. Kedia, M. Saliba, *Energy Environ. Sci.* **2021**.
- [60] K. L. Gardner, J. G. Tait, T. Merckx, W. Qiu, U. W. Paetzold, L. Kootstra, M. Jaysankar, R. Gehlhaar, D. Cheyns, P. Heremans, et al., *Adv. Energy Mater.* **2016**, *6*, 1–8.
- [61] Y. Vaynzof, *Adv. Energy Mater.* **2020**, *10*, 202003073.
- [62] L. Zeng, S. Chen, K. Forberich, C. J. Brabec, Y. Mai, F. Guo, *Energy Environ. Sci.* **2020**, *13*, 4666–4690.
- [63] J. Burschka, N. Pellet, S. J. Moon, R. Humphry-Baker, P. Gao, M. K. Nazeeruddin, M. Grätzel, *Nature* **2013**, *499*, 316–319.
- [64] S. Shahbazi, M. Malekshahi Byranvand, F. Tajabadi, S. Afshar, N. Taghavinia, *ChemPhysChem* **2016**, 2389–2394.

- [65] N. Ahn, D. Y. Son, I. H. Jang, S. M. Kang, M. Choi, N. G. Park, *J. Am. Chem. Soc.* **2015**, *137*, 8696–8699.
- [66] M. Xiao, F. Huang, W. Huang, Y. Dkhissi, Y. Zhu, J. Etheridge, A. Gray-Weale, U. Bach, Y. B. Cheng, L. Spiccia, *Angew. Chemie - Int. Ed.* **2014**, *53*, 9898–9903.
- [67] M. Liu, M. B. Johnston, H. J. Snaith, *Nature* **2013**, *501*, 395–398.
- [68] A. W. Lu, C., Czanderna, *Applications of Piezoelectric Quartz Crystal Microbalances*, Elsevier Science Publishers B.V., Amsterdam, **1984**.
- [69] D. N. Ariel-Sternberg, **2017**.
- [70] F. Fu, L. Kranz, S. Yoon, J. Löckinger, T. Jäger, J. Perrenoud, T. Feuerer, C. Gretener, S. Buecheler, A. N. Tiwari, *Phys. status solidi* **2015**, *212*, 2708–2717.
- [71] J. C. S. Costa, J. Azevedo, L. M. N. B. F. Santos, A. Mendes, *J. Phys. Chem. C* **2017**, *121*, 2080–2087.
- [72] O. Malinkiewicz, A. Yella, Y. H. Lee, G. M. Espallargas, M. Graetzel, M. K. Nazeeruddin, H. J. Bolink, *Nat. Photonics* **2014**, *8*, 128–132.
- [73] M. Era, T. Taira, T. Tsutsui, *Shinku/Journal Vac. Soc. Japan* **1996**, *39*, 598–602.
- [74] M. H. Abib, J. Li, H. Yang, M. Wang, T. Chen, E. Enzexu, Y. Jiang, *RSC Adv.* **2021**, *11*, 3380–3389.
- [75] O. Malinkiewicz, A. Yella, Y. H. Lee, G. M. Espallargas, M. Graetzel, M. K. Nazeeruddin, H. J. Bolink, *Nat. Photonics* **2014**, *8*, 128–132.
- [76] C. Roldán-Carmona, O. Malinkiewicz, A. Soriano, G. Mínguez Espallargas, A. Garcia, P. Reinecke, T. Kroyer, M. I. Dar, M. K. Nazeeruddin, H. J. Bolink, *Energy Environ. Sci.* **2014**, *7*, 994–997.
- [77] D. Yang, Z. Yang, W. Qin, Y. Zhang, S. Liu, C. Li, *J. Mater. Chem. A* **2015**, *3*, 9401–9405.

- [78] C. Momblona, L. Gil-Escrig, E. Bandiello, E. M. Hutter, M. Sessolo, K. Lederer, J. Blochwitz-Nimoth, H. J. Bolink, *Energy Environ. Sci.* **2016**, *9*, 3456–3463.
- [79] S. Olthof, K. Meerholz, *Sci. Rep.* **2017**, *7*, 1–10.
- [80] N. Droseros, G. Longo, J. C. Brauer, M. Sessolo, H. J. Bolink, N. Banerji, *ACS Energy Lett.* **2018**, *3*, 1458–1466.
- [81] A. M. Igual-Muñoz, J. Ávila, P. P. Boix, H. J. Bolink, *Sol. RRL* **2020**, *4*, 1–5.
- [82] C. Momblona, H. Kanda, A. A. Sutanto, M. Mensi, C. Roldán-Carmona, M. K. Nazeeruddin, *Sci. Rep.* **2020**, *10*, 1–8.
- [83] Y. H. Chiang, M. Anaya, S. D. Stranks, *ACS Energy Lett.* **2020**, *5*, 2498–2504.
- [84] J. Li, H. Wang, X. Y. Chin, H. A. Dewi, K. Vergeer, T. W. Goh, J. W. M. Lim, J. H. Lew, K. P. Loh, C. Soci, et al., *Joule* **2020**, *4*, 1035–1053.
- [85] J. Li, H. A. Dewi, H. Wang, J. Zhao, N. Tiwari, N. Yantara, T. Malinauskas, V. Getautis, T. J. Savenije, N. Mathews, et al., *Adv. Funct. Mater.* **2021**, *31*, 2103252.
- [86] S. Sun, T. Salim, N. Mathews, M. Duchamp, C. Boothroyd, G. Xing, T. C. Sum, Y. M. Lam, *Energy Environ. Sci.* **2014**, *7*, 399–407.
- [87] C. R. Dong, Y. Wang, K. Zhang, H. Zeng, *EnergyChem* **2020**, *2*, 100026.
- [88] S. Hubbard, in *Photovoltaic Sol. Energy*, **2016**, pp. 39–46.
- [89] G. Landi, H. C. Neitzert, C. Barone, C. Mauro, F. Lang, S. Albrecht, B. Rech, S. Pagano, *Adv. Sci.* **2017**, *4*.
- [90] G. J. A. H. Wetzelaer, M. Scheepers, A. M. Sempere, C. Momblona, J. Ávila, H. J. Bolink, *Adv. Mater.* **2015**, *27*, 1837–1841.
- [91] D. Luo, R. Su, W. Zhang, Q. Gong, R. Zhu, *Nat. Rev. Mater.* **2020**, *5*, 44–60.
- [92] J. Chen, N. G. Park, *Adv. Mater.* **2019**, *31*.

- [93] L. M. Pazos-Outón, T. P. Xiao, E. Yablonovitch, *J. Phys. Chem. Lett.* **2018**, *9*, 1703–1711.
- [94] J. Huang, Y. Yuan, Y. Shao, Y. Yan, *Nat. Rev. Mater.* **2017**, *2*, 17042.
- [95] T. Bin Song, Q. Chen, H. Zhou, C. Jiang, H. H. Wang, Y. M. Yang, Y. Liu, J. You, Y. Yang, *J. Mater. Chem. A* **2015**, *3*, 9032–9050.
- [96] H. He, Z. Yang, Y. Xu, A. T. Smith, G. Yang, L. Sun, *Nano Converg.* **2020**, *7*.
- [97] I. Hussain, H. P. Tran, J. Jaksik, J. Moore, N. Islam, M. J. Uddin, *Emergent Mater.* **2018**, *1*, 133–154.
- [98] H. J. H. Snaith, A. Abate, J. J. M. Ball, G. E. Eperon, T. Leijtens, N. K. Noel, S. D. Stranks, J. T.-W. Wang, K. Wojciechowski, W. Zhang, *J. Phys. Chem. Lett.* **2014**, *5*, 1511–1515.
- [99] T. Liu, K. Chen, Q. Hu, R. Zhu, Q. Gong, *Adv. Energy Mater.* **2016**, *6*, 1–17.
- [100] S. Li, Y. L. Cao, W. H. Li, Z. S. Bo, *Rare Met.* **2021**, *40*, 2712–2729.
- [101] D. Li, L. Chao, C. Chen, X. Ran, Y. Wang, T. Niu, S. Lv, H. Wu, Y. Xia, C. Ran, et al., *Nano Lett.* **2020**, *20*, 5799–5806.
- [102] H. Kim, S. U. Lee, D. Y. Lee, M. J. Paik, H. Na, J. Lee, S. Il Seok, *Adv. Energy Mater.* **2019**, *9*, 1–8.
- [103] D. Bogachuk, S. Zouhair, K. Wojciechowski, B. Yang, V. Babu, L. Wagner, B. Xu, J. Lim, S. Mastroianni, H. Pettersson, et al., *Energy Environ. Sci.* **2020**, *13*, 3880–3916.
- [104] M. Saliba, L. Etgar, *ACS Energy Lett.* **2020**, *5*, 2886–2888.
- [105] F. H. Alharbi, S. Kais, *Renew. Sustain. Energy Rev.* **2015**, *43*, 1073–1089.
- [106] J. Li, H. L. Cao, W. Bin Jiao, Q. Wang, M. Wei, I. Cantone, J. Lü, A. Abate, *Nat. Commun.* **2020**, *11*, 1–5.

- [107] A. L. Wani, A. Ara, J. A. Usmani, *Interdiscip. Toxicol.* **2015**, *8*, 55–64.
- [108] V. K. Ravi, B. Mondal, V. V Nawale, A. Nag, *ACS Omega* **2020**, *5*, 29631–29641.
- [109] M. Pantaler, K. T. Cho, V. I. E. Queloz, I. García Benito, C. Fettkenhauer, I. Anusca, M. K. Nazeeruddin, D. C. Lupascu, G. Grancini, *ACS Energy Lett.* **2018**, *3*, 1781–1786.
- [110] C. Wu, Q. Zhang, Y. Liu, W. Luo, X. Guo, Z. Huang, H. Ting, W. Sun, X. Zhong, S. Wei, et al., **2018**, *1700759*, 2–9.
- [111] J. Xu, J. B. Liu, B. X. Liu, B. Huang, *J. Phys. Chem. Lett.* **2017**, *8*, 4391–4396.
- [112] F. Aslam, B. Sabir, M. Hassan, *Appl. Phys. A Mater. Sci. Process.* **2021**, *127*, 1–12.
- [113] C. Momblona, H. Kanda, A. A. Sutanto, M. Mensi, C. Roldán-Carmona, M. K. Nazeeruddin, *Sci. Rep.* **2020**, *10*, 1–8.
- [114] T. Krishnamoorthy, H. Ding, C. Yan, W. L. Leong, T. Baikie, Z. Zhang, M. Sherburne, S. Li, M. Asta, N. Mathews, et al., *J. Mater. Chem. A* **2015**, *3*, 23829–23832.
- [115] I. Kopacic, B. Friesenbichler, S. F. Hoefler, B. Kunert, H. Plank, T. Rath, G. Trimmel, *ACS Appl. Energy Mater.* **2018**, *1*, 343–347.
- [116] E. Jokar, P. Y. Cheng, C. Y. Lin, S. Narra, S. Shahbazi, E. Wei-Guang Diao, *ACS Energy Lett.* **2021**, *6*, 485–492.
- [117] W. Ke, M. G. Kanatzidis, *Nat. Commun.* **2019**, *10*, 1–4.
- [118] G. Schileo, G. Grancini, *J. Mater. Chem. C* **2021**, *9*, 67–76.
- [119] A. J. Huckaba, D. T. Sun, A. A. Sutanto, M. Mensi, Y. Zhang, W. L. Queen, M. K. Nazeeruddin, **2020**, *2000239*, 1–6.
- [120] Y. Jiang, L. Qiu, E. J. Juarez-Perez, L. K. Ono, Z. Hu, Z. Liu, Z. Wu, L. Meng, Q. Wang, Y. Qi, *Nat. Energy* **2019**, *4*, 585–593.

- [121] “Gold price,” can be found under <https://goldprice.org/>,10.01.2022..
- [122] J. P. Bastos, S. Manghooli, M. Jaysankar, J. G. Tait, W. Qiu, R. Gehlhaar, M. De Volder, G. Uytterhoeven, J. Poortmans, U. W. Paetzold, *Appl. Phys. Lett.* **2017**, *110*, 233902.
- [123] J. W. Lee, D. H. Kim, H. S. Kim, S. W. Seo, S. M. Cho, N. G. Park, *Adv. Energy Mater.* **2015**, *5*, 1501310.
- [124] J. Borchert, R. L. Milot, J. B. Patel, C. L. Davies, A. D. Wright, L. Martínez Maestro, H. J. Snaith, L. M. Herz, M. B. Johnston, *ACS Energy Lett.* **2017**, *2*, 2799–2804.
- [125] W. Qiu, M. Buffière, G. Brammertz, U. W. Paetzold, L. Froyen, P. Heremans, D. Cheyns, *Org. Electron.* **2015**, *26*, 30–35.
- [126] T. Leijtens, G. E. Eperon, S. Pathak, A. Abate, M. M. Lee, H. J. Snaith, *Nat. Commun.* **2013**, *4*, 1–8.
- [127] K. Domanski, J. P. Correa-Baena, N. Mine, M. K. Nazeeruddin, A. Abate, M. Saliba, W. Tress, A. Hagfeldt, M. Grätzel, *ACS Nano* **2016**, *10*, 6306–6314.
- [128] Y. Deng, Q. Dong, C. Bi, Y. Yuan, J. Huang, *Adv. Energy Mater.* **2016**, *6*, 1–6.
- [129] Y. Kato, L. K. Ono, M. V Lee, S. Wang, S. R. Raga, Y. Qi, *Adv. Mater. Interfaces* **2015**, *2*, 2–7.
- [130] T. Leijtens, K. Bush, R. Cheacharoen, R. Beal, A. Bowring, M. D. McGehee, *J. Mater. Chem. A* **2017**, *5*, 11483–11500.
- [131] H. Zhang, J. Xiao, J. Shi, H. Su, Y. Luo, D. Li, H. Wu, Y. B. Cheng, Q. Meng, *Adv. Funct. Mater.* **2018**, *28*, 1802985.
- [132] K. Rakstys, C. Igci, M. K. Nazeeruddin, *Chem. Sci.* **2019**, *10*, 6748–6769.
- [133] W. S. Yang, J. H. Noh, N. J. Jeon, Y. C. Kim, S. Ryu, J. Seo, S. Il Seok, *Science* (80-.). **2015**, *348*, 1234–1237.



- 
- [134] G. W. Kim, H. Choi, M. Kim, J. Lee, S. Y. Son, T. Park, *Adv. Energy Mater.* **2020**, *10*, 1–30.
- [135] T. P. I. Saragi, T. Spehr, A. Siebert, T. Fuhrmann-Lieker, J. Salbeck, *Chem. Rev.* **2007**, *107*, 1011–1065.
- [136] J. Salbeck, N. Yu, J. Bauer, F. Weissörtel, H. Bestgen, *Synth. Met.* **1997**, *91*, 209–215.
- [137] S. Kundu, T. L. Kelly, *EcoMat* **2020**, *2*, 1–22.
- [138] H. Uoyama, K. Goushi, K. Shizu, H. Nomura, C. Adachi, *Nature* **2012**, *492*, 234–238.
- [139] G. E. Eperon, S. D. Stranks, C. Menelaou, M. B. Johnston, L. M. Herz, H. J. Snaith, *Energy Environ. Sci.* **2014**, *7*, 982.
- [140] T. M. Koh, K. Fu, Y. Fang, S. Chen, T. C. Sum, N. Mathews, S. G. Mhaisalkar, P. P. Boix, T. Baikie, *J. Phys. Chem. C* **2014**, *118*, 16458–16462.
- [141] N. Klipfel, C. Momblona, H. Kanda, N. Shibayama, Y. Nakamura, M. D. Mensi, C. Liu, C. Roldán-Carmona, M. K. Nazeeruddin, *Sol. RRL* **2021**, 2100191.
- [142] T. Liu, Y. Zong, Y. Zhou, M. Yang, Z. Li, O. S. Game, K. Zhu, R. Zhu, Q. Gong, N. P. Padture, *Chem. Mater.* **2017**, *29*, 3246–3250.
- [143] Y. Zhang, S. G. Kim, D. K. Lee, N. G. Park, *ChemSusChem* **2018**, *11*, 1813–1823.
- [144] B. Wang, L. Xue, S. Wang, Y. Li, L. Zang, H. Liu, Z. Zhang, Y. Li, *Appl. Phys. Lett.* **2021**, *119*, 133904.
- [145] M. Saliba, T. Matsui, J. Y. Seo, K. Domanski, J. P. Correa-Baena, M. K. Nazeeruddin, S. M. Zakeeruddin, W. Tress, A. Abate, A. Hagfeldt, et al., *Energy Environ. Sci.* **2016**, *9*, 1989–1997.
- [146] M. Saliba, T. Matsui, K. Domanski, J. Y. Seo, A. Ummadisingu, S. M. Zakeeruddin, J. P. Correa-Baena, W. R. Tress, A. Abate, A. Hagfeldt, et al., *Science (80-. )*. **2016**,

354, 206–209.

- [147] M. Kim, A. Alfano, G. Perotto, M. Serri, N. Dengo, A. Mezzetti, S. Gross, M. Prato, M. Salerno, A. Rizzo, et al., *Commun. Mater.* **2021**, *2*, 1–12.
- [148] J. Liu, Y. Wu, C. Qin, X. Yang, T. Yasuda, A. Islam, K. Zhang, W. Peng, W. Chen, L. Han, *Energy Environ. Sci.* **2014**, *7*, 2963–2967.
- [149] Y. Liu, Q. Chen, H. S. Duan, H. Zhou, Y. Yang, H. Chen, S. Luo, T. Bin Song, L. Dou, Z. Hong, et al., *J. Mater. Chem. A* **2015**, *3*, 11940–11947.
- [150] L. Zheng, Y. H. Chung, Y. Ma, L. Zhang, L. Xiao, Z. Chen, S. Wang, B. Qu, Q. Gong, *Chem. Commun.* **2001**, *50*, 11196–11199.
- [151] W. Shockley, H. J. Queisser, *J. Appl. Phys.* **1961**, *32*, 510–519.
- [152] S. Rühle, *Sol. Energy* **2016**, *130*, 139–147.
- [153] H. J. Queisser, *Mater. Sci. Eng. B Solid-State Mater. Adv. Technol.* **2009**, *159–160*, 322–328.
- [154] L. Gu, D. Zhang, M. Kam, Q. Zhang, S. Poddar, Y. Fu, X. Mo, Z. Fan, *Nanoscale* **2018**, *10*, 15164–15172.
- [155] B. Wang, X. Xiao, T. Chen, *Nanoscale* **2014**, *6*, 12287–12297.
- [156] J. Kim, S. H. Lee, J. H. Lee, K. H. Hong, *J. Phys. Chem. Lett.* **2014**, *5*, 1312–1317.
- [157] S. D. Stranks, P. K. Nayak, W. Zhang, T. Stergiopoulos, H. J. Snaith, *Angew. Chemie - Int. Ed.* **2015**, *54*, 3240–3248.
- [158] R. S. Bonilla, B. Hoex, P. Hamer, P. R. Wilshaw, *Phys. Status Solidi Appl. Mater. Sci.* **2017**, *214*, 1700293.
- [159] J. Kim, A. Ho-Baillie, S. Huang, *Sol. RRL* **2019**, *3*, 1–16.
- [160] F. Gao, Y. Zhao, X. Zhang, J. You, *Adv. Energy Mater.* **2020**, *10*, 1902650.

- 
- [161] R. Vidal, J. A. Alberola-Borràs, S. N. Habisreutinger, J. L. Gimeno-Molina, D. T. Moore, T. H. Schloemer, I. Mora-Seró, J. J. Berry, J. M. Luther, *Nat. Sustain.* **2021**, *4*, 277–285.
- [162] N. G. Park, *Nat. Sustain.* **2021**, *4*, 192–193.
- [163] B. Dänekamp, C. Müller, M. Sendner, P. P. Boix, M. Sessolo, R. Lovrincic, H. J. Bolink, *J. Phys. Chem. Lett.* **2018**, *9*, 2770–2775.
- [164] J. Borchert, R. L. Milot, J. B. Patel, C. L. Davies, A. D. Wright, L. Martínez Maestro, H. J. Snaith, L. M. Herz, M. B. Johnston, *ACS Energy Lett.* **2017**, *2*, 2799–2804.
- [165] R. Swartwout, M. T. Hoerantner, V. Bulović, *Energy Environ. Mater.* **2019**, *2*, 119–145.
- [166] B. Dänekamp, C. Müller, M. Sendner, P. P. Boix, M. Sessolo, R. Lovrincic, H. J. Bolink, *J. Phys. Chem. Lett.* **2018**, *9*, 2770–2775.
- [167] C. Roldán-Carmona, O. Malinkiewicz, R. Betancur, G. Longo, C. Momblona, F. Jaramillo, L. Camacho, H. J. Bolink, *Energy Environ. Sci.* **2014**, *7*, 2968–2973.
- [168] R. Karlicek, C. C. Sun, G. Zissis, R. Ma, *Handb. Adv. Light. Technol.* **2017**, 1–1185.
- [169] M. Roß, S. Severin, M. B. Stutz, P. Wagner, H. Köbler, M. Favin-Lévêque, A. Al-Ashouri, P. Korb, P. Tockhorn, A. Abate, et al., *Adv. Energy Mater.* **2021**, *11*.
- [170] D. P. McMeekin, G. Sadoughi, W. Rehman, G. E. Eperon, M. Saliba, M. T. Höerantner, A. Haghighirad, N. Sakai, L. Korte, B. Rech, et al., *Science (80-. )*. **2016**, *351*, 151–155.
- [171] S. Liu, Y. Guan, Y. Sheng, Y. Hu, Y. Rong, A. Mei, H. Han, *Adv. Energy Mater.* **2020**, *10*, 1–28.
- [172] Y. Vaynzof, *Adv. Energy Mater.* **2020**, *10*, 2003073.
- [173] L. K. Ono, M. R. Leyden, S. Wang, Y. Qi, *J. Mater. Chem. A* **2016**, *4*, 6693–6713.

- [174] M. J. Bækbo, O. Hansen, I. Chorkendorff, P. C. K. Vesborg, *RSC Adv.* **2018**, *8*, 29899–29908.
- [175] D. A. Williams, Alice E., Holliman, Peter J., Carnie, Matthew J., Davies, Matthew L., Worsley, T. M. Watson, *J. Mater. Chem. A* **2014**, *2*, 19338–19346.
- [176] J. T. W. Wang, Z. Wang, S. Pathak, W. Zhang, D. W. Dequillettes, F. Wisnivesky-Rocca-Rivarola, J. Huang, P. K. Nayak, J. B. Patel, H. A. Mohd Yusof, et al., *Energy Environ. Sci.* **2016**, *9*, 2892–2901.
- [177] T. Li, Y. Pan, Z. Wang, Y. Xia, Y. Chen, W. Huang, *J. Mater. Chem. A* **2017**, *5*, 12602–12652.
- [178] Y. Wu, X. Yang, W. Chen, Y. Yue, M. Cai, F. Xie, E. Bi, A. Islam, L. Han, *Nat. Energy* **2016**, *1*, 16148.
- [179] K. B. Lohmann, J. B. Patel, M. U. Rothmann, C. Q. Xia, R. D. J. Oliver, L. M. Herz, H. J. Snaith, M. B. Johnston, *ACS Energy Lett.* **2020**, *5*, 710–717.
- [180] B. S. Kim, G. H. Moon, S. C. Park, J. Jang, Y. S. Kang, *Mater. Lett.* **2019**, *242*, 191–194.
- [181] X. Jiang, X. Fu, D. Ju, S. Yang, Z. Chen, X. Tao, *ACS Energy Lett.* **2020**, *5*, 1797–1803.
- [182] E. S. Parrott, J. B. Patel, A. A. Haghighirad, H. J. Snaith, M. B. Johnston, L. M. Herz, *Nanoscale* **2019**, *11*, 14276–14284.
- [183] M. Roß, L. Gil-Escrig, A. Al-Ashouri, P. Tockhorn, M. Jošt, B. Rech, S. Albrecht, *ACS Appl. Mater. Interfaces* **2020**, *12*, 39261–39272.
- [184] F. Gao, Y. Zhao, X. Zhang, J. You, *Adv. Energy Mater.* **2020**, *10*.
- [185] J. Y. Kim, J. W. Lee, H. S. Jung, H. Shin, N. G. Park, *Chem. Rev.* **2020**, *120*, 7867–7918.
- [186] A. R. Bin Mohd Yusoff, M. Vasilopoulou, D. G. Georgiadou, L. C. Palilis, A. Abate,

- M. K. Nazeeruddin, *Energy Environ. Sci.* **2021**, *14*, 2906–2953.
- [187] J. Chen, N. G. Park, *ACS Energy Lett.* **2020**, *5*, 2742–2786.
- [188] S. Yang, J. Dai, Z. Yu, Y. Shao, Y. Zhou, X. Xiao, X. C. Zeng, J. Huang, *J. Am. Chem. Soc.* **2020**, *142*, 11937–11938.
- [189] X. Zheng, J. Troughton, N. Gasparini, Y. Lin, M. Wei, Y. Hou, J. Liu, K. Song, Z. Chen, C. Yang, et al., *Joule* **2019**, *3*, 1963–1976.
- [190] D. Wei, F. Ma, R. Wang, S. Dou, P. Cui, H. Huang, J. Ji, E. Jia, X. Jia, S. Sajid, et al., *Adv. Mater.* **2018**, *30*.
- [191] B. Rivkin, P. Fassel, Q. Sun, A. D. Taylor, Z. Chen, Y. Vaynzof, *ACS Omega* **2018**, *3*, 10042–10047.
- [192] S. K. Pathak, A. Abate, P. Ruckdeschel, B. Roose, K. C. Gödel, Y. Vaynzof, A. Santhala, S. I. Watanabe, D. J. Hollman, N. Noel, et al., *Adv. Funct. Mater.* **2014**, *24*, 6046–6055.
- [193] Q. An, Q. Sun, A. Weu, D. Becker-Koch, F. Paulus, S. Arndt, F. Stuck, A. S. K. Hashmi, N. Tessler, Y. Vaynzof, *Adv. Energy Mater.* **2019**, *9*, 1901257.
- [194] J. Cao, B. Wu, R. Chen, Y. Wu, Y. Hui, B. W. Mao, N. Zheng, *Adv. Mater.* **2018**, *30*.
- [195] J. Chen, X. Zhao, S. G. Kim, N. G. Park, *Adv. Mater.* **2019**, *31*.
- [196] L. E. Polander, P. Pöhner, M. Schwarze, M. Saalfrank, C. Koerner, K. Leo, *APL Mater.* **2014**, *2*, 1–6.
- [197] D. Pérez-Del-Rey, L. Gil-Escrig, K. P. S. Zanoni, C. Dreessen, M. Sessolo, P. P. Boix, H. J. Bolink, *Chem. Mater.* **2019**, *31*, 6945–6949.
- [198] S. Kar, N. F. Jamaludin, N. Yantara, S. G. Mhaisalkar, W. L. Leong, *Recent Advancements and Perspectives on Light Management and High Performance in Perovskite Light-Emitting Diodes*, **2021**.

- [199] X. Huang, Y. Guo, Y. Liu, *Chem. Commun.* **2021**, 57, 11429–11442.
- [200] J. Chen, W. Du, J. Shi, M. Li, Y. Wang, Q. Zhang, X. Liu, *InfoMat* **2020**, 2, 170–183.
- [201] H. P. Kim, M. Vasilopoulou, H. Ullah, S. Bibi, A. E. Ximim Gavim, A. G. Macedo, W. J. Da Silva, F. K. Schneider, A. A. Tahir, M. A. Mat Teridi, et al., *Nanoscale* **2020**, 12, 7641–7650.
- [202] C. C. Stoumpos, C. D. Malliakas, M. G. Kanatzidis, *Inorg. Chem.* **2013**, 52, 9019–9038.
- [203] M. J. P. Alcocer, T. Leijtens, L. M. Herz, A. Petrozza, H. J. Snaith, *Science (80-. )*. **2013**, 342, 341–344.
- [204] D. Shi, V. Adinolfi, R. Comin, M. Yuan, E. Alarousu, A. Buin, Y. Chen, S. Hoogland, A. Rothenberger, K. Katsiev, et al., *Science (80-. )*. **2015**, 347, 519–522.
- [205] C. Ran, J. Xu, W. Gao, C. Huang, S. Dou, *Chem. Soc. Rev.* **2018**, 47, 4581–4610.
- [206] T. S. Sherkar, C. Momblona, L. Gil-Escrig, J. Ávila, M. Sessolo, H. J. Bolink, L. J. A. Koster, *ACS Energy Lett.* **2017**, 2, 1214–1222.
- [207] H. Jin, E. Debroye, M. Keshavarz, I. G. Scheblykin, M. B. J. Roeffaers, J. Hofkens, J. A. Steele, *Mater. Horizons* **2020**, 7, 397–410.
- [208] X. Zhu, D. Yang, R. Yang, B. Yang, Z. Yang, X. Ren, J. Zhang, J. Niu, J. Feng, S. Liu, *Nanoscale* **2017**, 9, 12316–12323.
- [209] E. M. Hutter, R. J. Sutton, S. Chandrashekar, M. Abdi-Jalebi, S. D. Stranks, H. J. Snaith, T. J. Savenije, *ACS Energy Lett.* **2017**, 2, 1901–1908.
- [210] F. Palazon, D. Pérez-del-Rey, B. Dänekamp, C. Dreessen, M. Sessolo, P. P. Boix, H. J. Bolink, *Adv. Mater.* **2019**, 31, 1–6.
- [211] J. Ávila, C. Momblona, P. Boix, M. Sessolo, M. Anaya, G. Lozano, K. Vandewal, H. Míguez, H. J. Bolink, *Energy Environ. Sci.* **2018**, 11, 3292–3297.

- [212] J. Ávila, C. Momblona, P. P. Boix, M. Sessolo, H. J. Bolink, *Joule* **2017**, *1*, 431–442.
- [213] E. Climent-Pascual, B. C. Hames, J. S. Moreno-Ramírez, A. L. Álvarez, E. J. Juárez-Perez, E. Mas-Marza, I. Mora-Seró, A. De Andrés, C. Coya, *J. Mater. Chem. A* **2016**, *4*, 18153–18163.
- [214] G. Grancini, S. Marras, M. Prato, C. Giannini, C. Quarti, F. De Angelis, M. De Bastiani, G. E. Eperon, H. J. Snaith, L. Manna, et al., *J. Phys. Chem. Lett.* **2014**, *5*, 3836–3842.
- [215] V. D’Innocenzo, A. R. S. Kandada, M. De Bastiani, M. Gandini, A. Petrozza, A. R. Srimath Kandada, M. De Bastiani, M. Gandini, A. Petrozza, *J. Am. Chem. Soc.* **2014**, *136*, 17730–17733.
- [216] A. Babaei, K. P. S. Zanoni, L. Gil-Escrig, D. Pérez-del-Rey, P. P. Boix, M. Sessolo, H. J. Bolink, *Front. Chem.* **2020**, *7*, 1–6.
- [217] A. Babaei, C. Dreessen, M. Sessolo, H. J. Bolink, *RSC Adv.* **2020**, *10*, 6640–6646.
- [218] G. Grancini, A. R. Srimath Kandada, J. M. Frost, A. J. Barker, M. De Bastiani, M. Gandini, S. Marras, G. Lanzani, A. Walsh, A. Petrozza, *Nat. Photonics* **2015**, *9*, 695–701.
- [219] L. Oesinghaus, J. Schlipf, N. Giesbrecht, L. Song, Y. Hu, T. Bein, P. Docampo, P. Müller-Buschbaum, *Adv. Mater. Interfaces* **2016**, *3*, 1–11.
- [220] M. L. Herrera, R. W. Hartel, *JAOCs, J. Am. Oil Chem. Soc.* **2000**, *77*, 1177–1188.
- [221] P. Schulz, L. L. Whittaker-Brooks, B. A. Macleod, D. C. Olson, Y. L. Loo, A. Kahn, *Adv. Mater. Interfaces* **2015**, *2*, 1–5.
- [222] E. M. Miller, Y. Zhao, C. C. Mercado, S. K. Saha, J. M. Luther, K. Zhu, V. Stevanović, C. L. Perkins, J. Van De Lagemaat, *Phys. Chem. Chem. Phys.* **2014**, *16*, 22122–22130.
- [223] S. Chen, T. W. Goh, D. Sabba, J. Chua, N. Mathews, C. H. A. Huan, T. C. Sum, *APL*

- Mater.* **2014**, *2*, 1–7.
- [224] H. Wei, H. Ma, M. Tai, Y. Wei, D. Li, X. Zhao, H. Lin, S. Fan, K. Jiang, *RSC Adv.* **2017**, *7*, 34795–34800.
- [225] G. Longo, L. Gil-Escrig, M. J. Degen, M. Sessolo, H. J. Bolink, *Chem. Commun.* **2015**, *51*, 7376–7378.
- [226] D. Kim, J. H. Yun, M. Lyu, J. Kim, S. Lim, J. S. Yun, L. Wang, J. Seidel, *J. Phys. Chem. C* **2019**, *123*, 14144–14151.
- [227] A. A. Zhumekenov, M. I. Saidaminov, M. A. Haque, E. Alarousu, S. P. Sarmah, B. Murali, I. Dursun, X. H. Miao, A. L. Abdelhady, T. Wu, et al., *ACS Energy Lett.* **2016**, *1*, 32–37.
- [228] E. Alarousu, A. M. El-Zohry, J. Yin, A. A. Zhumekenov, C. Yang, E. Alhabshi, I. Gereige, A. Alsaggaf, A. V. Malko, O. M. Bakr, et al., *J. Phys. Chem. Lett.* **2017**, *8*, 4386–4390.
- [229] K. Wang, D. Yang, C. Wu, J. Shapter, S. Priya, *Joule* **2019**, *3*, 311–316.
- [230] S. D. Stranks, *ACS Energy Lett.* **2017**, *2*, 1515–1525.
- [231] W. Hicks, “NREL Research Pushes Perovskites Closer to Market Title,” can be found under <https://www.nrel.gov/news/features/2018/nrel-research-pushes-perovskites-closer-to-market.html>, **2018**.
- [232] K. P. Goetz, A. D. Taylor, Y. J. Hofstetter, Y. Vaynzof, *ACS Appl. Mater. Interfaces* **2021**, *13*, 1–17.
- [233] M. Cai, Y. Wu, H. Chen, X. Yang, Y. Qiang, L. Han, *Adv. Sci.* **2017**, *4*.
- [234] A. Binek, M. L. Petrus, N. Huber, H. Bristow, Y. Hu, T. Bein, P. Docampo, *ACS Appl. Mater. Interfaces* **2016**, *8*, 12881–12886.
- [235] K. P. Goetz, A. D. Taylor, Y. J. Hofstetter, Y. Vaynzof, *ACS Appl. Mater. Interfaces*



- 2021**, *13*, 1–17.
- [236] G. Divitini, S. Cacovich, F. Matteocci, L. Cinà, A. Di Carlo, C. Ducati, *Nat. Energy* **2016**, *1*, 15012.
- [237] Y. Han, S. Meyer, Y. Dkhissi, K. Weber, J. M. Pringle, U. Bach, L. Spiccia, Y. B. Cheng, *J. Mater. Chem. A* **2015**, *3*, 8139–8147.
- [238] N. Aristidou, I. Sanchez-Molina, T. Chotchuangchutchaval, M. Brown, L. Martinez, T. Rath, S. A. Haque, *Angew. Chemie - Int. Ed.* **2015**, *54*, 8208–8212.
- [239] K. Wojciechowski, T. Leijtens, S. Siprova, C. Schlueter, M. T. Hörantner, J. T. W. Wang, C. Z. Li, A. K. Y. Jen, T. L. Lee, H. J. Snaith, *J. Phys. Chem. Lett.* **2015**, *6*, 2399–2405.
- [240] G. E. Eperon, S. D. Stranks, C. Menelaou, M. B. Johnston, L. M. Herz, H. J. Snaith, *Energy Environ. Sci.* **2014**, *7*, 982–988.
- [241] T. Liu, Y. Zong, Y. Zhou, M. Yang, Z. Li, O. S. Game, K. Zhu, R. Zhu, Q. Gong, N. P. Padture, *Chem. Mater.* **2017**, *29*, 3246–3250.
- [242] M. Saliba, T. Matsui, K. Domanski, J. Y. Seo, A. Ummadisingu, S. M. Zakeeruddin, J. P. Correa-Baena, W. R. Tress, A. Abate, A. Hagfeldt, et al., *Science (80- )*. **2016**, *354*, 206–209.
- [243] N. Leupold, F. Panzer, *Adv. Funct. Mater.* **2021**, *31*, DOI 10.1002/adfm.202007350.
- [244] J. Ávila, C. Momblona, P. P. Boix, M. Sessolo, H. J. Bolink, *Joule* **2017**, *1*, 431–442.
- [245] P. Fan, D. Gu, G. X. Liang, J. T. Luo, J. L. Chen, Z. H. Zheng, D. P. Zhang, *Sci. Rep.* **2016**, *6*, 1–9.
- [246] L. Gil-Escrig, C. Dreessen, I. C. Kaya, B. S. Kim, F. Palazon, M. Sessolo, H. J. Bolink, *ACS Energy Lett.* **2020**, *5*, 3053–3061.
- [247] Y. H. Chiang, M. Anaya, S. D. Stranks, *ACS Energy Lett.* **2020**, *5*, 2498–2504.

- [248] L. Gil-Escrig, C. Dreessen, F. Palazon, Z. Hawash, E. Moons, S. Albrecht, M. Sessolo, H. J. Bolink, *ACS Energy Lett.* **2021**, *6*, 827–836.
- [249] M. Roß, S. Severin, M. B. Stutz, P. Wagner, H. Köbler, M. Favin-Lévêque, A. Al-Ashouri, P. Korb, P. Tockhorn, A. Abate, et al., *Adv. Energy Mater.* **2021**, *11*.
- [250] M. J. Crane, D. M. Kroupa, J. Y. Roh, R. T. Anderson, M. D. Smith, D. R. Gamelin, *ACS Appl. Energy Mater.* **2019**, *2*, 4560–4565.
- [251] Y. El Ajjouri, F. Palazon, M. Sessolo, H. J. Bolink, *Chem. Mater.* **2018**, *30*, 7423–7427.
- [252] M. P. U. Haris, S. Kazim, S. Ahmad, *ACS Appl. Energy Mater.* **2021**, *4*, 2600–2606.
- [253] D. B. Straus, S. Guo, R. J. Cava, *J. Am. Chem. Soc.* **2019**, *141*, 11435–11439.
- [254] Y. Zhang, S. Seo, S. Y. Lim, Y. Kim, S. G. Kim, D. K. Lee, S. H. Lee, H. Shin, H. Cheong, N. G. Park, *ACS Energy Lett.* **2020**, 360–366.
- [255] C. C. Stoumpos, C. D. Malliakas, M. G. Kanatzidis, *Inorg. Chem.* **2013**, *52*, 9019–9038.
- [256] F. Ma, J. Li, W. Li, N. Lin, L. Wang, J. Qiao, *Chem. Sci.* **2016**, *8*, 800–805.
- [257] D. Shi, V. Adinolfi, R. Comin, M. Yuan, E. Alarousu, A. Buin, Y. Chen, S. Hoogland, A. Rothenberger, K. Katsiev, et al., *Science (80-. )*. **2015**, *347*, 519–522.
- [258] Y. Yang, Y. Yan, M. Yang, S. Choi, K. Zhu, J. M. Luther, M. C. Beard, *Nat. Commun.* **2015**, *6*.
- [259] C. Igci, S. Paek, K. Rakstys, H. Kanda, N. Shibayama, V. Jankauskas, C. Roldán-Carmona, H. Kim, A. M. Asiri, M. K. Nazeeruddin, *Sol. RRL* **2020**, *4*, 1–9.
- [260] Y. Chen, J. Shi, X. Li, S. Li, X. Lv, X. Sun, X. Tao, J. Shi, Y. Z. Zheng, *J. Mater. Chem. A* **2020**, *8*, 6349–6359.
- [261] E. Akman, A. E. Shalan, F. Sadegh, S. Akin, *ChemSusChem* **2021**, *14*, 1176–1183.

- [262] Y. Zhang, S. G. Kim, D. Lee, H. Shin, N. G. Park, *Energy Environ. Sci.* **2019**, *12*, 308–321.
- [263] J. B. Patel, R. L. Milot, A. D. Wright, L. M. Herz, M. B. Johnston, *J. Phys. Chem. Lett.* **2016**, *7*, 96–102.
- [264] N. Klipfel, C. Momblona, H. Kanda, N. Shibayama, Y. Nakamura, M. D. Mensi, C. Liu, C. Roldán-Carmona, M. K. Nazeeruddin, *Sol. RRL* **2021**, 2100191.
- [265] Y. Yu, C. Wang, C. R. Grice, N. Shrestha, J. Chen, D. Zhao, W. Liao, A. J. Cimaroli, P. J. Roland, R. J. Ellingson, et al., *ChemSusChem* **2016**, *9*, 3288–3297.
- [266] D. B. Mitzi, S. Wang, C. A. Feild, C. A. Chess, A. M. Guloy, *Science* **1995**, *267*, 1473–6.
- [267] A. Dodabalapur, L. Torsi, H. E. Katz, *Science (80-. )*. **1995**, *268*, 270–271.
- [268] A. Kojima, K. Teshima, Y. Shirai, T. Miyasaka, *J. Am. Chem. Soc.* **2009**, *131*, 6050–6051.
- [269] J. Y. Jeng, Y. F. Chiang, M. H. Lee, S. R. Peng, T. F. Guo, P. Chen, T. C. Wen, *Adv. Mater.* **2013**, *25*, 3727–3732.
- [270] V. S. Chirvony, K. S. Sekerbayev, D. Pérez-del-Rey, J. P. Martínez-Pastor, F. Palazon, P. P. Boix, T. I. Taurbayev, M. Sessolo, H. J. Bolink, *J. Phys. Chem. Lett.* **2019**, *10*, 5167–5172.
- [271] D. Yang, R. Yang, S. Priya, S. (Frank) Liu, *Angew. Chemie - Int. Ed.* **2019**, *58*, 4466–4483.
- [272] M. Liu, M. B. Johnston, H. J. Snaith, *Nature* **2013**, *501*, 395–398.
- [273] F. Sahli, J. Werner, B. A. Kamino, M. Bräuninger, R. Monnard, B. Paviet-Salomon, L. Barraud, L. Ding, J. J. Diaz Leon, D. Sacchetto, et al., *Nat. Mater.* **2018**, *17*, 820–826.

- [274] L. L. Kazmerski, F. R. White, M. S. Ayyagari, Y. J. Juang, R. P. Patterson, *J Vac Sci Technol* **1976**, *14*, 65–68.
- [275] H. Holloway, J. L. Richards, L. C. Bobb, J. Perry, E. Zimmerman, *J. Appl. Phys.* **1966**, *37*, 4694–4699.
- [276] R. Swartwout, M. T. Hoerantner, V. Bulović, *Energy Environ. Mater.* **2019**, *2*, 119–145.
- [277] L. Gil-Escrig, C. Momblona, M. G. La-Placa, P. P. Boix, M. Sessolo, H. J. Bolink, *Adv. Energy Mater.* **2018**, *8*, 1–6.
- [278] C. C. Boyd, R. Cheacharoen, T. Leijtens, M. D. McGehee, *Chem. Rev.* **2019**, *119*, 3418–3451.
- [279] Y. Shao, Z. Xiao, C. Bi, Y. Yuan, J. Huang, *Nat. Commun.* **2014**, *5*, 1–7.
- [280] D. Liu, Q. Wang, C. J. Traverse, C. Yang, M. Young, P. S. Kuttipillai, S. Y. Lunt, T. W. Hamann, R. R. Lunt, *ACS Nano* **2018**, *12*, 876–883.
- [281] V. Arivazhagan, J. Xie, P. Hang, M. Manonmani Parvathi, A. Khan, C. Cui, D. Yang, X. Yu, *J. Phys. D. Appl. Phys.* **2019**, *52*, 225104.
- [282] D. Liu, Q. Wang, C. J. Traverse, C. Yang, M. Young, P. S. Kuttipillai, S. Y. Lunt, T. W. Hamann, R. R. Lunt, *ACS Nano* **2018**, *12*, 876–883.
- [283] C. Wang, C. Wang, X. Liu, J. Kauppi, Y. Shao, Z. Xiao, C. Bi, J. Huang, Y. Gao, *Appl. Phys. Lett.* **2015**, *106*.
- [284] C. Liu, M. Cai, Y. Yang, Z. Arain, Y. Ding, X. Shi, P. Shi, S. Ma, T. Hayat, A. Alsaedi, et al., *J. Mater. Chem. A* **2019**, *7*, 11086–11094.
- [285] D. Pérez-Del-Rey, P. P. Boix, M. Sessolo, A. Hadipour, H. J. Bolink, *J. Phys. Chem. Lett.* **2018**, *9*, 1041–1046.
- [286] T. Rabenau, A. Simon, R. K. Kremer, E. Sohmen, *Zeitschrift für Phys. B Condens.*

*Matter* **1993**, *90*, 69–72.

- [287] X. Liu, S. Yi, C. Wang, C. Wang, Y. Gao, *J. Appl. Phys.* **2014**, *115*, 111603.
- [288] T. W. Crothers, R. L. Milot, J. B. Patel, E. S. Parrott, J. Schlipf, P. Müller-Buschbaum, M. B. Johnston, L. M. Herz, *Nano Lett.* **2017**, *17*, 5782–5789.
- [289] M. M. Mandoc, F. B. Kooistra, J. C. Hummelen, B. De Boer, P. W. M. Blom, *Appl. Phys. Lett.* **2007**, *91*, 91–94.
- [290] G. Grancini, C. Roldán-Carmona, I. Zimmermann, E. Mosconi, X. Lee, D. Martineau, S. Narbey, F. Oswald, F. De Angelis, M. Graetzel, et al., *Nat. Commun.* **2017**, *8*, 1–8.
- [291] Y. Lin, Y. Fang, J. Zhao, Y. Shao, S. J. Stuard, M. M. Nahid, H. Ade, Q. Wang, J. E. Shield, N. Zhou, et al., *Nat. Commun.* **2019**, *10*, 1–11.
- [292] I. Zarazua, G. Han, P. P. Boix, S. Mhaisalkar, F. Fabregat-Santiago, I. Mora-Seró, J. Bisquert, G. Garcia-Belmonte, *J. Phys. Chem. Lett.* **2016**, *7*, 5105–5113.
- [293] P. Perkhun, W. Köntges, F. Pourcin, D. Esteouille, E. Barulina, N. Yoshimoto, P. Pierron, O. Margeat, C. Videlot-Ackermann, A. K. Bharwal, et al., *Adv. Energy Sustain. Res.* **2021**, *2*, 2000086.
- [294] I. Zarazua, J. Bisquert, G. Garcia-Belmonte, *J. Phys. Chem. Lett.* **2016**, *7*, 525–528.
- [295] H. S. Kim, I. Mora-Sero, V. Gonzalez-Pedro, F. Fabregat-Santiago, E. J. Juarez-Perez, N. G. Park, J. Bisquert, *Nat. Commun.* **2013**, *4*, 1–7.
- [296] S. M. Yoo, S. J. Yoon, J. A. Anta, H. J. Lee, P. P. Boix, I. Mora-Seró, *Joule* **2019**, *3*, 2535–2549.
- [297] A. Guerrero, G. Garcia-Belmonte, I. Mora-Sero, J. Bisquert, Y. S. Kang, T. J. Jacobsson, J. P. Correa-Baena, A. Hagfeldt, *J. Phys. Chem. C* **2016**, *120*, 8023–8032.
- [298] F. Ebadi, N. Taghavinia, R. Mohammadpour, A. Hagfeldt, W. Tress, *Nat. Commun.*

- 2019, 10, 1–9.
- [299] V. Babu, R. Fuentes Pineda, T. Ahmad, A. O. Alvarez, L. A. Castriotta, A. Di Carlo, F. Fabregat-Santiago, K. Wojciechowski, *ACS Appl. Energy Mater.* **2020**, 3, 5126–5134.
- [300] F. Fabregat-Santiago, M. Kulbak, A. Zohar, M. Vallés-Pelarda, G. Hodes, D. Cahen, I. Mora-Seró, *ACS Energy Lett.* **2017**, 2, 2007–2013.
- [301] A. O. Alvarez, R. Arcas, C. A. Aranda, L. Bethencourt, E. Mas-Marzá, M. Saliba, F. Fabregat-Santiago, *J. Phys. Chem. Lett.* **2020**, 11, 8417–8423.
- [302] E. Ghahremanirad, A. Bou, S. Olyaei, J. Bisquert, *J. Phys. Chem. Lett.* **2017**, 8, 1402–1406.
- [303] S. R. Raga, E. M. Barea, F. Fabregat-Santiago, *J. Phys. Chem. Lett.* **2012**, 3, 1629–1634.
- [304] M. Li, H. Li, J. Fu, T. Liang, W. Ma, *J. Phys. Chem. C* **2020**.
- [305] S. Zhang, G. Han, *Prog. Energy* **2020**, 2, 022002.
- [306] A. A. Sutanto, R. Szostak, N. Drigo, V. I. E. Queloz, P. E. Marchezi, J. C. Germino, H. C. N. Tolentino, M. K. Nazeeruddin, A. F. Nogueira, G. Grancini, *Nano Lett.* **2020**, 20, 3992–3998.
- [307] A. A. Sutanto, N. Drigo, V. I. E. Queloz, I. Garcia-Benito, A. R. Kirmani, L. J. Richter, P. A. Schouwink, K. T. Cho, S. Paek, M. K. Nazeeruddin, et al., *J. Mater. Chem. A* **2020**, 8, 2343–2348.
- [308] R. Brakkee, R. M. Williams, *Appl. Sci.* **2020**, 10.
- [309] F. Wang, S. Bai, W. Tress, A. Hagfeldt, F. Gao, *npj Flex. Electron.* **2018**, 22, 1–14.
- [310] A. Mahapatra, D. Prochowicz, M. M. Tavakoli, S. Trivedi, P. Kumar, P. Yadav, *J. Mater. Chem. A* **2020**, 8, 27–54.

- [311] N. D. Pham, V. T. Tiong, D. Yao, W. Martens, A. Guerrero, J. Bisquert, H. Wang, *Nano Energy* **2017**, *41*, 476–487.
- [312] S. Ghosh, T. Singh, *Nano Energy* **2019**, *63*, 1–12.
- [313] F. Wang, W. Geng, Y. Zhou, H. H. Fang, C. J. Tong, M. A. Loi, L. M. Liu, N. Zhao, *Adv. Mater.* **2016**, *28*, 9986–9992.
- [314] N. K. Noel, A. Abate, S. D. Stranks, E. S. Parrott, V. M. Burlakov, A. Goriely, J. S. Henry, *ACS Nano* **2014**, *8*, 9815–9821.
- [315] H. Liu, M. Wang, J. Bian, Y. Feng, Z. Wang, B. Zhang, Y. Shi, *Appl. Phys. Lett.* **2018**, *113*, 1–5.
- [316] T. A. Berhe, W. N. Su, C. H. Chen, C. J. Pan, J. H. Cheng, H. M. Chen, M. C. Tsai, L. Y. Chen, A. A. Dubale, B. J. Hwang, *Energy Environ. Sci.* **2016**, *9*, 323–356.
- [317] D. Bi, L. Yang, G. Boschloo, A. Hagfeldt, E. M. J. Johansson, C. H. Nh, P. P. Mesoscopic, S. Cells, D. Bi, L. Yang, et al., *J. Phys. Chem. Lett.* **2013**, *4*, 1532–1536.
- [318] S. Wang, Z. Huang, X. Wang, Y. Li, M. Günther, S. Valenzuela, P. Parikh, A. Cabrerros, W. Xiong, Y. S. Meng, *J. Am. Chem. Soc.* **2018**, *140*, 16720–16730.
- [319] S. Wang, M. Sina, P. Parikh, T. Uekert, B. Shahbazian, A. Devaraj, Y. S. Meng, *Nano Lett.* **2016**, *16*, 5594–5600.
- [320] S. N. Habisreutinger, N. K. Noel, H. J. Snaith, R. J. Nicholas, *Adv. Energy Mater.* **2017**, *7*, 1–8.
- [321] W. Yuan, H. Zhao, H. Hu, S. Wang, G. L. Baker, *ACS Appl. Mater. Interfaces* **2013**, *5*, 4155–4161.
- [322] S. Wang, W. Yuan, Y. S. Meng, *ACS Appl. Mater. Interfaces* **2015**, *7*, 24791–24798.
- [323] E. J. Juarez-Perez, M. R. Leyden, S. Wang, L. K. Ono, Z. Hawash, Y. Qi, *Chem. Mater.* **2016**, *28*, 5702–5709.

- [324] Z. Li, C. Xiao, Y. Yang, S. P. Harvey, D. H. Kim, J. A. Christians, M. Yang, P. Schulz, S. U. Nanayakkara, C. S. Jiang, et al., *Energy Environ. Sci.* **2017**, *10*, 1234–1242.
- [325] X. Guo, J. Li, B. Wang, P. Zeng, F. Li, Q. Yang, Y. Chen, M. Liu, *ACS Appl. Energy Mater.* **2020**, *3*, 970–976.
- [326] W. Li, H. Dong, L. Wang, N. Li, X. Guo, J. Li, Y. Qiu, *J. Mater. Chem. A* **2014**, *2*, 13587–13592.
- [327] L. Qiu, J. Zou, W. Chen, L. Dong, D. Mei, L. Song, J. Wang, P.-C. Jiang, P.-F. Du, J. Xiong, *Sustain. Energy Fuels* **2020**, *00*, 1–9.
- [328] C. Geffroy, E. Grana, T. Bessho, S. Almosni, Z. Tang, A. Sharma, T. Kinoshita, F. Awai, E. Cloutet, T. Toupance, et al., *ACS Appl. Energy Mater.* **2020**, *3*, 1393–1401.
- [329] J. Burschka, A. Dualeh, F. Kessler, E. Baranoff, N. L. Cevey-Ha, C. Yi, M. K. Nazeeruddin, M. Grätzel, *J. Am. Chem. Soc.* **2011**, *133*, 18042–18045.
- [330] E. S. Thibau, A. Llanos, Z. H. Lu, *Appl. Phys. Lett.* **2016**, *108*, 1–4.
- [331] W. Ke, D. Zhao, C. R. Grice, A. J. Cimaroli, G. Fang, Y. Yan, *J. Mater. Chem. A* **2015**, *3*, 23888–23894.
- [332] J. Höcker, D. Kiermasch, P. Rieder, K. Tvingstedt, A. Baumann, V. Dyakonov, *Zeitschrift für Naturforsch. - Sect. A J. Phys. Sci.* **2019**, *74*, 665–672.
- [333] F. Zu, T. Schultz, C. M. Wolff, D. Shin, L. Frohloff, D. Neher, P. Amsalem, N. Koch, *RSC Adv.* **2020**, *10*, 17534–17542.
- [334] M. S. Lee, S. Sarwar, S. Park, U. Asmat, D. T. Thuy, C. H. Han, S. J. Ahn, I. Jeong, S. Hong, *Sustain. Energy Fuels* **2020**, *4*, 3318–3325.
- [335] P. Guo, Q. Ye, X. Yang, J. Zhang, F. Xu, D. Shchukin, B. Wei, H. Wang, *J. Mater. Chem. A* **2019**, *7*, 2497–2506.
- [336] H. Xu, Y. Wu, J. Cui, C. Ni, F. Xu, J. Cai, F. Hong, Z. Fang, W. Wang, J. Zhu, et al.,



- Phys. Chem. Chem. Phys.* **2016**, *18*, 18607–18613.
- [337] V. Shutthanandan, M. Nandasiri, J. Zheng, M. H. Engelhard, W. Xu, S. Thevuthasan, V. Murugesan, *J. Electron Spectros. Relat. Phenomena* **2019**, *231*, 2–10.
- [338] L. Fu, H. Li, L. Wang, R. Yin, B. Li, L. Yin, *Energy Environ. Sci.* **2020**, *13*, 4017–4056.
- [339] J. Lu, X. Lin, X. Jiao, T. Gengenbach, A. D. Scully, L. Jiang, B. Tan, J. Sun, B. Li, N. Pai, et al., *Energy Environ. Sci.* **2018**, *11*, 1880–1889.
- [340] N. G. Park, *J. Phys. Chem. Lett.* **2013**, *4*, 2423–2429.
- [341] J. M. Frost, K. T. Butler, F. Brivio, C. H. Hendon, M. Van Schilfgarde, A. Walsh, **2014**.
- [342] H. Kanda, N. Shibayama, A. J. Huckaba, Y. Lee, S. Paek, N. Klipfel, C. Roldán-Carmona, V. I. E. Queloz, G. Grancini, Y. Zhang, et al., *Energy Environ. Sci.* **2020**, *13*, 1222–1230.
- [343] N. Tsvetkov, A. Nikolskaia, O. Shevaleevskiy, S. Kozlov, *Appl. Surf. Sci.* **2020**, *512*, 145666.
- [344] T. T. Ava, A. Al Mamun, S. Marsillac, G. Namkoong, *Appl. Sci.* **2019**, *9*.
- [345] A. Maurel, M. Armand, S. Grugeon, B. Fleutot, C. Davoisne, H. Tortajada, M. Courty, S. Panier, L. Dupont, *J. Electrochem. Soc.* **2020**, *167*, 070536.
- [346] Z. Li, J. Tinkham, P. Schulz, M. Yang, D. H. Kim, J. Berry, A. Sellinger, K. Zhu, *Adv. Energy Mater.* **2017**, *7*, 1–8.
- [347] R. Saive, A. M. Borsuk, H. S. Emmer, C. R. Bukowsky, J. V Lloyd, S. Yalamanchili, H. A. Atwater, *Adv. Opt. Mater.* **2016**, *4*, 1470–1474.
- [348] M. Abuhelaiqa, N. Shibayama, X. X. Gao, H. Kanda, M. K. Nazeeruddin, *ACS Appl. Energy Mater.* **2021**, *4*, 3424–3430.

- [349] C. Rodríguez-Seco, L. Cabau, A. Vidal-Ferran, E. Palomares, *Acc. Chem. Res.* **2018**, *51*, 869–880.
- [350] W. Tress, N. Marinova, T. Moehl, S. M. Zakeeruddin, M. K. Nazeeruddin, M. Grätzel, *Energy Environ. Sci.* **2015**, *8*, 995–1004.
- [351] F. Galatopoulos, A. Savva, I. T. Papadas, S. A. Choulis, *APL Mater.* **2017**, *5*, 076102.
- [352] A. Krishna, A. C. Grimsdale, *J. Mater. Chem. A* **2017**, *5*, 16446–16466.
- [353] J. Urieta-Mora, I. García-Benito, A. Molina-Ontoria, N. Martín, *Chem. Soc. Rev.* **2018**, *47*, 8541–8571.
- [354] L. Breloy, O. Yavuz, I. Yilmaz, Y. Yagci, D. L. Versace, *Polym. Chem.* **2021**, *12*, 4291–4316.
- [355] A. M. Schmidt, M. J. F. Calvete, *Molecules* **2021**, *26*, 1–22.
- [356] C. V. Kumar, G. Sfyri, D. Raptis, E. Stathatos, P. Lianos, *RSC Adv.* **2015**, *5*, 3786–3791.
- [357] W. Ke, D. Zhao, C. R. Grice, A. J. Cimaroli, G. Fang, Y. Yan, *J. Mater. Chem. A* **2015**, *3*, 23888–23894.
- [358] Y. Matsuo, K. Ogumi, Y. Matsuo, I. Jeon, T. Nakagawa, Y. Matsuo, H. Wang, K. Ogumi, *RSC Adv.* **2020**, *10*, 32678–32689.
- [359] T. Lei, J. Y. Wang, J. Pei, *Chem. Mater.* **2014**, *26*, 594–603.
- [360] Z. Dalkılıç, C. B. Lee, H. Choi, I. Nar, N. K. Yavuz, A. K. Burat, *J. Organomet. Chem.* **2020**, 922.
- [361] Y. Feng, Q. Hu, E. Rezaee, M. Li, Z.-X. Xu, A. Lorenzoni, F. Mercuri, M. Muccini, *Adv. Energy Mater.* **2019**, *9*, 1970104.
- [362] A. A. Chernonosov, E. A. Ermilov, B. Röder, L. I. Solovyova, O. S. Fedorova, *Bioinorg. Chem. Appl.* **2014**, 2014.

- [363] Q. D. Dao, A. Fujii, R. Tsuji, Y. Takeoka, M. Ozaki, *Org. Electron.* **2017**, *43*, 156–161.
- [364] C. Piechocki, J. Simon, A. Skoulios, D. Guillon, P. Weber, *J. Am. Chem. Soc.* **1982**, *104*, 5245–5247.
- [365] M. M. H. Desoky, M. Bonomo, R. Buscaino, A. Fin, G. Viscardi, C. Barolo, P. Quagliotto, *Energies* **2021**, *14*, 2279.
- [366] K. T. Cho, K. Rakstys, M. Cavazzini, S. Orlandi, G. Pozzi, M. K. Nazeeruddin, *Nano Energy* **2016**, *30*, 853–857.
- [367] K. T. Cho, M. Cavazzini, K. Rakstys, S. Orlandi, S. Paek, M. Franckevičius, H. Kanda, R. Gegevičius, Q. V. Emmanuel, G. Pozzi, et al., *ACS Appl. Energy Mater.* **2019**, *2*, 6195–6199.
- [368] G. Sfyri, N. Vamshikrishna, C. V. Kumar, L. Giribabu, P. Lianos, *Sol. Energy* **2016**, *140*, 60–65.
- [369] Y. Feng, Q. Hu, E. Rezaee, M. Li, Z. X. Xu, A. Lorenzoni, F. Mercuri, M. Muccini, *Adv. Energy Mater.* **2019**, *9*, 1–11.
- [370] Z. Ma, H. Geng, D. Wang, Z. Shuai, *J. Mater. Chem. C* **2016**, *4*, 4546–4555.
- [371] L. Calì, J. Follana-Berná, S. Kazim, M. Madsen, H. G. Rubahn, Á. Sastre-Santos, S. Ahmad, *Sustain. Energy Fuels* **2017**, *1*, 2071–2077.
- [372] Y. Chen, T. Liu, L. K. Ma, W. Xue, R. Ma, J. Zhang, C. Ma, H. K. Kim, H. Yu, F. Bai, et al., *J. Mater. Chem. A* **2021**, *9*, 7481–7490.
- [373] et al. . Frisch, M. J., Trucks, G. W., Schlegel, H. B., Scuseria, G. E., Robb, M. A., Cheeseman, J. R., Montgomery Jr. J. A., Vreven, T., Kudin, K. N., Burant, J. C., et al. rucks, G. W., Schlegel, H. B., Scuseria, G. E., Robb, M. A., Cheeseman, *Gaussian, Inc* **2009**.
- [374] Y. Feng, Q. Chen, L. Dong, Z. Zhang, C. Li, S. Yang, S. Cai, Z. X. Xu, *Sol. Energy*

- 2019, 184, 649–656.
- [375] G. Xing, N. Mathews, S. S. Lim, Y. M. Lam, S. Mhaisalkar, T. C. Sum, 2013, 6960, 498–500.
- [376] Z. Dalkılıç, C. B. Lee, H. Choi, I. Nar, N. K. Yavuz, A. K. Burat, *J. Organomet. Chem.* 2020, 922, DOI 10.1016/j.jorganchem.2020.121419.
- [377] K. T. Cho, O. Trukhina, C. Roldán-Carmona, M. Ince, P. Gratia, G. Grancini, P. Gao, T. Marszalek, W. Pisula, P. Y. Reddy, et al., *Adv. Energy Mater.* 2017, 7, 1–7.
- [378] M. Wang, Y. Lei, Y. Xu, L. Han, Z. Ci, Z. Jin, *Sol. RRL* 2020, 4, 1–28.
- [379] K. Rakstys, A. Abate, M. I. Dar, P. Gao, V. Jankauskas, G. Jacopin, E. Kamarauskas, S. Kazim, S. Ahmad, M. Grätzel, et al., *J. Am. Chem. Soc.* 2015, 137, 16172–16178.
- [380] T. Leijtens, T. Giovenzana, S. N. Habisreutinger, J. S. Tinkham, N. K. Noel, B. A. Kamino, G. Sadoughi, A. Sellinger, H. J. Snaith, *ACS Appl. Mater. Interfaces* 2016, 8, 5981–5989.
- [381] K. Odysseas Kosmatos, L. Theofylaktos, E. Giannakaki, D. Deligiannis, M. Konstantakou, T. Stergiopoulos, *Energy Environ. Mater.* 2019, 2, 79–92.
- [382] M. Kim, G. H. Kim, T. K. Lee, I. W. Choi, H. W. Choi, Y. Jo, Y. J. Yoon, J. W. Kim, J. Lee, D. Huh, et al., *Joule* 2019, 3, 2179–2192.
- [383] F. Zheng, C. Zuo, M. Niu, C. Zhou, S. J. Bradley, C. R. Hall, W. Xu, X. Wen, X. Hao, M. Gao, et al., *ACS Appl. Mater. Interfaces* 2020, 12, 25980–25990.
- [384] S. A. Odom, K. Lancaster, L. Beverina, K. M. Lefler, N. J. Thompson, V. Coropceanu, J. L. Bredas, S. R. Marder, S. Barlow, *Chem. - A Eur. J.* 2007, 13, 9637–9646.
- [385] S. H. Kang, I. T. Choi, M. S. Kang, Y. K. Eom, M. J. Ju, J. Y. Hong, H. S. Kang, H. K. Kim, *J. Mater. Chem. A* 2013, 1, 3977–3982

# Appendix A: Supplementary Information to Chapter 4

## *Materials and Methods*

### *Thin-film and device fabrication*

Thin films were fabricated on fluorine-doped tin oxide (FTO)-coated glass substrates (TEC-15AX, NSG group) previously cleaned by a sequential sonication treatment in a 2% Hellmanex solution, acetone, and isopropanol, followed by ultraviolet-ozone treatment for 15 min. A compact blocking layer of TiO<sub>2</sub> (planar-TiO<sub>2</sub>, 30 nm thick film) was then deposited onto the FTO-coated glass substrate by spray pyrolysis, using a titanium diisopropoxide bis(acetylacetonate) (TAA) solution (Sigma-Aldrich) in ethanol (1ml of TAA in 15ml ethanol), and then sintered at 450 °C for 30 min. A 200 nm-thick layer of mesoporous-TiO<sub>2</sub> (meso-TiO<sub>2</sub>, 30 NR-D Titania paste, Dyesol) was prepared from an ethanol dispersion (1g titanium oxide nanoparticle paste in 9ml ethanol) and spin-coated at 2000 rpm, for 15s (acc. 1000 r.p.m./s). Afterward, the samples were sintered at 500°C for 30 min in air. The NiO<sub>x</sub> layers were prepared by spray pyrolysis deposition method using a nickel acetate acetylacetonate (Sigma-Aldrich) solution in acetonitrile (0.04 M). The deposition temperature was 500 °C and kept by 20 min. The spiro-OMeTAD (Merck) underlayers were spin-coated at 4000 r.p.m. for 30 s (acc. 1000 r.p.m./s) from a chlorobenzene solution (80 mg in 1023 μl, 60 mM). The solution contained the dopants: bis(trifluoromethane)sulfonimide lithium salt (Li-TFSI) (19μl from a 517 mg·ml<sup>-1</sup> stock solution in acetonitrile), tert-butylpyridine (TBP) (32 μl) and tris(2-(1H-pyrazol-1-yl)-4-tert-butylpyridine)cobalt(II) di[bis(trifluoromethane)sulfonimide] (FK209 Co(II)TFSI salt) (14 μl from a 517 mg·ml<sup>-1</sup> stock solution in acetonitrile). PEDOT: PSS (CLEVIOS™ P VP AI 4083, Heraeus) underlayers were prepared via spin-coating. The solution was placed in an ultrasonic bath for 15min to reduce possible agglomeration of the material. Prior to the deposition, the cleaned FTO substrates were treated with UV/O<sub>3</sub> for 30 min to improve the wetting of the solution on the substrate. The PEDOT: PSS dispersion

was filtered with a PTFE 0.22  $\mu\text{m}$  pore size filter and spin-coated at 1000 r.p.m. for 50 s (acc.500 r.p.m./s). The layers were annealed at 150  $^{\circ}\text{C}$  for 15 min in air.

The prepared layers were transferred to the PRO Line PVD 75 vacuum chamber from Kurt J. Lesker Company, equipped with four thermally controlled sources. The crucibles were filled with the perovskite precursors,  $\text{PbI}_2$  and MAI, and heated up until the sublimation temperatures of 277  $^{\circ}\text{C}$  and 136  $^{\circ}\text{C}$  for C<sub>1</sub>, 297  $^{\circ}\text{C}$  and 139  $^{\circ}\text{C}$  for C<sub>2</sub>, 298  $^{\circ}\text{C}$  and 131  $^{\circ}\text{C}$  for C<sub>3</sub> and 319  $^{\circ}\text{C}$  and 165  $^{\circ}\text{C}$  for C<sub>4</sub> at a vacuum pressure of  $\sim 1 \cdot 10^{-6}$  mbar. During perovskite deposition, the deposition rate of each precursor was kept constant and monitored by independent quartz microbalance crystal sensors (QCMs). The substrates were kept at room temperature and under rotation of 5 r.p.m.

For device fabrication, the FTO-coated substrates were chemically etched with Zn powder and HCl solution. Once the perovskite layer was deposited, 20 nm of  $\text{C}_{60}$  (Sigma-Aldrich, 99.9%) was thermally evaporated, followed by 3 nm of bathocuproine (BCP, Sigma-Aldrich, 99.9%). Finally, 1 nm Cr and 70 nm Au were deposited by thermal evaporation as the top electrode.

#### *Thin-film characterization*

The XRD patterns of the prepared films were measured using a D8 Advance diffractometer from Bruker (Bragg-Brentano geometry, with an X-ray tube  $\text{Cu K}\alpha$ ,  $\lambda = 1.5406 \text{ \AA}$ ). The absorption spectra were registered with a Lambda 950S spectrophotometer (PerkinElmer, Inc.). Steady-state photoluminescence (PL) measurements were recorded with an LS-55 fluorescence spectrometer (PerkinElmer, Inc.) at an excitation wavelength  $\lambda = 450 \text{ nm}$ . 2D-detector images were measured on a Bruker D8 Venture equipped with a Photon 100 detector using a micro-focused Molybdenum Imus 2.0 source. Images were exposed at 120 seconds. The films were mounted on a standard Huber goniometer head by means of a custom-made magnetic adapter pin. Films were positioned vertically during measurement in order to choose the incidence angle, which was between  $2\theta = 10^{\circ}$  and  $\Omega = 3^{\circ}$ . 2D images were visualized and processed using Apex3 and EVA. Wide-angle

X-ray diffraction (WAXS) patterns represented in reciprocal lattice space were measured at the SPring-8 on beamline BL19B2. The sample was irradiated with an X-ray energy of 12.39 keV ( $\lambda = 1 \text{ \AA}$ ) with a fixed incident angle on the order of  $6.0^\circ$  through a Huber diffractometer. The WAXS patterns were recorded with a two-dimensional image detector (Pilatus 300 K).

To evaluate the crystal orientation, we calculated the diffraction intensities along  $\chi$ -arc  $I_q(\chi)$  according to the following equation,

$$I_q(\chi) = \int_{q_1}^{q_2} I(q, \chi) dq$$

where  $q$  is the magnitude of the scattering vector and  $\chi$  is the azimuthal angle. To analyze each diffraction peak, the integration interval from  $q_1$  to  $q_2$  was set appropriately.

An ultraviolet photoelectron spectrometer (UPS) equipped with a He-I source ( $h\nu = 21.22 \text{ eV}$ ) (AXIS Nova, Kratos Analytical Ltd, UK) was used for measuring the valence band energy, Fermi level, and the work function. The Fermi level of the samples was referenced to that of Au, which was in electrical contact with a sample in UPS measurements. The X-ray photoelectron spectroscopy (XPS) measurements were carried out on a VersaProbe II (Physical Electronics, Inc.) with a monochromatic Al  $K_\alpha$  X-ray source operating at 1486.6 eV. The spectra were referenced using the Pb 4f signal. Data was processed using CasaXPS.

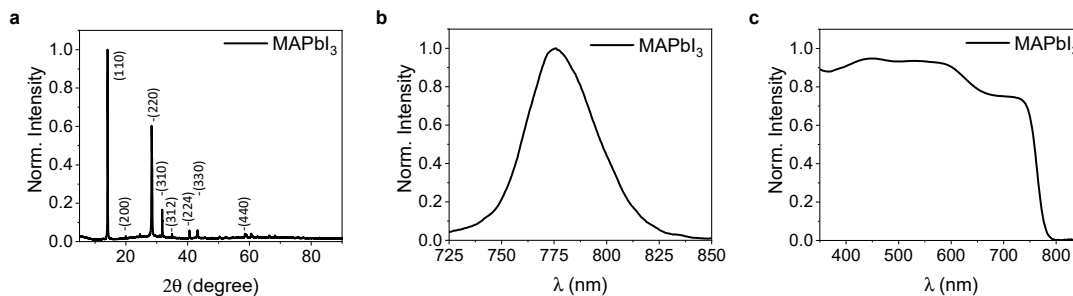
#### *Device characterization*

J - V curves were measured by using a 2400 Keithley system with a Xe-lamp Oriel sol3A sun simulator (Newport Corporation), which was calibrated to AM1.5G standard conditions by using an Oriel 91150 V reference cell (J-V curves scan rate of  $50 \text{ mV s}^{-1}$  and  $10 \text{ mV}$  voltage step). The light intensity was calibrated with an NREL-certified KG5-filtered Si-reference diode. Shadow masks with a metal aperture of  $0.16 \text{ cm}^2$  were used to define the active area of the solar. The cells were measured in air, at room temperature, and without encapsulation, at a constant rate  $10 \text{ mV}\cdot\text{s}^{-1}$  for reversed bias after 5s under light soaking. No anti-reflective

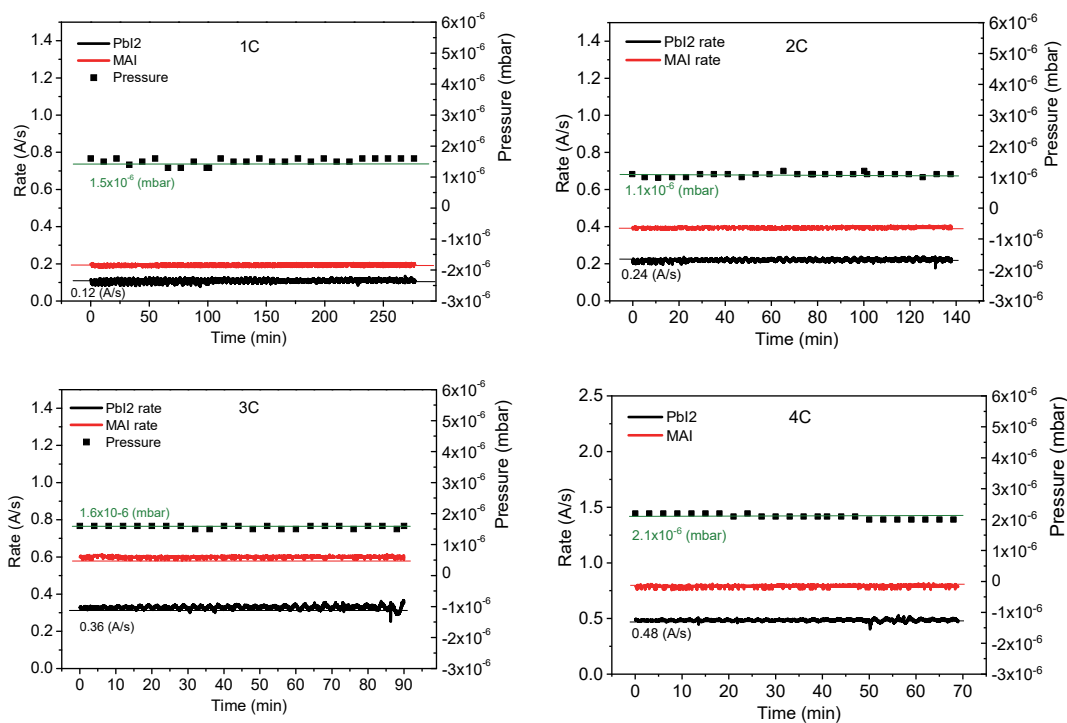
coating was used during the measurement. The stability test was performed as maximum power tracking under  $100 \text{ mW cm}^{-2}$  illumination with a LED power source. The samples were encapsulated in a measurement box which was purged with argon gas at 0% humidity and constantly kept at  $25 \text{ }^\circ\text{C}$  by a cooling system. EQE was measured with the IQE200B (Oriel) without bias light.



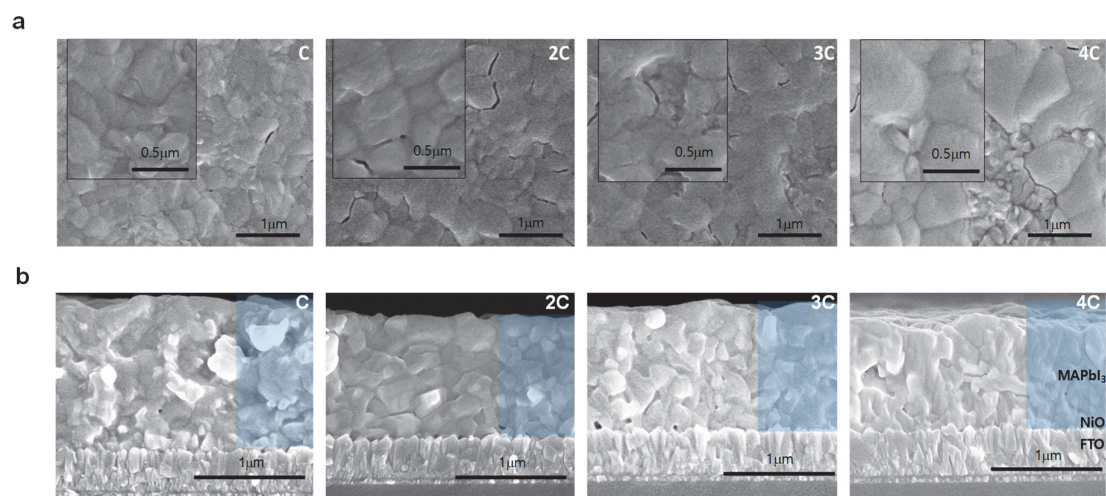
## Supporting Figures



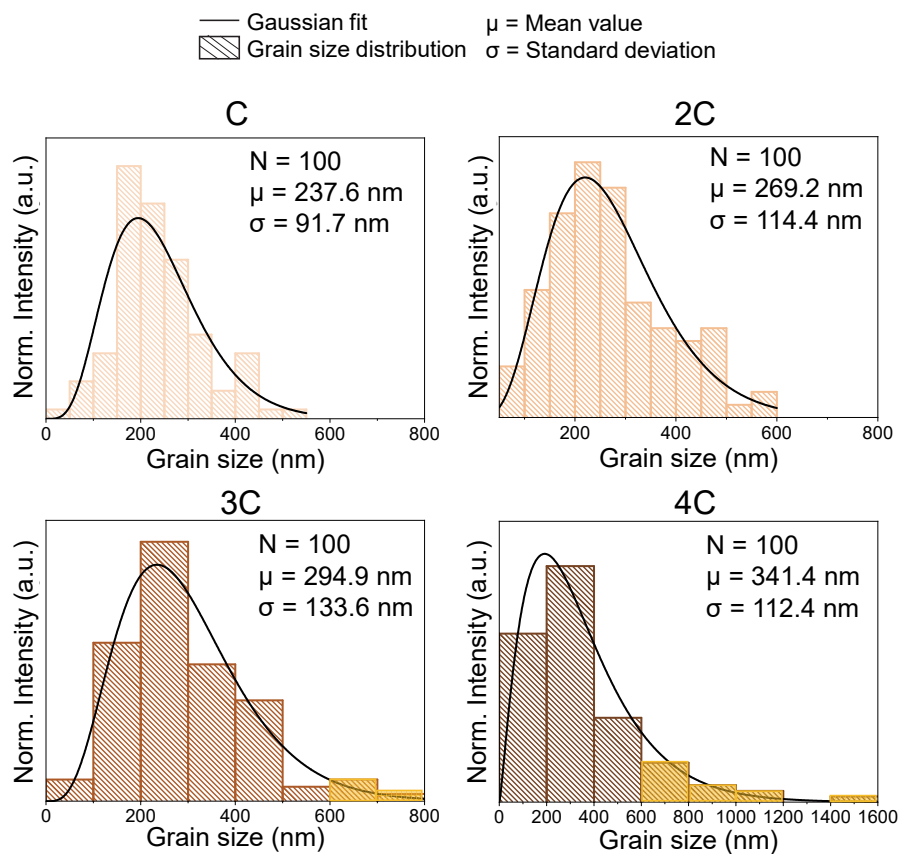
**Figure A. 1.** (a) XRD pattern, (b) photoluminescence (PL) spectrum excitation wavelength  $\lambda = 450\text{nm}$ , and (c) absorption spectrum of vacuum co-evaporated MAPbI<sub>3</sub>.



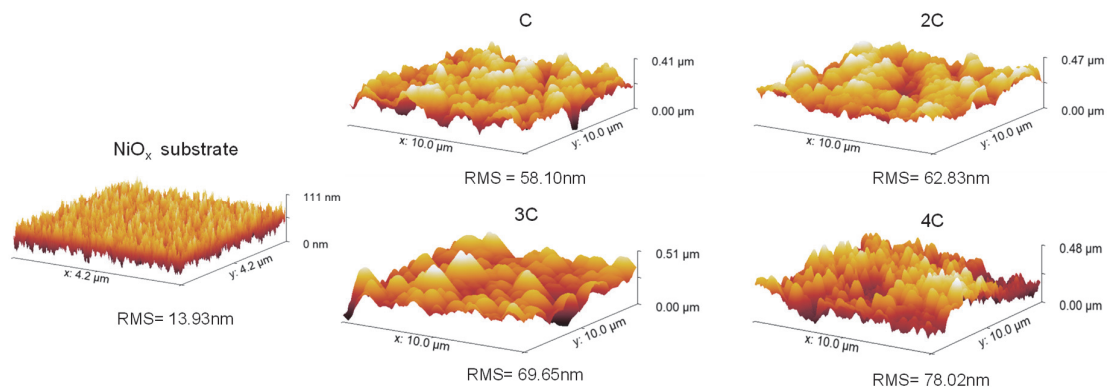
**Figure A. 2.** Evolution over time for PbI<sub>2</sub> rate, MAI rate, and chamber pressure for MAPbI<sub>3</sub> thermally evaporated performed at C- 4C conditions (indicated in each panel).



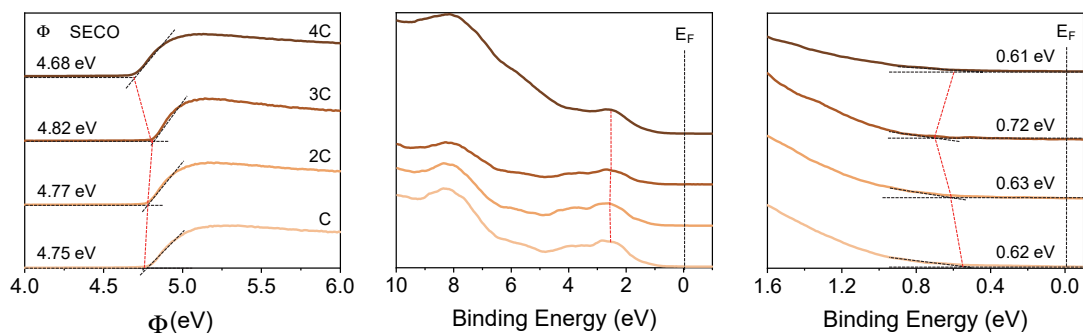
**Figure A. 3.** (a) Top view and (b) cross-sectional SEM images of the perovskite material formed on NiO<sub>x</sub> substrates under different evaporation rates (C to 4C).



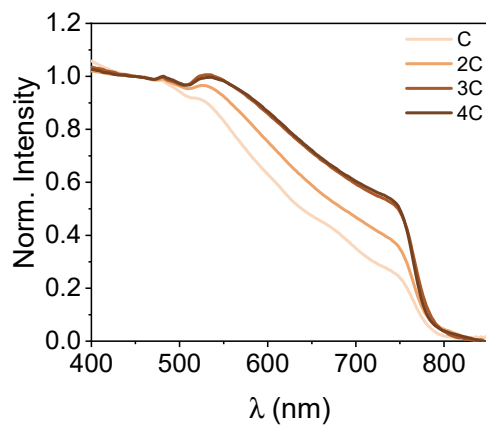
**Figure A. 4.** Estimated grain size distribution of MAPbI<sub>3</sub> films deposited on NiO<sub>x</sub> substrates under different evaporation rates (C to 4C). The orange region highlights the formation of large crystals over 600 nm.



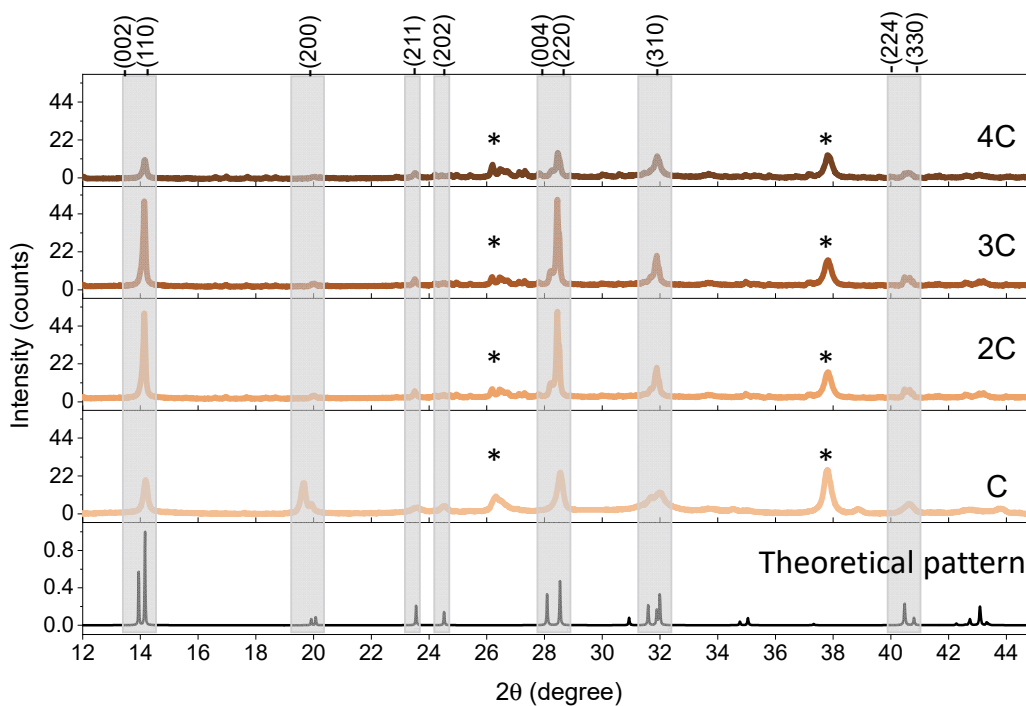
**Figure A. 5.** Atomic force microscopy images (AFM) of MAPbI<sub>3</sub> films deposited on NiO<sub>x</sub> substrates under different evaporation rates (C to 4C). The numbers below each picture indicate the root-mean-square (RMS) values. NiO<sub>x</sub> surface is also included as reference.



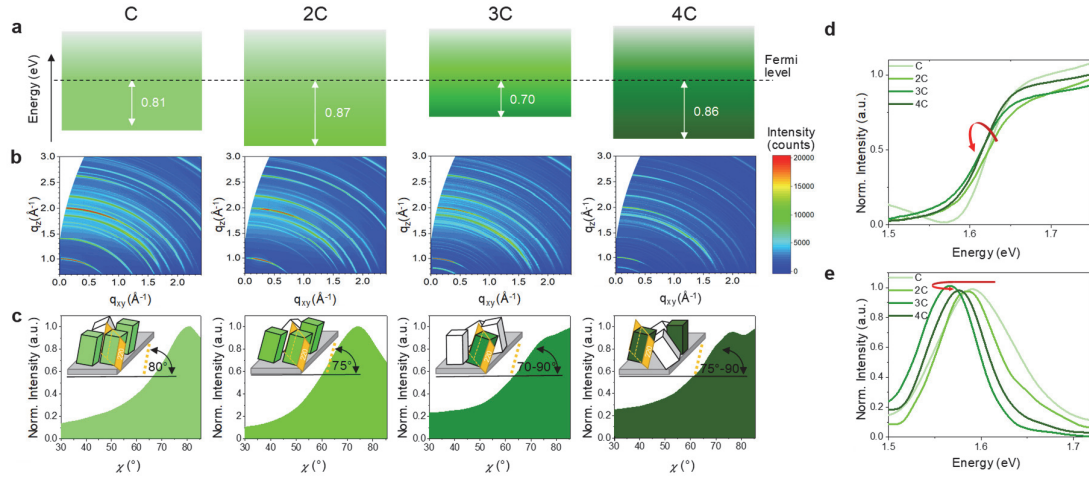
**Figure A. 6.** Secondary-electron cut-offs for work function determination (left) and wide (center) and narrow (right) binding energy range valence spectra of the MAPbI<sub>3</sub> samples prepared on NiO<sub>x</sub> at different evaporation rates (C to 4C).



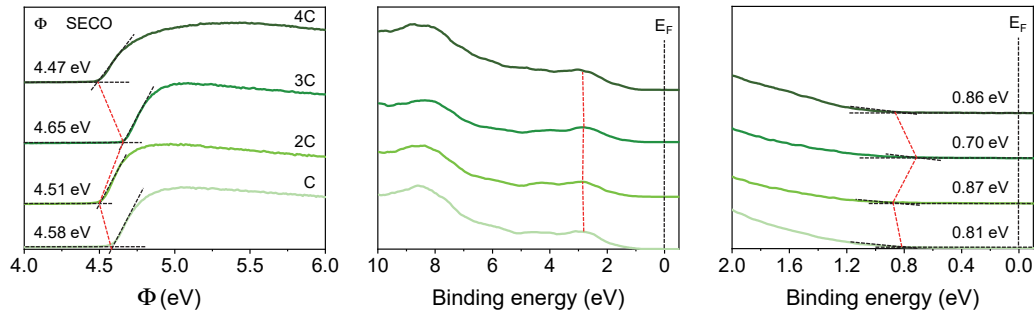
**Figure A. 7.** UV-visible absorption spectra of MAPbI<sub>3</sub> films on NiO<sub>x</sub>.



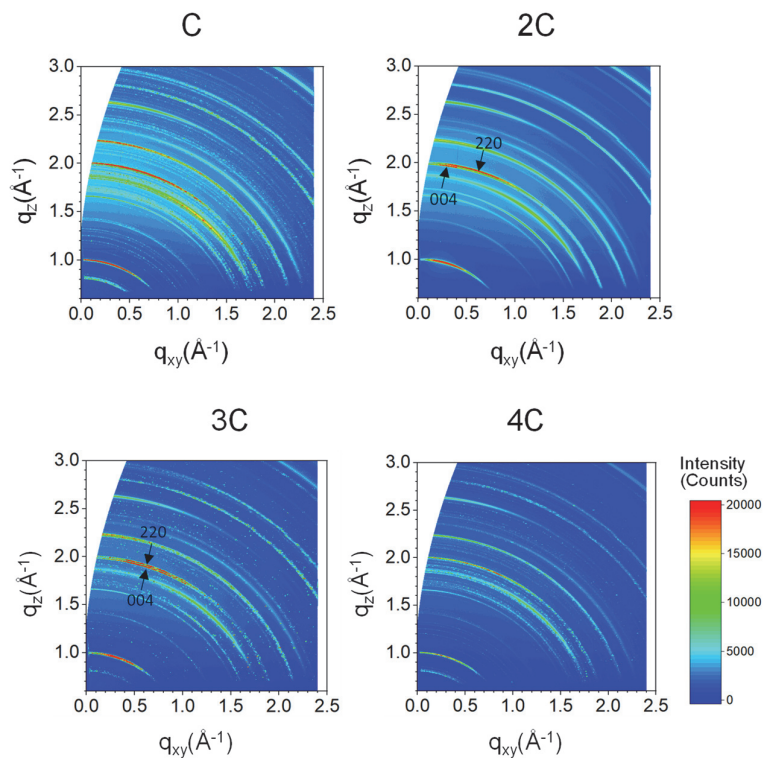
**Figure A. 8.** XRD spectra of MAPbI<sub>3</sub> films grown on NiO<sub>x</sub> at four different evaporation rates, from C to 4C. The star represents diffractions originating from the FTO/NiO<sub>x</sub> substrate.



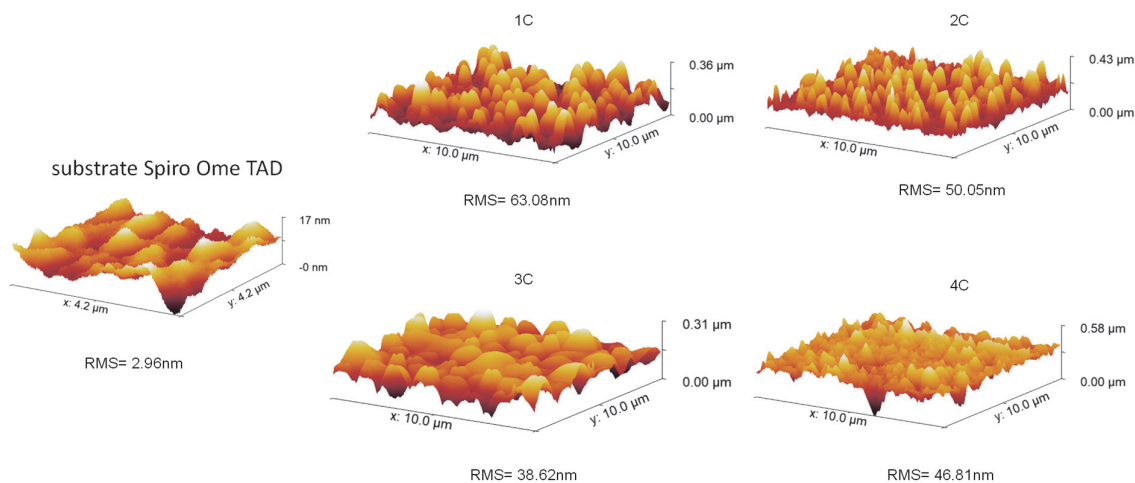
**Figure A. 9.** (a) Energy levels extracted from UPS measurements of films grown c-TiO<sub>2</sub> at several deposition rates (C to 4C). (b) WAXS images of films shown in a. (c) Integration of the azimuthal intensity along the 220 reflex in WAXS (at 2.0 Å<sup>-1</sup>). Inset: schematic of 220 lattice plane orientation showing out-of-plane alignment relative to the substrate plane (cubes with green shading: 220 lattice plane 80° (C), 75° (2C), and 77° (4C) from the substrate). Note the apparent trend in 3C, but with no clearly defined peak intensity (angle). Fewer white cubes indicate a more preferred orientation. (d) UV-visible absorption spectra and (e) PL spectra of films shown in a.



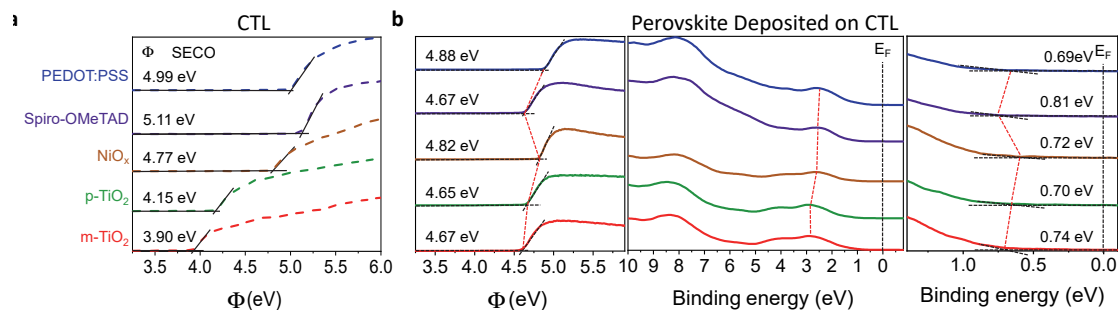
**Figure A. 10.** Secondary-electron cut-offs for work function determination (left) and wide (center) and narrow (right) binding energy range valence spectra of the MAPbI<sub>3</sub> samples deposited on c-TiO<sub>2</sub> at different evaporation rates (1C to 4C).



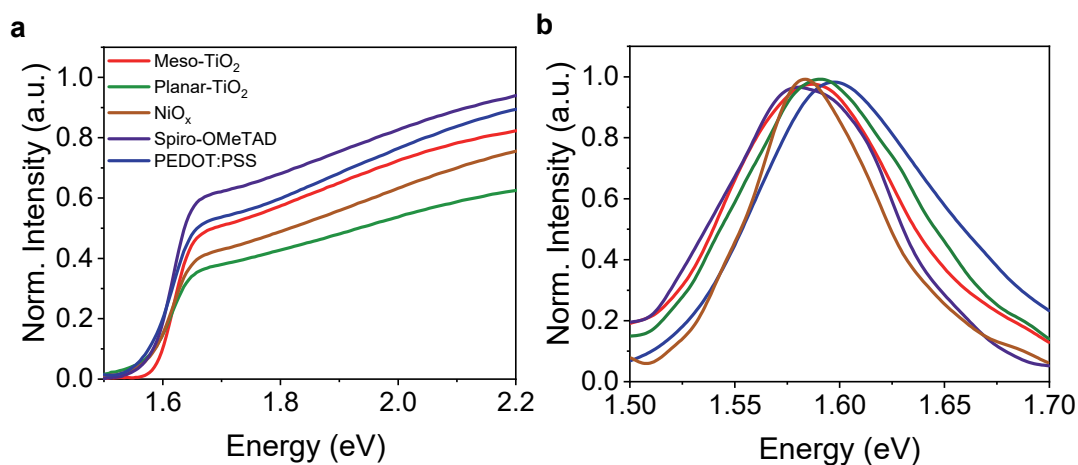
**Figure A. 11.** WAXS images of the MAPbI<sub>3</sub> on underlayer spiro-OMeTAD evaporated under perovskite growth rate (C-4C).



**Figure A. 12.** Atomic force microscopy images (AFM) of MAPbI<sub>3</sub> films deposited on spiro-OMeTAD substrates under different evaporation rates (C to 4C). The numbers below each picture indicate the root-mean-square (RMS) values. Spiro-OMeTAD surface is also included as a reference.

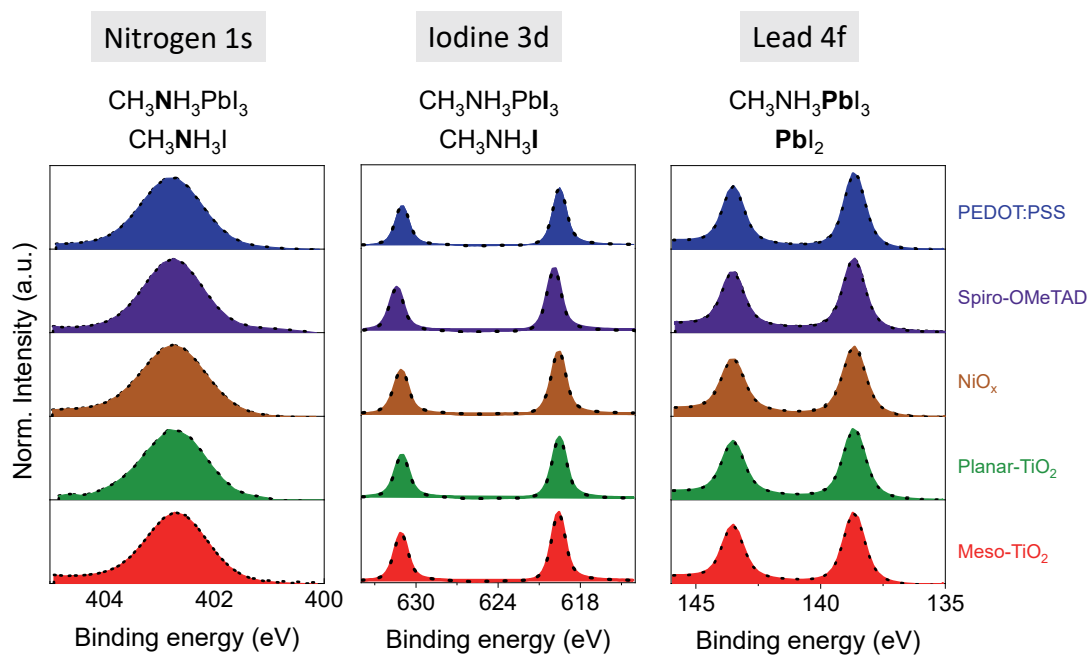


**Figure A. 13.** (a) Secondary-electron cut-off for work function determination of charge transport layers, CTL used in this study. (b) secondary-electron cut-offs for work function determination (left), and wide (center) and narrow (right) binding energy range valence spectra of the MAPbI<sub>3</sub> prepared on CTLs.

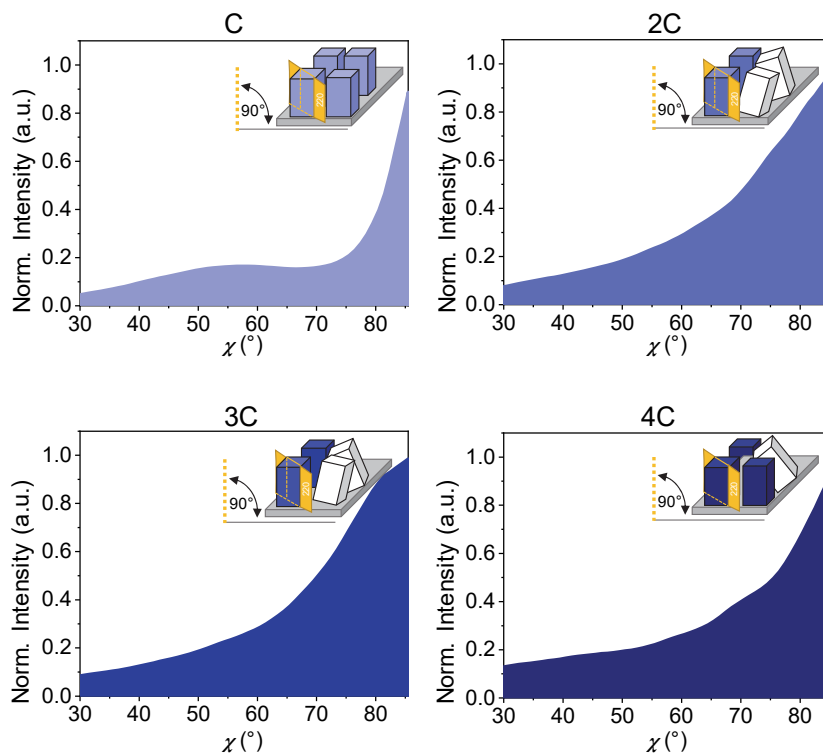


**Figure A. 14.** (a) Absorption spectra and (b) PL spectra of MAPbI<sub>3</sub> grown on n- and p-type semiconductor underlayers at the same evaporation condition (3C).

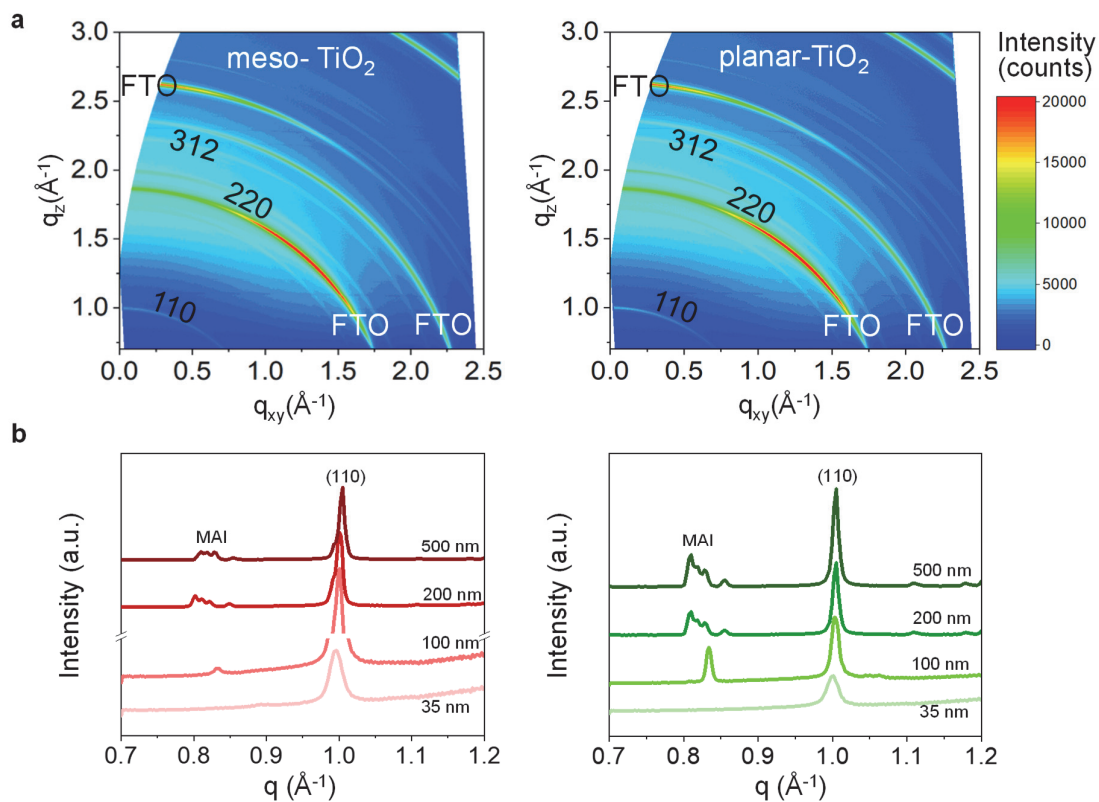




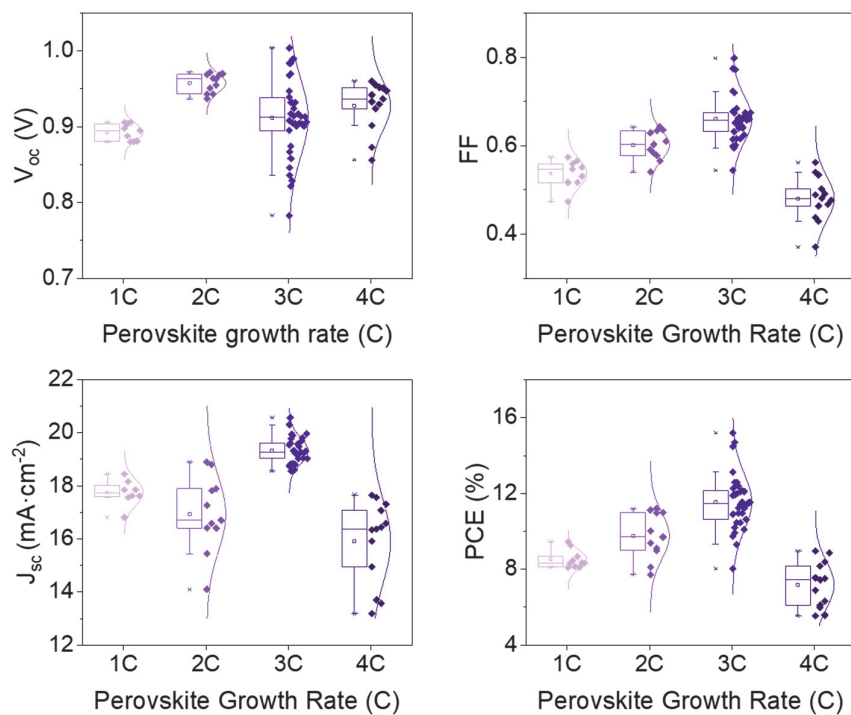
**Figure A. 15.** XPS spectra from MAPbI<sub>3</sub> formed on the different n- and p-type semiconductors.



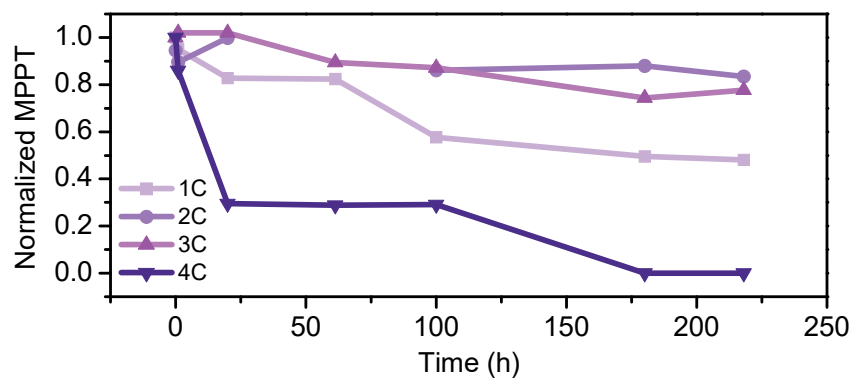
**Figure A. 16.** Azimuth integrated WAXS data for  $2.0 \text{ \AA}^{-1}$  for  $\text{MAPbI}_3$  deposited on PEDOT:PSS grown under several evaporation rates (from C to C<sub>4</sub>). Inset: schematic of grains with 220 lattice plane showing out-of-plane alignment relative to the substrate (cubes with blue shading always perpendicular to the substrate). Fewer white cubes indicate a more defined preferred orientation.



**Figure A. 17.** (a) WAXS images of the seeding layer MAPbI<sub>3</sub> (35 nm thickness). (b) Integrated q-data of the WAXS images for the four different thicknesses on meso-TiO<sub>2</sub> and planar-TiO<sub>2</sub> underlayers.



**Figure A. 18.** Statistics of PSCs performance ( $PCE$ ,  $V_{oc}$ ,  $J_{sc}$ , and  $FF$ ) of films deposited on spiro-OMeTAD under different crystallization speeds ( $PCE$ ,  $V_{oc}$ ,  $J_{sc}$ , and  $FF$ ) for a device with HTM spiro-OMeTAD.



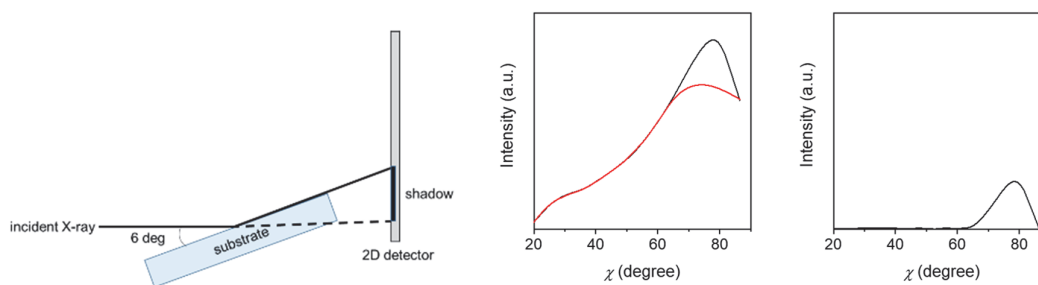
**Figure A. 19.** Stability test performed at maximum power point tracking (MPPT) under continuous illumination of MAPbI<sub>3</sub> cells prepared via thermal evaporation at different deposition rates (from C to 4C).

Table A. 1. Photovoltaic parameters of J-V curves shown in Figure 6.

Perovskite Growth Rate	$V_{oc}$ (V)	$J_{sc}$ ( $\text{mA}\cdot\text{cm}^{-2}$ )	FF	PCE (%)
C ( $0.18 \text{ \AA}\cdot\text{s}^{-1}$ )	0.89	18.45	0.574	9.46
2C ( $0.36 \text{ \AA}\cdot\text{s}^{-1}$ )	0.93	18.90	0.629	11.12
3C ( $0.54 \text{ \AA}\cdot\text{s}^{-1}$ )	0.98	19.94	0.774	15.19
4C ( $0.72 \text{ \AA}\cdot\text{s}^{-1}$ )	0.94	17.66	0.539	8.95

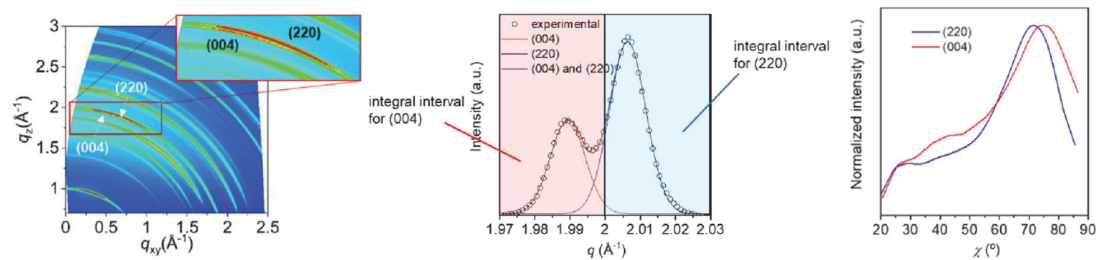
## Supporting Notes

Due to the instrument configuration, the substrate's shadow provides zero intensity in the  $\chi < 20$  region, and it is therefore neglected for the data analysis (see schematic below). All data include the background signal as it did not alter the signal interpretation. For reference, here below are represented two plots with (right) and without (left) background subtraction. The plots correspond to the Integration of the azimuthal intensity along with the 220 reflexes in the WAXS pattern of the film grown at C deposition rate (peak data in black, background in red).



For peak analysis, we selected the  $q_z \sim 2.0 \text{ \AA}^{-1}$  region, which contains two diffraction lines at  $1.99 \text{ \AA}^{-1}$  or  $2.01 \text{ \AA}^{-1}$  for (220) and (004) planes, respectively, and are clearly resolvable by 2D-WAXs (see below). Given that the significance of the peak shift is determined

by the total resolution of the measurement system, including the intensity resolution, small peak shifts in crystal orientation can be easily discerned by the 2D-WAXs profile.



# Appendix B: Supplementary Information to Chapter 5

## *Materials and methods*

### *Materials.*

All chemicals were purchased from Sigma Aldrich and were used as received without any further purification unless and otherwise stated.

### *Perovskite powder synthesis:*

The  $\delta$ -FAPbI<sub>3</sub> powder was synthesized through a previously reported room temperature precipitation method<sup>1</sup> where 2.675 mmol FAI (synthesized from formamidine acetate<sup>1</sup>) was dissolved in 30 ml of acetonitrile (HPLC grade, Alfa Aesar) by stirring. 2.075 mmol of PbI<sub>2</sub> (99%) was added to the stirring solution and continued the stirring for another 24 hours. The yellow powders were filtered, and the residual PbI<sub>2</sub> and FAI were removed by a five-time washing with acetonitrile solvent followed by a one-time wash with diethyl ether. Roto-evaporator was used to remove the solvents, and vacuum dried powder was used for further characterizations.

The  $\alpha$ -CsFAPbI<sub>3</sub> powder was synthesized by annealing the previously reported  $\delta$ -CsFAPbI<sub>3</sub> powder in a tube furnace at 150 °C for 1 hour under N<sub>2</sub> atmosphere. Then obtained  $\alpha$ -CsFAPbI<sub>3</sub> powder was transferred to a clean vial and kept in the glovebox until use.

### *Underlayer preparation*

Thin films were fabricated on fluorine-doped tin oxide (FTO)-coated glass substrates (TEC-15AX, NSG group) previously cleaned by a sequential sonication treatment in a 2% Hellmanex solution, acetone, and isopropanol, followed by ultraviolet–ozone treatment for 15 min. A compact blocking layer of TiO<sub>2</sub> (planar-TiO<sub>2</sub>, 30 nm thick film) was then deposited onto the FTO-coated glass substrate by spray pyrolysis, using a titanium diisopropoxide bis(acetylacetonate) (TAA) solution (Sigma-Aldrich) in ethanol (1ml of TAA in 15ml ethanol), and then sintered at 450 °C for 30 min. Then, a 20 nm SnO<sub>2</sub> was

prepared by dissolving  $\text{SnCl}_4$  (Acros) in deionized water (12  $\mu\text{l}$  in 988  $\mu\text{l}$  water). This solution was spin-coated at 3000 rpm for 30 s (1000 rpm/s acceleration) on top of the meso  $\text{TiO}_2$ . After annealing at 190°C for 1h a 20 nm thick layer was formed. The MeO-2PACz solution was prepared, weighing 1.5g into ethanol. The solution was sonicated for 15min. Then the solution was ITO substrates, which were cleaned 10min additionally in the oxygen plasma before the solution was spin-coated in a nitrogen-filled glove-box. The solution was spin-coated at 4000 rpm for 35s and directly annealed for 10 min at 100°C.  $\text{MoO}_3$ , TaTm, spiro-OMeTAD,  $\text{C}_{60}$  BCP were evaporated in a PRO Line PVD 75 vacuum chamber from Kurt J. Lesker Company equipped with four thermally controlled sources. 5nm  $\text{MoO}_3$  was evaporated at a rate of 0.1 Å/s at a 76 A, the 10nm spiro-OMeTAD was prepared at a rate of 0.5 Å/s at ~290°C, 10nm TaTm was evaporated at a rate of 0.1 Å/s at ~295-300°C.

The prepared layers were transferred to the PRO Line PVD 75 vacuum chamber from Kurt J. Lesker Company, equipped with four thermally controlled sources. The crucibles were filled with the perovskite precursors, and power was applied to sublime the perovskite powders.  $\text{CsFAPbI}_3$  perovskite powder was evaporated at 0.35Å/s (16.2% power), and  $\text{FAPbI}_3$  was evaporated at a rate of 1.0-1.5 Å/s (16.2%) during a vacuum pressure of  $\sim 1 \cdot 10^{-6}$  mbar. During perovskite deposition, the deposition rate of each precursor was kept constant and monitored by independent quartz microbalance crystal sensors (QCMs). The substrates were kept at room temperature and under rotation of 5 r.p.m.

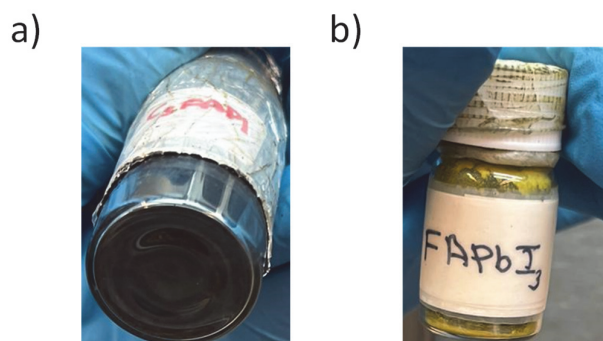
#### *Materials Characterizations:*

The XRD patterns of the prepared films were measured using a D8 Advance diffractometer from Bruker (Bragg-Brentano geometry, with an X-ray tube  $\text{Cu K}\alpha$ ,  $\lambda = 1.5406$  Å). Steady-state photoluminescence (PL) measurements were recorded with an LS-55 fluorescence spectrometer (PerkinElmer, Inc.) at an excitation wavelength  $\lambda = 450$  nm. TrPL was measured with a Fluorolog TCSPC (HORIBA, Ltd.) was used to measure time-resolved photoluminescence (TRPL) with 760nm as the detection wavelength.

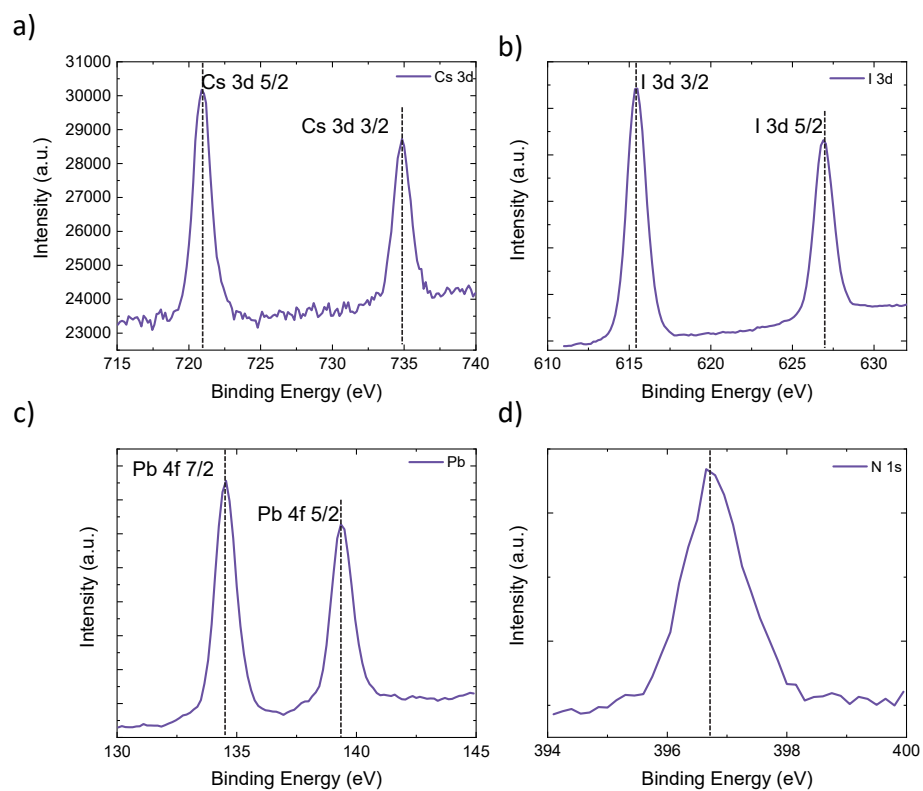


X-ray scattering (2D-WAXS) patterns represented in reciprocal lattice space were performed at SPring-8 on beamline BL19B2. The samples were irradiated with an X-ray energy of 12.39 keV ( $\lambda = 1 \text{ \AA}$ ) at a fixed incident angle on the order of  $0.12^\circ$  through through a Huber diffractometer. The 2D-WAXS patterns were measured with a two-dimensional image detector (Pilatus 300K). The X-ray photoelectron spectroscopy (XPS) measurements were carried out on a VersaProbe II (Physical Electronics, Inc.) with a monochromatic Al  $K_\alpha$  X-ray source operating at 1486.6 eV. The spectra were referenced using the Pb 4f signal. Data were processed using CasaXPS.

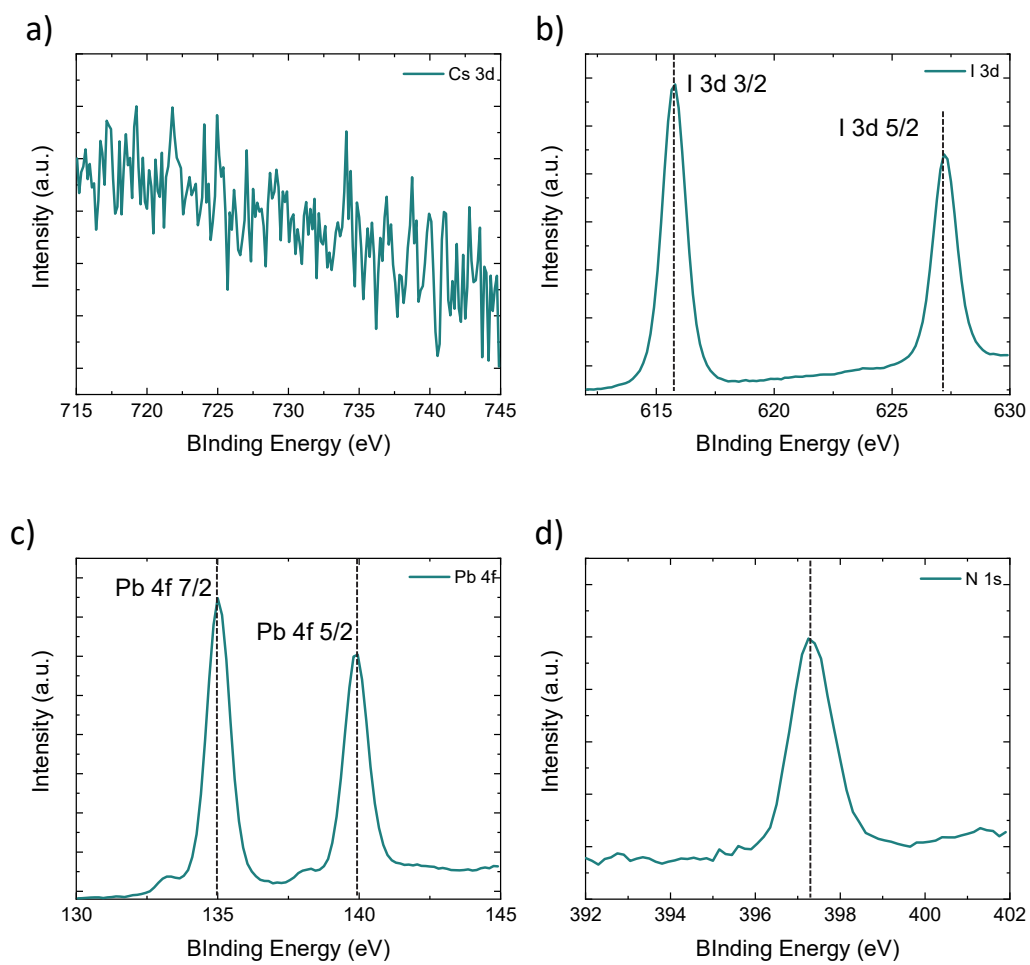
### *Supporting Figures*



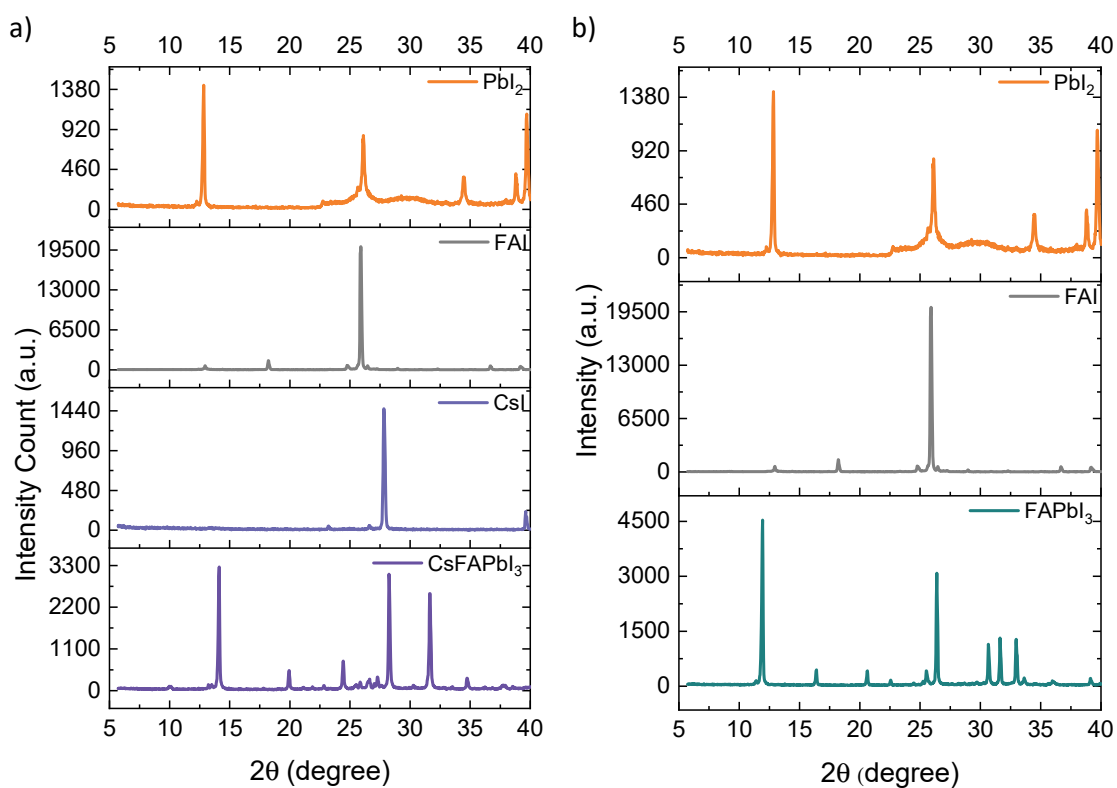
**Figure B. 1.** Photographs of the pre-synthesized perovskite material used for the single-source evaporation a)  $\delta$ -CsFAPbI<sub>3</sub> and b)  $\delta$ -FAPbI<sub>3</sub>



**Figure B. 2.** XPS spectra of pre-synthesized  $\delta$ -CsFAPbI<sub>3</sub> powder. a) Cs 3d; b) I 3d; c) Pb 4f; d) N 1s.

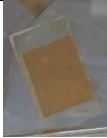
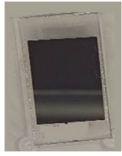
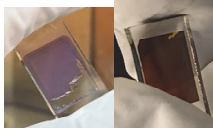
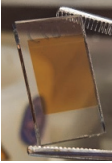
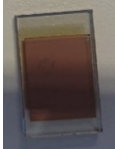


**Figure B. 3.** XPS spectra of pre-synthesized  $\delta$ -FAPbI<sub>3</sub> powder. a) Cs 3d b) I 3d c) Pb 4f d) N 1s.



**Figure B. 4.** The phase purity of synthesized powders and their precursor materials a)  $\alpha$ -CsFAPbI<sub>3</sub> powder and b)  $\delta$ -FAPbI<sub>3</sub> powder.

**Table B. 1.** Perovskite powder vacuum-deposition rate correlated to crystal phase with a photograph of the deposited film.

perovskite powder	deposition rate, Å/s	phase	photograph of the as-deposited layer
CsFAPbI <sub>3</sub>	0.25	δ	
	0.35	α	
	1.0-1.05	α/δ	
FAPbI <sub>3</sub>	1.0-1.05	δ	
	3.0-3.05	α/δ	

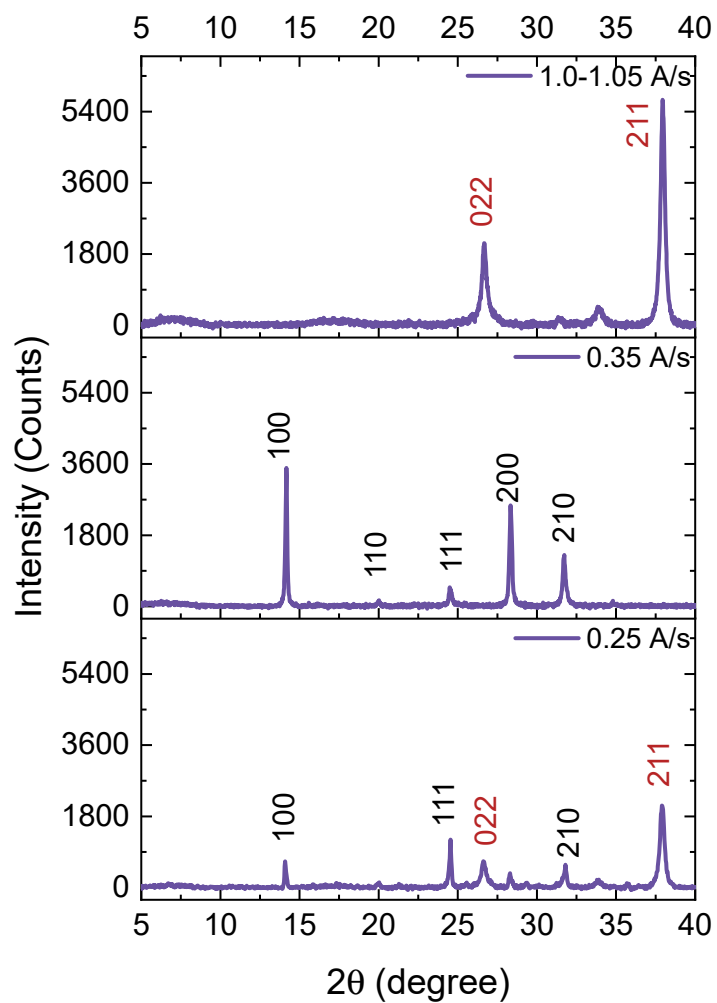


**Figure B. 5.** a) XRD pattern of a thin film of material deposited at a rate of 1.0-1.05 A/s, 0.35 A/s, and 0.25A/s. Planes in black indicate  $\alpha$ -CsFAPbI<sub>3</sub>, planes in brown indicate  $\delta$ -CsFAPbI<sub>3</sub>.

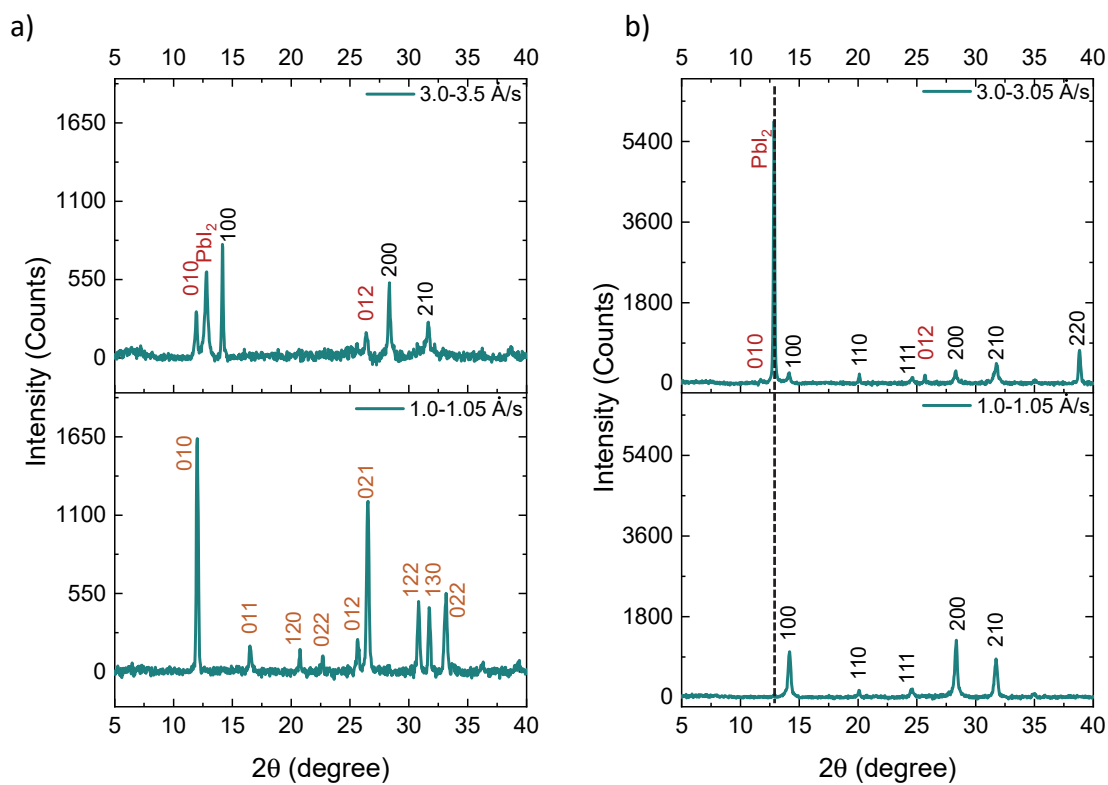


**Figure B. 6.** XRD pattern of a thin film of material deposited at a rate of 1.0-1.05 Å/s 3.0-3.05 Å/s.a) as-deposited b) after annealing. Planes in black indicate  $\alpha$ -FAPbI<sub>3</sub>, planes in brown indicate  $\delta$ -FAPbI<sub>3</sub>.

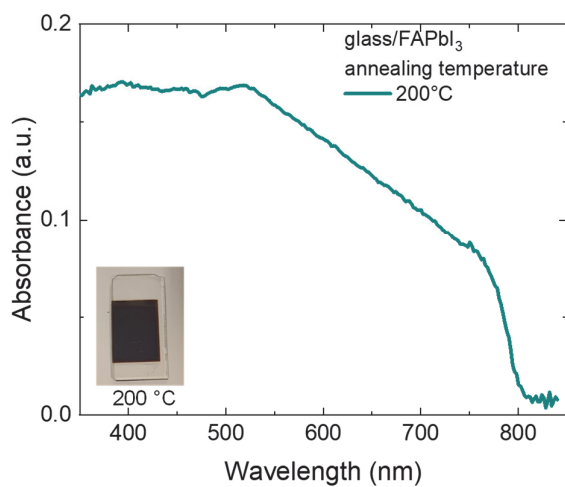


**Figure B. 7.** UV/Vis of FAPbI<sub>3</sub> sample deposited at a rate of 1.0-1.05 Å/s as-deposited and annealed at 200°C, inset photograph of the film annealed at 200°C.

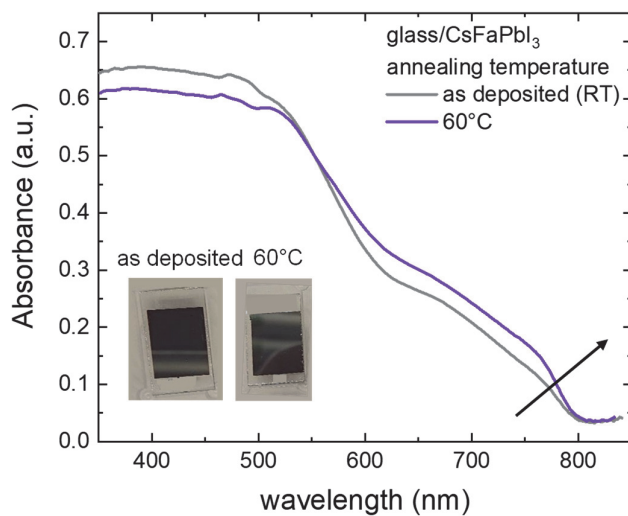


**Figure B. 8. a)** UV/Vis of CsFAPbI<sub>3</sub> as-deposited and annealed at 60°C of thin films deposited at a rate of 0.35 Å/s. Inset photograph of thin films.



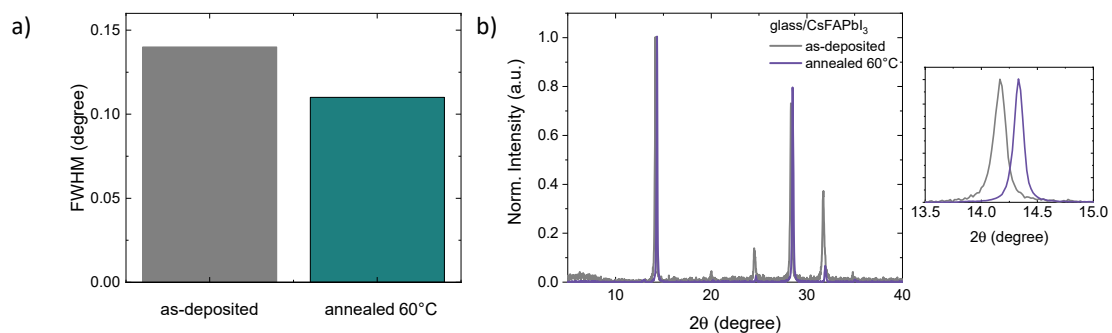


**Figure B. 9.** a) FWHM values for as-deposited and annealed CsFAPbI<sub>3</sub> films b) XRD pattern indicating shift for annealed CsFAPbI<sub>3</sub> film.

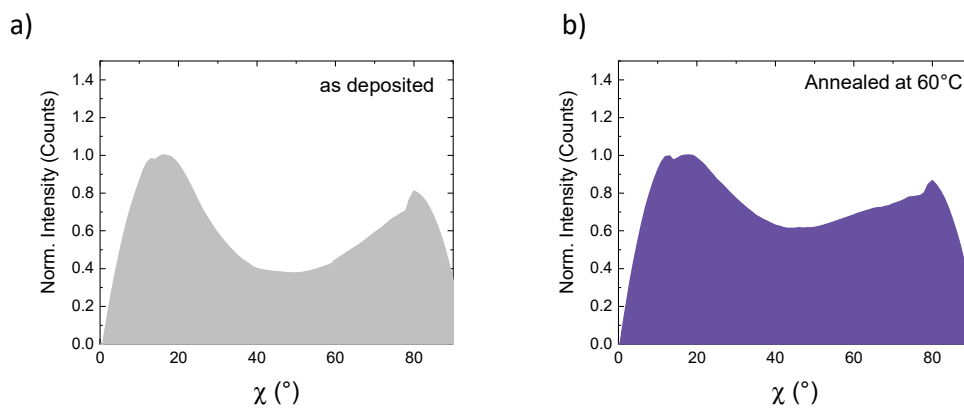


**Figure B. 10.** Integration of the azimuthal intensity along 100 reflex ( $1.0\text{\AA}^{-1}$ ) of GIWAXS images a) of the as-deposited CsFAPbI<sub>3</sub> film b) of the CsFAPbI<sub>3</sub> film annealed at 60°C.

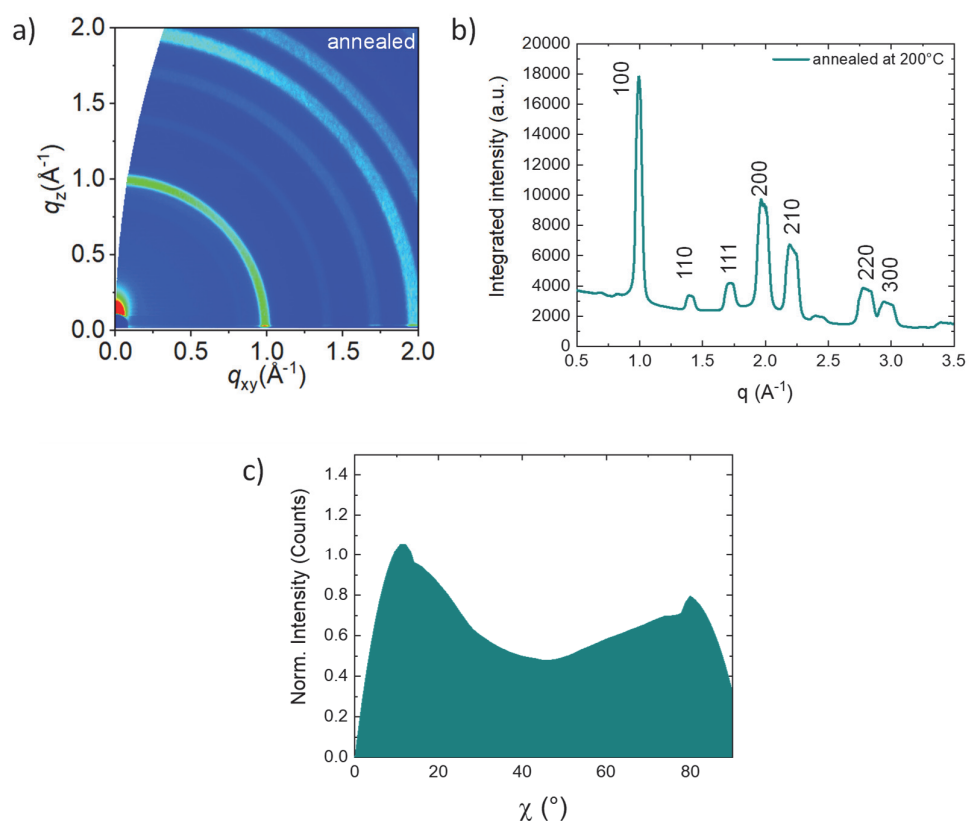


**Figure B. 11.** GIWAXS images taken at an angle of  $0.12^{\circ}$  of a) FAPbI<sub>3</sub> film as deposited annealed at 200°C b) Integrated  $q$ -data of the GIWAXS images for FAPbI<sub>3</sub> film after post-annealing at 200°C c) Integration of the azimuthal intensity along 100 reflex ( $1.0 \text{ \AA}^{-1}$ ) of GIWAXS images of annealed FAPbI<sub>3</sub> film.

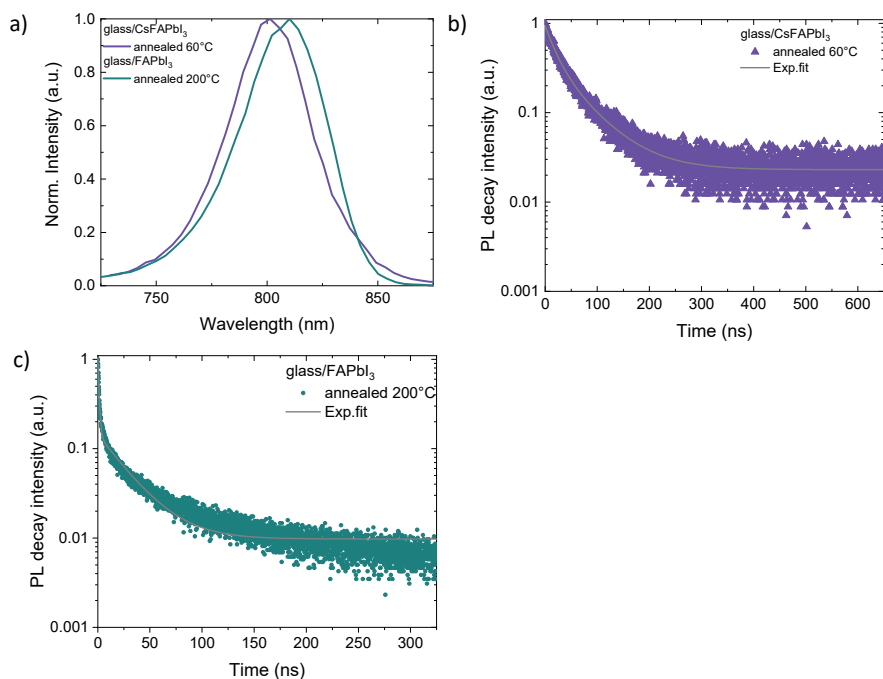


**Figure B. 12.** a) PL spectra of annealed glass/CsFAPbI<sub>3</sub> and glass/FAPbI<sub>3</sub> film b) TRPL decay ( $\lambda_{exc}=640\text{nm}$ ) of the annealed glass/CsFAPbI<sub>3</sub> film, c) TRPL decay ( $\lambda_{exc}=640\text{nm}$ ) of the annealed glass/FAPbI<sub>3</sub> film.

**Table B. 2.** Fitted decay parameters extracted from time-resolved photoluminescence (TrPL) spectra.

Name		$\tau_1$ (ns)	$\tau_2$ (ns)
CsFAPbI <sub>3</sub>	As deposited	$20.26 \pm 0.32$	$76.95 \pm 0.46$
	Annealed 60°C	$18.89 \pm 0.45$	$61.61 \pm 1.24$
FAPbI <sub>3</sub>	As deposited	$3.12 \pm 0.03$	$24.07 \pm 0.19$
	Annealed 200°C	$1.09 \pm 0.01$	$27.03 \pm 0.25$

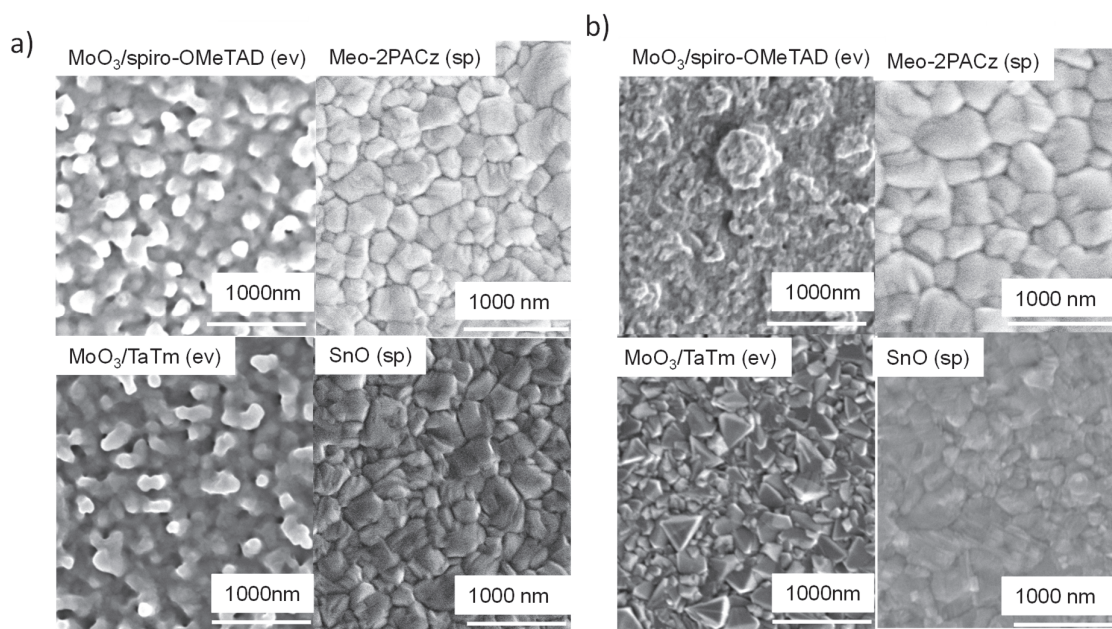


**Figure B. 13.** Top-view SEM images of annealed perovskite deposited on different underlayers a)  $\alpha$ -CsFAPbI<sub>3</sub> (0.35 Å/s) b)  $\alpha$ -FAPbI<sub>3</sub> (1.0-1.05 Å/s): (ev)=evaporated layer and (sp)=spin-coated layer deposited at 0.35 Å/s.

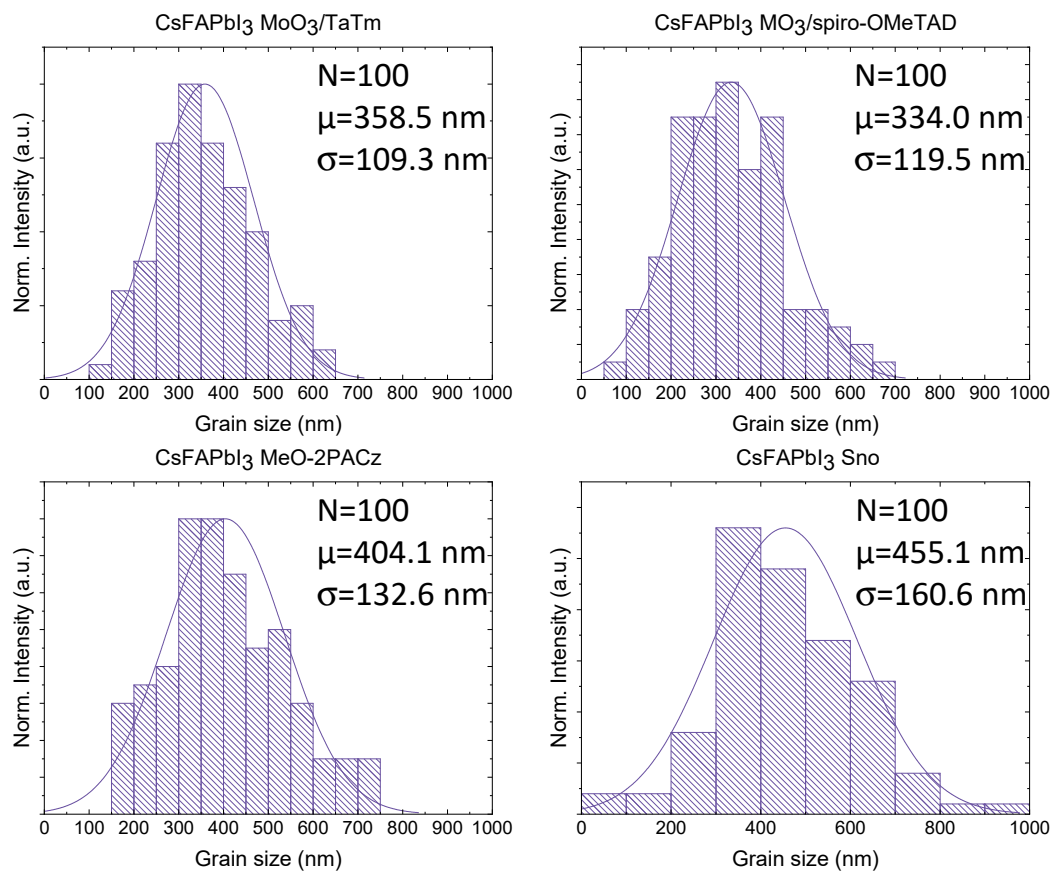


**Figure B. 14.** Grain size distribution extracted from top-view SEM images for  $\eta$ -CsFAPbI<sub>3</sub> on top of the different underlayers.

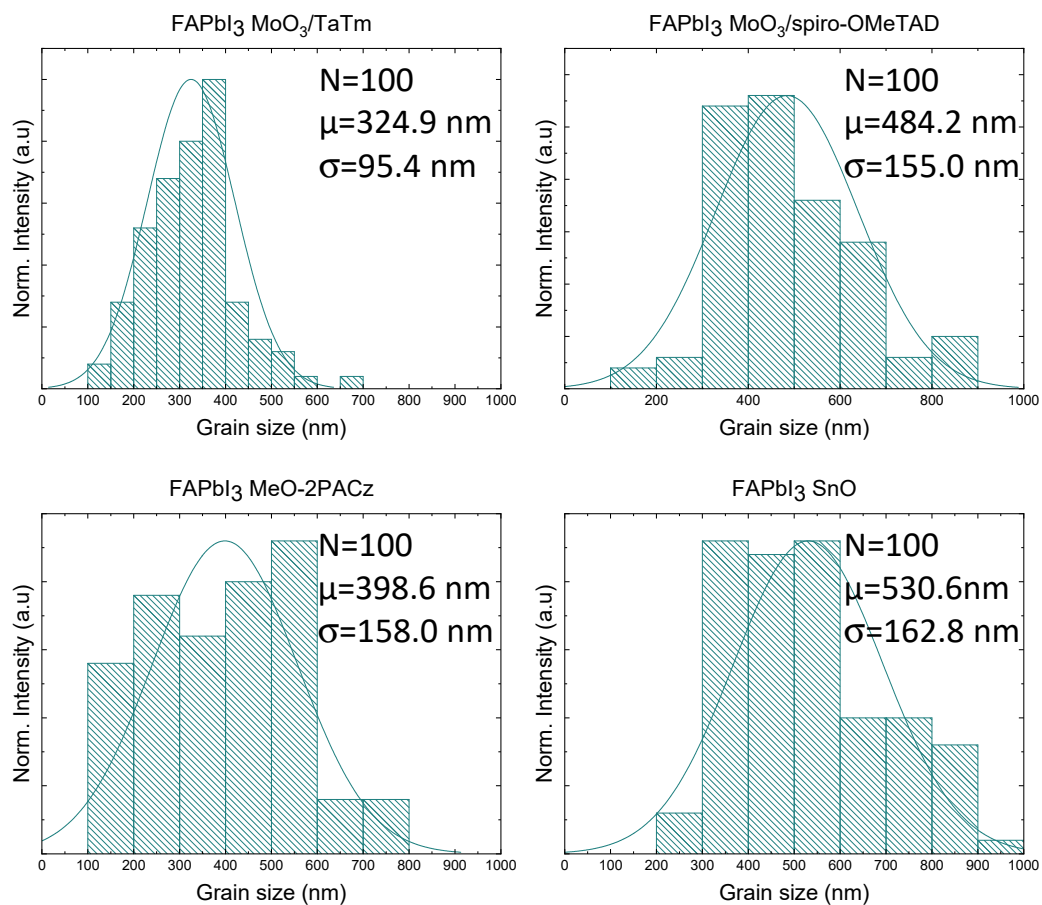


**Figure B. 15.** Grain size distribution extracted from top-view SEM images for  $\alpha$ -FAPbI<sub>3</sub> on top of the different underlayers.

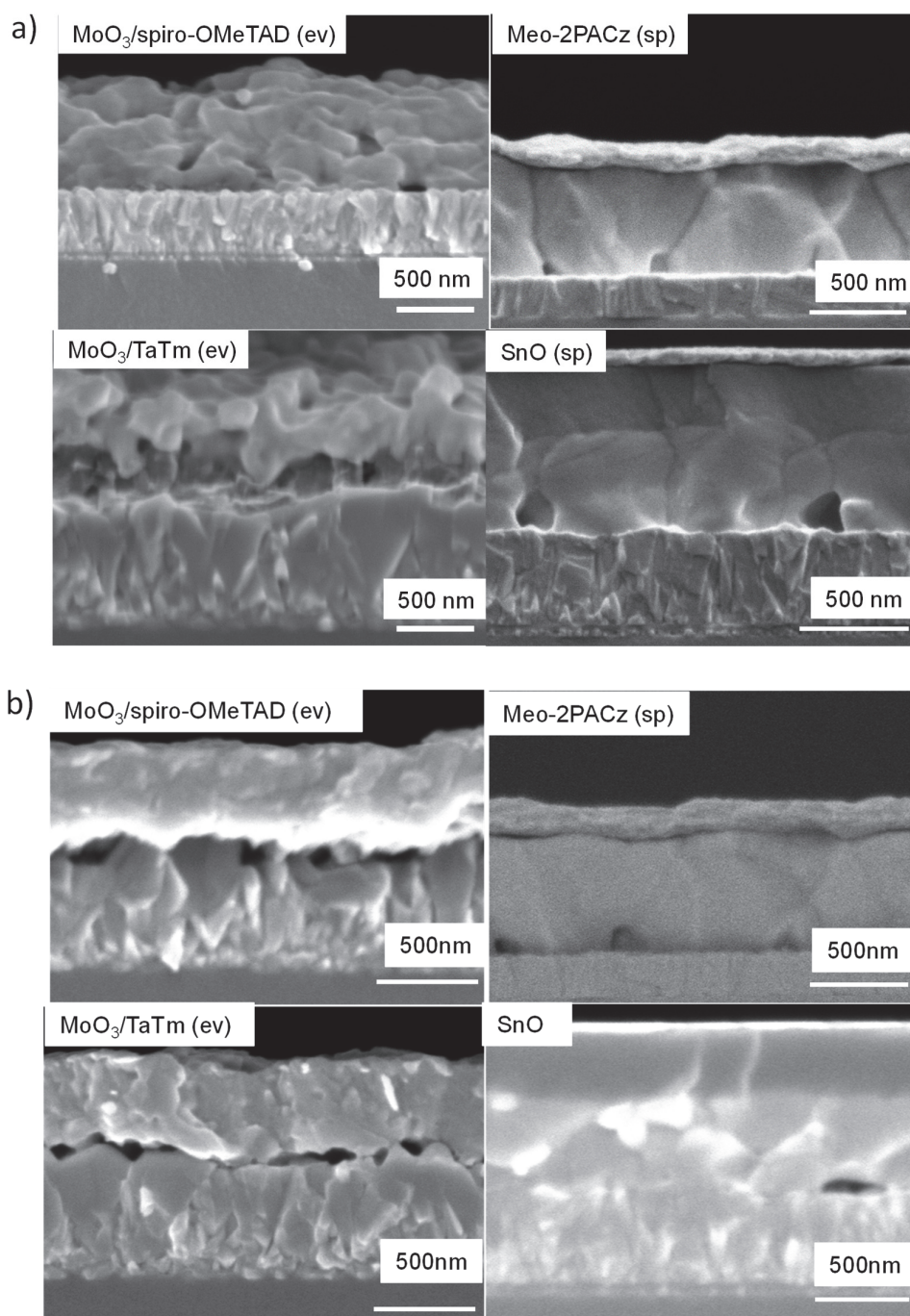


**Figure B. 16.** Cross-section SEM images of annealed perovskite deposited on different under-layers a)  $\alpha$ -CsFAPbI<sub>3</sub> (0.35 Å/s) b)  $\alpha$ -FAPbI<sub>3</sub>, (1.0-1.05 Å/s): (ev)=evaporated layer and (sp)=spin-coated layer deposited at 0.35 Å/s.





# Appendix C: Supplementary Information to Chapter 6

## *Methods*

### *Perovskite thin-film and solar cell fabrication*

Thin films were fabricated on fluorine-doped tin oxide (FTO)-coated glass substrates (TEC-15AX, NSG group) which were cleaned by a sequential sonication treatment (10 min each) in a 2% Helmanex solution, water, deionized water, and isopropanol. The cleaning of the FTO was then followed by ultraviolet- $O_3$  treatment for 30 min. For the samples containing  $cTiO_2$ , titanium diisopropoxide bis(acetylacetonate)(TAA) (Sigma Aldrich) in isopropanol solution (1:15 v/v) was deposited by spray pyrolysis, forming after annealing at  $450^\circ C$  for 30 min a 30nm thick compact  $TiO_2$  layer. The prepared layers were then transferred to the PRO Line PVD 75 vacuum chamber from Kurt J. Lesker Company, equipped with four thermally-controlled sources.  $C_{60}$  was filled into a crucible and heated up until the sublimation temperature of  $\sim 450^\circ C$  at a vacuum pressure of  $\sim 1 \cdot 10^{-6}$  mbar. The deposition rate was kept constant at  $0.15 \text{ \AA s}^{-1}$  and was monitored by an independent quartz microbalance crystal sensor (QCMs). The substrates were kept at a rotation of 5 r.p.m at room temperature during the perovskite deposition. The perovskite precursors,  $PbI_2$  (TCI) and methylammonium iodide (MAI) (Lumtec) were filled into the crucibles and heated up until the sublimation temperatures of  $\sim 140^\circ C$  for  $PbI_2$  and  $\sim 120^\circ C$  for MAI at a vacuum pressure of  $\sim 1 \cdot 10^{-6}$  mbar. The deposition rate of each precursor was kept constant at 3.6 and  $0.6 \text{ \AA s}^{-1}$  and monitored by independent QCMs. The substrates were kept at a rotation of 5 r.p.m. at room temperature during the perovskite deposition. For the device fabrication, the FTO-coated substrates were laser etched. The spiro-OMeTAD (Merck) underlayers were deposited by spin-coating at 4000 r.p.m. for 30 s (acc.  $1000 \text{ r.p.m. s}^{-1}$ ) from a chlorobenzene solution (80 mg in 1023  $\mu l$ , 60 mM). The solution was doped with 19  $\mu l$  from a  $517 \text{ mg}\cdot\text{ml}^{-1}$  LiTFSI stock solution and 14  $\mu l$  from a  $376.4 \text{ mg}\cdot\text{ml}^{-1}$  CoTFSI stock solution, both in acetonitrile, then 32  $\mu l$  of TBP was added to all the prepared spiro-OMeTAD solutions.

*Thin-film characterization*

The XRD patterns of the as-prepared films were measured using a D8 Advance diffractometer from Bruker with an X-ray tube Cu K $\alpha$ ,  $\lambda = 1.5406 \text{ \AA}$  Bragg-Brentano geometry. The absorbance spectra were recorded with a Lambda 950S spectrophotometer (PerkinElmer, Inc.). Time-resolved photoluminescence (TRPL) and photoluminescence (PL) spectroscopy were performed by Fluorolog TCSPC (HORIBA, Ltd.) with a picosecond laser with an excitation wavelength of 640 nm and 475 nm, respectively. The detection wavelength of Time-resolved photoluminescence was 760 nm. An ultraviolet photoelectron spectrometer (UPS) equipped with a He-I source ( $h\nu = 21.22 \text{ eV}$ ) (AXIS Nova, Kratos Analytical Ltd, UK) was used to measure the valence band energy, Fermi level, and the work function. The Fermi level of the samples was referenced to that of Au, which was in electrical contact with a sample in UPS measurements. Scanning electron microscopy (SEM) images were recorded by an in-lens detector of FEI Teneo Schottky Field Emission SEM at a tension of 3 kV for top-view and cross-section analysis.

*Device characterization*

$J - V$  curves were measured using a 2400 Keithley system with a Xe-lamp Oriel sol3A sun simulator (Newport Corporation). The system was calibrated to AM1.5G standard conditions using an Oriel 91150 V reference cell ( $J - V$  curves scan rate of  $50 \text{ mV s}^{-1}$  and  $10 \text{ mV}$  voltage step). An NREL-certified KG5-filtered Si-reference diode was used for light intensity calibration. The active area of the cell was defined through shadow masks with a metal aperture of  $0.16 \text{ cm}^2$ . The cells were measured at room temperature in air and without encapsulation. The  $JV$  measurements were done at a constant rate of  $10 \text{ mV s}^{-1}$  and  $10 \text{ mV}$  voltage step for reversed bias after  $5 \text{ s}$  under light soaking. No anti-reflective coating was applied during the measurement.

The impedance spectroscopy (IS) measurements were performed with a BioLogic SP-200 potentiostat. A  $20 \text{ mV}$  AC perturbation was applied. The low-frequency and high-frequencies limits were  $0.1 \text{ Hz}$  and  $1 \text{ MHz}$ , respectively. The analysis of all spectra was done using Zview software.

## Supporting Figures

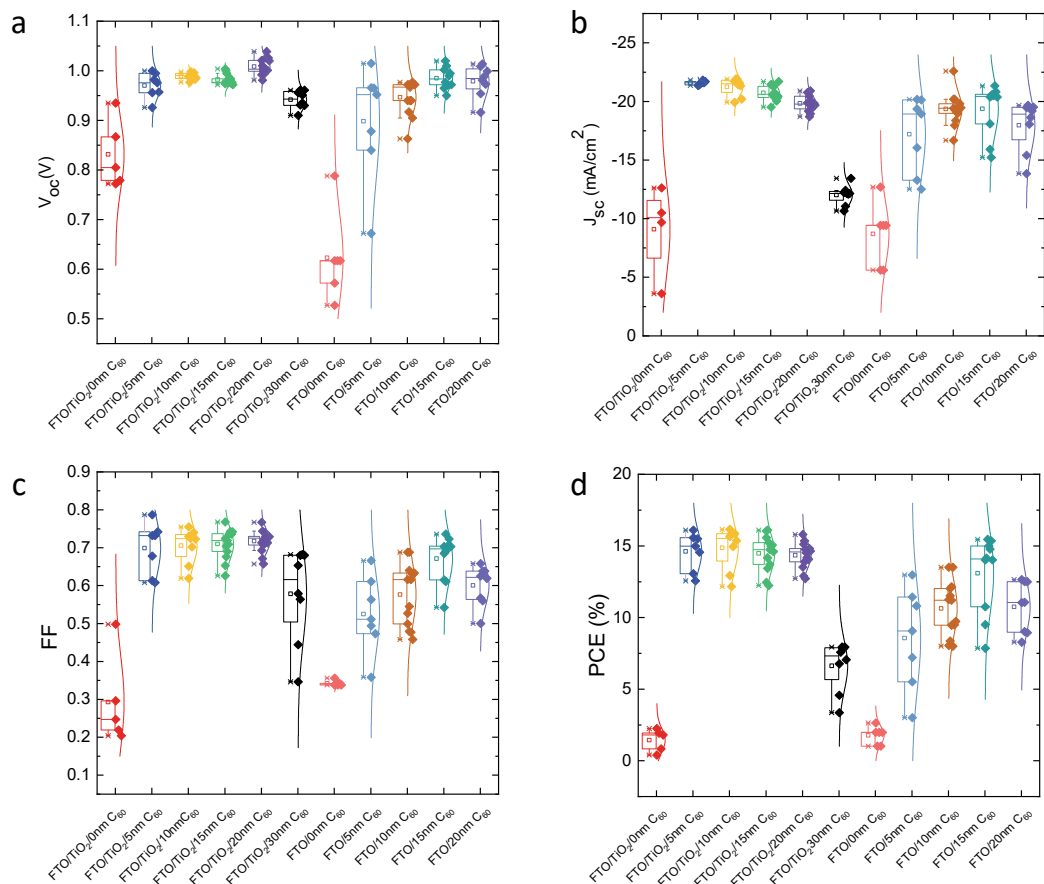


**Figure C. 1.** Statistical data of PSCs containing co-evaporated MAPbI<sub>3</sub> thin films deposited on top of FTO/cTiO<sub>2</sub>/C<sub>60</sub> with the C<sub>60</sub> thicknesses being: 0nm, 5nm, 10nm, 15nm, 20nm, and 30nm and FTO/C<sub>60</sub> with the C<sub>60</sub> thicknesses being: 5nm, 10nm, 15nm, and 20nm, respectively. a) Open-circuit voltage, b) short-circuit current density, c) fill factor, and d) power conversion efficiency.

**Table C. 1.** Average values of the PV parameters are presented in the statistical data.

	C <sub>60</sub> thick- ness (nm)	J <sub>sc</sub> (mA/cm <sup>2</sup> )	V <sub>oc</sub> (V)	FF	PCE (%)
FTO/C <sub>60</sub>	5	-17 ± 3	0.90 ± 0.12	0.53 ± 0.10	9 ± 4
	10	-19.4 ± 1.4	0.95 ± 0.03	0.58 ± 0.08	10.6 ± 1.9
	15	-19 ± 2	0.99 ± 0.02	0.67 ± 0.06	13 ± 3
	20	-18 ± 2	0.98 ± 0.03	0.60 ± 0.05	10.8 ± 1.8
FTO/cTiO <sub>2</sub> /C <sub>60</sub>	5	-21.6 ± 0.2	0.97 ± 0.03	0.70 ± 0.07	14.6 ± 1.3
	10	-21.3 ± 0.8	0.989 ± 0.007	0.71 ± 0.05	14.9 ± 1.4
	15	-20.8 ± 0.6	0.982 ± 0.010	0.71 ± 0.04	14.7 ± 1.1
	20	-19.9 ± 0.7	1.009 ± 0.016	0.72 ± 0.03	14.6 ± 0.8
	30	-12.0 ± 0.8	0.942 ± 0.018	0.58 ± 0.12	6.6 ± 1.7

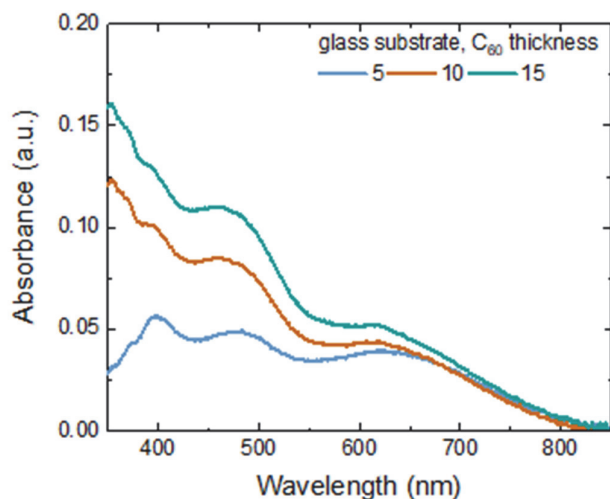


Figure C. 2. Absorbance spectra of the C<sub>60</sub> layers deposited on glass.

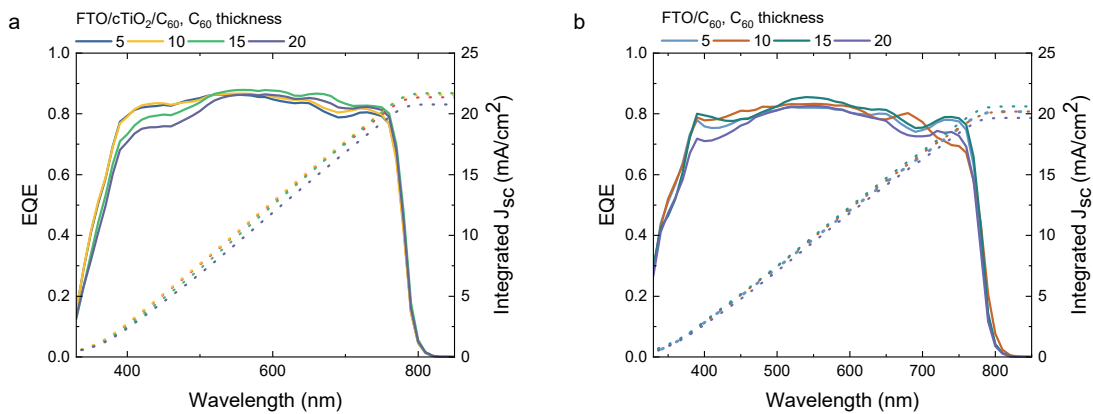
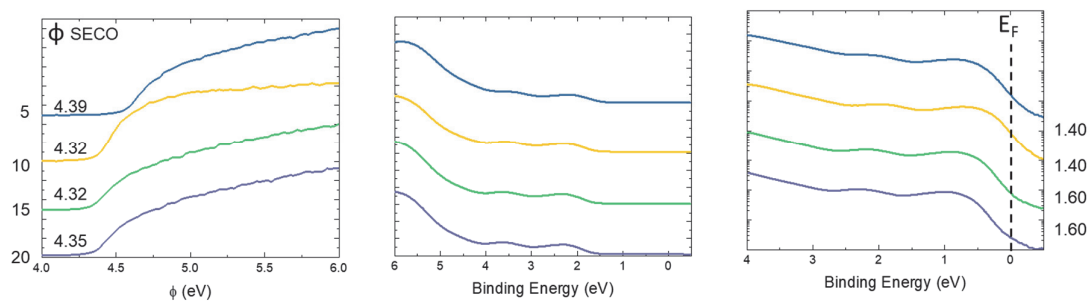
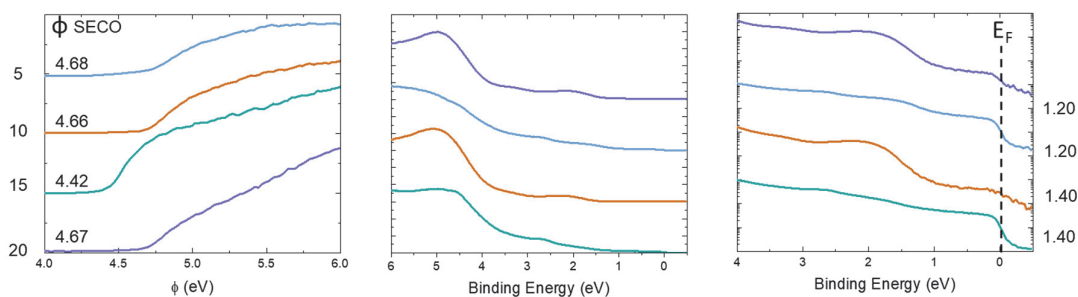


Figure C. 3. External quantum efficiency (EQE) and calculated short-circuit current density integrated from the corresponding EQE spectra for a) FTO/cTiO<sub>2</sub>/C<sub>60</sub> and b) FTO/C<sub>60</sub> with the C<sub>60</sub> thickness being: 5nm, 10nm, 15nm, and 20nm, respectively.



**Figure C. 4.** UPS measurement of the perovskite layer deposited on top of FTO/cTiO<sub>2</sub>/C<sub>60</sub> and different C<sub>60</sub> thicknesses: a) cut-off region, b) and c) valence band region. The work function (WF) can be calculated as  $WF=h\nu-SECO$ ,  $h\nu=21.22$  eV being the energy of the incident photons from a He(I) UV source.



**Figure C. 5.** UPS measurement of the perovskite layer deposited on top of FTO/C<sub>60</sub> and different C<sub>60</sub> thicknesses: a) cut-off region, b) and c) valence band region. The work function (WF) can be calculated as  $WF=h\nu-SECO$ ,  $h\nu=21.22$  eV being the energy of the incident photons from a He(I) UV source.

**Table C. 2.** Co-evaporated MAPbI<sub>3</sub> deposited on top of FTO/cTiO<sub>2</sub>/C<sub>60</sub> and FTO/C<sub>60</sub>, with different C<sub>60</sub> thicknesses. Energy cut-off, work function, and valence band energy level extracted from the corresponding UPS spectra.

	C <sub>60</sub> thickness (nm)	Energy cut-off (eV)	WF (eV)	Ionisation potential IP (eV)
FTO/C <sub>60</sub>	5	1.20	4.68	5.88
	10	1.20	4.66	5.86
	15	1.40	4.42	5.82
	20	1.40	4.67	6.07
FTO/cTiO <sub>2</sub> /C <sub>60</sub>	5	1.40	4.39	5.79
	10	1.40	4.32	5.72
	15	1.60	4.32	5.92
	20	1.60	4.35	5.95

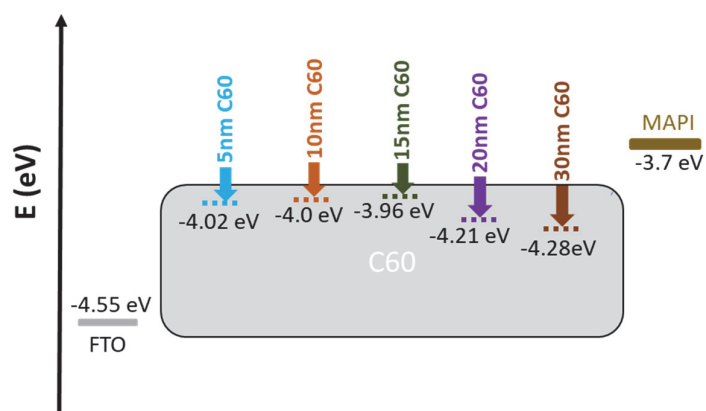


**Figure C. 6.** Energy level diagram for C<sub>60</sub> layers on glass/FTO, displaying the valence band.



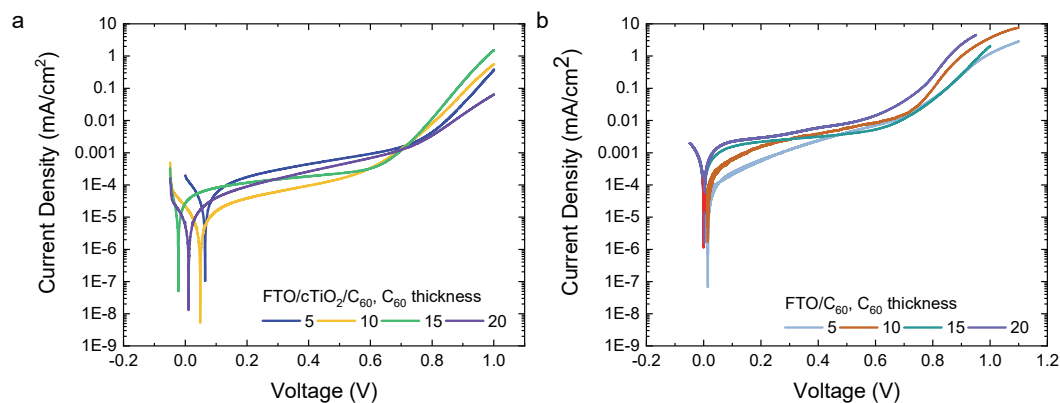


**Figure C. 7.**  $J$ - $V$  curve measured in the dark and presented in log scale for co-evaporated MAPbI<sub>3</sub> thin films deposited on top of a) FTO/cTiO<sub>2</sub>/C<sub>60</sub> and b) FTO/C<sub>60</sub>. (C<sub>60</sub> = 5nm, 10nm, 15nm, 20nm).

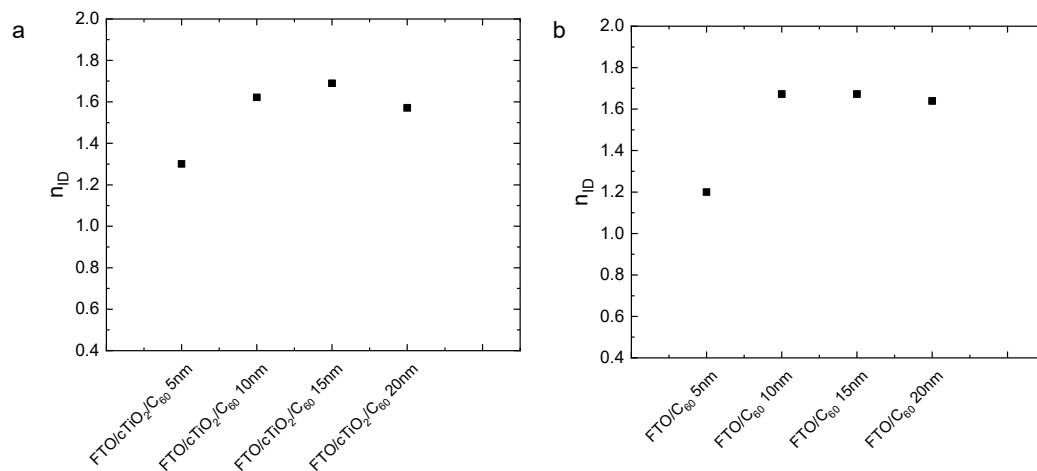


**Figure C.8.** a) Ideality factor for samples on FTO/cTiO<sub>2</sub>/C<sub>60</sub>/MAPbI<sub>3</sub>/spiro-OMeTAD/Au, C<sub>60</sub> different thicknesses, b) Ideality factor for devices with architecture FTO/C<sub>60</sub>/MAPbI<sub>3</sub>/spiro-OMeTAD/Au, C<sub>60</sub> different thicknesses.

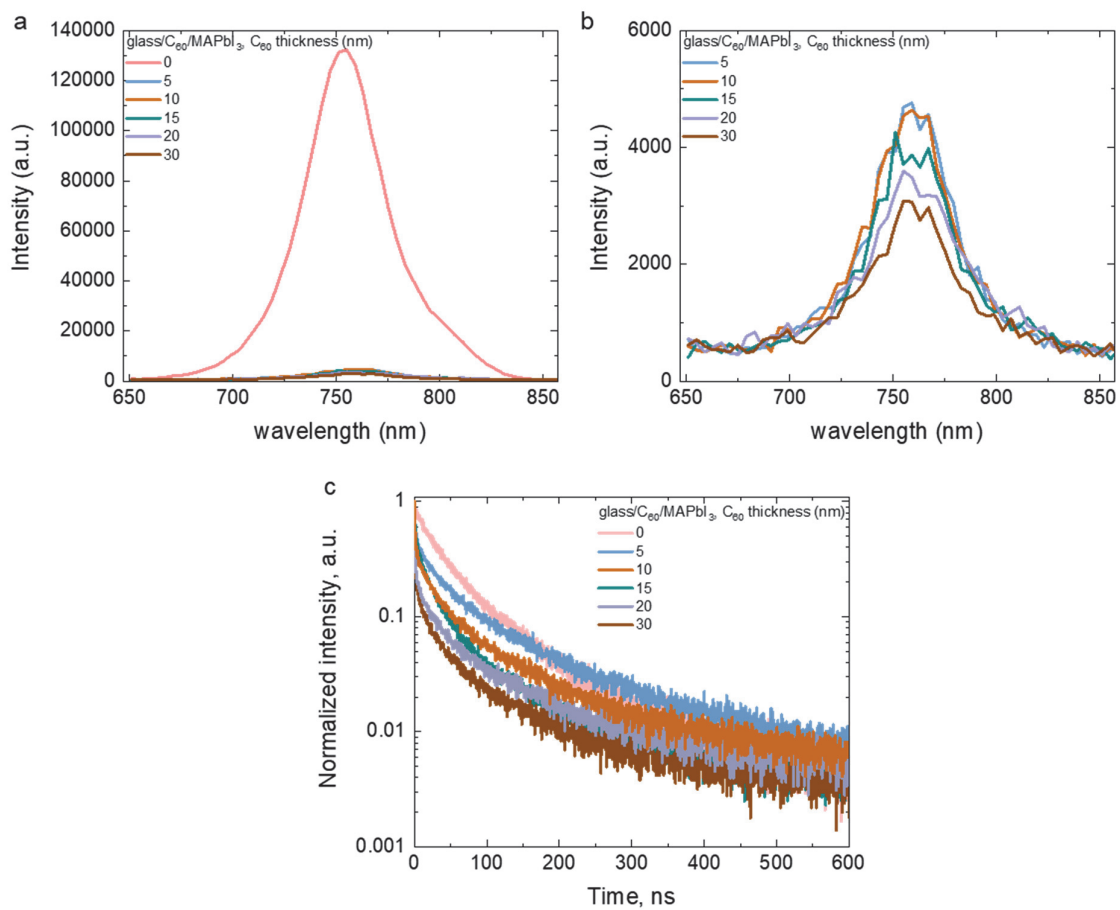


**Figure C. 9.** a, b) Steady-state PL spectra ( $\lambda_{exc}=475$  nm) and c) time-resolved PL decay ( $\lambda_{exc} = 655$  nm) of glass/C<sub>60</sub>/MAPbI<sub>3</sub> with increasing C<sub>60</sub> thickness.

**Table C. 3.** Fitted decay parameters derived from the time-resolved photoluminescence (TrPL) spectra.

	C <sub>60</sub> thickness (nm)	T <sub>1</sub> (ns)	T <sub>2</sub> (ns)
C <sub>60</sub> /MAPbI <sub>3</sub>	0	27.8	92.2
	5	2.5	74.3
	10	1.5	54.9
	15	1.7	36.3
	20	0.9	55.1
	30	1.2	49.8
cTiO <sub>2</sub> /C <sub>60</sub> /MAPbI <sub>3</sub>	0	23.3	81.7
	5	13.8	94.5
	10	8.9	58.0
	15	1.3	58.0
	20	1.2	69.5
	30	1.0	47.1

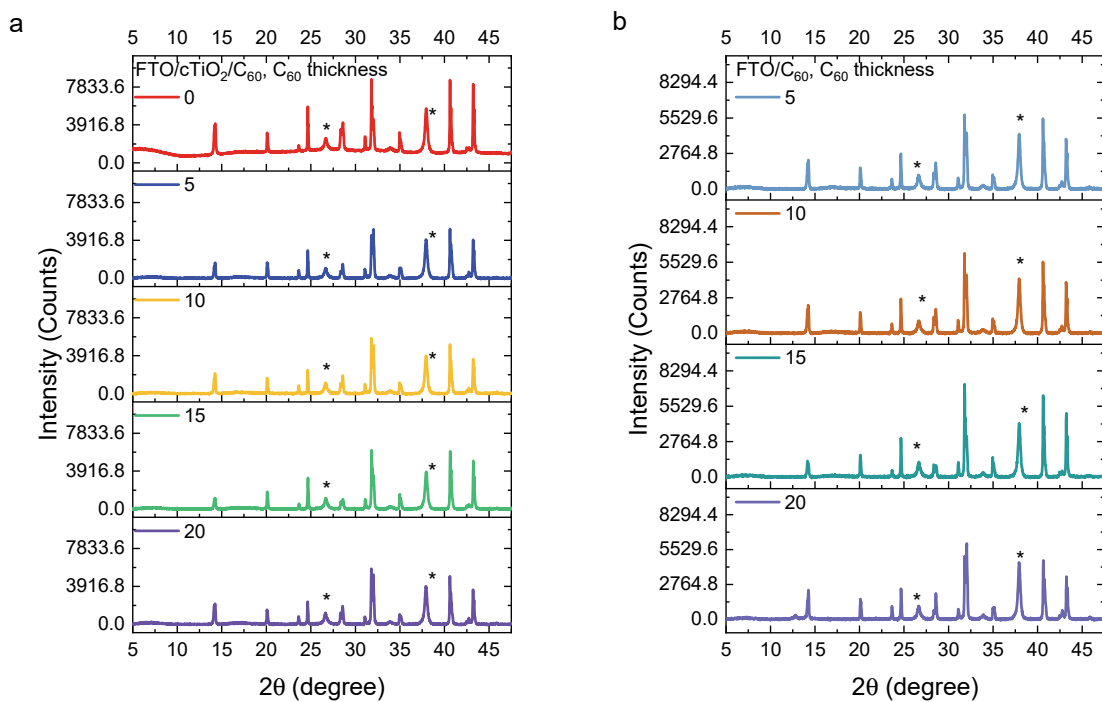


**Figure C. 10.** XRD patterns of co-evaporated MAPbI<sub>3</sub> thin films deposited on top of a) FTO/cTiO<sub>2</sub>/C<sub>60</sub> with the C<sub>60</sub> thicknesses being: 0nm, 5nm, 10nm, 15nm, and 20nm and b) FTO/C<sub>60</sub> with the C<sub>60</sub> thicknesses being: 5nm, 10nm, 15nm, and 20nm, respectively, the star is indicating the FTO diffraction.

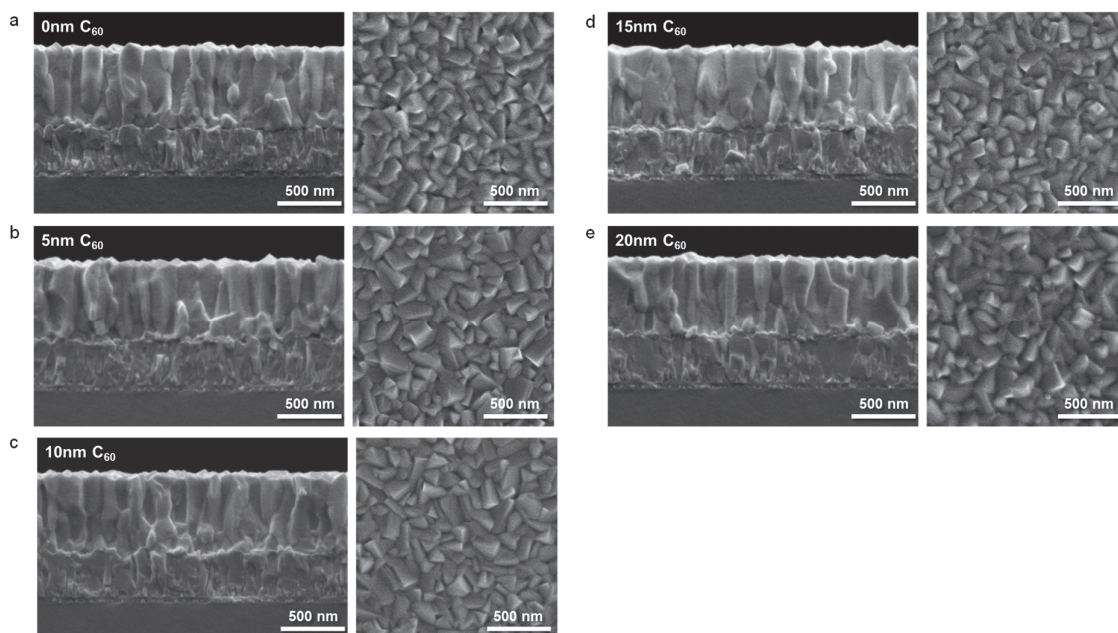


**Figure C. 11.** SEM top-view and cross-sectional images of co-evaporated MAPbI<sub>3</sub> thin films deposited on top of FTO/cTiO<sub>2</sub>/C<sub>60</sub>, with the C<sub>60</sub> thicknesses being: 0nm, 5nm, 10nm, 15nm, and 20nm, respectively.

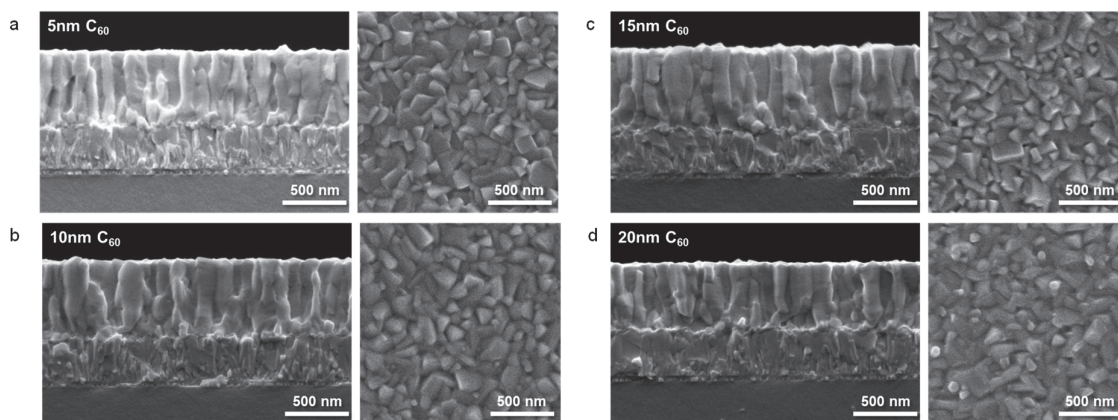


**Figure C. 12.** Top-view and cross-sectional SEM images of co-evaporated MAPbI<sub>3</sub> thin films deposited on top of FTO/C<sub>60</sub>, with the C<sub>60</sub> thicknesses being: 5nm, 10nm, 15nm, and 20nm, respectively.

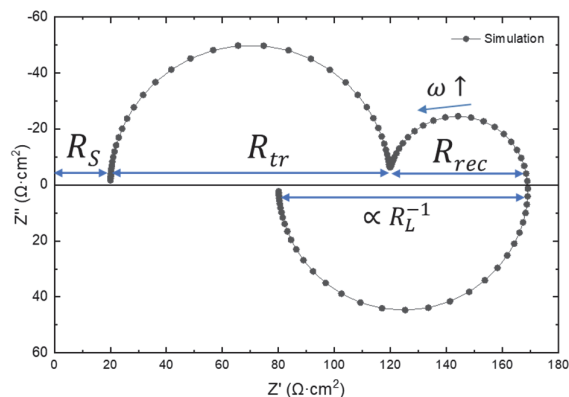


**Figure C. 13.** Simulation of the equivalent circuit in Figure 1c with:  $R_s = 20 \Omega$ ,  $C_g = 1 \times 10^{-7} \text{ F}$ ,  $R_{tr} = 100 \Omega$ ,  $R_{rec} = 50 \Omega$ ,  $C_{\mu} = 1 \times 10^{-4} \text{ F}$ ,  $R_L = 100 \Omega$ ,  $L = 100 \text{ H}$  and Area =  $1 \text{ cm}^2$ .

**Table C. 4.** Parameters obtained from the fitting of the impedance spectra with the equivalent circuit, as shown in Figures 3 and 4.

	$C_{60}$ nm	$R_s$ $\Omega$	$C_g$ nF $\text{cm}^{-2}$	$R_{tr}$ $\Omega \text{ cm}^2$	$R_{rec}$ $\Omega \text{ cm}^2$	$C_{int}$ $\text{mF cm}^{-2}$	$R_L$ $\Omega \text{ cm}^2$	$L$ $\text{H cm}^2$
	0	2.11	665	18.7	3.47	67.2	--	--
	5	1.72	375	3.5	2.87	8.3	--	--
cTiO <sub>2</sub> /C <sub>60</sub> /MAPbI <sub>3</sub>	10	1.64	430	2.1	1.97	9.6	--	--
	15	1.95	438	3.3	1.05	9.8	--	--
	20	1.83	445	3.0	0.63	13.9	--	--
	30	1.93	984	1.4	0.09	66.3	1.67	4.15
C <sub>60</sub> /MAPbI <sub>3</sub>	15	1.95	482	2.5	2.06	4.0	--	--

Comment: Large  $R_{\text{rec}}$  in  $\text{cTiO}_2/\text{MAPbI}_3$  partially compensates the low short circuit current in the device to still provide a reasonable  $V_{\text{oc}}$ , see Tables 1 and S1.

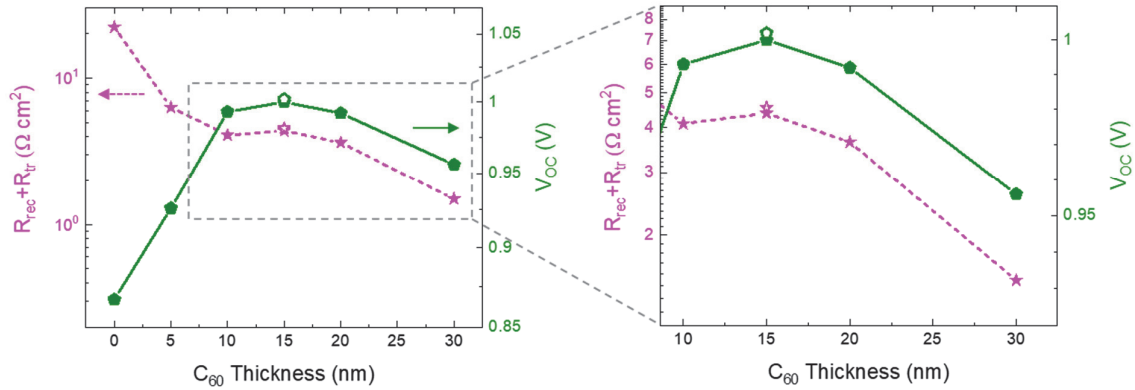


**Table C. 5.** Comparison of  $V_{\text{oc}}$  and the sum of  $R_{\text{rec}}$  and  $R_{\text{tr}}$  for the samples with different thicknesses of the  $C_{60}$  layer. For the thicker samples ( $\geq 10\text{nm}$ ),  $V_{\text{oc}}$  and  $R_{\text{rec}} + R_{\text{tr}}$  are directly correlated, indicating that the recombination contribution to  $R_{\text{tr}}$  dominates. Meanwhile, for the thinner samples, the rise of  $R_{\text{rec}} + R_{\text{tr}}$ , which is due to the large values attained by  $R_{\text{tr}}$ , is opposite to the decrease in  $V_{\text{oc}}$ . In these cases,  $R_{\text{tr}}$ , as explained in the main text is dominated by the difficulties to transfer charge from perovskite to  $\text{TiO}_2$  layer. The still large value of  $R_{\text{tr}}$  at 5nm, See also Figure 4b, indicates that the coverage of  $\text{TiO}_2$  by the  $C_{60}$  layer is uncomplete and so despite  $R_{\text{tr}}$  being 1/3 of the value at 0  $C_{60}$ , it is still dominated by charge transfer. Performance data of FTO/ $C_{60}$  samples with a 5nm  $C_{60}$  layer in Figure S1 and Table S1 also suggest the presence of pin holes in the  $C_{60}$  layer.





## Appendix D: Supplementary Information to Chapter 7



Schematics 1. Illustration of the dopant migration mechanism

### *Materials and Methods*

#### *Perovskite thin-film and solar cell fabrication*

Thin films were fabricated on fluorine-doped tin oxide (FTO)-coated glass substrates (TEC-15AX, NSG group) which were cleaned by a sequential sonication treatment (10 min each) in a 2% Helmanex solution, water, deionized water, and isopropanol. The cleaning of the FTO was then followed by ultraviolet- $O_3$  treatment for 30 min. The spiro-OMeTAD (Merck) underlayers were deposited by spin-coating at 4000 r.p.m. for 30 s (acc. 1000 r.p.m./s) from a chlorobenzene solution (80 mg in 1023  $\mu$ l, 60 mM). According to our study, different dopant concentrations were added to the spiro-OMeTAD solution. For the sample noted as **Li-tBP**, 19  $\mu$ l from a 517 mg·ml<sup>-1</sup> LiTFSI stock solution in

acetonitrile was added. For the preparation of **Co-tBP**, 14  $\mu\text{l}$  from a 517  $\text{mg}\cdot\text{ml}^{-1}$  CoTFSI stock solution in acetonitrile was added. The **3Co-tBP** solution was prepared by adding 14  $\mu\text{l}$  from a 1551  $\text{mg}\cdot\text{ml}^{-1}$  stock solution in acetonitrile, achieving three times the dopant concentration than the previous Co-tBP solution. Finally, our reference sample named **Li-Co-tBP** was doped with 19  $\mu\text{l}$  from a 517  $\text{mg}\cdot\text{ml}^{-1}$  LiTFSI stock solution and 14  $\mu\text{l}$  from a 517  $\text{mg}\cdot\text{ml}^{-1}$  CoTFSI stock solution, both in acetonitrile. 32  $\mu\text{l}$  of TBP was added to all the prepared spiro-OMeTAD solutions. Note that the sample containing spiro-OMeTAD and TBP will be named **tBP**. The prepared layers were then transferred to the PRO Line PVD 75 vacuum chamber from Kurt J. Lesker Company, equipped with four thermally-controlled sources. The perovskite precursors,  $\text{PbI}_2$  (TCI) and methylammonium iodide (MAI) (Lesker) were filled into the crucibles and heated up until the sublimation temperatures of  $\sim 140^\circ\text{C}$  for  $\text{PbI}_2$  and  $\sim 120^\circ\text{C}$  for MAI at a vacuum pressure of  $\sim 1\cdot 10^{-6}$  mbar. The deposition rate of each precursor was kept constant at 3.6 and 0.6  $\text{\AA}/\text{s}$  and monitored by independent quartz microbalance crystal sensors (QCMs). The substrates were kept at a rotation of 5 r.p.m. at room temperature during the perovskite deposition. The samples for EDX analysis were deposited on top of indium-doped tin oxide (ITO). For the device fabrication, the FTO-coated substrates were laser etched. Once the perovskite layer was deposited, 20 nm of  $\text{C}_{60}$  (Sigma-Aldrich, 99.9%) was thermally evaporated, followed by 3 nm of bathocuproine (BCP, Sigma-Aldrich, 99.9%). As top electrode, 1 nm Cr and 70 nm Au were deposited by thermal evaporation.

Solution-processed  $\text{MAPbI}_3$  layers were deposited on top of the glass for being used as standard samples for EDX determination. 1.45 M of  $\text{PbI}_2$  and MAI was dissolved in DMSO, and 0.49, 0.97, and 1.9 % F atomic concentration was added by LiTFSI incorporation. The solution was spin-coated at 2000 rpm (acc. 200 rpm/s) for 12 s followed by 4000 rpm (acc. 2000 rpm/s) for 30 s. 110  $\mu\text{l}$  of chlorobenzene was added 10 seconds before finishing the second step. The samples were annealed at  $100^\circ\text{C}$  for 1 h in an inert atmosphere.

*Thin-film characterization*

The XRD patterns of the as-prepared films were measured using a D8 Advance diffractometer from Bruker with an X-ray tube Cu K $\alpha$ ,  $\lambda = 1.5406 \text{ \AA}$  Bragg-Brentano geometry. The absorbance spectra were recorded with a Lambda 950S spectrophotometer (PerkinElmer, Inc.). Time-resolved photoluminescence (TRPL) and photoluminescence (PL) spectroscopy were performed by Fluorolog TCSPC (HORIBA, Ltd.) with a picosecond laser with an excitation wavelength of 640 nm and 475nm, respectively. The detection wavelength of Time-resolved photoluminescence was 760 nm. An ultraviolet photoelectron spectrometer (UPS) equipped with a He-I source ( $h\nu = 21.22 \text{ eV}$ ) (AXIS Nova, Kratos Analytical Ltd, UK) was used to measure the valence band energy, Fermi level, and the work function. The Fermi level of the samples was referenced to that of Au, which was in electrical contact with a sample in UPS measurements. The X-ray photoelectron spectroscopy (XPS) measurements were carried out on a VersaProbe II (Physical Electronics, Inc.) with a monochromatic Al K $\alpha$  X-ray source operating at 1486.6 eV. All spectra were referenced using the Pb 4f signal, and the data was processed using the software CasaXPS. Scanning electron microscopy (SEM) images were recorded by the in-lens detector of FEI Teneo Schottky Field Emission SEM at a tension of 1.5 kV for top-view imaging and 1 kV for cross-section analysis. Energy-dispersive X-ray spectroscopy (EDX) was performed in the FEI Teneo Schottky Field Emission SEM with an XFlash Silicon drift detector. The EDX spectra were collected at a tension of 5 kV, current of 6.4 nA with 300 s integration time. In order to obtain accurate EDX data of the fluorene concentration, we carried out a standard-based analysis on the perovskite layers. For this purpose, perovskite standards with well-known stoichiometry were synthesized by spin coating, where the F concentration ranged from 0.5% - 1.9 %. The I-M/F-M line ratio in these samples was accurately measured by analyzing the I-M and F-K lines. This resulted in calibration curves of the F concentration in the perovskite layers. These calibration curves were then used to obtain the F-concentrations in perovskite samples. Conductivity measurements were carried out using the 2.5  $\mu\text{m}$  channel (channel width 10 mm and height 40 nm) of an organic field-effect transistor (OFET, Fraunhofer IPMS) with two/contact electrical

conductivity set-up. The substrates were cleaned with 20 min oxygen plasma following the HTM deposition by spin-coating at 4000 rpm for the 20s. The measurements were carried by sweeping from -10 to 10 V (source-drain voltage) at a scan rate of 1 V s<sup>-1</sup> with a Keithley 2612A. The data were recorded with the KickStart software program, and the conductivity was calculated from a linear fit of the J-V measurement and Ohm's law.

#### *Device characterization*

J - V curves were measured by using a 2400 Keithley system with a Xe-lamp Oriel sol3A sun simulator (Newport Corporation). The system was calibrated to AM1.5G standard conditions by using an Oriel 91150 V reference cell (J - V curves scan rate of 50 mV s<sup>-1</sup> and 10 mV voltage step). An NREL-certified KG5-filtered Si-reference diode was used for light intensity calibration. The active area of the cell was defined through shadow masks with a metal aperture of 0.16 cm<sup>2</sup>. The cells were measured at room temperature in air and without encapsulation. The measurement was done at a constant rate of 10 mV s<sup>-1</sup> and 10 mV voltage step for reversed bias after 5s under light soaking. No anti-reflective coating was applied during the measurement. The stability test was performed as maximum power tracking under 100 mW cm<sup>-2</sup> illumination with a LED power source. The samples were encapsulated in a measurement box which was purged with nitrogen gas until 0% humidity and constantly kept at 25 °C by a cooling system. EQE was measured with the IQE200B (Oriel) without bias light.

## Supporting Figures

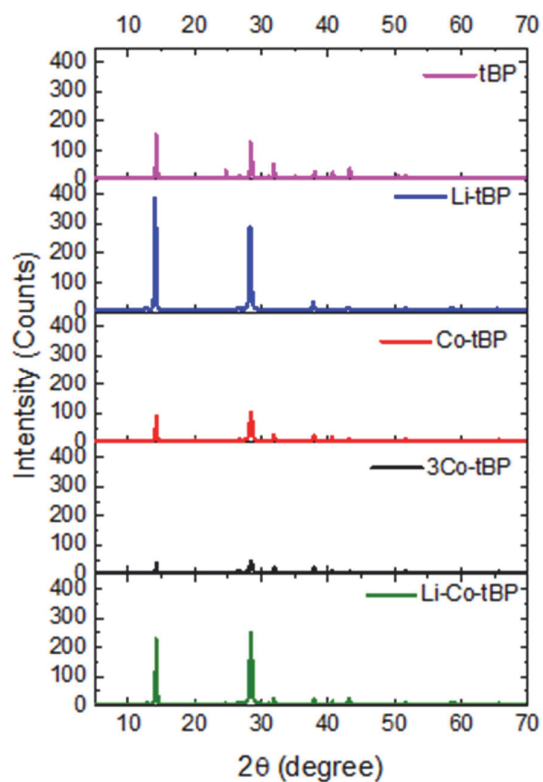


**Figure D. 1.** XRD patterns of co-evaporated MAPbI<sub>3</sub> thin films deposited on top of glass/HTM, being the HTM: tBP, Li-tBP, Co-tBP, 3Co-tBP and Li-Co-tBP, respectively.

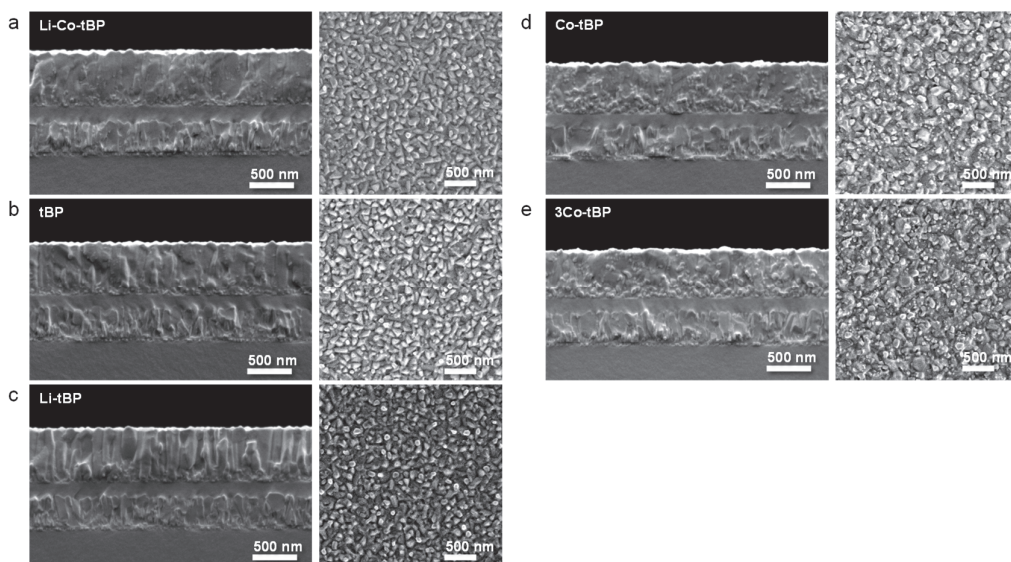


**Figure D. 2.** SEM top-view and cross-sectional images of co-evaporated  $\text{MAPbI}_3$  thin films deposited on top of glass/FTO/HTM, being the HTM: (a) **Li-Co-tBP**, (b) **tBP**, (c) **Li-tBP**, (d) **Co-tBP** and (e) **3Co-tBP**.

**Table D. 1.** Fitted decay parameters derived from the time-resolved photoluminescence (TrPL) spectra.

Sample	$\tau_1$ (ns)	$\tau_2$ (ns)
$\text{MAPbI}_3$	$4.36 \pm 0.13$	$122.54 \pm 0.46$
tBP	$7.40 \pm 0.01$	$54.44 \pm 0.41$
Li-tBP	$4.57 \pm 2.50$	$177.30 \pm 2.27$
Co-tBP	$5.36 \pm 4.83$	$185.78 \pm 3.56$
3Co-tBP	$3.21 \pm 1.25$	$136.20 \pm 1.28$
Li-Co-tBP	$1.28 \pm 0.01$	$151.86 \pm 0.50$

**Table D. 2.** Atomic concentration values were extracted from the fitting of the corresponding XPS spectra. The samples were measured as-deposited for 30nm and 500nm after 1 and 3 weeks and stored in N<sub>2</sub> atmosphere in the dark at room temperature—perovskite thickness: 500 nm.

Perovskite thickness nm	Surface atomic concentration, %				Ratio			
		F1s	I3d	N1s	Pb4f	F1s/ Pb4f	I3d/ Pb4f	
30	As-deposited	Li-tBP	0.83	64.70	18.00	16.5	0.039	3.92
		Co-tBP	0.84	57.40	19.00	19.1	0.044	3.00
		3Co-tBP	2.35	60.50	16.20	21.0	0.11	2.88
		Li-Co-tBP	1.72	63.00	17.30	18.0	0.09	3.50
500	As-deposited	Li-tBP	1.07	63.90	17.10	17.9	0.059	3.57
		Co-tBP	1.01	62.60	15.60	20.8	0.049	3.00
		3Co-tBP	1.72	63.80	15.40	19.0	0.090	3.35
		Li-Co-tBP	1.20	61.90	17.10	19.2	0.062	3.22
	1 week	Li-tBP	1.81	63.50	16.60	18.0	0.10	2.99
		Co-tBP	1.31	61.60	15.90	21.2	0.06	2.90
		3Co-tBP	1.63	63.80	15.10	19.5	0.08	3.27
		Li-Co-tBP	0.76	63.20	16.40	19.7	0.04	3.20
3 weeks	Li-tBP	0.37	63.90	16.60	19.2	0.02	3.32	
	Co-tBP	0.25	60.06	15.90	21.0	0.01	2.86	
	3Co-tBP	0.77	63.90	14.2	21.1	0.04	3.03	
	Li-Co-tBP	0.00	63.70	17.4	19.0	0.00	3.35	

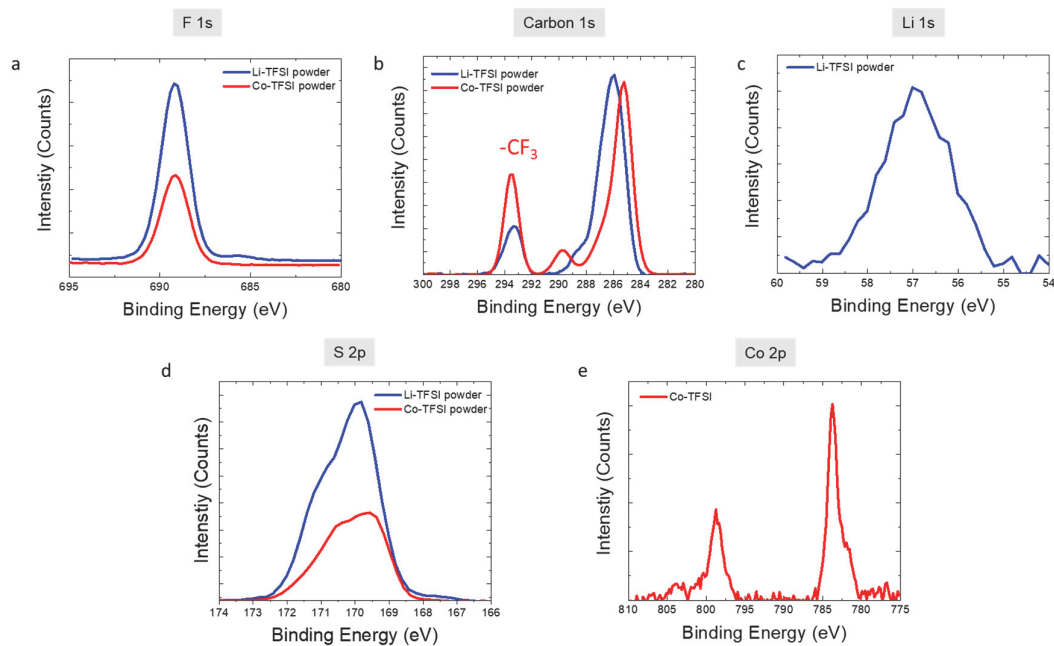


**Figure D. 3.** XPS spectra of LiTFSI and CoTFSI powders: (a) F1s, (b) C1s, (c) Li1s, (d) S2p and (e) Co2p.

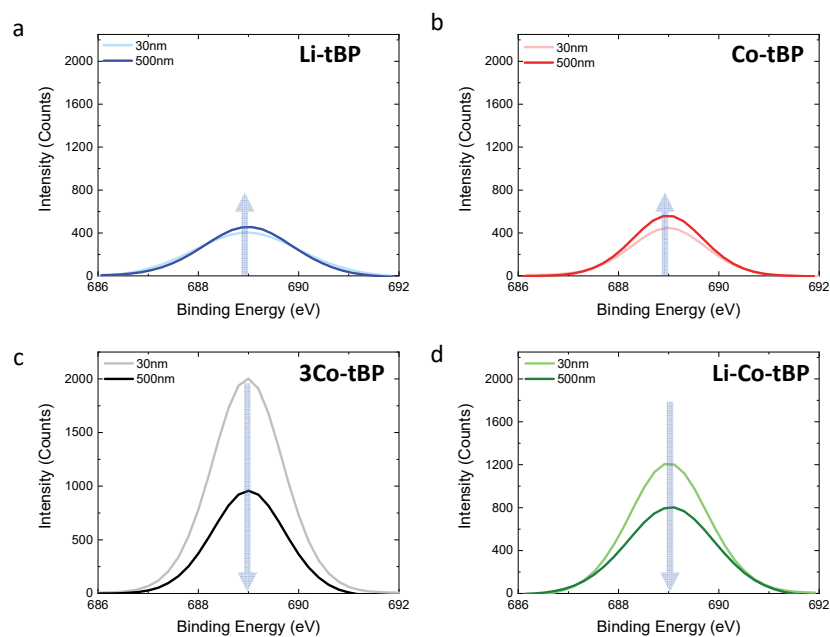


**Figure D. 4.** Comparison of F 1s XPS spectra of 30 and 500 nm perovskite layer deposited on top of doped-HTM: (a) Li-tBP, (b) Co-tBP, (c) 3Co-tBP and (d) Li-Co-tBP.



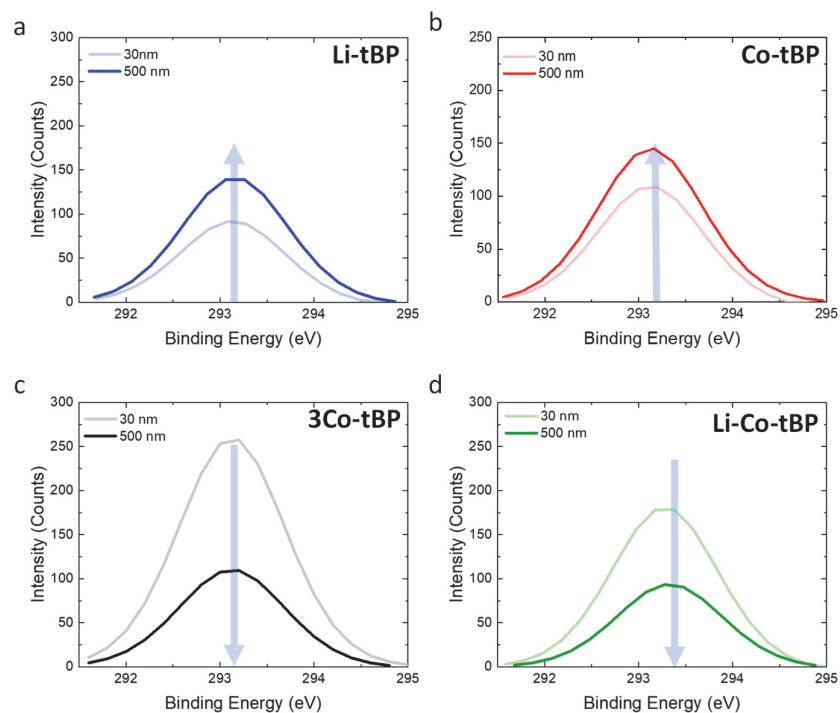


**Figure D. 5.** Comparison of  $-\text{CF}_3$  signal in  $\text{C}_{1s}$  XPS spectra of 30 and 500 nm perovskite layer deposited on top of doped-HTM: (a) Li-tBP, (b) Co-tBP, (c) 3Co-tBP and (d) Li-Co-tBP.

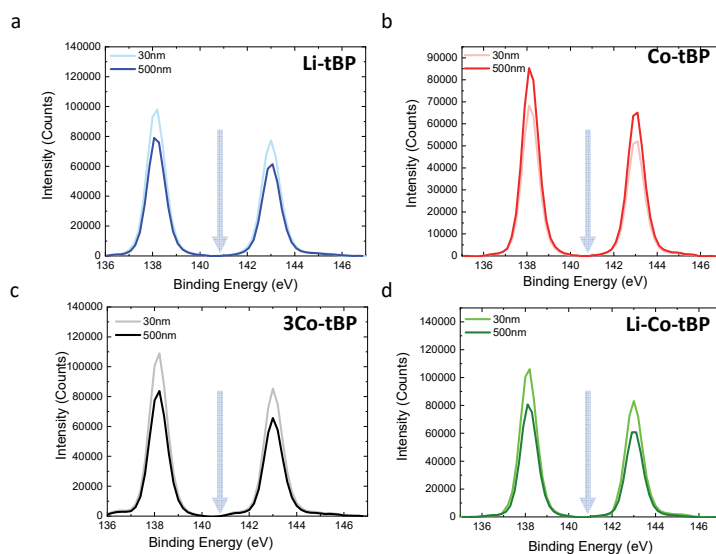


**Figure D. 6.** Comparison of  $-\text{Pb}^{2+}$  signal in Pb 4f XPS spectra of 30 and 500 nm perovskite layer deposited on top of doped-HTM: (a) Li-tBP, (b) Co-tBP, (c) 3Co-tBP and (d) Li-Co-tBP.

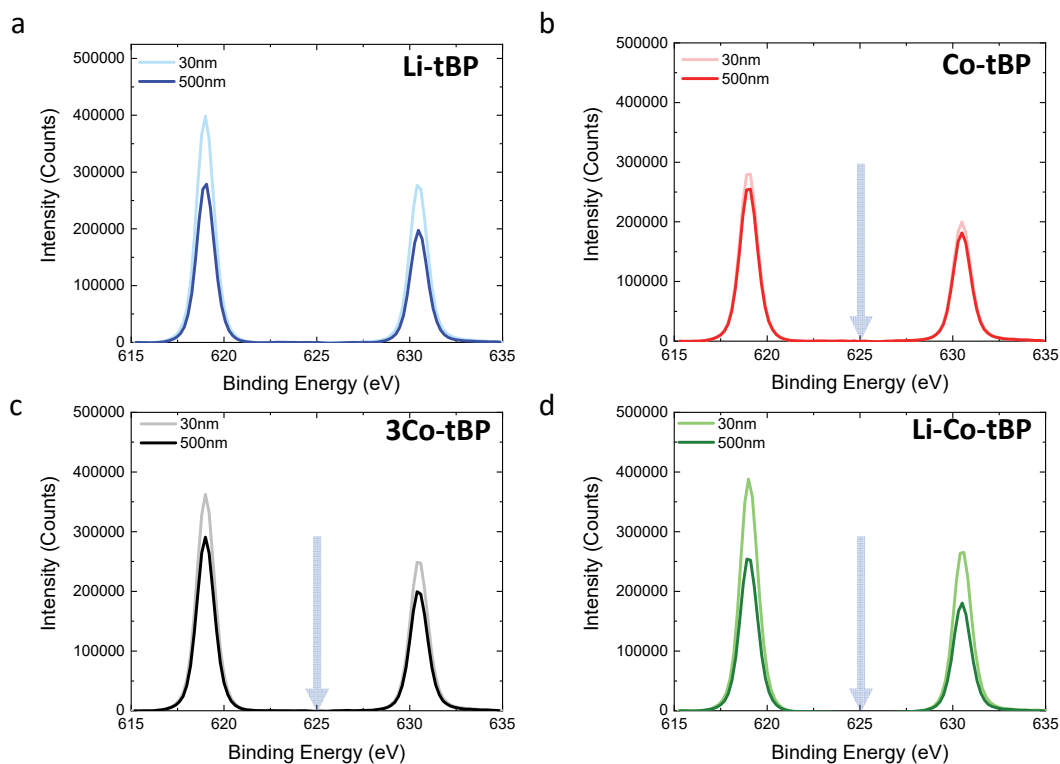


**Figure D. 7.** Comparison of -I signal in I<sub>1s</sub> XPS spectra of 30 and 500 nm perovskite layer deposited on top of doped-HTM: (a) Li-tBP, (b) Co-tBP, (c) 3Co-tBP and (d) Li-Co-tBP.

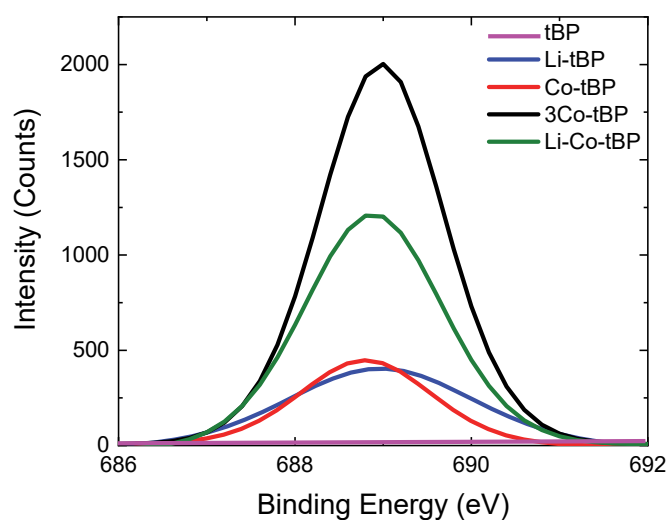


**Figure D. 8.** F 1s XPS spectra 30 nm perovskite layer deposited on top of doped-HTM.

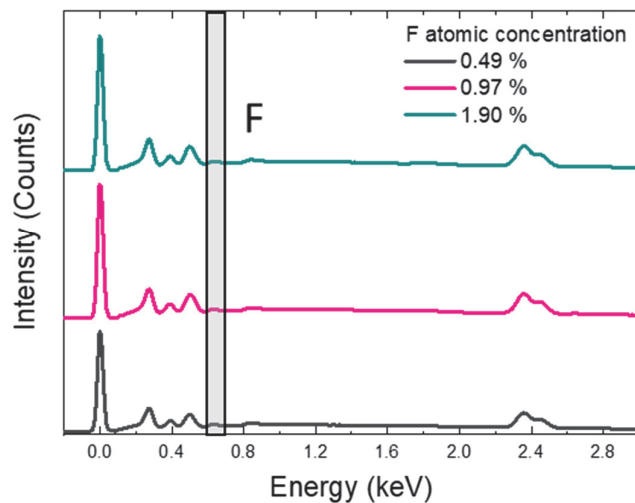


**Figure D. 9.** EDX spectra of different standard MAPbI<sub>3</sub> samples incorporating F.

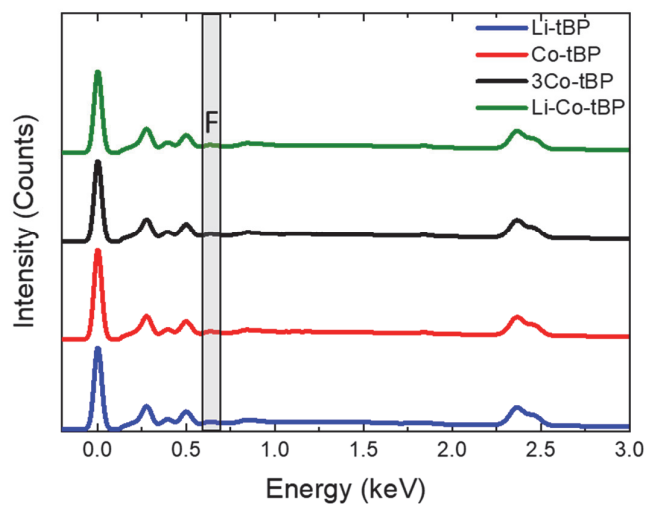


**Figure D. 10.** EDX results spectra of different co-evaporated MAPbI<sub>3</sub> on top of doped-spiro-OMeTAD layers.

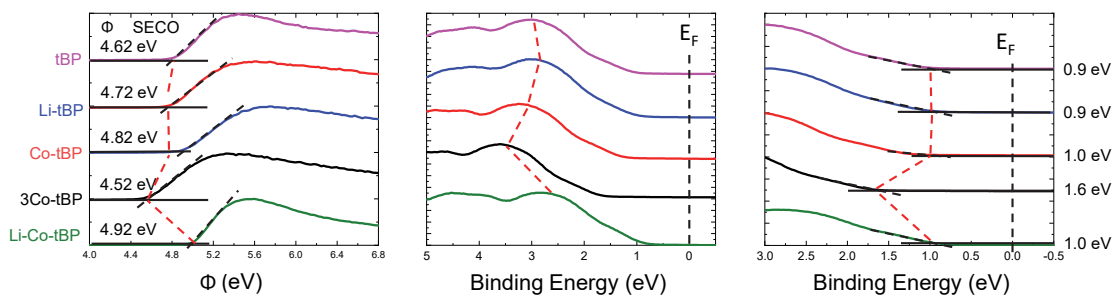


**Figure D. 11.** UPS measurement of the perovskite layer deposited on top of different HTM conditions: (a) cut-off region, (b), and (c) valence band region. The work function (WF) can be calculated as  $WF = h\nu - SECO$ ,  $h\nu = 21.22$  eV being the energy of the incident photons from a He(I) UV source.

**Table D. 3.** Co-evaporated MAPbI<sub>3</sub> deposited on top of different HTM conditions: Energy cut-off, work function, and valence band energy level extracted from the corresponding UPS spectra.

	Energy cut-off <sub>0</sub> (eV)	WF (eV)	Ionisation potential, IP (eV)
tBP	0.91	4.62	5.52
Li-tBP	0.98	4.72	5.62
Co-tBP	1.04	4.82	5.82
3Co-tBP	1.60	4.52	6.12
Li-Co-tBP	1.00	4.92	5.92

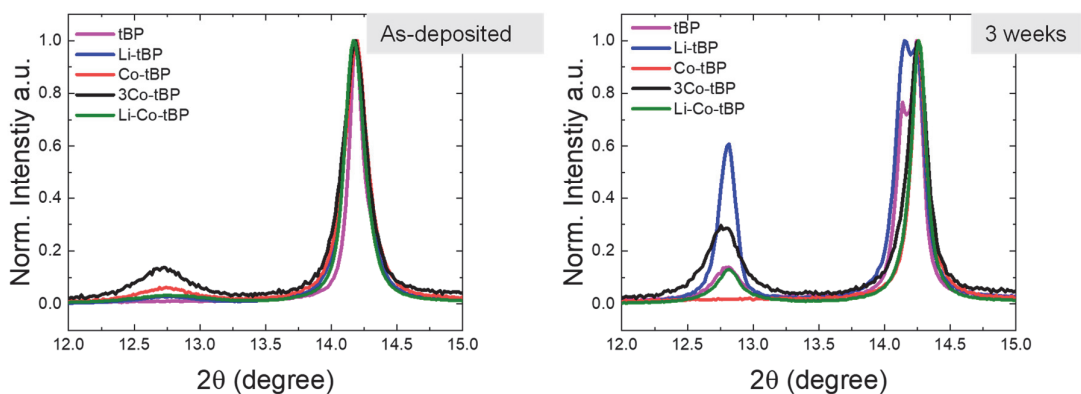


**Figure D. 12.** XRD spectra of co-evaporated MAPbI<sub>3</sub> thin films deposited on top of glass/HTM (tBP, Li-tBP, Co-tBP, 3Co-tBP and Li-Co-tBP) samples: (a) as-deposited and (b) after 3 weeks stored in dark at relative humidity below 10%.

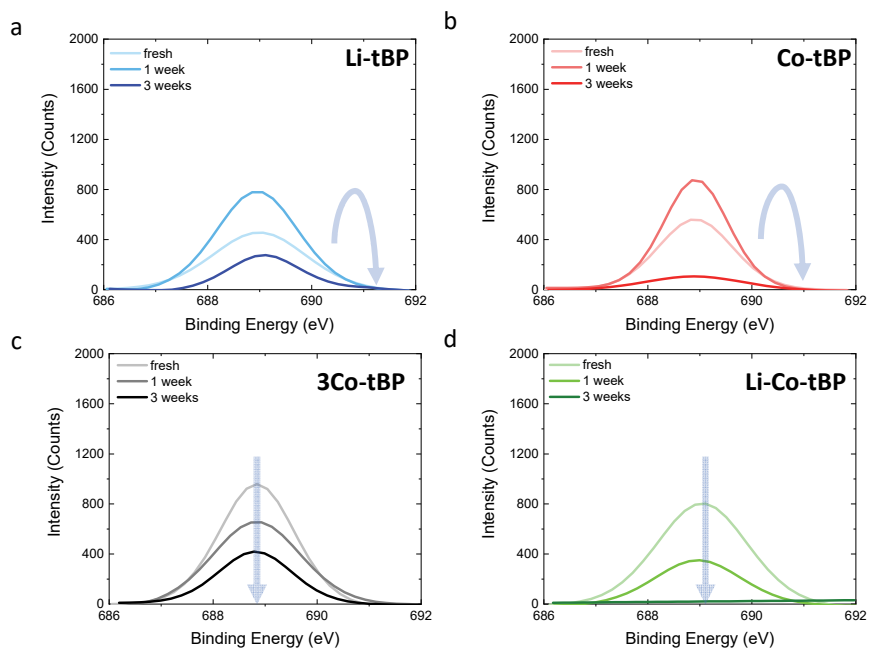


**Figure D. 13.** Stability of co-evaporated MAPbI<sub>3</sub> films deposited on top of different HTM: F 1s (-F signal) XPS spectra.

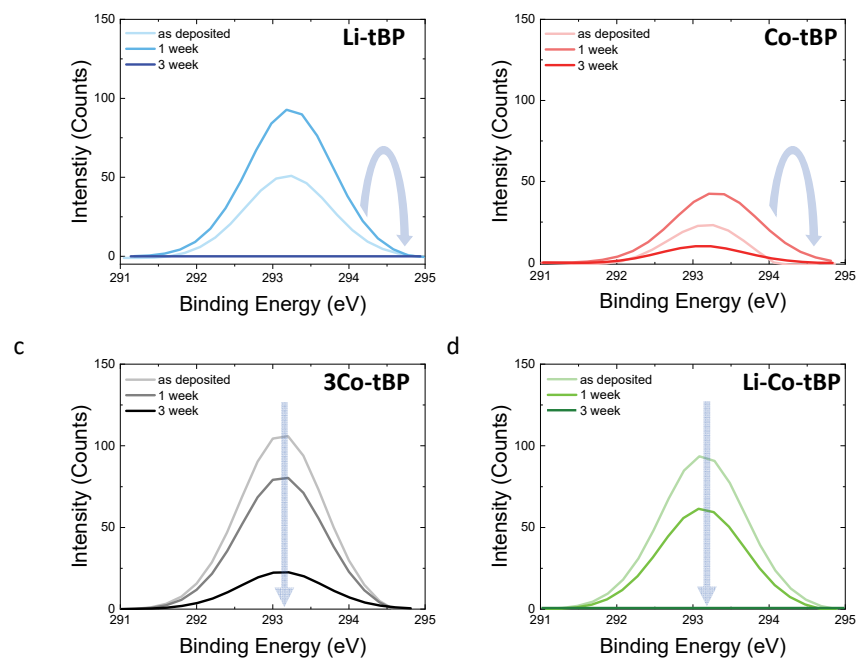


**Figure D. 14.** Stability of co-evaporated MAPbI<sub>3</sub> films deposited on top of different HTM: C1s (-CF<sub>3</sub> signal) XPS spectra.

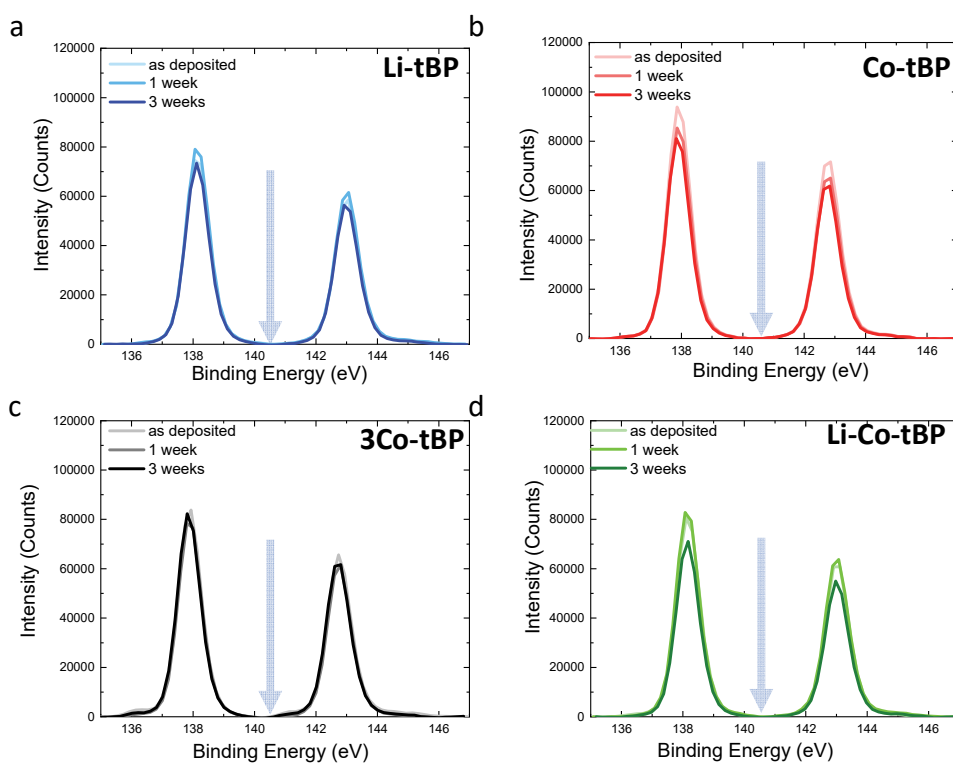


**Figure D. 15.** Stability of co-evaporated MAPbI<sub>3</sub> films deposited on top of different HTM: Pb 4f (Pb<sup>2+</sup>-signal) XPS spectra. Stability of co-evaporated MAPbI<sub>3</sub> films deposited on top of different HTM: C1s (-CF<sub>3</sub> signal) XPS spectra.

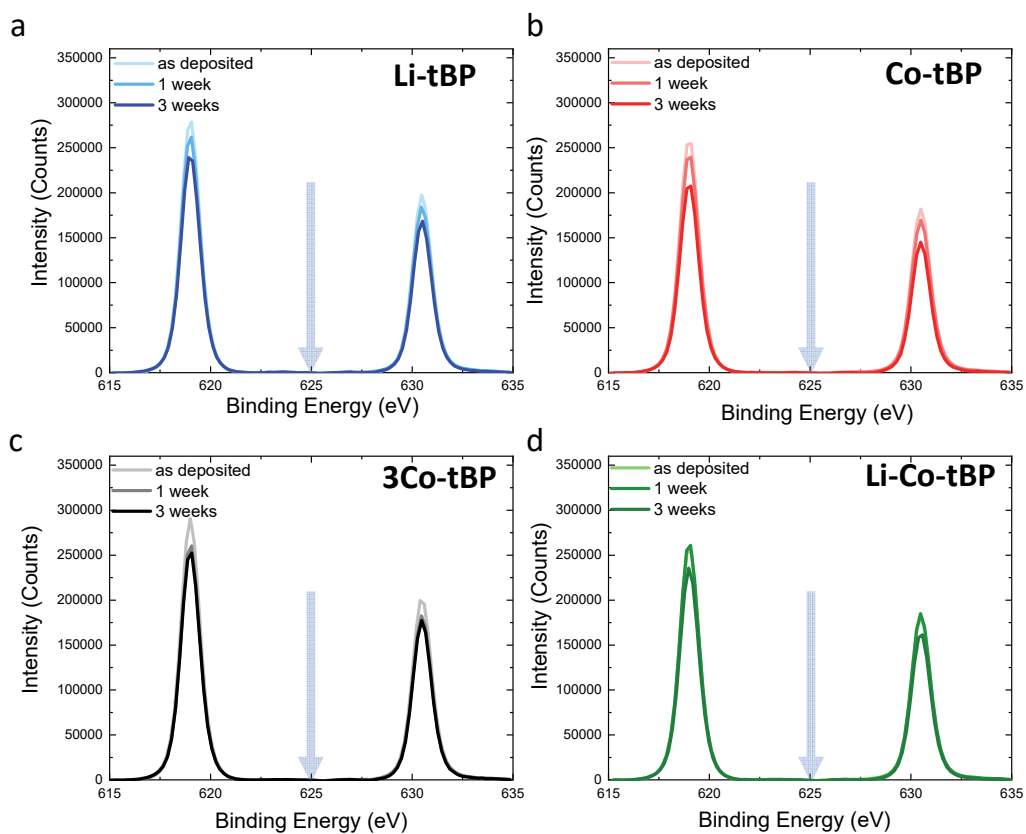


**Figure D. 16.** Stability of co-evaporated MAPbI<sub>3</sub> films deposited on top of different HTM: I<sub>2</sub>s (I-signal) XPS spectra.

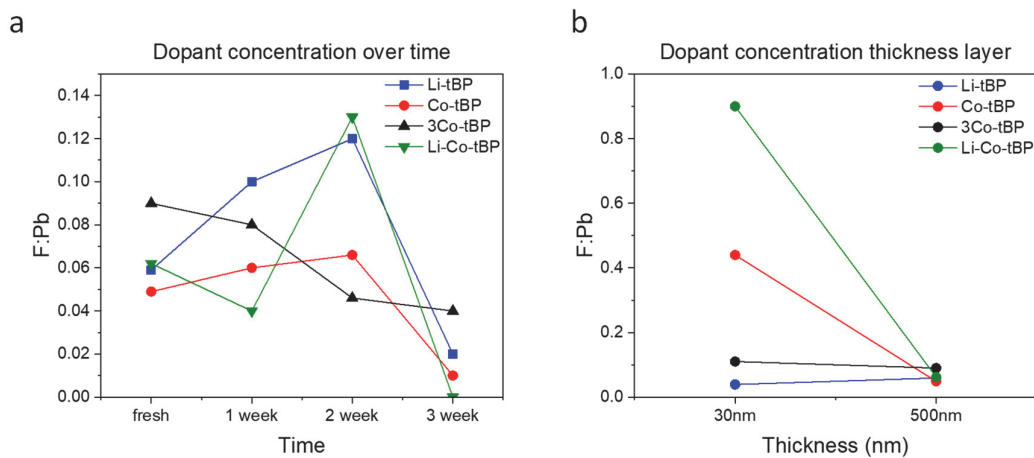


**Figure D. 17.** Comparison of the stability of perovskite layers followed by the F/Pb ratio XPS.



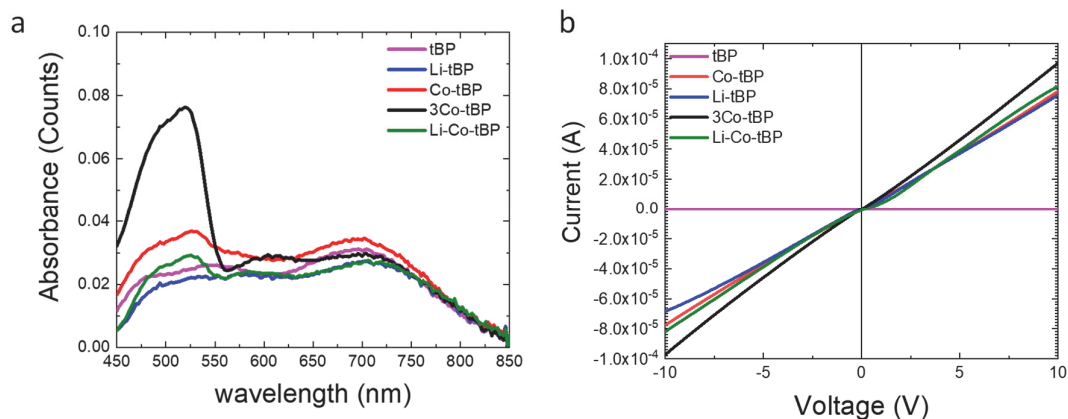


**Figure D. 18.** (a) Absorbance spectra of the doped-HTM layers deposited on glass and (b) conductivity of the doped-HTM layers measured on OFET substrates.

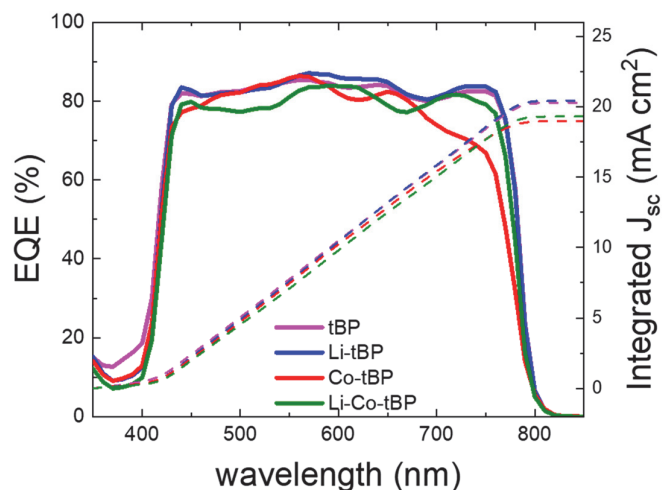


**Figure D. 19.** External quantum efficiency (EQE) and calculated short-circuit current density integrated from the corresponding EQE spectra for devices containing tBP, Li-tBP, Co-tBP, 3Co-tBP, and Li-Co-tBP.

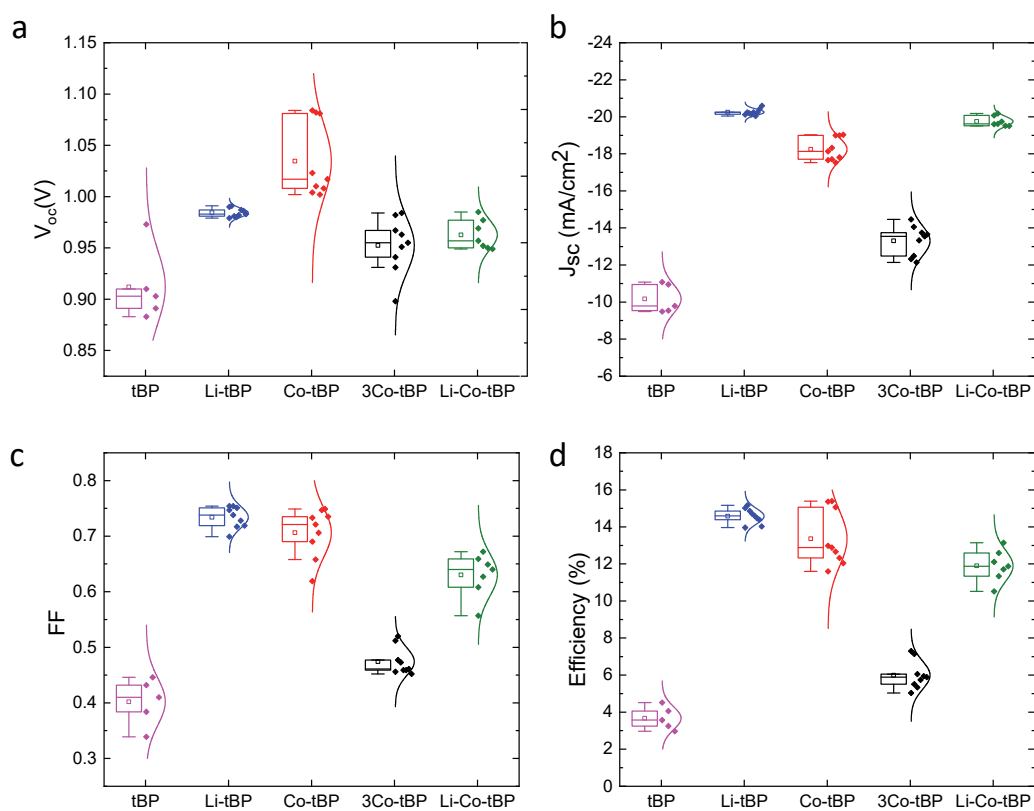


**Figure D. 20.** Statistical data of PSC containing co-evaporated  $\text{MAPbI}_3$  thin films deposited on top of glass/HTM (tBP, Li-tBP, Co-tBP, 3Co-tBP and Li-Co-tBP) samples: (a)  $V_{oc}$ , (b)  $J_{sc}$ , (c) FF and (d) PCE.

**Table D. 4.** PV parameters were extracted from the corresponding J-V curves presented in the statistical study.

	Device performance			
	J <sub>sc</sub> (mA/cm <sup>2</sup> )	V <sub>oc</sub> (V)	FF	PCE (%)
tBP	-9.49	0.973	0.43	4.0
	-9.54	0.883	0.38	3.2
	-9.79	0.891	0.34	3.0
	-11.08	0.910	0.45	4.5
	-10.95	0.903	0.41	4.1
Li-tBP	-20.12	0.990	0.75	14.9
	-20.24	0.991	0.75	15.0
	-20.19	0.981	0.75	14.8
	-20.14	0.980	0.75	14.8
	-20.24	0.979	0.74	14.6
	-20.04	0.982	0.72	14.2
	-20.25	0.987	0.73	14.6
	-20.43	0.986	0.72	14.5
	-20.59	0.983	0.70	14.2
Co-tBP	-17.71	1.010	0.72	13.0
	-17.53	1.023	0.71	12.9
	-17.81	1.002	0.69	12.6
	-18.14	1.008	0.66	12.3
	-18.32	1.017	0.62	12.0
	-19.00	1.084	0.75	15.3
	-19.00	1.082	0.75	15.4
	-19.03	1.081	0.74	15.1

Appendix D

	Device	perfor-	Device	perfor-
	mance	mance	mance	mance
3Co-tBP	-14.46	0.982	0.51	7.3
	-14.06	0.984	0.52	7.2
	-12.32	0.898	0.46	5.0
	-12.49	0.931	0.48	5.5
	-12.14	0.941	0.47	5.4
	-13.33	0.951	0.46	5.8
	-13.74	0.967	0.46	6.1
	-13.55	0.955	0.46	6.0
	-13.66	0.963	0.45	5.9
Li-Co-tBP	-19.60	0.969	0.56	10.6
	-19.62	0.957	0.61	11.4
	-19.74	0.952	0.63	11.8
	-19.52	0.950	0.65	12.0
	-19.51	0.949	0.66	12.2
	-20.08	0.985	0.64	12.7
	-20.18	0.977	0.67	13.2

**Table D. 5.** Average values of the PV parameters are presented in the statistical data.

	Device performance			
	$J_{sc}$ (mA/cm <sup>2</sup> )	$V_{oc}$ (V)	FF	PCE (%)
tBP	-10.17 ± 0.8	0.91 ± 0.78	0.40 ± 0.04	3.7 ± 0.6
Li-tBP	-20.25 ± 0.2	0.98 ± 0.01	0.73 ± 0.02	14.5 ± 0.4
Co-tBP	-18.24 ± 0.6	1.04 ± 0.04	0.71 ± 0.04	13.5 ± 1.5
3Co-tBP	-13.31 ± 0.8	0.95 ± 0.03	0.47 ± 0.02	5.9 ± 0.8
Li-Co-tBP	-19.75 ± 0.3	0.96 ± 0.27	0.63 ± 0.04	11.9 ± 0.8

# Appendix E: Supplementary Information to Chapter 8

## *Synthesis of Metallophthalocyanines*

### *Materials and methods*

Commercially available reagents were used as received. Bis(4-*n*-butoxyphenyl)amine and bis(4-[(2-ethylhexyl)oxy]phenyl)amine were synthesized as previously reported in the literature.<sup>[384,385]</sup> Solvents were purified by standard methods and dried if necessary. Reactions were monitored by thin-layer chromatography (TLC) conducted on plates precoated with silica gel Si 60-F254 (Merck, Germany). Column chromatography was conducted using silica gel Si 60, 0.063–0.200 mm (normal) or 0.040–0.063 mm (flash) (Merck, Darmstadt, Germany). Melting points were determined with a capillary melting point apparatus Büchi B-540. UV-Vis measurements in solution were performed on a Nicolet Evolution 500 spectrophotometer (Thermo Electron Corporation). FTIR was performed on a Cary 530 instrument (Agilent Technologies). <sup>1</sup>H NMR and <sup>13</sup>C NMR spectra were recorded on a Bruker Avance 400 spectrometer; chemical shifts are indicated in parts per million downfield from SiMe<sub>4</sub>, using the residual proton (CHCl<sub>3</sub> = 7.26 ppm, CH<sub>2</sub>Cl<sub>2</sub> = 5.32 ppm, Pyridine = 7.22 ppm) and carbon (CDCl<sub>3</sub> = 77.0 ppm, CD<sub>2</sub>Cl<sub>2</sub> = 54.0 ppm) solvent resonances as the internal reference. Coupling constant values *J* are given in Hz.

### *4-[Bis(4-*n*-butoxyphenyl)amino]phthalonitrile 1*

A flame dried Schlenk tube equipped with a stir bar was charged with 4-iodophthalonitrile (560 mg, 2.2 mmol), bis(4-*n*-butoxyphenyl)amine (627 mg, 2.0 mmol), Ruphos (9 mg, 0.02 mmol) and Ruphos Pd (17 mg, 0.02 mmol). The Schlenk tube was evacuated and backfilled with nitrogen three times. Degassed toluene (4 mL) and dry Cs<sub>2</sub>CO<sub>3</sub> (715 mg, 2.2 mmol) were added, and the reactor was brought into an oil bath preheated at 115°C. The reaction mixture was stirred at this temperature for 16 h. After cooling to room temperature, the mixture was diluted with CH<sub>2</sub>Cl<sub>2</sub> and filtered on Celite. The solvent was evaporated under reduced pressure. The residue was purified by flash column chromatography (silica gel, hexane/EtOAc 85/15) to give the title compound a thick oil

that slowly solidifies on standing (408 mg, 93%). Mp 145-147 °C. <sup>1</sup>H NMR (400 MHz, CD<sub>2</sub>Cl<sub>2</sub>) δ 7.43 (d, *J* = 8.9 Hz, 1H), 7.19-7.12 (m, 4H), 7.04 (d, *J* = 2.5 Hz, 1H), 6.97-6.92 (m, 5H), 3.98 (t, *J* = 6.5 Hz, 4H), 1.83-1.73 (m, 4H), 1.58-1.45 (m, 4H), 0.99 (t, *J* = 7.4 Hz, 6H). <sup>13</sup>C NMR (101 MHz, CD<sub>2</sub>Cl<sub>2</sub>) δ 158.42, 152.87, 137.37, 134.68, 128.72, 120.31, 119.37, 117.34, 116.97, 116.63, 116.48, 102.71, 68.56, 31.77, 19.74, 14.17.

**4-[Bis(4-[(2-ethylhexyl)oxy]phenyl)amino]phthalonitrile 2**

Palladium-catalyzed amination of 4-iodophthalonitrile (560 mg, 2.2 mmol) with bis(4-[(2-ethylhexyl)oxy]phenyl)amine (851 mg, 2.0 mmol) was performed as described for phthalonitrile **1**. Flash column chromatography (petroleum ether/EtOAc 93/7) gave the title compound as a thick oil that slowly solidifies on standing (970 mg, 88%). Mp 48-51 °C. <sup>1</sup>H NMR (400 MHz, CDCl<sub>3</sub>) δ 7.41 (d, *J* = 8.9 Hz, 1H), 7.10 (d, *J* = 8.7 Hz, 4H), 7.01 (d, *J* = 2.2 Hz, 1H), 6.94-6.90 (m, 5H), 3.84 (d, *J* = 5.6 Hz, 4H), 1.79-1.75 (m, 2H), 1.54-1.24 (m, 16H), 0.92 (m, 12H). <sup>13</sup>C NMR (101 MHz, CDCl<sub>3</sub>) δ 158.20, 152.45, 136.89, 134.37, 128.16, 120.23, 119.11, 116.85, 116.76, 116.20, 116.11, 102.53, 70.90, 39.51, 30.65, 29.22, 23.98, 23.17, 14.22, 11.26.

**Zinc Phthalocyanine Zn-BL54**

In a flame dried Schlenk tube, phthalonitrile **1** (439 mg, 1.0 mmol) and Zn(OAc)<sub>2</sub>·2H<sub>2</sub>O (55 mg, 0.25 mmol) were suspended in 1-pentanol (3 mL). The mixture was stirred for 15 min under a nitrogen atmosphere, then DBU (150 μL, 1 mmol) was added, and the mixture was heated at 145 °C for a further 24 h. After cooling to room temperature, the reaction mixture was poured into MeOH, and the insoluble ZnPcs was collected by filtration on a Büchner funnel. The crude compound was thoroughly washed with MeOH and dried under reduced pressure. Subsequent purification was achieved by column chromatography (silica gel, THF/hexane 4/1). The isolated ZnPcs was then dissolved in DCM (30 mL) and reprecipitated by adding MeOH (15 mL). The title compound was obtained as a mixture of positional isomers (298 mg, 65%). UV-Vis (THF): λ<sub>max</sub>/nm (log ε) = 358 (5.01), 514 (4.44), 663 (4.67), 739 (5.32). FTIR (KBr): ν<sub>max</sub>/cm<sup>-1</sup> = 3060, 3035, 2958, 2923, 2871, 1727, 1605, 1506, 1470, 1402, 1384, 1338, 1240, 1172, 1126, 1096, 1055, 827, 762. <sup>1</sup>H NMR (400 MHz, Pyridine-d<sub>5</sub>, 80 °C) δ 9.58-9.36 (m, 4H), 9.25-9.13 (m, 1H), 8.02-7.71

(m, 4H), 7.61–7.44 (m, 20H), 7.24–7.13 (m, 20H), 4.14–4.05 (m, 16H), 1.93–1.79 (m, 16H), 1.67–1.51 (m, 16H), 1.05–0.95 (m, 24H). HRMS (MALDI-TOF):  $m/z$  calcd for  $(C_{112}H_{116}N_{12}O_8Zn)^+$  1820.833. Found: 1820.815.

#### *Copper Phthalocyanine Cu-BL57*

In a flame dried Schlenk tube, phthalonitrile **1** (439 mg, 1.0 mmol) and  $CuCl_2$  (34 mg, 0.25 mmol) were suspended in 1-pentanol (3 mL). The mixture was stirred for 15 min under a nitrogen atmosphere, then DBU (150  $\mu$ L, 1 mmol) was added, and the mixture was heated at 145 °C for a further 24 h. After cooling to room temperature, the reaction mixture was poured into MeOH, and the insoluble CuPcs was collected by filtration on a Büchner funnel. The solid was thoroughly washed with MeOH and dried under reduced pressure. Subsequent purification of the crude product was achieved by column chromatography (silica gel, DCM). The isolated CuPcs was then dissolved in DCM (10 mL) and reprecipitated by adding MeOH (20 mL). The title compound was obtained as a mixture of positional isomers (265 mg, 58%). UV-Vis (THF):  $\lambda_{max}/nm$  ( $\log \epsilon$ ) = 345 (4.97), 512 (4.43), 668 (4.59), 744 (5.25). FTIR (KBr):  $\nu_{max}/cm^{-1}$  = 3060, 3035, 2959, 2926, 2870, 1727, 1607, 1505, 1471, 1403, 1384, 1338, 1239, 1172, 1127, 1095, 1055, 825, 759. HRMS (MALDI-TOF):  $m/z$  calcd for  $(C_{112}H_{116}N_{12}O_8Cu)^+$  1819.834. Found: 1819.822.

#### *Zinc Phthalocyanine Zn-BL58*

Zn(II)-templated cyclotetramerization of phthalonitrile **2** (551 mg, 1.0 mmol) was performed as described for **Zn-BL54**. The crude product was purified by column chromatography (silica gel, THF/hexane 1/1). The isolated ZnPcs was then dissolved in DCM (12 mL) and reprecipitated by the addition of MeOH (20 mL). The title compound was obtained as a mixture of positional isomers (317 mg, 56%). UV-Vis (THF):  $\lambda_{max}/nm$  ( $\log \epsilon$ ) = 359 (4.98), 515 (4.41), 663 (4.63), 739 (5.28). FTIR (KBr):  $\nu_{max}/cm^{-1}$  = 3060, 3035, 2957, 2926, 2859, 1725, 1604, 1505, 1468, 1384, 1333, 1238, 1169, 1127, 1086, 1045, 825, 758.  $^1H$  NMR (400 MHz, Pyridine- $d_5$ ) 9.63–9.36 (m, 4H), 9.24–9.07 (m, 4H), 8.02–7.70 (m, 4H), 7.65–7.45 (m, 20H), 7.28–7.17 (m, 20H), 4.05–3.92 (m, 16H), 1.89–1.24 (m, 72H), 1.08–0.78 (m, 48H). HRMS (MALDI-TOF):  $m/z$  calcd for  $(C_{136}H_{165}N_{12}O_8Zn)^+$  2158.217. Found: 2158.211.

*Copper Phthalocyanine Cu-BL61*

Cu(II)-templated cyclotetramerization of phthalonitrile **2** (551 mg, 1.0 mmol) was performed as described for **Cu-BL57**. The crude product was purified by column chromatography (silica gel, DCM/Hexane 3/2). The isolated CuPsc was then dissolved in DCM (15 mL) and reprecipitated by the addition of MeOH (30 mL). The title compound was obtained as a mixture of positional isomers (300 mg, 53%). UV-Vis (THF):  $\lambda_{\text{max}}/\text{nm}$  ( $\log \epsilon$ ) = 345 (5.02), 507 (4.46), 665 (4.63), 745 (5.27). FTIR (KBr):  $\nu_{\text{max}}/\text{cm}^{-1}$  = 3059, 3037, 2957, 2926, 2859, 1727, 1607, 1505, 1468, 1403, 1385, 1338, 1239, 1172, 1130, 1095, 1034, 891, 824, 760. HRMS (MALDI-TOF):  $m/z$  calcd for  $(\text{C}_{136}\text{H}_{165}\text{N}_{12}\text{O}_8\text{Cu})^+$  2157,217. Found: 2157.236. Voltammograms of HTMs were measured in a 0.1 M *n*-Bu<sub>4</sub>NPF<sub>6</sub>/DCM solution, with glassy carbon working electrode, Pt wire reference, counter electrodes, ferrocene/ferrocenium (Fc/Fc<sup>+</sup>) as internal standard. Potentials were converted to the normal hydrogen electrode (NHE) by adding +0.64 V and -4.44 eV.

*Perovskite thin-film and solar cell fabrication for triple cation perovskite*

Laser scribed fluorine-doped tin oxide (FTO) coated glass substrates were cleaned with 2% Helmanex solution, water, deionized water, and isopropanol in an ultrasonic bath for 5 minutes each and 30 min of UV/O<sub>3</sub> treatment. Titanium diisopropoxide bis(acetylacetonate)(TAA) (Sigma Aldrich) in isopropanol solution (1:15 v/v) was deposited by spray pyrolysis, forming after annealing at 450°C for 30 min a 30nm thick compact TiO<sub>2</sub> layer. From a TiO<sub>2</sub> paste (Dyesol 30 NR-D) solution (1 gr. in 9 mL ethanol dilution), a mesoporous TiO<sub>2</sub> (m-TiO<sub>2</sub>) was prepared by spin-coating 45  $\mu\text{l}$  at 5000 rpm (1000 rpm/s acceleration, 20 s). Sintering at a hot plate at 500°C for 20 min followed. Then, a 20 nm SnO<sub>2</sub> was prepared dissolving SnCl<sub>4</sub> (Acros) in deionized water (12  $\mu\text{l}$  in 988  $\mu\text{l}$  water). This solution was spin-coated at 3000 rpm for 30 s (1000 rpm/s acceleration) on top of the meso TiO<sub>2</sub>. After annealing at 190°C for 1h a 20 nm thick layer was formed. For the triple cation perovskite solution 17.41 mg MABr, 27.02 mg CsI, 57.06 mg PbBr<sub>2</sub>, 178.94 mg FAI and 548.60 mg PbI<sub>2</sub> and it was dissolved in 1 ml of DMF:DMSO (0.78:0.22 v/v) to receive the following composition  $[(\text{FAPbI}_3)_{0.87}(\text{MAPbBr}_3)_{0.13}]_{0.92}(\text{CsPbI}_3)_{0.08}$ . The solution was spin-coated for the first step at 2000 rpm for 10s, followed by 5000 rpm for



30s. The antisolvent chlorobenzene (100  $\mu$ l) was dropped during the second step at 15s before finishing. Annealing the films at 100°C for 1h followed. After cooling of the samples the HTM was spin-coated on top of the samples in the same ways as described below.

*Materials for device fabrications for double cation perovskite*

Titanium diisopropoxide bis(acetylacetonate) (TAA), 4-tertbutylpyridine (tbp), tin(IV) chloride pentahydrate, bis(trifluoromethane) sulfonamide lithium salt, and FK209 [tris(2-(1H-pyrazol-1-yl)-4-tert-butylpyridine)-cobalt(III) tris(bis(trifluoromethylsulfonyl) imide)], chlorobenzene (CB), dimethylsulphoxide (DMSO), dimethylformamide (DMF) were supplied from Sigma-Aldrich. FAI, MAI and PbBr<sub>2</sub> were purchased from GreatCell Solar. Lead iodide was purchased from Alfa Aesa. Spiro-OMeTAD was purchased from Merck. PCBM was supplied from lumintac. The SnO<sub>2</sub> nanoparticle was supplied from Alfa Aesar. All of the purchased chemicals were used as received without further purification.

*Device fabrication for the double cation perovskite composition*

The chemically etched FTO glass (Nippon Sheet Glass) was cleaned with detergent solution, acetone, and ethanol. For the compact TiO<sub>2</sub> (c-TiO<sub>2</sub>) layer, TAA solution in ethanol (0.2 mL of TAA in 6 mL of anhydrous ethanol) was sprayed at 450 °C. SnO<sub>2</sub> nanoparticle were diluted in deionized water with a ratio of 1:4 and spin-coated on the c-TiO<sub>2</sub> substrate at a speed of 3000 rpm for 20 s with a ramp-up of 2000 rpm s<sup>-1</sup>. Finally the samples were heated at 150 °C for 10 min. The PCBM layer was dissolved in chlorobenzene at a concentration of 10 mg/mL and spin-coated on the SnO<sub>2</sub> layer at a speed of 3000 rpm for 20 s with a ramp-up of 2000 rpm s<sup>-1</sup>. Finally the samples were heated at 100 °C for 10 min. Afterwards the perovskite solution (The ratio of PbI<sub>2</sub>, MAI, FAI, PbBr<sub>2</sub> is 1: 0.16: 0.84: 0.11) was spin-coated. The concentration of PbI<sub>2</sub> is 1.38 mmol/mL, the MAI is 0.305 mmol/mL which was additionally added into the perovskite solution. The solvent used for the perovskite solution is composed by DMSO and DMF with a ratio of 1:4. The layers are spin-coated on the substrates at 1000 rpm for 10s and 5000 rpm for 30s, respectively. 200  $\mu$ L of chlorobenzene was dropped in 10 s at 5000 rpm. Then the

perovskite films were annealed at 150 °C for 10 min. For Spiro-OMeTAD, The solution was prepared by dissolving 75 mg of Spiro-OMeTAD (Merck) with additives (23 µL of Li-bis(trifluoromethanesulfonyl), 10 µL of FK209 and 39 µL of 4-tert-butylpyridine) in 1 mL of chlorobenzene. The concentration of **BL**-series HTMs was 20 mM. The molar ratio of additives for **spiro-OMeTAD** and each doped BL-HTM solution was 0.5 for LiTFSI from a 1.8 M stock solution in acetonitrile, 3.3 for tBP and 0.03 for FK209 from a 0.25 M stock solution in acetonitrile. The HTM layers were formed by spin-coating the solution at 4000 rpm for 20 s and followed by the deposition of the 70 nm thick Au electrode by a thermal evaporation. All the preparative work to deposit PCBM, perovskite and Spiro-OMeTAD was done inside the glove box filled with nitrogen to minimize the influence of moisture.

#### *Thin-film characterization*

A Lambda 950S spectrophotometer (PerkinElmer, Inc.) was used to record the absorbance spectra. A Fluorolog TCSPC (HORIBA, Ltd.) was used to measure time-resolved photoluminescence (TRPL) and photoluminescence (PL) spectroscopy, with a picosecond laser with an excitation wavelength of 640 nm and 475nm, respectively. 760nm was the detection wavelength of time-resolved photoluminescence. An AXIS Nova, Kratos Analytical Ltd, UK ultraviolet photoelectron spectrometer (UPS), equipped with a He-I source ( $h\nu = 21.22$  eV) was used to measure the valence band energy, Fermi level and the work function. The Fermi level of the samples was referenced to that of Au which was in electrical contact with a sample in UPS measurements. A FEI Teneo Schottky Field Emission SEM was used for recording the scanning electron microscopy (SEM) images by an in-lens detector of at tension of 1.5 kV for top-view imaging and 1 kV for cross-section analysis. Conductivity measurements were carried out using the 2.5 µm channel (channel width 10 mm and height 40 nm) of an organic field-effect transistor (OFET, Fraunhofer IPMS) with two/contact electrical conductivity set-up. The substrates were cleaned with 20 min oxygen plasma following the HTM deposition by spin-coating at 4000 rpm for 20s. The measurements were carried by sweeping from -10 to 10 V (source-drain voltage) at a scan rate of 1 V s<sup>-1</sup> with a Keithley 2612A. The data were recorded with

the KickStart software program and the conductivity was calculated from a linear fit of the  $J$ - $V$  measurement and Ohm's law. Water-contact angle measurements on the top of the thin layers of the HTMs were measured using the KRUSS DSA100 optical contact angle instrument. Measurements were conducted using the sessile drop program with a 0.5 mm needle size. Drops of water at a rate of 0.01 mL/min and a volume of 12  $\mu$ L were created. Substrates were prepared by spin coating 20 mM HTM solutions onto glass/perovskite layers. The image was recorded 1 s after the interaction of the water drop with the HTM layer. Two-dimensional wide-angle X-ray scattering (2D-WAXS) samples were prepared by spin-coating on silicon wafers the octasubstituted MPCs with the same solution concentration and processing method than in the device fabrication. Two-dimensional wide-angle X-ray scattering (2D-WAXS) patterns represented in reciprocal lattice space were performed at SPring-8 on beamline BL19B2. The samples were irradiated with X-ray energy of 12.39 keV ( $\lambda = 1 \text{ \AA}$ ) at a fixed incident angle on the order of  $0.12^\circ$  through a Huber diffractometer. The 2D-WAXS patterns were measured with a two-dimensional image detector (Pilatus 300K).

#### *Device characterization*

The EQE was measured with the IQE200B (Oriel) without bias light. Before measuring the  $J - V$  curves a NREL-certified KG5-filtered Si-reference diode was used for light intensity calibration. Then a 2400 Keithley system with a Xe-lamp Oriel sol3A sun simulator (Newport Corporation) was used for the  $J - V$  measurements. The system was calibrated to AM1.5G standard conditions by using an Oriel 91150 V reference cell ( $J - V$  curves scan rate of 50 mV s<sup>-1</sup> and 10 mV voltage step. A shadow mask with a metal aperture of 0.16 cm<sup>2</sup>, defined the active area of the cell. All cells were measured without encapsulation at room temperature, and without antireflective light coating. A constant rate of 10 mV s<sup>-1</sup> and 10 mV voltage step was applied for reversed bias after 5s under light soaking. A LED power source was used for the stability test which performed as maximum power tracking under 100 mW cm<sup>-2</sup>. During the measurement a constant temperature of 25°C was kept by a cooling system. 0% humidity was ensured through encapsulation in a measurement box which was purged with nitrogen gas.

## Supporting Figures

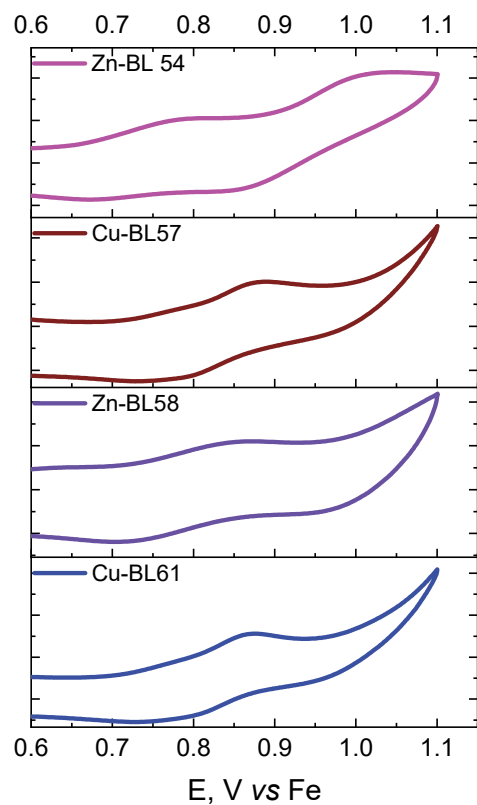
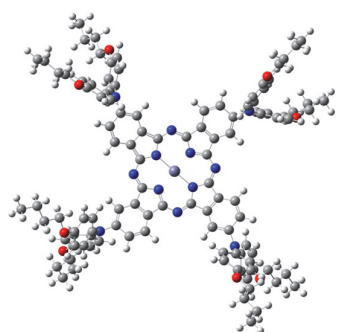


**Figure E. 1.** Cyclic Voltammetry of undoped HTMs in dichloromethane solution containing 0.1M  $n\text{-Bu}_4\text{NPF}_6$  as a supporting electrolyte. Oxidation potential was calibrated against ferrocene used as an internal standard.

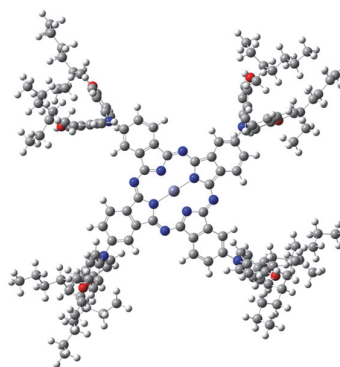
**Table E. 1.** Energy-cut off, work-function, and valence band energy level extracted from the corresponding UPS spectra of doped HTM layers deposited on top of perovskite.

HTM	$E_{\text{HOMO}}^{\text{a}}$ (eV)	Energy cut-off <sup>b</sup> (eV)	WF <sup>b</sup> (eV)	Ionization potential, IP <sup>b</sup> (eV)
<b>spiro-OMe-TAD</b>		-0.50	-4.79	-5.29
<b>Zn-BL54</b>	-5.37	-1.02	-4.49	-5.51
<b>Cu-BL57</b>	-5.48	-0.96	-4.65	-5.61
<b>Zn-BL58</b>	-5.36	-1.16	-4.74	-5.44
<b>Cu-BL61</b>	-5.46	-1.16	-4.41	-5.57

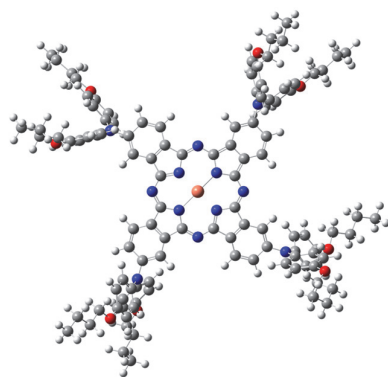
<sup>a</sup> HOMO obtained by cyclic voltammetry, <sup>b</sup> values extracted from the corresponding UPS measurements.



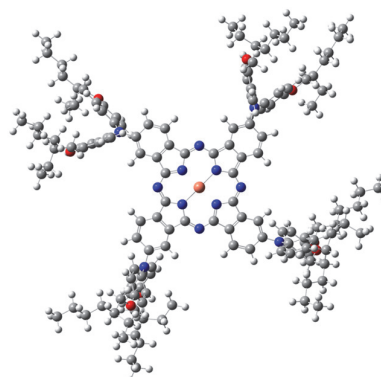
Zn-BL 54



Cu-BL 57



Zn-BL 58



Cu-BL 61

**Figure E. 2.** Optimized molecular structures. Gaussian 09W, BL<sub>3</sub>YP/6-311G.

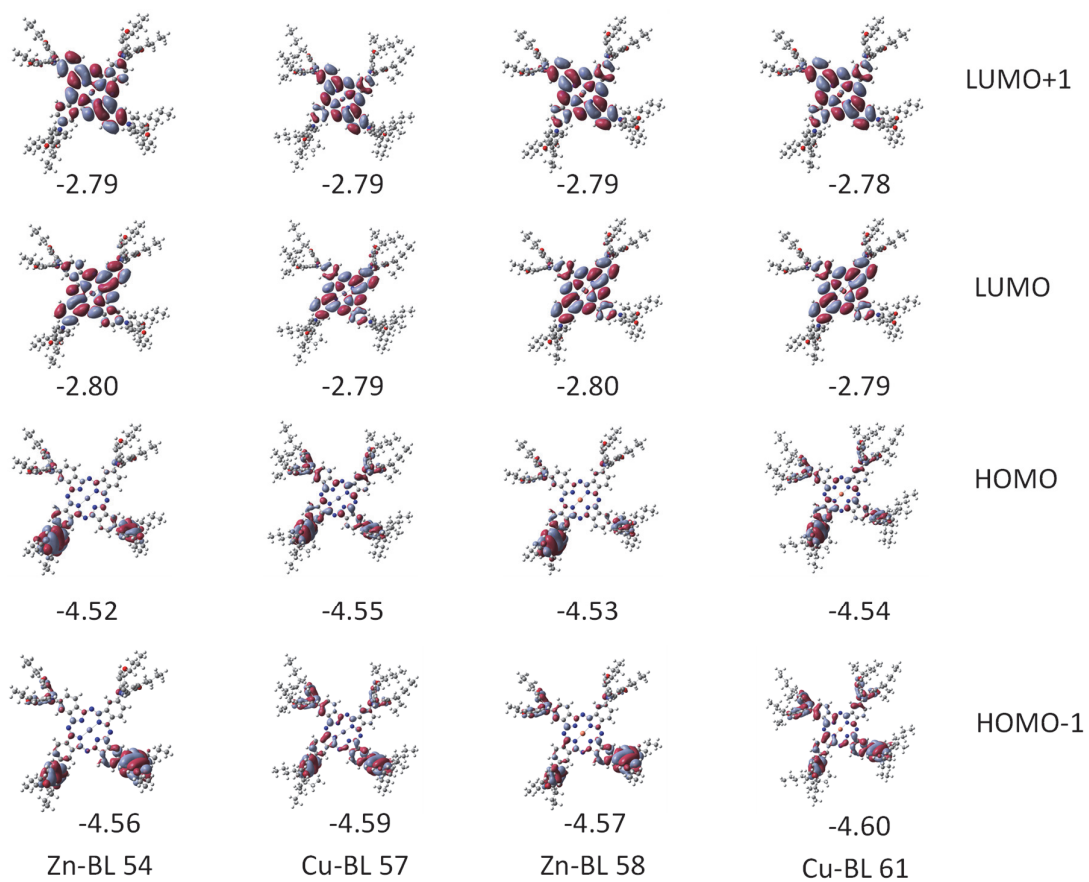


**Figure E. 3.** The electron density distribution for LUMO+1, LUMO, HOMO, and HOMO-1, for all the HTMs.

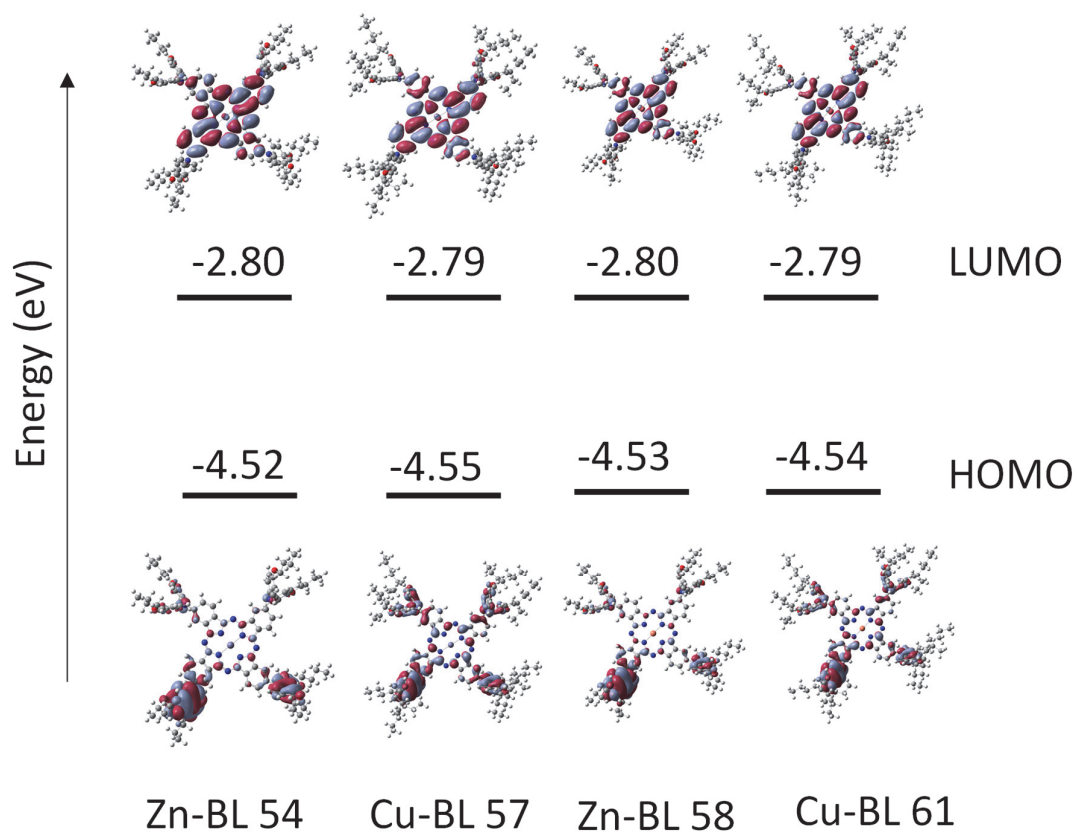


**Figure E. 4.** Scheme showing the frontier molecular orbitals and their respective energies of BL54, BL57, BL58, and BL61 MPCs calculated with DFT B<sub>3</sub>LYP in 6-31G basis set.

**Table E. 2.** The values of HOMO, LUMO, and HOMO-LUMO energy gap ( $\Delta$ FUND) calculated using DFT and MP2 methods with two basis sets (3-21G and 6-31G).

	Zn-BL 54	Cu-BL 57	Zn-BL 58	Cu-BL 61
LUMO <sub>+1</sub>	-2.79	-2.79	-2.79	-2.78
LUMO	-2.80	-2.79	-2.80	-2.79
HOMO	-4.52	-4.55	-4.53	-4.54
HOMO <sub>-1</sub>	-4.56	-4.59	-4.57	-4.60



**Table E. 3.** Percentage of HTM quenching calculated from the steady-state photoluminescence spectra (considered the perovskite emission as 100%).

HTM	%
<b>spiro-OMeTAD</b>	30
<b>Zn-BL45</b>	98
<b>Cu-BL57</b>	99
<b>Zn-BL58</b>	83
<b>Cu-BL61</b>	89

**Table E. 4.** Fitted decay parameters extracted from time-resolved photoluminescence (TrPL) spectra.

Name	$\tau_1$ (ns)	$\tau_2$ (ns)
Perovskite	139.50±11.13	336.05±10.84
<b>spiroOMeTAD</b>	4.28±0.24	12.18±0.44
<b>Zn-BL54</b>	35.08±1.97	79.49±22.78
<b>Cu-BL57</b>	5.08±0.14	32.64±0.23
<b>Zn-BL58</b>	48.42±3.28	143.95±13.46
<b>Cu-BL61</b>	22.63±1.06	101.67±1.25

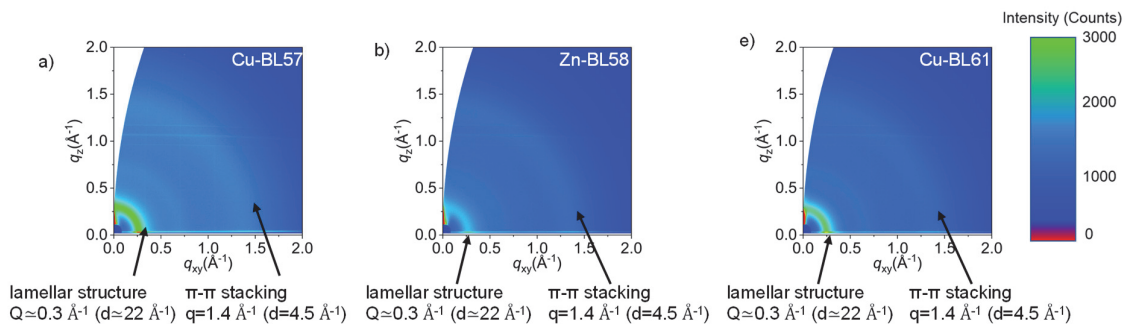


**Figure E. 5.** GIWAXS pattern of the films coated on a silicon wafer. a) Cu-BL57 b) Zn-BL58 c) Cu-BL61.

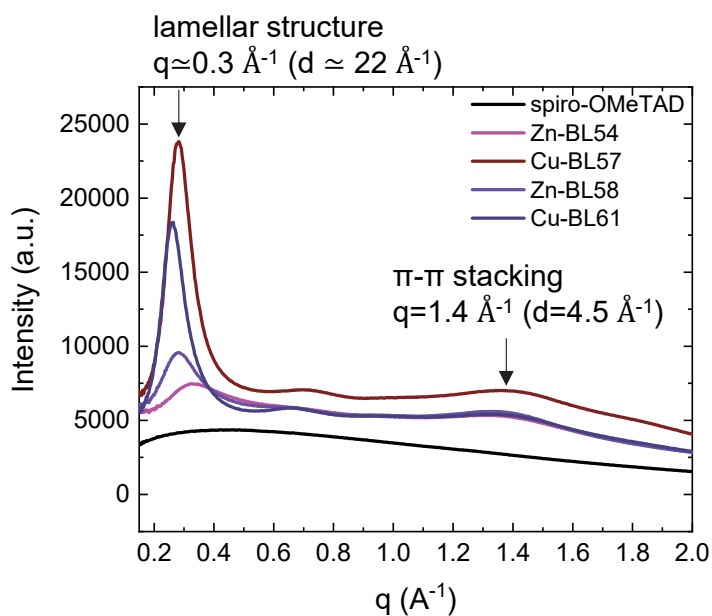


**Figure E. 6.** Lamellar structure and  $\pi$ - $\pi$  stacking of the HTMs extracted from the GIWAXS data.

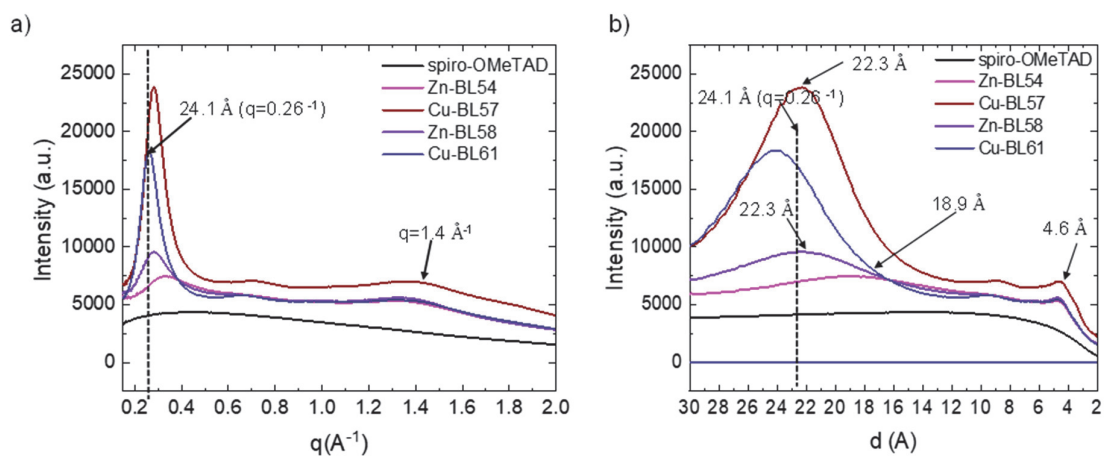


**Figure E. 7.** a) Azimuth integrated intensity profile calculated from 2D GIWAXS spectra for the different HTMs and b) lattice distance calculated for HTMs from 2D GIWAXS spectra.

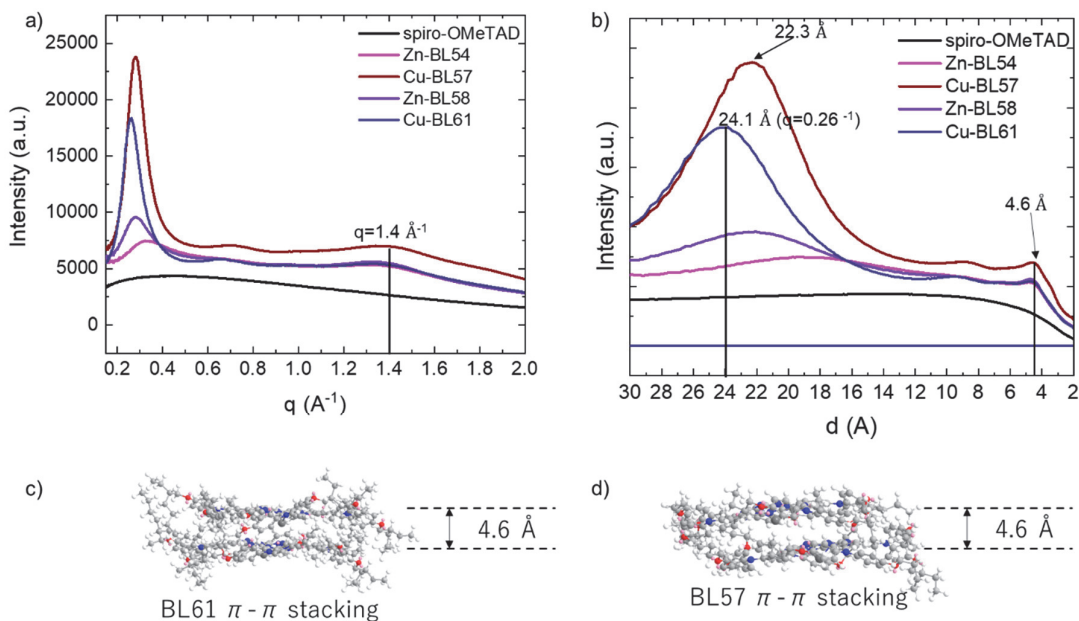


**Figure E. 8.** a) calculation of  $d$ -spacing for  $\pi$ - $\pi$  stacking structure and the intercolumnar organization b) lattice distance calculated for HTMs from 2D GIWAXS spectra,  $\pi$ - $\pi$  stacking distance calculated from MM2 simulation for c) **Cu-BL61** and d) **Zn-BL57**.

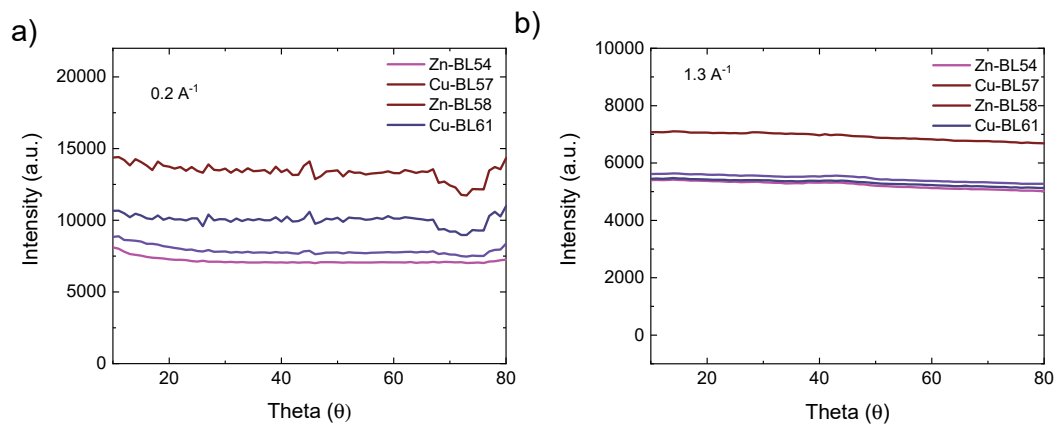


**Figure E. 9.** Azimuth integration as a function of theta at an approx. integrated peak a)  $q = 0.3 \text{ \AA}^{-1}$ , b)  $q = 0.7 \text{ \AA}^{-1}$  c)  $q = 1.4 \text{ \AA}^{-1}$

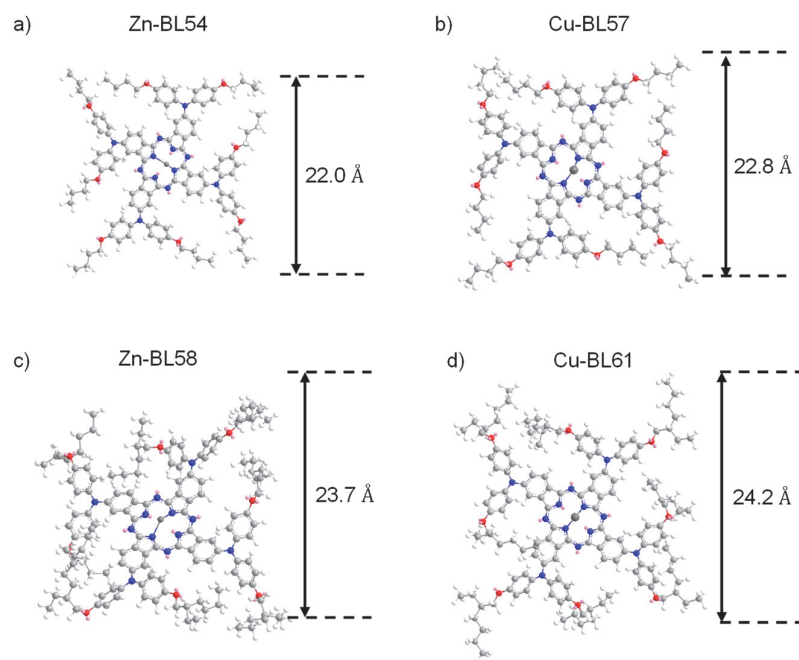


**Figure E. 10.** The simulated molecular size of the HTMs.

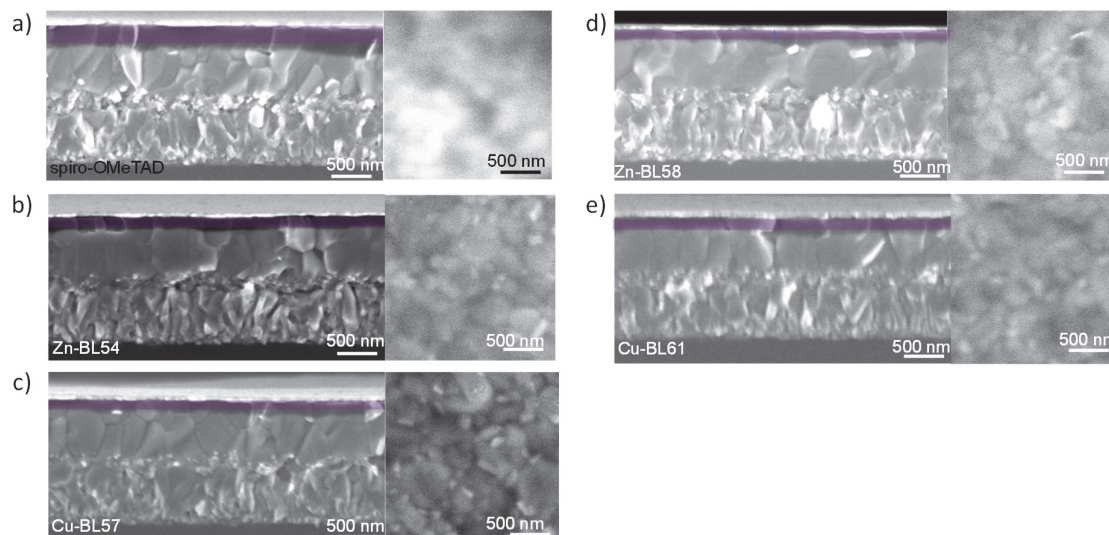


**Figure E. 11.** Cross-section SEM images of the devices and top-view SEM images of the doped HTM thin films. The HTM layer is highlighted in purple.

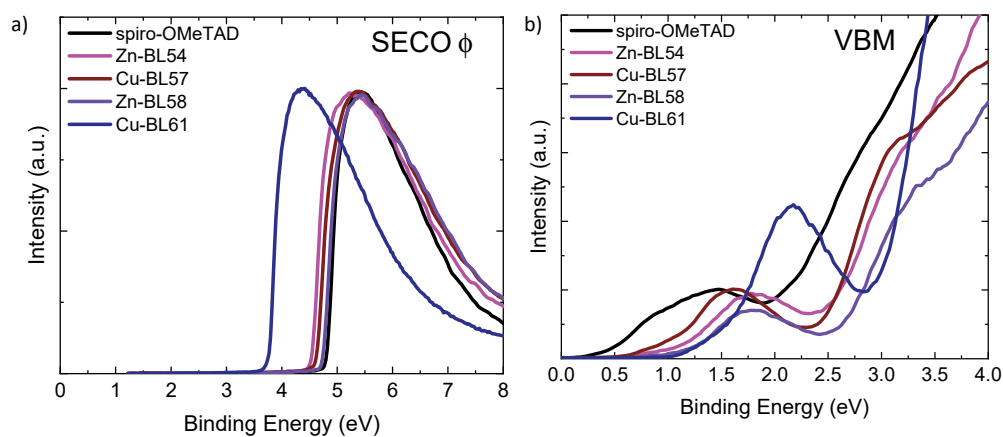


**Figure E. 12.** a) Secondary-electron cut-off work function of doped HTM layers on top of triple cation perovskite b) Valence band spectra of doped HTM layers on top of perovskite.

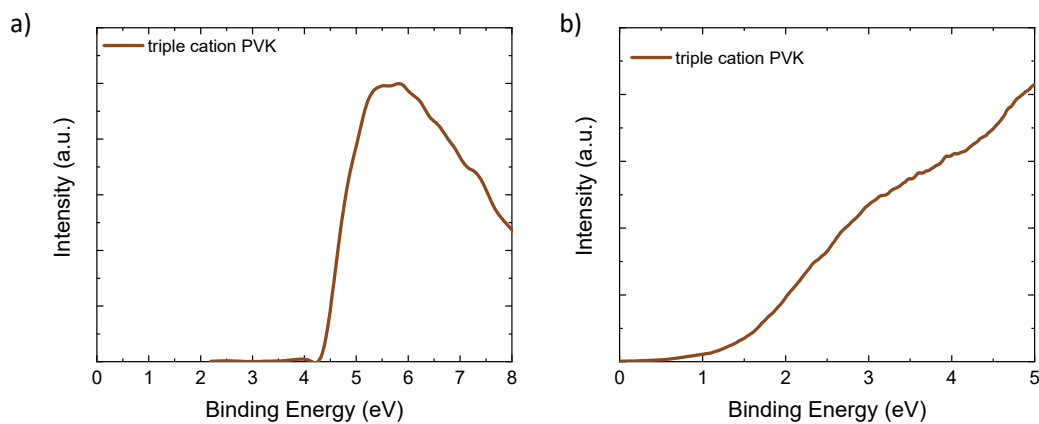


**Figure E. 13.** a) Secondary-electron cut-off work function of triple cation perovskite b) Valence band spectra of triple cation perovskite.

**Table E. 5.** Energy cut-off, work function extracted from UPS measurements, and calculated ionization potential for triple cation perovskite.

HTM	Energy cut-off (eV)	WF (eV)	Ionization potential, IP (eV)
PVK	-1.32	-4.38	-5.70

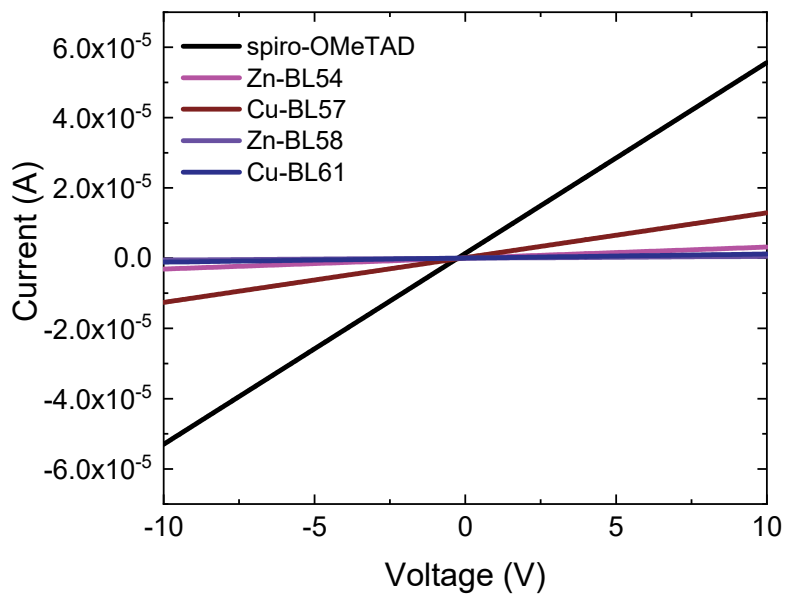


**Figure E. 14.** Lateral conductivity of the doped HTM layers measured on OFET substrates.

**Table E. 6.** Lateral conductivity values of doped HTMs calculated from their respective I-V curves.

HTM	$\sigma$ (S cm <sup>-1</sup> )
<b>spiro-OMeTAD</b>	3.4x10 <sup>-4</sup>
<b>Zn-BL54</b>	1.96x10 <sup>-5</sup>
<b>Cu-BL57</b>	7.97x10 <sup>-5</sup>
<b>Zn-BL58</b>	3.22x10 <sup>-6</sup>
<b>Cu-BL61</b>	7.3x10 <sup>-6</sup>

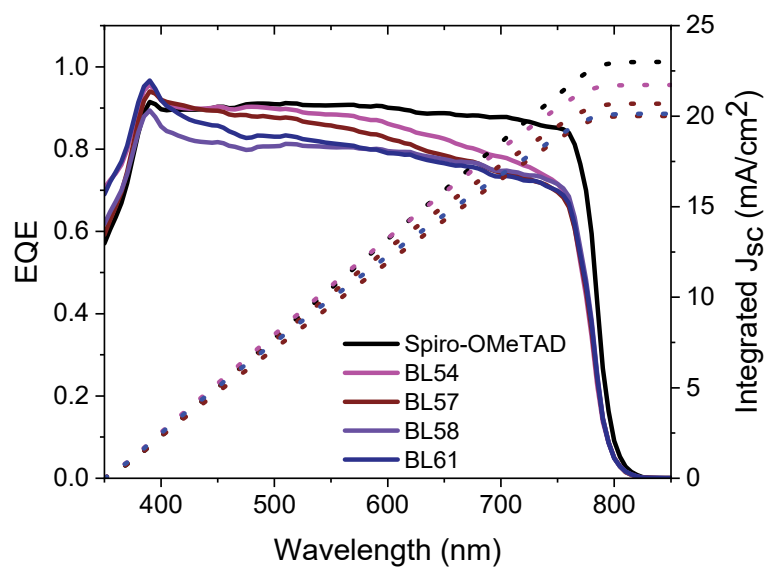


**Figure E. 15.** EQE spectra and calculated short-circuit current density integrated from the corresponding EQE of the most efficient devices with triple cation perovskite.

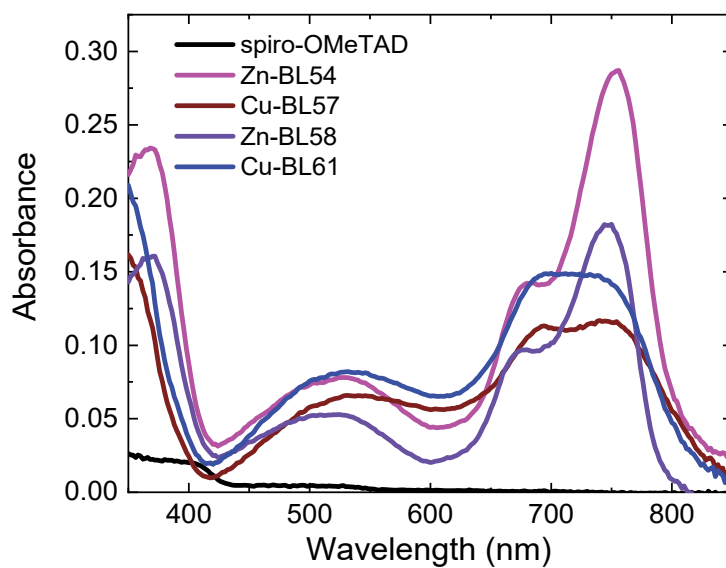


**Figure E. 16.** Absorbance spectra of the doped HTM films on a glass substrate.



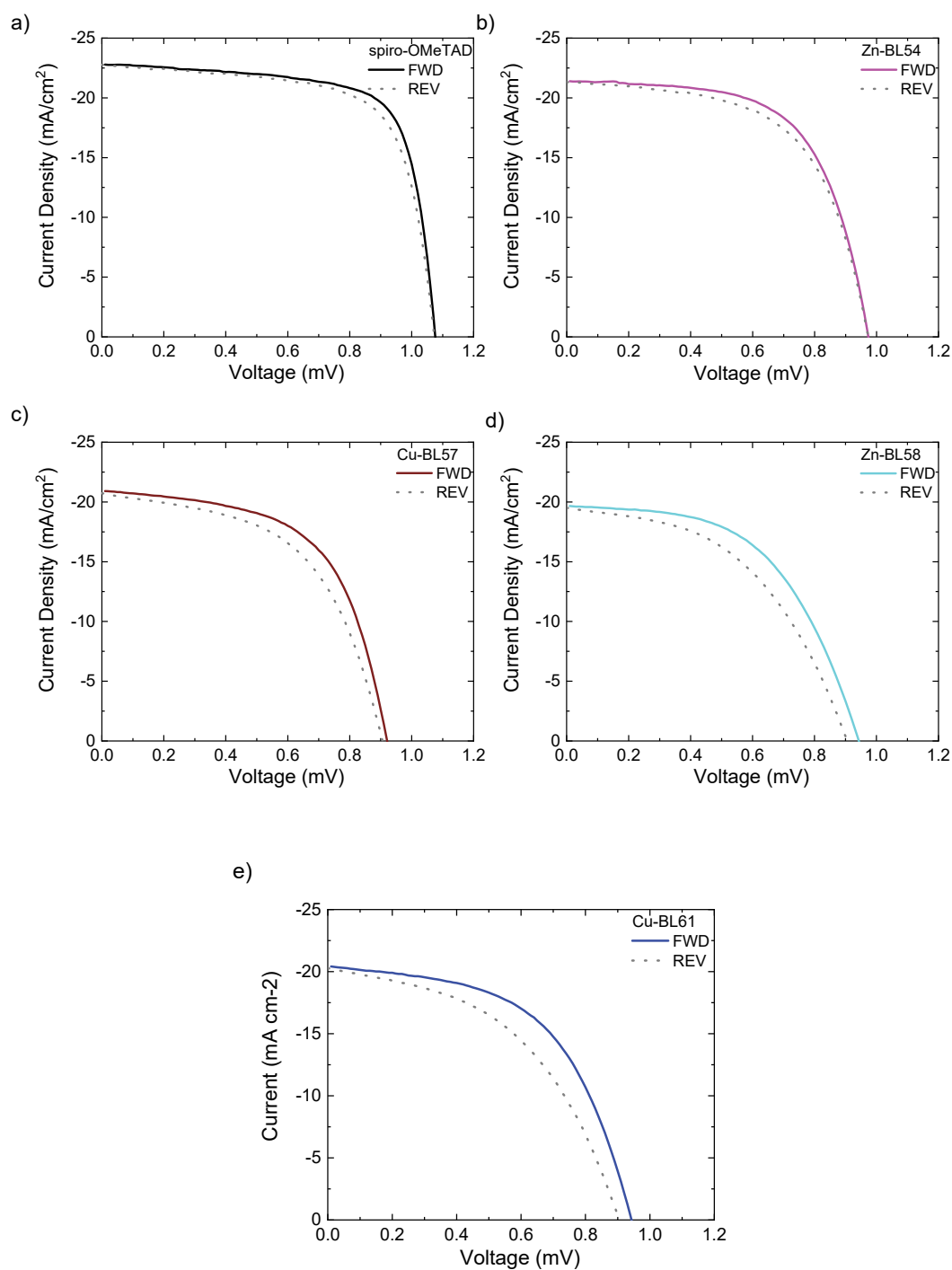


**Figure E. 17.** Hysteresis of all devices employing the different HTMs. a) **spiro-OMeTAD**, b) **Zn-BL54**, c) **Cu-BL57**, d) **Zn-BL58** and e) **Cu-BL61**.

**Table E. 7.** *J-V* parameters for hysteresis curve and calculated hysteresis index. FWD: from  $J_{sc}$  to  $V_{oc}$  scan direction and REV: from  $V_{oc}$  to  $J_{sc}$  scan direction.

HTM	Scan direction	$J_{sc}$ (mA/cm <sup>2</sup> )	$V_{oc}$ (V)	$FF$	PCE (%)	Hysteresis index
<b>spiro-OMe-TAD</b>	FWD	-22.78	1.073	0.69	16.79	0.05
	REV	-22.79	1.076	0.72	17.64	
<b>Zn-BL54</b>	FWD	-21.34	0.948	0.59	12.22	0.05
	REV	-21.40	0.973	0.62	12.90	
<b>Cu-BL57</b>	FWD	-20.73	0.906	0.53	10.04	0.07
	REV	-20.96	0.921	0.58	11.20	
<b>Zn-BL58</b>	FWD	-19.51	0.905	0.48	8.46	0.14
	REV	-19.66	0.943	0.54	9.91	
<b>Cu-BL61</b>	FWD	-20.29	0.905	0.47	8.76	0.16

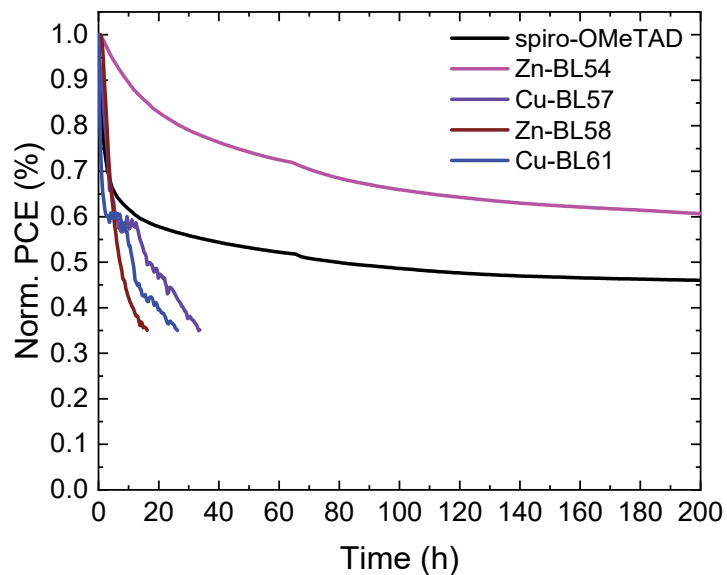


**Figure E. 18.** Long-term stability of unencapsulated triple cation devices measured under continuous light illumination at 25°C in a nitrogen atmosphere up to 200 h.

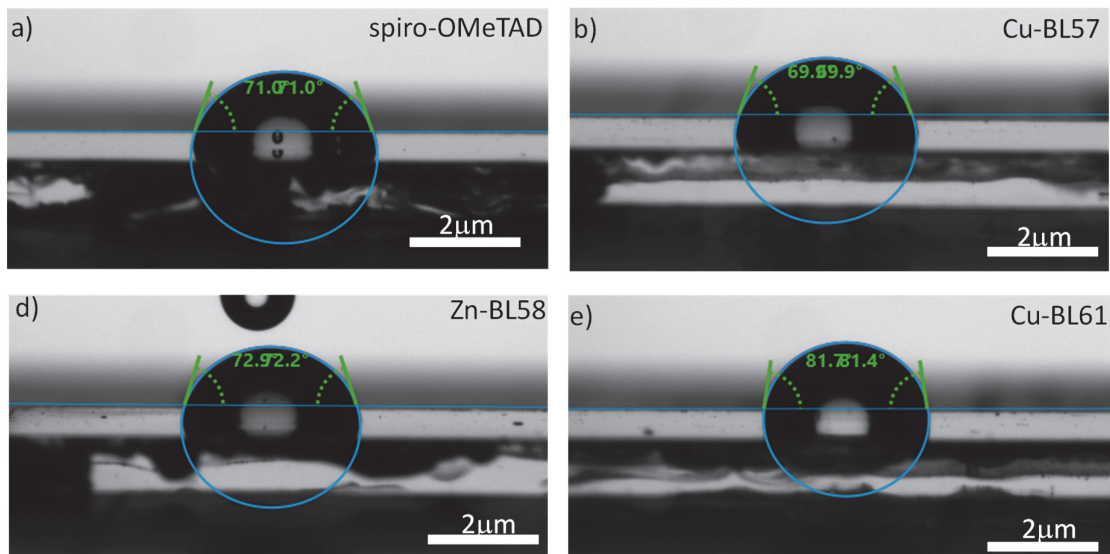


**Figure E. 19.** The water contact angle was measured on glass/perovskite/doped HTMs samples.

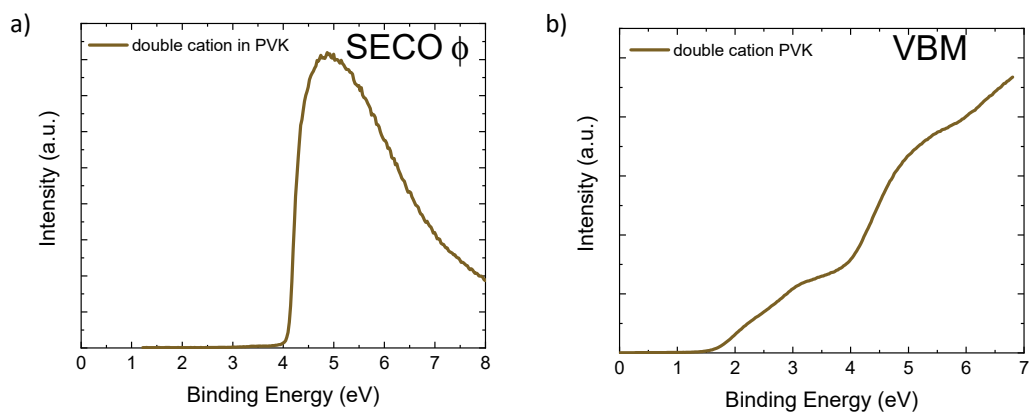


**Figure E. 20.** a) Secondary-electron cut-off work function of the double cation perovskite b) Valence band spectra of double cation perovskite.

**Table E. 8.** Energy cut-off, work function extracted from UPS measurements, and calculated ionization potential for double cation perovskite.

HTM	Energy cut-off (eV)	WF (eV)	Ionization po- tential, IP (eV)
PVK	-1.67	-4.08	-5.75

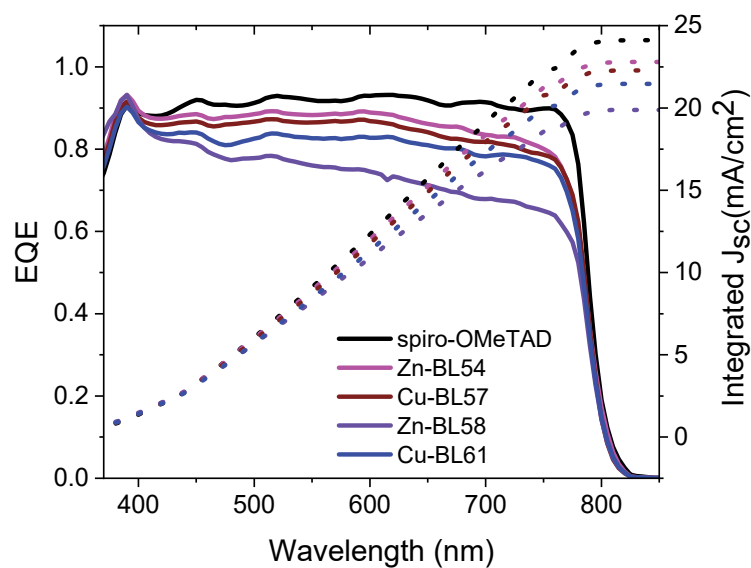


**Figure E. 21.** EQE spectra and calculated short-circuit current density integrated from the corresponding EQE of the most efficient double cation perovskite devices.

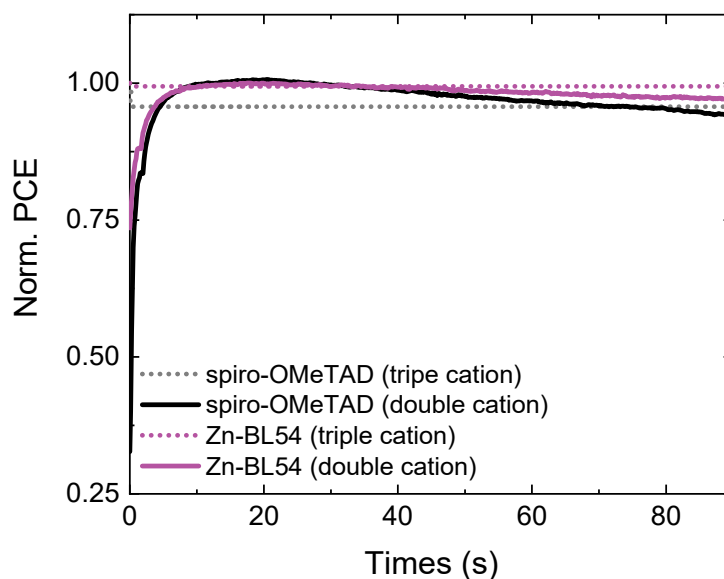


**Figure E. 22.** Maximum power point tracking (MPPT) of triple/double cation perovskite devices with the reference **spiro-OMeTAD** and **Zn-BL54** measured in unencapsulated devices under  $N_2$  atmosphere.

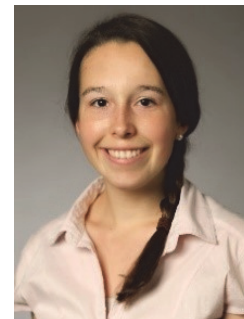


**Curriculum Vitae**

---

# Curriculum Vitae

Nadja Klipfel



## CONTACT INFORMATION

Nadja Klipfel

Chemin du Vieux Canal 15

1950 Sion

Email: [nadja.klipfel@outlook.de](mailto:nadja.klipfel@outlook.de)

+41 76 367 63 37

## STRENGTHS

### **Project Management**

Handling multiple projects with larger teams at a time, ensuring their deadlines, and offering training for equipment's and safety rules in my role as the lab safety delegate

### **Creative Project Solving/Flexibility**

Adjusting to changing situations fast and using innovative solutions to unforeseen problems to achieve the results or keep the lab running.

### **Organization Skills**

Organizing lab cleaning, inventory, maintenance work within our group to ensure a good working environment.

### **Representative and Trust Person**

Representation of the early-stage researchers from my European project in front of the board, adviser, and person of trust towards colleagues to help them solve their challenges.

## SKILLS

**Soft:** analytic reasoning, out-of-the-box thinking, learning agility, teamwork, communication, project ownership, responsibility

**IT:** C++, PPT, Origin Lab, material analysis software



**Technical skills:** wet lab, organic synthesis, monomer chemistry, material science, XRD, SEM, XPS/UPS, GWAXS, GC/MS, HPLC, XRD, glovebox, safety in lead lab, Raman, AFM

**Writing Skills:** 3 publications as main author and 3 publications as co-author

**Communication Skills:** *Prize* for best research presentation in front of international audience, giving chemistry classes for EPFL students, regular project update to project manager

**Languages:** at ease with four languages, German: Mother tongue, English: C1, French: B2, Spanish: A2

## CORE EXPERIENCE

### **GMF EPFL, Switzerland, Ph.D. in chemistry and chemical engineering**

-**Thesis:** Optimization of crystal growth/ morphology of perovskite by thermal evaporation

-*Marie Curie Scholarship* including Ph.D. funding and training workshops all over Europe within the network, including 4-month research stay in Spain at Universidad Jaume I

-Coordinator of Lab Safety, ensuring a safe and healthy work environment

-Launched collaborations with international teams between research groups of different universities all over the world, allowing an easier exchange of knowledge and data

### **ISIC Teaching assistant**

-Led organic chemistry teaching sessions and analytical chemistry lab with up to 100 students in French and English

### **BASF Plant Optimization of Specialty Monomer Plant**

-Executed changes by leading a team of production workers, engineers, business associates, managed research experiments with R&D department, implemented modification led to a significant gain in daily revenue, presented business case to BASF vice presidents, and filed a patent

## EDUCATION

- 2018-present**            **Ph.D. in Chemistry and Chemical Engineering, EPFL, Lausanne**  
Lab: Group for molecular engineering of functional materials
- 2015-2017**            **Master of Chemistry at LMU Munich, Germany**  
-*Scholarship* for research stays at the University of Heidelberg and Sorbonne Paris
- 2012-2015**            **B.Sc. of Chemistry at LMU Munich, Germany**  
-Lab: Chemical Biology and Genetics
- 2008-2011**            **Abitur at Leibniz Gymnasium, Germany**  
-Focus: Science, *Prize* for best achievements in Biology
- 2007-2008**            1 year stay at Pelham High-School Alabama, USA

### INTERESTS

Rock climbing, skiing, cooking, member of the club Montagne EPFL, member of the Swiss Chemical Society, urban gardening

# List of Publications

1. Meenakshi Pegu, Samrana Kazim, Abolfazl Ghaderian, **Nadja Klipfel**, Hiroyuki Kanda, Mohammad Khaza Nazeeruddin, Shahzada Ahmad. Fluorinated-triazatruxene based hole transporting material for stable perovskite solar cells. *Manuscript in preparation*.
2. Meenakshi Pegu, Samrana Kazim, **Nadja Klipfel**, Hiroyuki Kanda, Mohammad Khaza Nazeeruddin, Shahzada Ahmad. Interface engineering of the perovskite layer by trifluoroacetyl-carbazole based small molecule for efficient and stable solar cells. *Manuscript in preparation*.
3. **Nadja Klipfel**, Muhammed Harris, Albertus Sutanto, Naoyuki Shibayama, Hiroyuki Kanda, Cansu Igci, Cristina Momblona, Ahmad Shahzada, Mohammad Khaja Nazeeruddin. Structural and optoelectrical characterization of Single-source evaporation of phase pure CsFAPb<sub>3</sub> and FAPb<sub>3</sub> perovskite thin films. *Manuscript in preparation*.
4. **Nadja Klipfel**, Jianxing Xia, Pavel Čulík, Simonetta Orlandi, Marco Cavazzini Naoyuki Shibayama, Hiroyuki Kanda, Cansu Igci, Abdullah M. Asiri, Cristina Momblona, Gianluca Pozzi, Mohammad Khaja Nazeeruddin. Zn(II) and Cu(II) tetrakis(diarylamine)phthalocyanines as hole-transporting materials for perovskite solar cells. *Manuscript under review*.
5. **Nadja Klipfel**, Agustin O. Alvarez, Hiroyuki Kanda, Albertus Adrian Sutanto, Cansu Igci, Cristina Roldan-Carmona, Cristina Momblona, Francisco Fabregat-Santiago, Mohammad Khaja Nazeeruddin. C<sub>60</sub> thin films in perovskite solar cells: efficient or limiting charge transport layer. *ACS Appl. Energy Mater.* 2022, XXXX, XXX, XXX-XXX. <https://doi.org/10.1021/acsaem.1c03060>.
6. Jianxing Xia, Marco Cavazzini, Cansu Igci, Cristina Momblona, Simonetta Orlandi, Bin Ding, Yi Zhang, Hiroyuki Kanda, **Nadja Klipfel**, Sher Bahadar Khan, Abdullah Mohamed Asiri, Paul Joseph Dyson, Gianluca Pozzi, Mohammad Khaja Nazeeruddin. Molecular Engineering of Thienyl Functionalized Ullazines as Hole-Transporting Materials for Perovskite Solar Cells. *Sol. RRL*, 2021, 2100926. <https://doi.org/10.1002/solr.202100926>.
7. **Nadja Klipfel**, Hiroyuki Kanda, Albertus Sutanto, Mounir Mensi, Cansu Igci, Klaus Leifer, Keith Brooks, Sachin Kinge, Cristina Roldan-Carmona, Cristina Momblona, Paul J. Dyson, Mohammad Khaja Nazeeruddin. Mechanistic insights into the role of the bis(trifluoro-methanesulfonyl)imide ion in co-evaporated p-i-n perovskite solar cells. *ACS Appl. Mater. Interfaces* 2021, 13, 44, 5245-52460. <https://doi.org/10.1021/acsaami.1c10117>.

8. Jorge Labella, Cristina Momblona, **Nadja Klipfel**, Hiroyuki Kanda, Sachin Kinge, Mohammad Khaja Nazeeruddin and Tomás Torres. Subphthalocyanine-based electron-transport materials for perovskite solar cells. *J. Mater. Chem. C*, 2021, **9**, 16298-16303, <https://doi.org/10.1039/D1TC02600C>.
9. Nadja Klipfel, Cristina Momblona, Hiroyuki Kanda, Naoyuki Shibayama, Yuiga Nakamura, Mounir Driss Mensi, Cheng Lui, Cristina Roldan-Carmona, Mohammad Nazeeruddin. Crystallographically Oriented Perovskites via Thermal Vacuum Deposition. *Sol. RRL* 5.8 (2021):2100191, <https://doi.org/10.1002/solr.202100191>.
10. Hiroyuki Kanda, Naoyuki Shibayama, Mousa Abuhelaiqa, Sanghyun Paek, Ryuji Kaneko, **Nadja Klipfel**, Albertus Adrian Sutanto, Cristina Roldán Carmona, Aron Joel Huckaba, Hobeom Kim, Cristina Momblona, Abdullah M. Asiri and Mohammad Khaja Nazeeruddin. Gradient band structure: high performance perovskite solar cells using poly(bisphenol A anhydride-co-1,3-phenylenediamine). *J. Mater. Chem. A*, 2020, **8**, 17113-17119, <https://doi.org/10.1039/DoTA05496H>.
11. Hiroyuki Kanda, Naoyuki Shibayama, Aron Joel Huckaba, Yonghui Lee, Sanghyun Paek, **Nadja Klipfel**, Cristina Roldán-Carmona, Valentin Ianis Emmanuel Queloz, Giulia Grancini, Yi Zhang, Mousa Abuhelaiqa, Kyung Taek Cho, Mo Li, Mounir Driss Mensi, Sachin Kinge and Mohammad Khaja Nazeeruddin. Band-bending induced passivation: high performance and stable perovskite solar cells using perhydropoly(silazane) precursor. *Energy Environ. Sci.*, 2020, **13**, 1222-1230, <https://doi.org/10.1039/C9EE02028D>.